EVALUATION OF PREVOST'S ELASTO-PLASTIC MODELS

by

Ahmed Derradji-Aouat

A thesis submitted to
the School of Graduate Studies
in partial fulfillment of the requirements for the
degree of Master of Applied Science
in
Civil Engineering

Department of Civil Engineering
Faculty of Engineering
University of Ottawa

ISBN 0-315-53785-X

SUMMARY

In recent years, considerable attention has been given to the formulation of constitutive equations for soil media. Elastic models, endochronic models, and many elasto-plastic models with various degrees of complexity have been developed. Prevost (1986) proposed a multisurface plasticity model to describe the soil nonlinearity, elasto-plasticity, hysteretic behaviour and stress path dependency including shear stress induced anisotropy. Yielding is controlled by a set of nested yield surfaces which are described as a family of ellipsoidal cylindrical surfaces in the principal stress space. During shearing, the motion of the yield surfaces was expressed by a combination of the isotropic and kinematic hardening rules of plasticity. The model requires a set of parameters related to each yield surface. These are the geometric configuration of the yield surfaces and their associated plastic parameters. Prevost used the model to analyze a number of soil-structure interaction problems. However, the verification of the capabilities of the model has been carried out by Prevost alone. This is due to the complexity of the model, and the insufficient information in the literature regarding the techniques used for the identification of the model parameters, the details of the constitutive equations and the hardening rule.

The objective of this research work is to asses merits and shortcomings of Prevost's model. The mathematical derivation of the model parameters, the constitutive equations and the hardening rule are also presented in detail. The accuracy and the versatility of the model are highlited by comparing the model predictions with the actual tests data.

A laboratory testing program provided some of the data to be used in this research work. The soil tested was a crushed quartz sand. The following tests were performed.

1. A series of drained conventional triaxial compression, CTC, tests carried out on loose, medium dense and dense sands at different confining pressures.

2. A series of undrained conventional triaxial compression, CTC, tests carried out on loose, medium dense and dense sands at different confining pressures.

3. A series of isotropic compression, ICT, tests carried out on loose,medium dense and dense sands.

4. A series of drained and undrained conventional triaxial extension, CTE, tests carried out on loose, medium dense and dense sands.

5. A stress path test carried out on a dense sample under 137.89 kPa of initial mean stress.

In addition to these tests, the published data of Montreal Workshop (1980) were used to generate a larger data base for the model evaluation. Moreover, Tatsuoka and Ishihara's (1974) cyclic tests were used to investigate the capabilities of the model in simulating the cyclic behaviour of Fuji river sand.

The model was coded into three computer programs. The details of these programs are given in the following:

1. PARAMETER is a computer program developed for the purpose of the determination of the initial model parameters for both clay and sand in drained and undrained conditions. The program also permits the prediction of the initial model parameters of any other test from the given triaxial compression and extension tests.

2. PREDICTIONS is a three dimensional stress driven computer program. It simulates the soil behaviour in drained conditions for monotonic or cyclic loading. A numerical solution technique is proposed for the implementation of the model in a computer program. The objective of this solution technique is to control the given stress increment so that the overlapping of the yield surfaces will be avoided.

3. SIMULATIONS is a three dimensional stress driven computer program. It allows for the model predictions of the soil behaviour in undrained tests. Since the effect of the volumetric strain on the initial geometric configuration of the yield surfaces is absent, the values of the converged effective stress increments were computed from the zero volumetric strain condition, $\epsilon_v = 0$.

The initial model parameters of the crushed quartz sand, Ottawa sand and Fuji river sand were determined. These initial parameters were obtained by combining the triaxial compression and extension test results. The smooth experimental data were approximated by linear segments of a constant tangent moduli. Each segment can be viewed as a region bounded by two yield surfaces. Thus, the stress space is devided by a family of yield surfaces of which the outermost yield surface is the bounding failure surface.

Prevost's pressure sensitive model was used to predict the drained behaviour of crushed quartz sand. The model predictions were compared with the experimental values. The conclusion was that the model simulates successfully the shear stress strain behaviour. The initial stiffness of the soil was modelled well and the shear stress strain curves agreed with the experimental values at least up to 80 % of the shear strength. During some predictions, the model underestimated or overestimated the observed strength of the soil. The reasons for this are the motion of the outermost yield surface and the model parameter identification technique.
A shortcoming of the model is apparent in its predictions of the volumetric strains. The reason for this is the type of non-associative flow rule used in the model formulation. It is suggested that the volumetric strain rate equation should be made a function of the current soil porosity or the current soil relative density to reflect the gradual increase of the soil density as the loading process continues.
The capabilities of the model were further tested for complicated stress path tests in three dimensional stress space using Ottawa sand. Although the model predictions agreed well with the experimental values, the failure loads were not captured occasionally. The initial stiffness of the soil was modelled well and the predicted shear stress strain curves agreed with the experimental values up to 80 % to 90 % in all cases.

The capabilities of the pressure non-sensitive model for describing the undrained soil behaviour was evaluated by comparing the results of undrained CTC-CTE tests carried out on crushed quartz sand samples with the predicted curves. It was shown that the model was able to predict the shear stress-strain-pore water pressure curves successfully. However, some inaccuracies in the model predictions were observed. The model was not able to simulate the ultimate loads of a number of tests and the predictions were ended before the failure load could be reached.
It should be noted that the pressure non sensitive model is not able to simulate the softening of the soil after the soil strength has been reached. When the stress point reaches the outermost yield surface, the sample is considered failed, because the plastic modulus related to the outermost yield surface is equal to zero during all stages of shearing. Thus, it is recommended that the model should include an additional parameter to model the softening of the undrained shear stress strain

curves after the shear strenght has been reached.

The present research was extended to investigate the following aspects of the pressure sensitive model.

1. The ability of the model to simulate the strain softening,

2. The ability of the model to simulate the shakedown phenomenon,
3. The ability of the model to simulate the behaviour of sand samples subjected to small, large and variable amplitude of cyclic loading.

On the basis of these investigations, the following conclusions were reached:
1. The pressure sensitive model is capable of reproducing the softening of the stress-strain curve, but at larger level of axial strain than the observed values.
2. The model simulates successfully the hysteretic soil behaviour and its accumulative strains, however it fails in simulating the shakedown phenomenon.
3. A shortcoming of the model is clear in its predictions of the volumetric strain. It was believed that the reason for this is the type of non associative flow rule used in the derivations of the constitutive relations of the model. Somehow, the effect of the current relative density should be included in the model formulations.

Acknowledgements

I wish to express my gratitude to the individuals who made this work possible. My deepest thanks go to my supervisor, Professor Erman Evgin, who was a constant source of inspiration and helpful guidance during my years at the University of Ottawa. His intellectual support, expressed in numerous exchanges and discussions, played a significant role in the rapid progress of my research.
The author would like to express his sincere appreciation to the professors of the Civil Engineering Department for their guidance and instructions during the course work.
My grateful appreciation is extended towards Mr. R. J. Moore for his assistance in manufacturing the instruments required in the laboratory testing and his help throughout the experimental program. I would like to express my gratitude to R. Bank, computer adviser, for his cooperation. Mr. A. Altaee, graduate student at the University of Ottawa, is thanked for his valuable discussions especially in geotechnical modelling area.

The writer is thankful to the government of Algeria for providing financial assistance in carrying this research.

Dedication

This thesis is dedicated to my parents.

Glossary of Notations

Only the stress and strain tensors notations are presented in this glossary. The remaining notations and symbols used in the thesis are defined in the text.

σ_{ij}	stress tensor
$\dot{\sigma}_{ij} = d\sigma_{ij}$	stress tensor increment
σ'_{ij}	effective stress tensor
$\dot{\sigma}'_{ij} = d\sigma'_{ij}$	effective stress tensor increment
S_{ij}	deviatoric stress tensor
$\dot{S}_{ij}$	deviatoric stress tensor increment
P	mean pressure
$\dot{P}$	mean pressure increment
P'	effective mean pressure
$\dot{P}'$	effective mean pressure increment
δ_{ij}	Kronecker delta
$P\delta_{ij}$	spherical stress tensor
$I_1 = J_1$	1^{st} invariant of the stress tensor, $trace(\sigma)$
J_2	2^{nd} invariant of the stress tensor, $\frac{1}{2}trace(\sigma)^2$
J_3	3^{rd} invariant of the stress tensor, $\frac{1}{3}trace(\sigma)^3$
J_{2D}	2^{nd} invariant of the deviatoric stress tensor, $\frac{1}{2}trace(S)^2$
J_{3D}	3^{rd} invariant of the deviatoric stress tensor, $\frac{1}{3}trace(S)^3$
ϵ_{ij}	strain tensor
$\dot{\epsilon}_{ij} = d\epsilon_{ij}$	strain tensor increment
e_{ij}	deviatoric strain tensor
$\dot{e}_{ij} = de_{ij}$	deviatoric strain tensor increment
$\epsilon_{ij}\delta_{ij}$	spherical strain tensor
$\epsilon_{ii} = \epsilon_v$	volumetric strain
$d\epsilon_{ii} = \dot{e}psilon_v$	volumetric strain increment
$\epsilon^e_{ii} = \epsilon^e_v$	elastic volumetric strain
$d\epsilon^e_{ii} = \dot{\epsilon}^e_v$	elastic volumetric strain increment
$\epsilon^p_{ii} = \epsilon^p_v$	plastic volumetric strain
$d\epsilon^p_{ii} = \dot{\epsilon}^p_v$	plastic volumetric strain increment
e^e_{ij}	elastic deviatoric strain tensor
$\dot{e}^e_{ij}$	elastic deviatoric strain tensor increment
e^p_{ij}	plastic deviatoric strain tensor
$\dot{e}^p_{ij}$	plastic deviatoric strain tensor increment
q	deviatoric stress, $\sigma'_1 - \sigma'_3$
$\dot{q}$	deviatoric stress increment
$\bar{\epsilon}$	strain difference, shear strain, $\epsilon_1 - \epsilon_3$
$\dot{\bar{\epsilon}}$	strain difference increment
ϵ^p	equivalent plastic deviatoric shear strain, $\int(\frac{2}{3}e^p_{ij}e^p_{ij})^{1/2}$

Contents

List of Tables

Chapter 1

INTRODUCTION

1.1 General

The numerical techniques used to solve the load-deformation problems must satisfy the conditions of compatibility of strains, the boundary conditions, the equilibrium equations and the stress-strain relations. Linear and nonlinear elastic, visco-elastic and elasto-plastic models have been used to idealize the stress-strain behaviour of soils. It is the choice of the constitutive law determines whether the solution obtained is realistic and meaningful. In recent years much effort has been devoted to the development of constitutive laws for soils, and several schools of thought on the philosophy of constitutive modelling have emerged. A rough count shows that there are nearly 50 models published in the literature. However, there has been insufficient evaluation of these models with respect to actual soil behaviour .

1.2 Statement of the Problem

Prevost used the multisurface theory of plasticity proposed by Mroz (1967) and Iwan (1967) to develop two elasto-plastic models to describe the non-linear, anisotropic, and stress-path dependent behaviour of soils subjected to complex loading paths involving loading and subsequently unloading-reloading in an arbitrary direction. These models were named pressure non-sensitive model and pressure sensitive model, Prevost (1977a, 1986). The first model was restricted to describe only the undrained clay behaviour in which the effect of the hydrostatic pressure on yielding of the soil was ignored. The model used a series of nesting yield surfaces subdividing the stress space into regions of a constant work-hardening moduli. It was recognized, Prevost (1977a), that the soil undergo both elastic and plastic deformations upon loading. The elastic behaviour was assumed to be isotropic and linear. The anisotropy and non linearity result from the plastic behaviour of the soil. During shearing, the change in the plastic properties is expressed by the translations and expansions or contractions of the yield surfaces. Prevost (1978) has generalized the pressure non-sensitive model to include the drained conditions by introducing the hydrostatic pressure term into the yield functions. This is called pressure sensitive model. It was based on the same concept as the pressure non sensitive model. In the pressure sensitive model, the elastic behaviour was considered to be isotropic but non-linear. The anisotropy resulted from the plastic soil behaviour. A new hardening rule was selected to describe the motion of the yield surfaces during the plastic flow. The model was further generalized by introducing a new flow rule in the formulation, Prevost (1986).

Prevost's model [1] is a general model applicable for both clay and sand. Its constitutive formulation incorporates drained and undrained situations involving a set of model parameters. These are the geometric configuration of the yield surfaces and their associated elastic and plastic shear and bulk moduli. A non associative flow rule was used, Prevost (1986), with a degree of non associativity parameter related to each yield surface.

Prevost used the model to analyze bearing capacity problems, Prevost (1979a), stability of dams, Prevost et al. (1985a, 1985b), and offshore gravity structures, Prevost et al. (1981c) for monotonic, cyclic and dynamic loading conditions. However, it appears that the verification of the performance of the model is limited to Prevost's research work. The reason for this is the model complexity. The model uses a large number of parameters. These parameters are inter-connected and not constants. They vary with the applied stresses and the volumetric strains developed. During shearing, the yield surfaces translate and expand or contract isotropically.

[1]The term Prevost's model refers to the pressure sensitive model which degenerates to the pressure non sensitive model when it is used to idealize the undrained soil behaviour.

Two types of expansions were introduced, Prevost (1986). Instantaneous expansion due to the total volumetric strain developed in the soil element and a permanent expansion due to the plastic strains developed in the soil sample. The stress point moves in the stress space pushing the inner yield surfaces to the exterior and the soil deformations are computed in an incremental fashion. This concept complicates the computations for the model simulations, because the motions of the yield surfaces during loading and unloading events have to be remembered.

The statement of the problem relevant to the present study can be expressed as follows:

In the literature, Prevost (1977a, 1977b, 1979a, 1979b, 1979c, 1980, 1981a, 1981b, 1981c, 1985a, 1985b, 1985c, 1986), the model is not well documented with respect to the mathematical derivation of the model parameters, the techniques used for the model parameter identification from experiments and the mathematical derivation of the hardening rule. In addition, there is no evidence of the ability of the model to simulate to the following aspects of the soil behaviour:

1. The failure loads, meaning the observed strength of the soil,
2. The softening of the soil after the peak strength has been reached, and
3. Shake-down aspect, meaning the densification of the loose soil subjected to cyclic loading.

1.3 Research Objectives

The main goal of this research work is to assess the merits and shortcomings of Prevost's model. Within this general framework, the efforts are aimed to achieve the following objectives:

1. to investigate of the versatility and accuracy of the model by comparing the model simulations with the actual test data,
2. to evaluate the accuracy of the model in defining the failure loads,
3. to study the performance of the model in simulating the softening of sand samples after the shear strength has been reached,
4. to investigate the ability of the model in simulating the shake down,
5. to examine the response of the model to a large or a small amplitude cyclic loading.
6. to review the assumptions involved in the derivation of the constitutive relation,

hardening rule. flow rule and the identification of the model parameters to clarify their influenc on the performance of the model.

1.4 Scope of Research

The steps taken in this research to achieve its objectives are listed as follows :

1. A literature review
2. An extensive study of Prevost's model
3. Laboratory testing
4. Development of a computer program to obtain the model parameters
5. Implementation of the model into computer programs
6. Simulations of stress strain behaviour and comparisons with actual test data
7. A study of the ability of the model in simulating the strain softening, failure states, shake-down aspect and the response of the model for large or small amplitude of cyclic loading.

The details of these steps are described below :

1. The literature review involves a study of the theory of elasticity, the classical theory of plasticity, the plasticity theory applied to soils and a review of the elasto-plastic soil models with the emphasis on the concept of critical state and cap models.

2. The derivation of the constitutive equations and the hardening rule of Prevost's model will be given in details. This section will include an explanation of how the model works to simulate the mechanical behaviour of soils during shearing.

3. The laboratory testing will include a series of triaxial tests carried out on a crushed quartz sand. The following tests will be performed:
a) A series of drained conventional triaxial compression, CTC, tests carried out on loose, medium dense and dense sands at different confining pressures.
b) A series of undrained conventional triaxial compression, CTC, tests carried out on loose, medium dense and dense sands at different confining pressures.
c) A series of isotropic compression, ICT, tests carried out on loose, medium dense and dense sands.

d) A series of drained and undrained conventional triaxial extension, CTE, tests carried out on loose, medium dense and dense sands.

e) Stress path tests.

These tests will be used to determine Prevost's model parameters. Following the parameter identification, the model will be used to predict the constitutive behavior of the soil subjected to different confining pressures.

4. This step concerns with the determination of the model parameters of the crushed quartz sand, Ottawa sand and Fuji river sand.

5. The model will be implemented in a three dimensional stress-driven computer program. The flowchart, program listing, the program manual and samples of input data and output results will be presented.

6. It is the purpose of this step to obtain the model simulations of the laboratory tests. Since the experimental program is restricted to the conventional testing in the triaxial plane, the experimental data of Montreal Workshop (1980) will also be used to generate a larger data base for the model evaluation for different stress paths in a three dimensional stress space. Moreover, Tatsuoka and Ishihara's (1974) cyclic tests will be used to investigate the performance of the model in simulating the cyclic behaviour of soils.

7. An investigation will be conducted to study the ability of the model in simulating the softening, shake down aspect, failure loads and its response to large and small amplitude of cyclic loading. Concluding remarks will be given and ways of improvement of the model will be proposed.

Chapter 2

ELASTICITY AND CLASSICAL PLASTICITY THEORIES

2.1 Introduction

A brief review of the elasticity and the classical plasticity theories is presented in this chapter, because the formulations of the elasto-plastic models of Prevost fall within the framework of these theories. This review gives the main assumptions involved in the derivation of an elasto-plastic constitutive relation and emphasizes the need for certain modifications and extensions to the classical theory of plasticity when it is applied to soils.

Prevost's constitutive relations use the normality rule of plasticity to compute the plastic strain increments, employ an ellipsoidal shape yield surface and combine the isotropic and kinematic hardening rules. In view of this, a review of Drucker's postulate, various shapes of yield surfaces and hardening rules used in the geotechnical field are presented in Section 2.4.

2.2 Theory of Elasticity

The majority of the constitutive relations for soils are based on the energy principles of a continuous media. The energy principles state that any body can possess energy in various ways. If it is in motion, it possesses kinetic energy. Any other energy not related to its motion is called intrinsic energy. The total energy is the sum of the kinetic and intrinsic energies, Kurdaze et al. (1979). The assumption of the linear elastic material behavior is the simplest way to model the soil behavior under a given set of stresses.

$$\sigma_{ij} = C_{ijkl}\epsilon_{kl} \tag{2.1}$$

where C_{ijkl} are 81 coefficients of a symmetrical fourth order tensor.
The existence of the strain energy function and the assumption of homogenous-isotropic material reduces the 81 coefficients to 2, Solomon (1968).

$$\sigma_{ij} = \lambda(\epsilon_{kk})\delta_{ij} + 2G\epsilon_{ij} \tag{2.2}$$

where λ and G are Lame's constants, δ_{ij} is the Kronecker delta.
The application of this idealization to soil ignores its plasticity and its nonlinearity. However, soil non-linearity can be preserved. In this case, the coefficients C_{ijkl} are not constants but depend on the applied stresses. This is usually accomplished by fitting the stress-strain data for a given test in mathematical functions and determining the relationships between the coefficients C_{ijkl} and the other parameters such as density, confining pressure, etc. Specific examples are the hyperbolic idealization, Duncan and Chang (1970), and spline functions, Desai (1971).

2.3 Classical Theory of Plasticity

The objective of the classical theory of plasticity is to offer a mathematical description of the mechanical behavior of a material in the plastic range. It was based on certain simplifying assumptions, Hill (1950):
a. The stress-strain relations are time independent.
b. The material is isotropic and Bauschinger effect is neglected.

In general, a constitutive model based on the classical theory of plasticity contains
1. A yield criterion specifying the state of stress at which the plastic flow occurs.

2. A hardening rule specifying the change of plastic properties of the material in the course of plastic flow.
3. A flow rule specifying the direction of the plastic strain rate vector for given stresses and stress rate vectors.

2.3.1 Concept of the Yield Surface and Yield Criterion

A state of stress at a generic point in a medium is defined in a nine dimensional stress space. Any program of loading can be regarded as a path in this space. For many materials, it is assumed that there exists about the origin a domain called the elastic range in which a change of stress, $d\sigma_{ij}$, produces no change in the permanent strains. If the permanent strains occur, the medium is said to be in plastic state. The plastic domain is bounding the elastic range and defines a yield surface. A yield criterion is a law defining the limit of the elasticity under any possible combination of stresses, Hill (1950).
In the one dimensional stress space, the yield surface is represented by a point, called a yield stress which is the limit of a pure elastic zone. Generally, the magnitude of the yield stress in tension is not the same as in compression. This phenomena is called Bauschinger effect, Calladine (1969). Furthermore, if the orientation of the individual grains of the material skeleton are randomly distributed and they have no preferred direction during straining, the yield stress and the macroscopic stress-strain relations do not vary with direction. In this case, the material is said to be isotropic. It follows that the isotropic yielding depends only on the magnitude of the principal stresses and not on their directions. Thus, the yield criterion can be expressed as a function of the three invariants of the stress tensor.

$$f(J_1, J_2, J_3) = 0. \tag{2.3}$$

It should be emphasized that only functions symmetrical in the three principal stress space are permissible to be a possible yield function. It is observed experimentally that yielding of metals is unaffected by the hydrostatic pressure either applied alone or superposed on some state of combined stress, Hill (1950). This means that there is no plastic volume change due to the applied hydrostatic stresses,

$$d\epsilon^p_{ii} = 0 \tag{2.4}$$

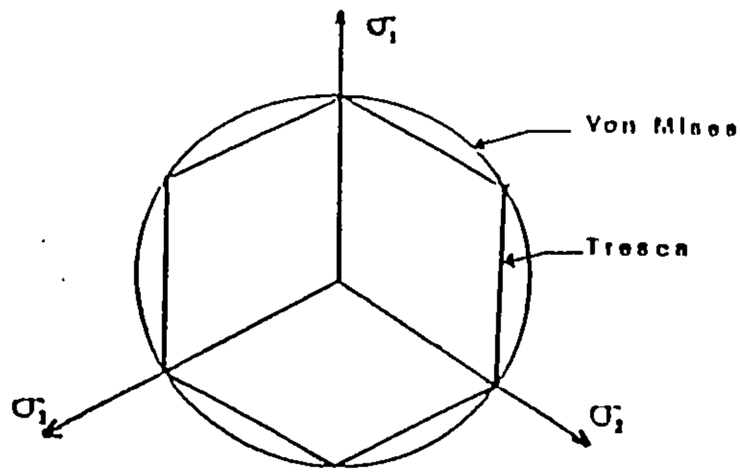

Figure 2.1: Tresca and von Mises yield criteria on the π plane.

and Eq 2.3 reduces to the form:

$$f(J_2, J_3) = 0. \tag{2.5}$$

The negligence of Bauschinger effect and the assumption of the isotropy of the material implies that the yield surface may be represented, in the stress space, by a piecewise smooth uniform cylinder of infinite length whose axis is the space diagonal $\sigma_1 = \sigma_2 = \sigma_3$. The well known Tresca and von Mises yield criteria, Fig 2.1, are represented by a rectangular hexagon and a circle on the π plane respectively.

2.3.2 Hardening Concept

When dealing with hardening materials, the yield surface changes shape and location as the plastic deformation occurs. The hardening rule describes the response of the yield surface during a loading process. It is assumed that the motion of the yield surface should be restricted to merely increase in size without any change in shape, Hill (1950). It follows, for example, that the von Mises yield surface is always a circle in π plane, expanding uniformly during loading.
However, the loading, unloading and neutral loading are defined according to whether the direction of the vector $d\sigma$ is directed towards the exterior or the interior of the

yield surface or tangential to it, Prager (1949).

$$\frac{\partial f}{\partial \sigma}d\sigma > 0 \qquad f = 0. \qquad loading \tag{2.6}$$

$$\frac{\partial f}{\partial \sigma}d\sigma = 0 \qquad f = 0. \qquad neutral..loading \tag{2.7}$$

$$\frac{\partial f}{\partial \sigma}d\sigma < 0 \qquad f = 0. \qquad unloading \tag{2.8}$$

In soils, the above definitions of loading and unloading may be violated when one deals with the softening of the material. Under a loading process the yield surface decrease its size after the peak strength has been reached.

In metal plasticity two measures of hardening are used, Hill (1950), the plastic work (W_p) and the equivalent plastic strain (ϵ^p). The reason for this, the elastic work cannot produce hardening and the equivalent plastic strain provides a measure of the plastic distortion. If the hardening is formulated in terms of plastic work, the material is said to work harden whereas when the hardening is formulated in terms of the plastic strain it is said to strain harden. The assumption that hardening occurs if the plastic work is done implies that the radius of the von Mises yield surface, for example, is a function of W_p

$$W_p = \int \sigma_{ij} d\epsilon_{ij}^p \tag{2.9}$$

The equivalent plastic strain in this case is :

$$\epsilon^p = \int (\frac{2}{3} d\epsilon_{ij}^p d\epsilon_{ij}^p)^{\frac{1}{2}} \tag{2.10}$$

where the integrations in Eqs 2.9 and 2.10 are carried over the strain paths.

2.3.3 General Stress-Strain Relations and Flow Rules

The development of the stress-strain relations in the plastic range requires the satisfaction of the following conditions:

1. Irreversibility condition
2. Continuity condition
3. Uniqueness condition
4. Consistency condition

Note that on account of the irreversible character of plastic deformation, the work

expended on plastic deformation cannot be reclaimed. This means that the plastic work increment is always positive for any change in plastic deformations, $W_p > 0$.
If the discontinuities in the stress-strain relation are to be avoided, the neutral change of the stress is considered as a limiting case for either the loading or unloading cases, Prager (1949). This is called the condition of continuity which requires that, $df = \frac{\partial f}{\partial \sigma_{ij}} d\sigma_{ij} = 0$.
For neutral loading, the condition $d\epsilon^p_{ij} = 0$ is satisfied by assuming that:

$$d\epsilon^p_{ij} = G_{ij} df \tag{2.11}$$

where G_{ij} is a symmetric tensor. The elements of G_{ij} are functions of the stress components but not their increments. Thus Eq 2.11 takes the following form:

$$d\epsilon^p_{ij} = G_{ij} \frac{\partial f}{\partial \sigma_{kl}} d\sigma_{kl} \tag{2.12}$$

where k and l are dummy subscripts.
The function G_{ij} must satisfy the condition that the principal axes of the plastic strain increment must coincide with the principal stress axis. This is called the uniqueness condition, Prager (1949), and it is satisfied by choosing:

$$G_{ij} = h \frac{\partial g}{\partial \sigma_{ij}} \tag{2.13}$$

In which $G_{ii} = 0$ to ensure zero plastic volume change. Thus, Eq 2.12 will be:

$$d\epsilon^p_{ij} = h \frac{\partial g}{\partial \sigma_{ij}} \frac{\partial f}{\partial \sigma_{kl}} d\sigma_{kl} \tag{2.14}$$

In Eq 2.14, g and h are scalar functions of the deviatoric stress invariants, h represents the rate of strain hardening. The function g is called the plastic potential function.
Eq 2.14 defines the plastic strain increment vector as normal to the plastic potential g. This is called the normality rule, Hill (1950). Once h and g are chosen, Eq 2.14 determines $d\epsilon^p_{ij}$ and a new yield surface is thereby produced. Since the new yield surface must pass through the new stress point, the functions g and h cannot be chosen arbitrarily but must satisfy the consistency condition, Prager (1949), which states that loading from a plastic state must lead to another plastic state.
When the functions g and f are chosen to be the same, the term associative flow rule is used whereas the term non-associative follow rule is used when the functions g and f are different.

2.4 Plasticity Applied to Soils

It is the purpose of this Section to present a brief review of Drucker's postulate, various shapes of the yield surfaces and hardening rules used in geotechnical field.

2.4.1 Drucker's Postulate

Drucker's postulate, Drucker (1950), as applied to an elasto-plastic solid is stated as follows:
Consider an element initially in some state of stress. Distinct from the previously existing state of stress, an additional set of stresses are applied and then removed. The work done by the added set of stresses, in cycle of application and the removal of the added stresses, is not negative. This implies that the yield surface must be convex and the plastic strain increment vector must be normal to it.

$$d\sigma_{ij} d\epsilon_{ij}^{p} > 0 \tag{2.15}$$

$$d\epsilon_{ij}^{p} = \lambda \frac{\partial f}{\partial \sigma_{ij}} \tag{2.16}$$

In which λ is a positive scalar factor of proportionality. Mathematical proof of the convexity and the normality was given by Philips and Seirakowski (1965).
Note that in soils, Drucker's postulate is violated in the zone of the strain softening after the peak strength. Simply, because the quantity given by Eq 2.15 would be negative.

2.4.2 Shape of the Yield Surface

Various shapes of yield surfaces have been suggested. Roscoe and Burland (1968) proposed an ellipsoidal yield surface in the three dimensional stress space. Schofield and Worth (1968) suggested a bullet shape. An open ended and capped cones were proposed by Drucker and Prager (1955) and Lade (1977). Ellipsoidal cylinder shape was proposed by Prevost (1977a, 1978, 1986).

2.4.3 Hardening Rules

During plastic deformations, the material experiences a hardening and this results in a change of the plastic material properties. An initially isotropic material may remain isotropic or become anisotropic. A perfectly plastic material experience no hardening, Desai and Siriwardane (1984).

When the stress point touch the yield surface and attempts to move beyond it, the consistency condition requires that the yield boundary has to move with it. In isotropic hardening case, the yield surface expands uniformly without change in the form or position, Fig 2.2a. However, the kinematic hardening rule does not permit the change in size or form of the yield surface and the hardening of the material gives the change in position of the yield surface as a function of stress increment, Scott (1985). Thus, the yield surface is dragged by the stress point to satisfy the consistency condition, Fig. 2.2b.

A more general case than the previous two can be postulated to accommodate both translation and expansion of the yield surface. This was achieved by combining both isotropic and kinematic hardening rules, Iwan (1967), Mroz (1967; 1978), Mroz et al. (1979), Prevost (1977a, 1978, 1986).

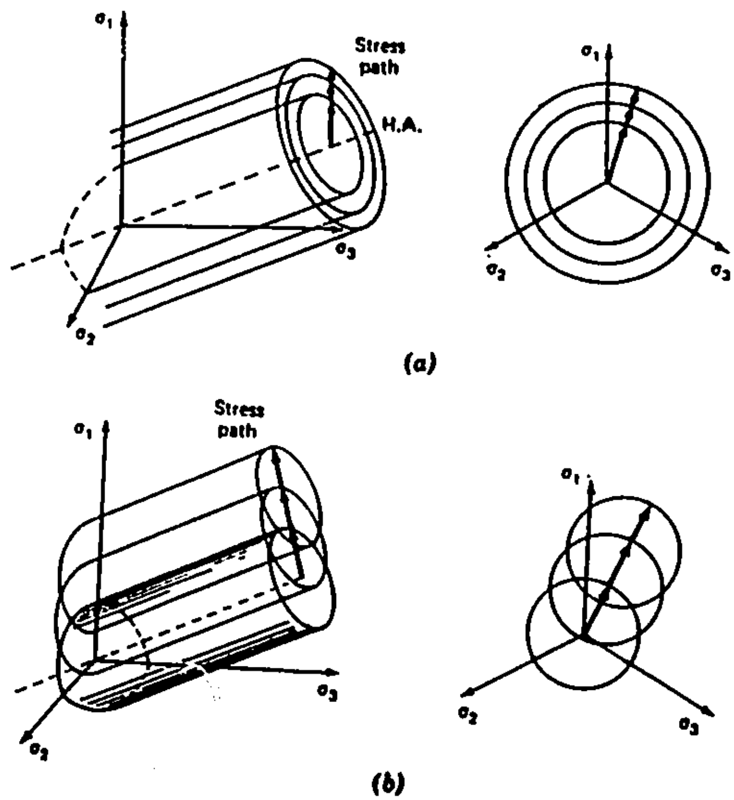

Figure 2.2: Hardening rules of plasticity: a) Isotropic. b) Kinematic. (From Scott, 1985)

Chapter 3

ELASTO-PLASTIC SOIL MODELS

3.1 Introduction

Soils are extremely complicated engineering material whose constitutive response depends on a large number of factors including density, grain size distribution, types of minerals, chemistery of pore water, drainage condition, confining pressure, stress path, Ko and Scott (1967). Moreover, the material characteristics such as heterogeneity and anisotropy play a fundamental role in the microstructural behavior of soils and require the consideration of parameters at the microstructure level, Vijay and Tien (1976).

Since it is not possible to review all the existing elasto-plastic soil models, the scope of this chapter was restricted to review Drucker-Prager model, the critical state concept involving both Cam clay and Cap models, multisurface models and the bounding surface models. Drucker-Prager model is presented as an example of the elastic-perfectly plastic idealization. The critical state concept is presented to establish a theoretical background towards an understanding of the role of the outermost yield surface which eventually becomes the failure surface in Prevost's model. The bounding surface model have a similar concept as the multisurface models.

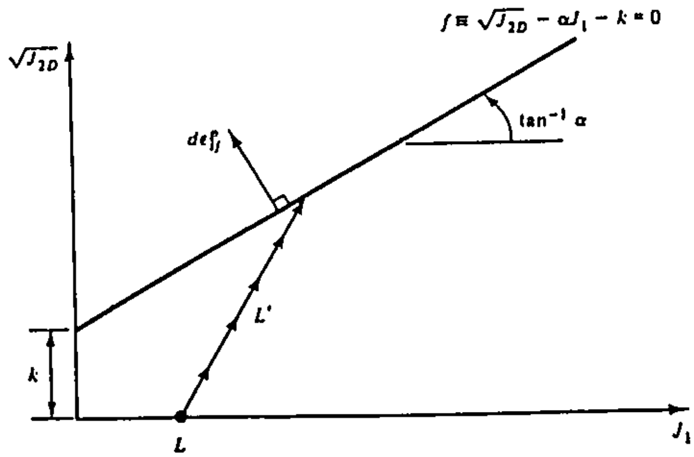

Figure 3.1: Representation of Drucker-Prager model.
(From Desai and Siriwardane, 1984)

3.2 Drucker-Prager Model

In an attempt to include the effect of the hydrostatic stresses on yielding of soils, Drucker and Prager (1952) suggested a generalized yield criterion which includes the effect of all principal stresses. They assumed that the soil is an isotropic and elastic-perfectly plastic material. The von Mises yield criterion was modified to have a cone shape yield surface rather than a cylinder.

$$f = \sqrt{J_{2D}} - \alpha J_1 - k = 0. \tag{3.1}$$

In which α and k are material parameters related to the frictional and cohesive strengths of the material. The total strain increment is considered to be the sum of the elastic and plastic strain increments. The elastic strains were calculated using Hooke's law and the normality rule of plasticity was used to compute the plastic strain increments. The stress strain relation was given as, Chen and Baladi (1985).

$$d\sigma_{ij} = K\epsilon_{kk}\delta_{ij} + 2Gde_{ij} - \lambda\left(-3K\alpha\delta_{ij} + \frac{GS_{ij}}{\sqrt{J_{2D}}}\right) \tag{3.2}$$

in which K and G are the elastic bulk and shear moduli. λ is the same as defined in Eq 2.16.

As shown in Fig 3.1, the plastic strain increment vector has a negative component which indicates a negative plastic volume change.
The use of the model leads always to a prediction of dilation accompanying a shearing action which is not observed for all types of soils. Normally consolidated clays and loose sands may not dilate during shearing.

3.3 Critical State Concept

A soil element, undergoing shear distortion, eventually reaches a critical state condition in which it can continue to distort without further change of void ratio and shearing resistance. *Roscoe (1958)*

The introduction of isotropic hardening rule, led to a generation of a family of soil models developed by the Cambridge soil mechanics group. The critical state concept was introduced as a general description of the soil behavior and its failure criterion, Atkinson and Bransby (1977). Any state of soil defined by P', q, e [1] can be represented in a three dimensional P', q, e space. In drained conventional triaxial tests, it was observed that the stress paths follow a unique surface in the P', q, e space. This is called the state boundary surface.
Any soil element in a state of equilibrium will lie inside the volume enclosed by the boundary surfaces and the planes $e = e_{max}$ and $e = e_{min}$, Fig 3.2. The critical state line, $E-F$, is the locus of the failure points for all shear stresses under both drained and undrained conditions. Its projection onto the $P'-q$ and $e-lnP'$ subspaces are straight lines .

$$q = MP' \tag{3.3}$$

$$e = e_0 - \lambda lnP' \tag{3.4}$$

e_0 is the value of the void ratio for $P' = 1.0$ KN m^{-2}.
M is the slope of the critical state line.
λ is the slope of the virgin line in $e - lnP'$ plot.

[1] e is the current void ratio

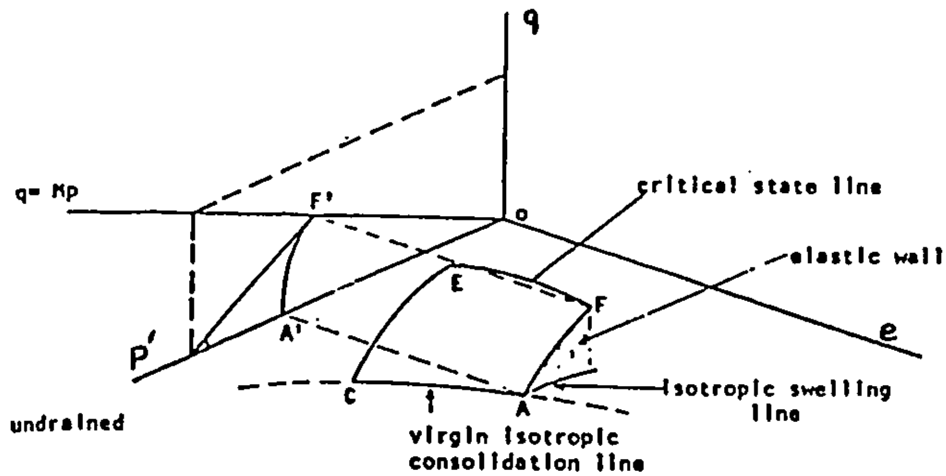

Figure 3.2: Representation of the critical state concept.
(From Ansal, 1977)

The shape of the state boundary surface was expressed by the following equation, Roscoe and Burland (1968).

$$P_e = e^{(e_0 - e)/\lambda} \tag{3.5}$$

3.3.1 Cam-clay Models

The projection of the critical state line onto $q - P'$ plot is treated as an open ended fixed outermost yield envelope. An additional set of yield loci may be added to account for the continuous yielding of the material during the plastic flow. Cam-clay formulation was the first comprehensive mathematical description of the soil behavior based on this concept, Chen and Baladi (1985). Roscoe (1963) suggested the following function of the yield locus:

$$\frac{dq}{dP'} + \frac{d\eta}{\eta + \psi} = 0. \tag{3.6}$$

where $\eta = \frac{q}{P'}$ and $\psi = -\frac{dq}{dP'}$

The yield locus expands uniformly during plastic deformation. The total strain increment is assumed to be the sum of the elastic and plastic strain increments and

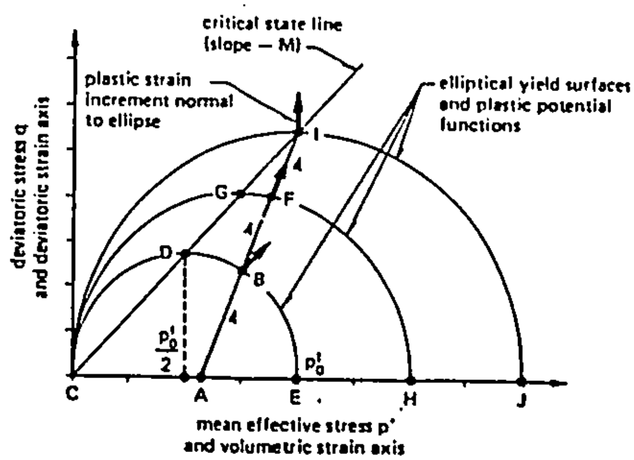

Figure 3.3: Representation of the modified Cam clay model.
(From Dungar, 1986)

there is no recoverable energy associated with the shear distortion .

$$d\epsilon = d\epsilon^e + d\epsilon^p \tag{3.7}$$

$$d\epsilon_s = d\epsilon_s^p \tag{3.8}$$

$$d\epsilon_s^e = 0. \tag{3.9}$$

The elastic volumetric strain is determined from the isotropic compression test.

$$d\epsilon_v^e = \frac{k}{(1+e)}\frac{dP'}{P'} \tag{3.10}$$

k is the slope of the swelling line in the $e - lnp$ plot .
The normality rule of plasticity governs the formulation of the plastic stress-strain relations:

$$d\epsilon_v^p = \frac{\lambda - k}{1+e}\left(\frac{dP'}{P'} + \frac{d\eta}{\psi + \eta}\right) \tag{3.11}$$

$$d\epsilon_s^p = \frac{1}{M+\eta} d\epsilon_v^p \tag{3.12}$$

Later, this model was modified by Roscoe and Burland (1968) in which an ellipsoidal shape of the yield locus was chosen, Fig 3.3. This choice was based on a consideration of the energy dissipated in the soil element. This is the so-called 'the modified cam clay model ''. It was assumed only part of the volumetric strain is recoverable, however, the elastic shear strain does not exist.

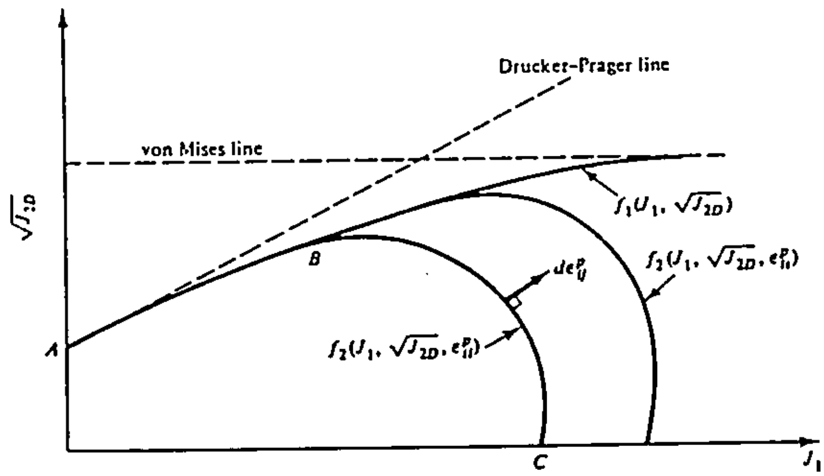

Figure 3.4: Representation of the Cap model.
(From Desai and Siriwardane, 1984)

3.3.2 Cap Models

In the Cam clay models, the behavior of the soil was expressed by using quantities relevant to the conventional triaxial tests where the effect of the intermediate stress was ignored. In an attempt to use the concept of the critical state to three dimensional stress-strain relations, a nonlinear, elasto-plastic and isotropic work hardening model was developed by DiMaggio and Sandler (1971). The proposed yield function consists of two parts. A fixed ultimate envelope joining the initial part of Drucker-Prager to the von Mises yield surfaces with smooth transition as shown in Fig 3.4. The second part is a moving cap serves to express the hardening of the material during the plastic deformations. The shape of the cap was governed by the following conditions:

1. Under a hydrostatic loading condition, no shear deformations occur.
2. Once the stress point reaches the fixed envelop no more volume change will occur.

In order to achieve these conditions an elliptical shape of the cap was assumed. It forms a right angle with J_1 axis and intersects with the fixed envelop in a way that the tangent to the cap, at the intersection point with the envelop, is parallel to the J_1 axis.

The total strain increment is equal to the sum of the elastic and plastic strain increments.

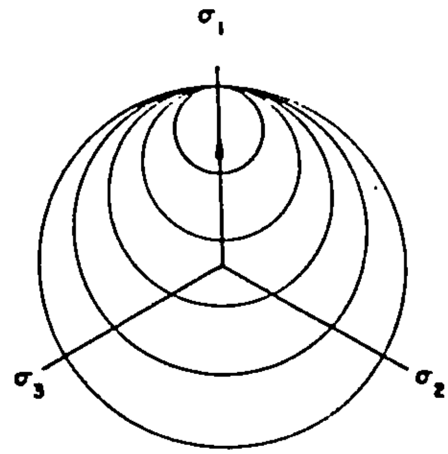

Figure 3.5: Representation of the multisurface model.
(From Iwan, 1967)

The rule of isotropic work hardening used in the above models implies that during unloading the material behaves elastically.
However, soil tests indicate that upon unloading both elastic and plastic deformations occur well before the stress is fully reversed, Prevost (1977). This is similar to Bauschinger effect observed for metals. In order to account for the inverse plastic deformations, Prevost (1978a) proposed a multisurface elasto-plastic model with a combination of the isotropic and kinematic rules in which the yield surface is allowed to translate in the stress space and change its size as well.

3.4 Multisurface Models

A theoretical development in plasticity by Iwan (1967) showed how continuously occurring yielding in a single element can be represented by a set of nested surfaces in the principal stress or any other stress space, Fig 3.5. A similar concept was proposed by Mroz (1967) to describe the behavior of metals. Later, this concept was extended to model the soil behavior, Prevost (1978a). The details concerning the multisurface modelling are given in the next chapter.

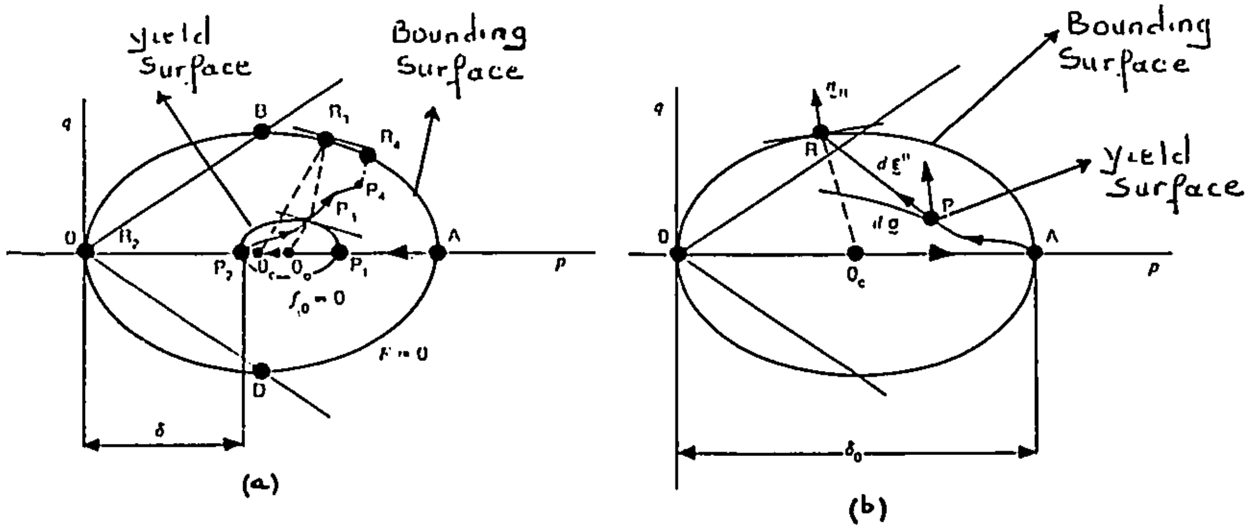

Figure 3.6: Representation of the bounding surface model.
(From Mroz et al., 1979)

3.5 Bounding Surface Models

The multisurface models can be reduced to a simplified version in which only two surfaces are considered, Fig 3.6a, a yield surface and a bounding surface, Mroz et al., (1979). The plastic moduli can be obtained by an interpolation along the distance joining the stress point on the yield surface, and its conjugate point on the bounding surface [2]. The yield surface is allowed to change its size, expand or contract, and translate in the stress space similarly to the concept adopted for the nested surfaces.

If the size of the yield surface may be degenerates to a point, the pure elastic domain vanishes Fig 3.6b. In this case, only the bounding surface and the stress point are considered.

[2]The definition of the conjugate point is given in the next chapter.

Chapter 4

PREVOST'S MODEL

4.1 Introduction

Prevost (1986) proposed a mathematical model to describe the nonlinearity, anisotropy, elasto-plasticity, and stress path dependency of saturated soils subjected to complex loading paths involving loading and subsequently unloading-reloading in an arbitrary direction. The model accounts for both drained and undrained conditions. It combines the isotropic and kinematic hardening rules, developed originally by Iwan (1967) and Mroz (1967).
The objective of this chapter is to present the mathematical derivation of Prevost's stress strain relations. The main assumptions involved in the model formulation will be pointed out. A general interpretation of the Prevost's model is presented in Section 4.6 which will clarify how the model works in predicting the mechanical behaviour of soils during shearing.

4.2 Stress Strain Relations

Prevost(1978) recognized that soils undergo both elastic and plastic deformation simultaneously upon loading. The elastic behaviour is considered nonlinear isotropic. The anisotropy, however, is assumed to be the result of plastic deformations. The elastic strain rate components are related to the components of the stress tensor by the generalized Hooke's law, Eq 2.1. The normality rule of plasticity was used to compute the plastic strain rate vector and a non-associative flow rule was adopted. The plastic strain rate vector was given as follows:

$$\dot{\epsilon}^p_{ij} = \frac{< L >}{|Q|^2} P \tag{4.1}$$

In which P and Q are the vectors normal to the plastic potential surface, g, and the yield surface, f, respectively:

$$Q_{ij} = \frac{\partial f}{\partial \sigma_{ij}} \tag{4.2}$$

$$P_{ij} = \frac{\partial g}{\partial \sigma_{ij}} \tag{4.3}$$

$$|Q| = \left(\frac{\partial f}{\partial \sigma_{ij}} \frac{\partial f}{\partial \sigma_{ij}} \right)^{1/2} \tag{4.4}$$

$< L >$ is the plastic loading function which is related to the projection of the stress rate vector onto the normal of the yield surface:

$$< L >= \frac{1}{H} Q \dot{\sigma} \tag{4.5}$$

H is the plastic modulus associated with the yield function f.
The bracket symbol $<>$, used in Eq 4.1, is defined as:
$< L >= L$ if $L > 0$, and $< L >= 0$ if $L < 0$.
The yield surface was visualized as a surface in the stress space represented by a function of the type:

$$f(\sigma - \xi) - K^n = 0 \tag{4.6}$$

in which ξ is the position of center coordinates of the yield surface and K is a measure of its size. The exponent, n, was taken equal to 2, Prevost (1978).
The stress space was viewed as hydrostatic and deviatoric stress subspace.

$$\sigma = S + P'\delta \tag{4.7}$$

$S(s_{ij})$ is the deviatoric stress tensor, P' is the effective mean normal stress and $\delta(\delta_{ij})$ is the Kronecker delta.
By analogy with Eq 4.7, the parameter ξ was introduced as:

$$\xi = \alpha + \beta\delta \tag{4.8}$$

α and β are the deviatoric and hydrostatic components of ξ.
Following this analogy, the vectors Q and P can be decomposed:

$$Q = Q' + Q''\delta \tag{4.9}$$

$$P = P' + P''\delta \tag{4.10}$$

In which Q', Q'', P' and P'' are the projections of the vectors Q and P onto the hydrostatic and deviatoric stress subspaces.

$$Q' = \frac{\partial f}{\partial S} \qquad 3Q'' = \frac{\partial f}{\partial P'} \tag{4.11}$$

$$P' = Q' \qquad 3P'' = \frac{\partial g}{\partial P'} \tag{4.12}$$

The plastic strain rate vector was decomposed into volumetric and deviatoric components.

$$\dot{\epsilon}^p_v = \dot{\epsilon}^p \delta \tag{4.13}$$

$$\dot{e}^p = \dot{\epsilon}^p - \frac{1}{3}\dot{\epsilon}^p_v \delta \tag{4.14}$$

Combining Eqs 4.1, 4.9, and 4.10, the plastic stress strain relations can be written as follows:

$$\dot{\epsilon}^p_v = \frac{1}{|Q|^2} < L > 3P'' \tag{4.15}$$

$$\dot{e}^p = \frac{1}{|Q|^2} < L > P' \tag{4.16}$$

In which the plastic loading function $< L >$ can be determined from Eq 4.5 :

$$< L >= \frac{1}{H}\left(Q'\dot{S} + 3Q''\dot{P}\right) \tag{4.17}$$

The details concerning the derivation of the general elasto-plastic stress strain relations are presented in Appendix A.

The functions f and g in Eqs 4.2 and 4.3 and the parameters H and ξ in Eqs 4.5 and 4.6 cannot be chosen arbitrarily but must satisfy the necessary conditions, Prager (1949), as explained in chapter 2.
Once f and g are chosen, Eq 4.1 determines the plastic strain rate vector due to a given stress rate vector. A new plastic state is thereby produced at the new stress state and it is represented by an update yield function in agreement with the consistency condition, Prager (1949).

$$\frac{\partial f}{\partial \sigma}(\sigma - \xi) - nK^{n-1}\dot{K} = 0 \tag{4.18}$$

where $\dot{K}$ is the change in size of the yield surface.

4.3 Field Work-Hardening Moduli Concept

The concept of field work-hardening moduli was first proposed by Mroz (1967) to model the metal behaviour. Later, Prevost (1977a, 1978, 1986) applied it to model the behaviour of soils. According to this concept, Prevost (1978), a collection of yield surfaces, $f_0, f_1, f_2, ...f_p$ with respective sizes $K_0, K_1, K_2, ...K_p$, divide the stress space into regions of constant tangent moduli, as explained in Section 4.6. These surfaces are similar in shape. Thus, Eq 4.6 can be written in a general form:

$$f_m(\sigma_{ij}^m - \xi_{ij}^m) = (K_m)^n \tag{4.19}$$

In which the superscript or subscript m indicates the quantities corresponding to the yield surface f_m.

A set of yield surfaces are allowed to translate and expand or contract. The stress point moves from a yield surface f_m towards f_{m+1} pushing the inner yield surfaces $f_1 - f_m$. Note that all yield surfaces expand or contract uniformly depending on the volumetric strain developed in the soil element. Thus all yield surfaces which are not reached by the stress point expand or contract isotropically whereas the remaining surfaces are in mutual contact at the stress point undergoing both translation and expansion or contraction. A plastic moduli is associated with each yield surface, and it is allowed to vary as explained later. The surface, f_p, is a failure surface and plays the role of a bounding surface. The stress point and the inner yield surfaces, $f_0, f_1, ..., f_{p-1}$, cannot go beyond f_p. The plastic moduli associated with the outermost yield surface, H_p, is allowed to be less than zero for unstable materials and greater than a zero for stable materials [1]. At the critical state condition,H_p is equal to zero. The variation of H_p along the outermost yield surface was expressed as, Prevost (1978).

$$H_p = \frac{3}{2}\lambda(P - \beta^m)\frac{Q^p \dot{\sigma}}{(K^p)^2} \tag{4.20}$$

In which λ is a material parameter to be determined from the consolidation test results, β represents the center of coordinates of the yield surface. Equation 4.20 was derived on the basis of the following assumption, at the critical state condition, the hydrostatic stress does not effect the yielding of the soil and the value of the plastic modulus in Eq 4.5 plays the role of the plastic shear modulus. Moreover,

[1] Unstable materials present a softening of the stress strain curve after the peak strength whereas stable materials exhibit only hardening of the stress strain curve.

its expansion or contraction was considered to be function of the plastic volumetric strain alone, as explained in Section 4.5. During shearing, the outermost yield surface expands or contracts towards the critical state condition defined as $H_p = 0$. Similarly, the variation of H_m along the yield surface f_m is selected such that:

$$H_m = h_m + \sqrt{3}\frac{Q''_m}{|Q_m|}B'_m \tag{4.21}$$

In which h_m and $(h_m + B'_m)$ are the plastic shear modulus and the plastic bulk modulus respectively .
The surface f_1 enclosing a pure elastic region can be chosen as a degenerate yield surface $K_1^0 = 0$. In this case, f_1 coincides with the stress point and represents the current state of stress.

4.4 Flow Rule

A non-associative flow rule is adopted. The plastic potential function, g_m, associated with the yield surface, f_m, is selected such that:

$$P' = Q' \tag{4.22}$$

$$P'' = Q'' + A_m(Q' : Q')^{\frac{1}{2}} \tag{4.23}$$

A_m is the degree of a non-associativity parameter which is determined from the experimental result. Note that an associative flow rule was assumed for the outermost yield surface, f_p, Prevost (1986). Eqs 4.22 and 4.23 were selected such that the rate vector of the deviatoric component of plastic strains remains normal to the projection of the yield surface in the deviatoric stress subspace.

4.5 Hardening Rule

Prevost(1978) selected a new hardening rule to describe the motion of the yield surfaces during the loading process. Prevost's hardening rule consists of an isotropic expansion or contraction and the translations of the yield surfaces during loading. In the following both translation and expansion or contraction rules are derived.

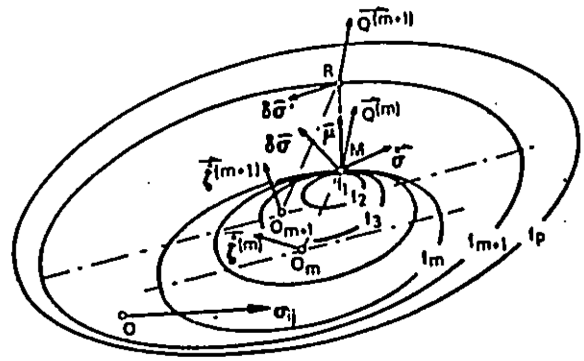

Figure 4.1: Typical representation of the field work-hardening comcept.
(From Prevost, 1978)

4.5.1 Translation Rule

Eq 4.19 represents a family of yield surfaces. All the surfaces are similar in shape. By similarity, the following equation can be derived:

$$.... = \frac{\sigma_{ij}^{m-1} - \xi^{m-1}}{K^{m-1}} = \frac{\sigma_{ij}^{m} - \xi^{m}}{K^{m}} = \frac{\sigma_{ij}^{m+1} - \xi^{m+1}}{K^{m+1}} = ... \qquad (4.24)$$

For any point M on the surface f_m, there exists a conjugate point R on the surface f_{m+1} for which the gradient vectors $\frac{\partial f_m}{\partial \sigma}$ and $\frac{\partial f_{m+1}}{\partial \sigma}$ have the same direction. The two surfaces cannot overlap or intersect but they contact each other at the conjugate point, Mroz (1967).

In Fig 4.1, M denotes a point on f_m. Its conjugate on f_{m+1} is R.

Let μ be the vector connecting the point M to R. The vector μ can be defined as follows:

$$\mu = \frac{K^{m+1}}{K^{m}}(\sigma - \xi^{m}) - (\sigma - \xi^{m+1}) \qquad (4.25)$$

Let $\delta\sigma$ and $\delta\sigma'$ denote the motions of the stress points M and R during the loading action.

$\delta\sigma$ and $\delta\sigma'$ must satisfy two conditions;

1. The consistency condition.
2. The translation must occurs along the local normal on the yield surface.
At points M and R, Eq 4.18 takes the form:

$$\dot{\sigma}^m = \dot{\xi}^m + n(K^m)^{n-1}\dot{K}^m \frac{Q^m}{|Q^m|^2} \tag{4.26}$$

$$\dot{\sigma}^{m+1} = \dot{\xi}^{m+1} + n(K^{m+1})^{n-1}\dot{K}^{m+1} \frac{Q^m}{|Q^m|.|Q^{m+1}|} \tag{4.27}$$

in which $Q^m\dot{\sigma}^m = Q^m\delta\sigma$ and $Q^m\dot{\xi}^{m+1} = 0$.
In order to avoid overlapping, the instantaneous translations $\dot{\xi}^m$ and $\dot{\xi}^{m+1}$ must occur such that:

$$\delta\sigma = \delta\sigma' + \delta\mu\mu \tag{4.28}$$

in which $\delta\mu$ is a scalar parameter.
Combining Eqs 4.26, 4.27 and 4.28 one gets:

$$\dot{\xi}^m - \dot{\xi}^{m+1} = n\left(\frac{(K^{m+1})^{n-1}\dot{K}^{m+1}}{|Q^{m+1}|} - \frac{(K^m)^{n-1}\dot{K}^m}{|Q^m|}\right)\frac{Q^m}{|Q^m|} + \delta\mu\mu \tag{4.29}$$

$\delta\mu$ can be determined from the consistency condition:

$$\delta\mu = \frac{Q^m(\delta\sigma - \delta\sigma')}{Q^m\mu} \tag{4.30}$$

The translation of the yield surface, ξ^m, can be decomposed into hydrostatic and deviatoric components, as shown in Eq 4.8:

$$\dot{\xi}^m = \dot{\lambda}\mu' + \dot{\beta}\delta \tag{4.31}$$

in which μ' is the projection of the vector μ onto the deviatoric subspace, β is the hydrostatic component of ξ and λ is scalar parameter.
From Eq 4.26 one gets :

$$\dot{\xi}^m = \dot{\sigma}^m - n(K^m)^{n-1}\dot{K}^m \frac{Q^m}{|Q^m|^2} = \dot{\lambda}\mu' + \dot{\beta}\delta \tag{4.32}$$

From Eq 4.7, 4.9 and 4.32, one may write:

$$\dot{\beta}^m = \dot{P} - n(K^m)^{n-1}\dot{K}^m \frac{(Q'')^m}{|Q^m|^2} \tag{4.33}$$

$$\dot{\lambda}\mu' = \dot{S} - n(k^m)^{n-1}\dot{K}^m \frac{(Q')^m}{|Q^m|^2} \tag{4.34}$$

Comparing Eq 4.34 and 4.8 one gets:

$$\dot{\lambda}\mu' = \dot{\alpha} \tag{4.35}$$

The consistency condition allows the determination of λ, and Eq 4.35 will be :

$$\dot{\alpha}^m = \left(\frac{Q'^m \dot{S} - n(K^m)^{n-1} \dot{K}^m (\frac{|Q'^m|}{|Q^m|})^2}{Q'^m \mu'} \right) \mu' \tag{4.36}$$

4.5.2 Expansion/ Contraction Rule

The expansion or contraction of the outermost yield surface f_p is assumed to be a function of the current density. Prevost (1978) selected the following expression for the isotropic expansion or contraction of the yield surface.

$$K^p = K_0^p e^{\lambda \epsilon_v^p} \tag{4.37}$$

Eq 4.37 is similar to the logarithmic relationship between the void ratio and effective mean stress used for the derivation of the equation of the critical state line, Eq 3.4. In order to ensure the isotropic expansion or contraction of the yield surfaces, it was assumed that all surfaces expand or contract uniformly:

$$...\dot{K}^{m-2} = \dot{K}^{m-1} = \dot{K}^m = \lambda K_0^m \dot{\epsilon}_v^p \tag{4.38}$$

In which K_0^m is the initial size of the surface currently pushed by the stress point.

Note that Eq 4.29 describes the following hardening rules:

If $\dot{K}^m = \dot{K}^{m+1} = 0$ and $\dot{\xi}^m = \dot{\xi}^{m+1} \neq 0 \rightarrow$ pure kinematic hardening.

If $\dot{K}^m = \dot{K}^{m+1} \neq 0$ and $\dot{\xi}^m = \dot{\xi}^{m+1} \neq 0 \rightarrow$ isotropic-kinematic hardening.

If $\dot{K}^m = \dot{K}^{m+1} \neq 0$ and $\dot{\xi}^m = \dot{\xi}^{m+1} = 0 \rightarrow$ pure isotropic hardening.

4.6 Interpretation of Prevost's Model

This Section concerns with a general interpretation of Prevost's model to clarify how the model predicts the mechanical behavior of soils during shearing. Note that all stresses are effective and the compressive stresses are considered to be positive. Also, let's consider Y as a vertical axis and X and Z are the horizontal axes of the stress space.

4.6.1 Yield Functions

For a three dimensional stress state, a yield criterion can be generalized by incorporating all the invariants of the deviatoric stress tensor, Hill (1950). Since yielding of soils is effected by the hydrostatic pressure, a yield criterion has to include the first invariant of the stress tensor, Mroz et al., (1979). Prevost's model ignores the effect of the third invariant of the deviatoric stress tensor and uses a von Mises type yield criterion. Equation 4.19 was given as follows, Prevost (1978).

$$\frac{3}{2}(S_{ij} - \alpha_{ij}^{m})(S_{ij} - \alpha_{ij}^{m}) + C^2(P' - \beta_{ij}^{m})^2 = (K^m)^2 \tag{4.39}$$

Equation 4.39 is an ellipsoidal cylinder surface in the stress space whose main axis is parallel to the space diagonal. α and β are the coordinates of the center of its deviatoric section.
$C = \frac{3}{\sqrt{2}}$: axis ratio of the ellipse.
K : size of the ellipse.

4.6.2 Stress-Induced Anisotropy

Prevost (1977a) assumed that the soil anisotropy is developed during its consolidation and deposition process which, in most cases, takes place under no lateral strain. In Equation 4.39, the tensor α is not proportional to the Kronecker delta, δ, therefore yielding is anisotropic. If Y coincides with the consolidation direction, $\alpha_x = \alpha_z$ and $\alpha_{xz} = \alpha_{zx} = 0$. The initial positions of the yield surfaces reflect the past stress strain history. In particular, α_{ij}^{m} are a direct expression of the material memory associated with the loading history. From the hardening rule adopted, Eq 4.36, it follows that $d\alpha_{ij} = 0$ (for $i \neq j$) and the material's transverse isotropy is preserved.

4.6.3 Interpretation of the Field Work Hardening Concept

Prevost's models were based on the concept of the field work hardening, Mroz (1967), which was described in Section 4.3. In order to explain this concept further, let us consider a specimen of initially isotropic material subjected to a monotonically increasing load in tension. The smooth experimental curves are approximated by a linear segments. Each segment is regarded as a region bounded between two yield surfaces. Thus, the model consists of a series of nested yield surfaces subdividing the stress space into regions of a constant tangent moduli, Fig 4.2b. Each region is called a field of constant work-hardening, Iwan (1967). Obviously, the degree of accuracy achieved by this representation is dependent on the number of segments used, Fig 4.2a.
The process of loading and subsequently unloading-reloading can be described as follows:

When the stress point moves from the origin along the vertical axis towards point B, Fig 4.2b, it reaches the elastic limit at the point A, Fig 4.2a. The circle f_0 moves along this axis until it contacts the circle f_1 at B. At this stage, all other circles remain fixed and the plastic moduli between A and B is defined as a constant parameter H_1. When the stress point moves from B to C, the circles f_0, f_1 are translated together by the stress point until they reach the circle f_2 at C. Up to now, the circles $f_2, ...f_p$ remained fixed. The plastic moduli, H_2, between B and C is constant. When the stress point moves from C to D, the circles f_0, f_1, f_2 are translated until they reach the nesting surface f_3 and the surfaces $f_3, ...f_n$ remain fixed .

Consider now the process of loading in the inverse direction, i.e, unloading. After reaching point G [2], the circle f_0 is translated until it contacts the circle f_1 at H. The circles $f_1, f_2....f_n$ remain fixed. Note that the process of unloading can be described as in loading case, as explained above. It should be emphasized that the stress difference between G and H is twice the difference between stresses at A and B, Mroz (1967).

[2]Point G represents the elastic limit upon unloading.

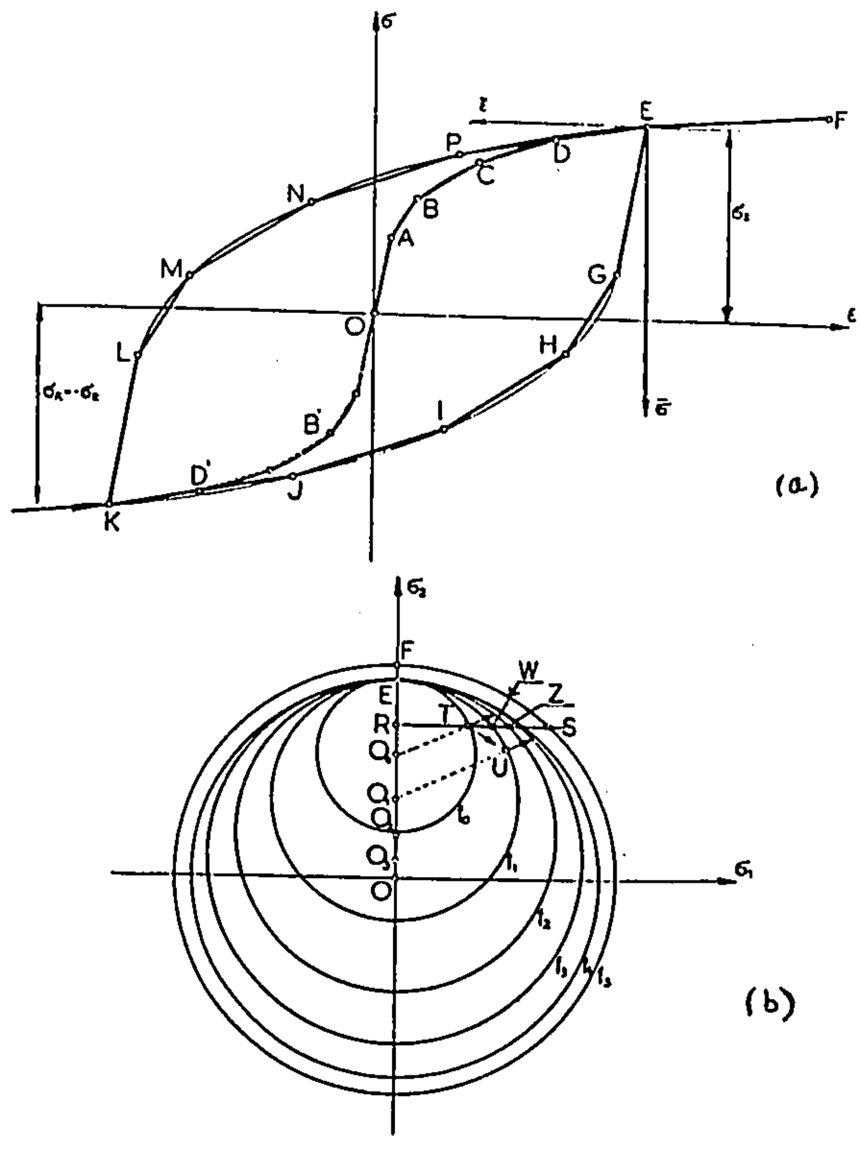

Figure 4.2: Multisurface representation of loading-unloading-reloading process. (From Mroz, 1967)

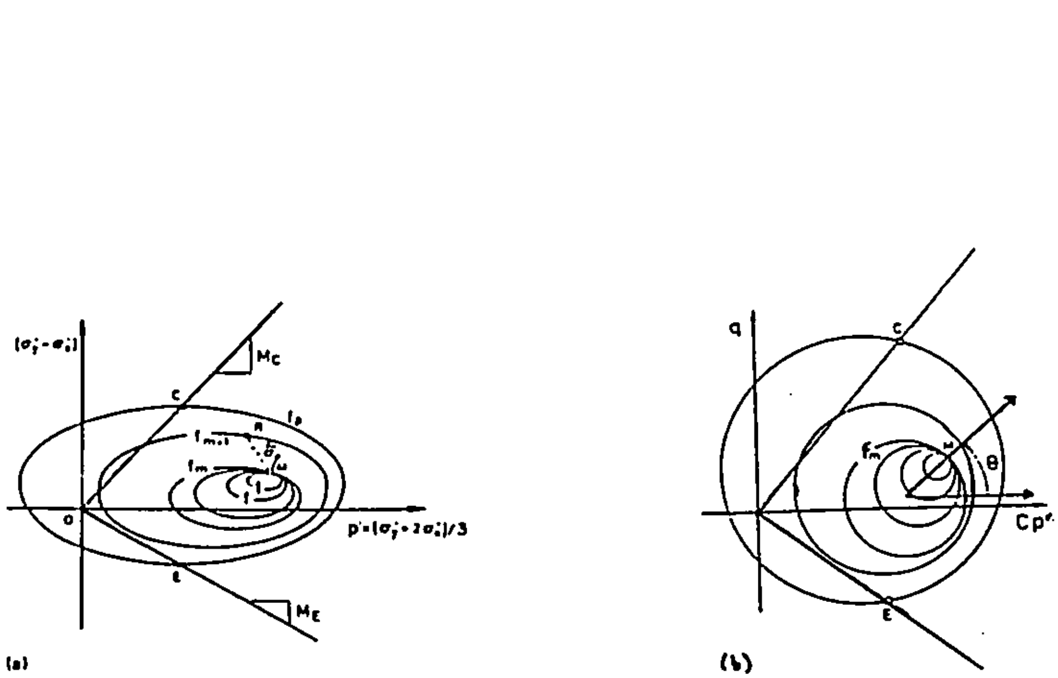

Figure 4.3: Representation geometric of the yield surfaces in:
a) $P' - q$ stress subspace. b) $CP' - q$ stress plot.
(From Prevost, 1986)

4.6.4 Pressure Sensitive Model

The term pressure sensitive model was used, Prevost (1986), to name Prevost's model when it is applied to simulate the drained soil behaviour.
In drained conventional triaxial tests $\sigma_x = \sigma_z$, therefore, the yield function reduces to:

$$(q - \alpha^m)^2 + C^2(P' - \beta^m)^2 = K_m^2 \tag{4.40}$$

$$q = \sigma_y - \sigma_x \tag{4.41}$$

$$\alpha_y = \frac{2}{3}\alpha \tag{4.42}$$

$$\alpha_x = \alpha_z = -\frac{1}{3}\alpha \tag{4.43}$$

In Eq 4.40, the yield surfaces are all ellipses in the $(P' - q)$ stress subspace or all circles in the transformed plot $(q - CP')$, Fig 4.3. OC and OE are the critical state lines for both compression and extension respectively. The points O and E on the outermost yield surface define the critical state condition.

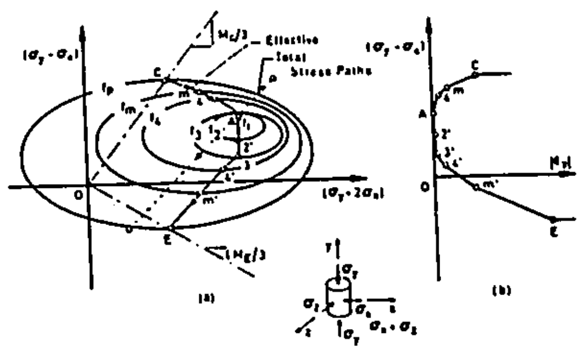

Figure 4.4: Representation of the pressure non-sensitive model.
(From Prevost, 1978)

4.6.5 Pressure Non-Sensitive Model

If Prevost's model is applied to simulate the undrained soil behaviour, the term pressure non-sensitive model will be used.
Undrained shearing of saturated soils imposes the condition $\epsilon_v = 0$ and generates pore water pressure. The derivation of the model parameters is explained in appendix B. The constitutive equations, Eq A.1 and Eq A.2, reduce to the following form:

$$d\epsilon_y = (\frac{1}{3G} + \frac{2}{3H})d(\sigma_y - \sigma_x) \tag{4.44}$$

$$dP' = 3\frac{B}{H}Ad(\sigma_y - \sigma_x) \tag{4.45}$$

The change in the pore water pressure is related to the change in the effective stresses by, Terzaghi (1943):

$$\dot{\sigma}_{ij} = \dot{\sigma}'_{ij} + \dot{P}_w\delta_{ij} \tag{4.46}$$

in which $\dot{P}_w$ is the change in the pore water pressure given as follows, Prevost (1978):

$$\dot{P}_w = \frac{9A(B+H)}{H(\frac{1}{G} + \frac{2}{H})}\dot{\epsilon}_y \tag{4.47}$$

Equations 4.33 and 4.36 express the translation of the yield surfaces during shearing. Since $\epsilon_v = 0$, $\dot{K} = 0$, the stress point moves along a stress path joining the apexes of the yield surfaces, $P = \beta^m$, Fig 4.4. Thus, the hydrostatic component of the yield function vanishes and Eq 4.39 reduces to the following form:

$$\frac{3}{2}(S_{ij} - \alpha_{ij}^m)(S_{ij} - \alpha_{ij}^m) - (K^m)^2 = 0. \tag{4.48}$$

The translation rule, Eq 4.33 and Eq 4.36 simplify to the form :

$$\dot{\beta} = \dot{P}' \tag{4.49}$$

$$\dot{\alpha} = \dot{\lambda}\mu \tag{4.50}$$

in which μ in Eq 4.25 takes the form:

$$\mu = \frac{1}{K^m}(K^{m+1} - K^m)S_{ij} - (\alpha_{ij}^m K^{m+1} - \alpha_{ij}^{m+1} K^m) \tag{4.51}$$

It should be noted that Prevost's kinematic rule is preserved in any stress subspace. When some stress component vanish, a set of the initial yield surfaces are represented by the non vanishing components. In the pressure non-sensitive model, the change in parameters H (plastic moduli) and K (size) are made to be function of the ϵ_{ij}^p, Prevost (1977a). The parameter K starts to change upon the first loading reversal. Once the yield surfaces reach their limiting sizes [3], Their associated plastic moduli start to vary.

Under cyclic loading conditions, the update sizes of the yield surfaces are given as follows:

$$K^m = K_0^m + \delta \tag{4.52}$$

In which K_0^m and K^m are the initial size and the update sizes of the yield surface f_m. The functions δ are found by comparing the experimental cyclic (rapid, strain controlled simple shear test) and monotonic (slow, monotonic increasing loading) stress strain curves, as shown in Fig 4.5. After a number of cycles, the decrease in the peak amplitude vanishes and the yield surfaces reach their limiting sizes. At this stage, the parameters H_m start to change. Their variations are determined by fitting into a parabolic function the experimental stress strain curve where the ultimate limiting values of K^m are substituted, Prevost (1977a).

Under cyclic loading conditions, the pressure non-sensitive model simplifies to a total stress model. It cannot be considered as particular case of the pressure sensitive model because the hardening of the material is not the same in both models.

[3]After a number of loading unloading reloading cycles, the yield surfaces reach a state where the change in applied stresses produce no change in sizes.

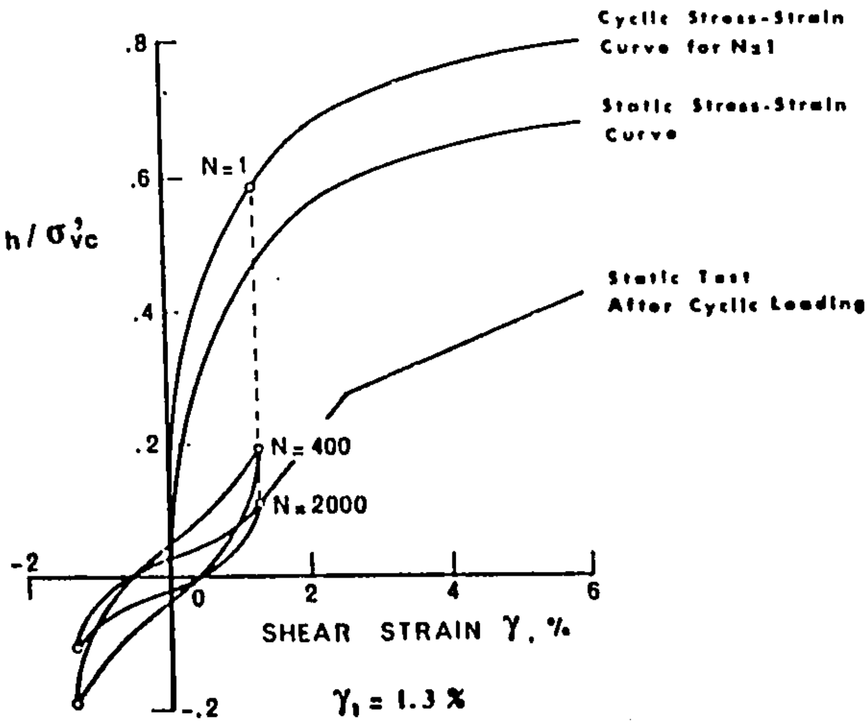

Figure 4.5: Comparison of the rapid (cyclic) and slow (monotonic) simple shear test results.
(From Prevost, 1977a)

The procedure of determining the change of the parameters K and H was based on a curve fitting procedure using spline functions, Prevost (1977a), rather than an analytical procedure as shown in the pressure sensitive model.

4.6.6 Model Parameters

The model requires a set of parameters. These are elastic parameters and the geometric configuration of the yield surfaces and their associated plastic parameters, as listed in Appendix B, Section B.1. Their dependency upon the effective mean normal stress and the volumetric strain are assumed as follows, Prevost (1986).

$$X = X_0\left(\frac{P'}{P'_0}\right)^n \tag{4.53}$$

$$Y = Y_0^{(\lambda\epsilon_v)} \tag{4.54}$$

in which $X = B, G, h, B'$ and $Y = \alpha, \beta, K$.

P': Current effective mean normal stress.

P'_0: Initial effective mean normal stress.

The subscript zero is used for the initial values at the reference mean effective stress P'_0.

In Eq 4.20, the parameter λ is computed from the isotropic compression test:

$$\lambda = \frac{1}{P'} \frac{dP'}{d\epsilon_v} \tag{4.55}$$

The list of the model parameters, experimental data needed and a complete mathematical derivation of the model parameters are presented in Appendix B. The details concerning the technique used to approximate the experimental stress strain curves, identification of the initial geometric configuration of the yield surfaces and their associated plastic parameters are presented in Chapter 6.

Chapter 5

LABORATORY TESTING

5.1 Introduction

The objective of this experimental work is to obtain data to be used in this research work. The tests were used to determine the parameters of Prevost's model. Following the parameter identification, the model was used to predict the behaviour of the soil subjected to different loading paths under different confining pressures. The laboratory testing involved a series of conventional drained and undrained triaxial tests. A total of 23 tests were carried out on a crushed quartz sand, as summarized in Table 5.2. The following tests were performed.

1. A series of drained conventional triaxial compression, CTC, tests carried out on loose, medium dense and dense sand at different confining pressures.
2. A series of undrained conventional triaxial compression, CTC, tests carried out on loose, medium dense and dense sands at different confining pressures.
3. A series of isotropic compression, ICT, tests carried out on loose, medium dense and dense sands.
4. A series of drained and undrained conventional triaxial extension, CTE, tests carried out on loose, medium dense sands.
5. A stress path test carried out on a dense sample under 137.89 kPa of initial mean stress.

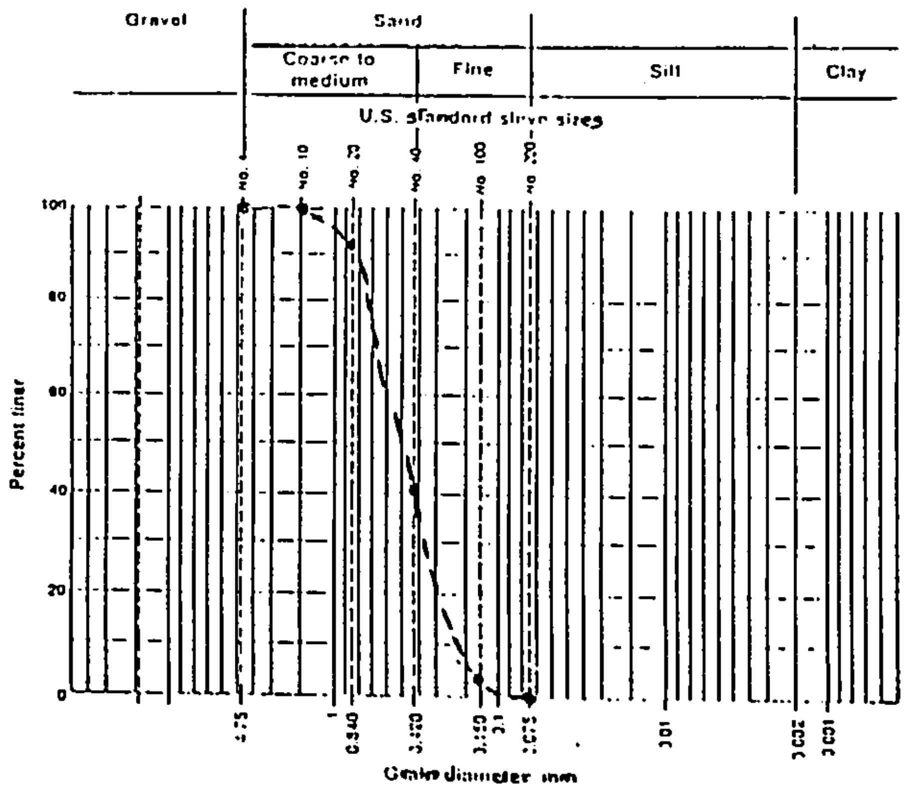

Figure 5.1: Grain size distribution

5.2 Description of the Sand Tested

The sand used in this investigation is a factory crushed quartz sand. The manufacturer designated the sand as a silica -24. The particle shape is angular and the coefficient of uniformity is 2.6. From the grain size distribution curve it would appear that it is a fine to medium sand, Fig 5.1.

The specific gravity, the minimum and the maximum void ratios are $G_s = 2.65$, $e_{max} = 1.10$ and $e_{min} = 0.42$ respectively. The minimum void ratio was obtained by vibrating the sand in the relative density mold using an electrical vibrator, model V 30. The maximum void ratio was obtained using the ASTM standard method D 2049-69.

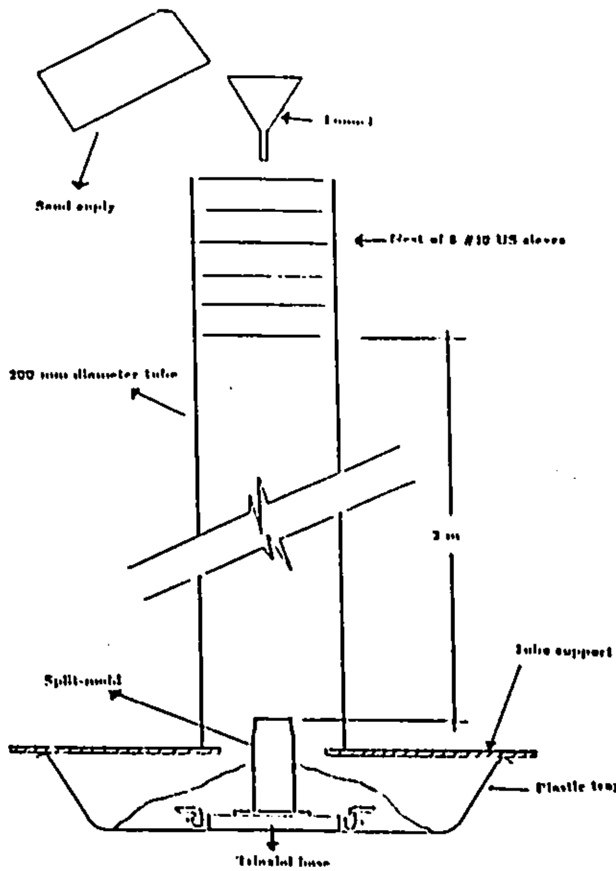

Figure 5.2: Sketch of the raining device

5.3 Preparation of the Samples

A raining device was used to prepare the soil sample. The raining device is a 200 mm diameter tube, placed over the cell base with the split-mold and topped with a set of 5 sieves # 10 US standard, Fig 5.2. The samples were prepared by depositing the sand with the use of funnels and allowing a free fall of the sand into the split mold through the set of sieves. A series of calibration tests were performed. The results obtained show that any state of density can be obtained by varying the height of the raining tube, Fig 5.3. The uniformity of the density was checked by using the raining device and pouring the sand into a graduate cylinder and check the density at different stages.
A heights of 10cm, 90cm and 200cm of the raining tube were used to prepare the loose, medium-dense and dense soil samples respectively.

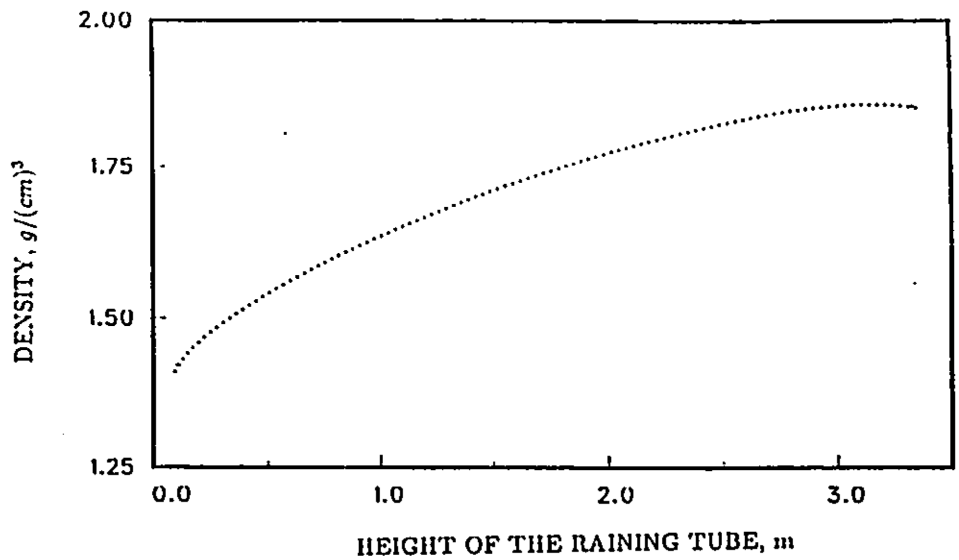

Figure 5.3: Density versus height of the raining tube relationship

5.4 Testing Procedure

All tests were preformed using a triaxial machine. The soil samples were prepared into a 5cm in diameter and 10cm in height cylindrical split-mold. Then, the sample was placed into the triaxial chamber. After filling the chamber with deaired water, the desired confining pressure was applied.

All samples were saturated by applying 15 kPa of back pressure and the degree of saturation was checked by determining Skempton's B parameter at the start of each test. To enhance the saturation rate, the samples were first purged with a carbon dioxide.

The rate of strain was 0.12 mm/min to avoid any development of pore water pressure in the drained series and to avoid any non- uniformity of the pore water pressure generation in the undrained series, Bishop and Henkel (1962).

The triaxial compression tests, CTC, were carried out by increasing the axial stress. The load and the axial displacement were recorded from dial gages. The volume change was monitored from the burrette of the volume change device. However, the pore water pressure was monitored by using a pressure transducer for the undrained series.

An electrically driven, hydraulically actuated triaxial machine, known as U.B.C triaxial machine, was used to carry out the conventional triaxial extension, CTE, tests. The sample preparation was the same as for the CTC series. The tests were carried out by decreasing the axial stress and keeping the lateral stresses constant. The upward load was applied by pulling up the loading ram while the cell pressure was kept constant throughout the test. The axial load was monitored by using a load transducer. The volume change and the axial displacement were monitored by using two L.S.G.T known as linear strain gage transducers.

The usual apparatus for the triaxial cell was used to carry out a series of isotropic compression tests, ITC. The hydrostatic stresses were applied by using the constant pressure mercury pot system. The volume change was recorded from the burrette of the volume change device.

5.5 Test Results

As commonly used in Geotechnical Engineering, the compressive stresses are considered to be positive. The stress parameters used in this investigation are the effective mean principal stress, $P' = \frac{(\sigma_1' + 2\sigma_3')}{3}$, and the deviatoric stress, $q = \sigma_1' - \sigma_3'$, in which σ_1' and σ_3' are the axial and the radial effective stresses. The volumetric strain is defined as $\epsilon_v = \epsilon_{ii} = (\epsilon_1 + 2\epsilon_3)$ where ϵ_1 and ϵ_3 are the axial and the radial components of the strains developed in the soil sample.
The test results are presented in Appendix C. Table 5.1 shows a sample of the results of a drained, CTC, test carried out on loose soil sample at $\sigma_3 = 68.94kPa$. Table 5.2 shows the tests performed together with the corresponding figures.

5.6 Interpretation of Test Results

5.6.1 Isotropic Compression Tests

Figures C.1, C.2 and C.3 show the isotropic compression test results for three different initial densities represented in the $(P' - \epsilon_v)$ plot. Each test includes a swelling curve where the plastic vo: :metric strains can be observed. These tests were used to determine the isotropic parameter λ, Eq 4.55.

5.6.2 Drained CTC Tests

Figures C.4 and C.5 show the effect of initial density on the stress-strain behaviour of the sand for confining pressures of 68.94 kPa and 137.89 kPa. Increasing values of relative density lead to an increase in the ultimate deviatoric stress values. In other words, the dense material exhibits a higher shearing resistance than the loose material.
The dilatancy is the tendency of the material to expand as the shear takes place. The dense material is strongly dilatant with the degree of dilatancy decreasing as the initial density decreases, Figs C.4b and C.5b. For example, the tendency for compression of loose samples is much greater than the dense samples. This effect can be seen by comparing Figs C.6, C.7 and C.8.
As illustrated in Fig C.6, an increasing confining pressure has two major effects on the stress-strain characteristics of the loose samples. It increases the strain values at the ultimate deviatoric stresses, and reduces the tendency of the soil to dilate. Similar effect was observed for both dense, Fig C.8, and medium dense samples, Fig C.7.

5.6.3 Drained Stress Path Test

Many existing models fail in predicting the plastic strain and the soil nonlinearity during unloading. Prevost's model uses a set of nesting yield surfaces and the stress increment vector is always directed towards the exterior of the yield surface. Thus, during shearing the soil sample is considered to be in loading at all stages of shearing regardless of whether the applied stresses are increasing or decreasing. Therefore, the soil experiences plastic straining under any loading path accept for the neutral loading.
The stress path test was performed for the purpose of investigating the capabilities of Prevost's model in simulating the behaviour of a given soil subjected to complex loading paths. Using the U.B.C triaxial machine, the test was carried out by increasing or decreasing the axial stress while the variation of the applied confining

pressure was controlled by changing the cell pressure. The back pressure was kept constant.

Another objective of this test is to evaluate the capability of Prevost's model in simulating the behaviour of soils near failure conditions. At near failure stages the plastic moduli approaches zero and most of the mathematical models for soils predict large non-recoverable strains which may not be observed in experiments. Further, this test allows a study of the effect of the inversion of the strain direction on the stress strain volume change characteristics of the soil. For these purposes, the state of stress was brought up near the failure line and then was reduced as indicated by points 2,5 and 7 in Fig C.9a. Note that the decrease of the deviatoric stress, shown in paths $2-3$ and $7-8$, was accompanied by a decrease in the confining pressure. The path $5-6$ was obtained by keeping the deviatoric stress constant and increasing the confining pressure. Figure C.9b shows the stress strain curve obtained. The corresponding volumetric strain is shown in Fig C.10a and the axial strain volume change relationship is presented in Fig C.10b.

5.6.4 Undrained CTC Tests

Investigations similar to that described above were conducted for the undrained behaviour of the soil. Undrained shearing of a fully saturated soil generates a pore water pressure. During shearing, the generation of the pore water pressure can be explained on the basis of the dilatancy behaviour of the soil tested. The dense samples tend to dilate, this tendency for dilatancy leads to a decrease of the pore water pressure which causes an increase in the effective stresses. As the pore water pressure continue to decrease, the effective confining pressure continue to increase until it reaches one of the following limiting conditions, Seed and Lee (1967):

1. The effective confining pressure builds up to a value equal to a critical value at which there is no further tendency for the sample to dilate. Thus, the pore water pressure would have no tendency to change and the failure of the sample occurs with the effective confining pressure equal to the critical confining pressure value.

2. The pore water pressure drops to a value equal to -1 atmosphere. At this stage, cavitation occurs. In this case the soil sample will be brought to failure under a

known pore water pressure equal to -1 atmosphere.

The effect of the initial density on the stress-strain characteristics is shown in Fig C.11. The loose samples, Fig C.12, would tend to compress with a resulting increase in the pore water pressure. During shearing the effective confining pressure continue to decrease until it reaches a stage in which there would be no tendency for the volume to change and correspondingly no change in the pore water pressure, and the failure occurs with the effective confining pressure equal to its critical value. By comparing Fig C.12 and Fig C.13, it is clear that the shearing resistance of the medium dense samples are higher than those obtained for the loose samples. This is due to effect of the initial density. However, the pore water pressure generation is directly dependent on the tendency of the soil to dilate as explained above.

5.6.5 Drained and Undrained CTE Tests

Prevost's model combines the extension stress-strain curves with the corresponding compression curves to determine a set of elastic and plastic parameters. These parameters control the model simulation of the mechanical behaviour of the soil for both extension and compression loading conditions.

Figure C.14 shows the drained extension, CTE, test results for three initial state of densities at σ_3 = 137.89 kPa. The corresponding volume change curves are also represented in the same figure. The effect of the initial density on the stress strain volume change characteristics is similar as explained for the CTC tests. Figure C.15 represents the undrained CTE test results. The corresponding pore water pressures are presented in the same figure.

5.7 Summary of the Data for Peak Points

A survey was done on the tests summarized in Table 5.2 to determine the failure conditions. Prevost's model uses an outermost yield surface as a bounding failure surface. The parameters related to this surface, such as size and position, are determined from the peak values of CTC and CTE test results. During shearing, the plastic moduli related to this surface decreases or increases towards zero depending on whether the material is stable or not. Then, the soil fails when the stress point reaches the critical state line. Tables 5.3, 5.4, 5.5, and 5.6 summarize the peak values. Table 5.7 gives the peak friction angle and the corresponding slopes of the failure lines in $(q - P')$ stress subspace for both compression and extension.

Note:

Note that the parameters used in Table 5.1 are defined as follows:

NUMB..................... Number of data point.

STRA..................... Axial strain, ϵ_1, (%).

DST...................... Deviatoric stress, $\sigma_1 - \sigma_3$, kPa.

PST...................... Vertical stress, σ_1, kPa.

STRR..................... Stress ratio, $\frac{\sigma_1}{\sigma_3}$.

V,STR.................... Volumetric strain, ϵ_v, (%).

TRIAXIAL COMPRESSION TEST
****

DRAINED TEST
****

LOCATION OF PROJECT	UNIVERSITY OF OTTAWA
SOIL DESCRIPTION	SAND
TESTED DY	DERRADJI-AOUAT AHMED
DAY OF TESTING	3/21/1987
CONFINING PRESSURE	68.94 KPA

SAMPLE DATA

SAMPLE WEIGHT........................	279.590 G
AVERAGE DIAMETER......................	49.450 MM
SAMPLE HEIGHT.........................	106.000 MM
CROSS SECTION AREA....................	19.205 SQ CM
VOLUME OF THE SAMPLE..................	203.577 CU CM
DENSITY OF THE SOIL...................	1.373 G/CU CM
LOADING RING CONSTANT.................	1.263 lbs/div

NUMB	STRA %	DST KPA	PST KPA	STRR	V,STR %
1	0.000	0.000	68.944	1.000	0.000
2	0.189	52.571	121.515	1.763	-0.049
3	0.340	75.821	144.765	2.100	-0.074
4	0.481	90.274	159.218	2.309	-0.098
5	0.632	98.860	167.804	2.434	-0.098
6	0.764	104.536	173.480	2.516	-0.098
7	0.925	110.165	179.109	2.598	-0.098
8	1.066	115.798	184.742	2.680	-0.074
9	1.245	121.367	190.311	2.760	-0.049
10	1.387	124.079	193.023	2.800	-0.049
11	1.245	60.684	129.628	1.880	-0.098
12	1.208	0.000	68.944	1.000	-0.098
13	1.396	115.411	184.355	2.674	-0.123
14	1.698	132.317	201.260	2.919	-0.147
15	2.000	137.645	206.589	2.996	-0.147
16	2.340	142.884	211.828	3.072	-0.147
17	2.642	145.291	214.235	3.107	-0.049
18	2.925	147.709	216.653	3.142	-0.049
19	3.245	150.052	218.996	3.176	-0.025
20	3.575	153.772	222.716	3.230	0.000
21	3.868	154.713	223.656	3.244	0.000
22	4.189	157.000	225.944	3.277	0.025
23	4.500	162.079	231.023	3.351	0.025
24	4.802	161.566	230.510	3.343	0.025
25	5.113	162.426	231.370	3.356	0.049
26	5.745	165.481	234.425	3.400	0.049
27	6.387	169.833	238.777	3.463	0.098
28	7.000	171.442	240.386	3.487	0.123
29	7.642	174.313	243.257	3.528	0.147
30	8.142	177.402	246.346	3.573	0.172

Table 5.1: Test results, drained CTC test, $\sigma_3 = 137.89kPa$

Table 5.2: Summary of the Tests Performed

Test #	Test type	Drainage condition	Initial confining pressure (kPa)	Initial dry density (g/cm^2)	Initial relative density (%)	Initial void ratio (%)	Figure	Sample category
1	ICT			1.385	37.86	.913	C-1	Loose
2	ICT			1.524	59.18	.739	C-2	Medium - dense
3	ICT			1.800	93.33	.472	C-3	Dense
4	CTC	Drained	68.94	1.373	34.69	.93	C-6	Loose
5	CTC	Drained	137.89	1.398	39.11	.895	C-6	Loose
6	CTC	Drained	275.78	1.399	39.29	.894	C-6	Loose
7	CTC	Drained	413.66	1.383	36.48	.916	C-6	Loose
8	CTC	Drained	68.94	1.544	62.07	.716	C-7	Medium - Dense
9	CTC	Drained	137.89	1.559	64.18	.700	C-7	Medium - Dense
10	CTC	Drained	275.78	1.548	61.91	.712	C-7	Medium - Dense
11	CTC	Drained	68.94	1.809	94.25	.465	C-8	Dense
12	CTC	Drained	137.89	1.801	93.43	.471	C-8	Dense
13	CTC	Undrained	137.89	1.394	38.42	.901	C-12	Loose
14	CTC	Undrained	275.78	1.397	38.94	.896	C-12	Loose
15	CTC	Undrained	413.66	1.386	37.01	.912	C-12	Loose
16	CTC	Undrained	68.94	1.542	61.78	.718	C-13	Medium - Dense
17	CTC	Undrained	137.89	1.521	58.74	.742	C-13	Medium - Dense
18	CTE	Drained	137.89	1.360	32.33	.948	C-14	Loose
19	CTE	Drained	137.89	1.571	65.71	.687	C-14	Medium - Dense
20	CTE	Drained	137.89	1.800	93.33	.472	C-14	Dense
21	CTE	Undrained	137.89	1.351	30.48	.963	C-15	Loose
22	CTE	Undrained	137.89	1.526	59.47	.736	C-15	Medium - Dense
23	SPT	Drained	137.89	1.801	93.43	.471	C-9 C-10	Dense

Table 5.3: Summary of the Drained CTC Test Results

Test #	Initial confining pressure (kPa)	Initial relative density (%)	Ultimate deviatoric stress (kPa)	Ultimate hydrostatic pressure (kPa)	Axial strain (%)	Volumetric strain (%)	Figure
4	68.94	34.69	177.40	128.073	8.14	0.179	C.6
5	137.89	39.11	303.00	238.890	9.00	-0.781	C.6
6	275.78	39.29	568.70	465.347	9.53	-1.333	C.6
7	413.66	36.48	790.64	677.207	9.40	-2.11	C.6
8	68.94	62.07	225.76	144.199	6.46	2.198	C.7
9	137.89	64.18	476.68	296.783	7.36	1.694	C.7
10	275.78	61.91	856.59	561.309	9.35	1.766	C.7
11	68.94	94.25	307.532	171.451	5.538	3.223	C.8
12	137.89	93.43	560.761	324.810	5.731	1.731	C.8

Table 5.4: Summary of the Undrained CTC Test Results

Test #	Initial confining pressure (kPa)	Initial relative density (%)	Ultimate deviatoric stress (kPa)	Ultimate effective hydrostatic pressure (kPa)	Axial strain (%)	Pore water pressure (kPa)	Figure
13	137.89	38.42	280.44	209.570	19.03	21.798	C.12
14	275.78	38.94	497.69	374.612	18.57	67.071	C.12
15	413.66	37.01	526.291	388.580	10.40	200.53	C.12
16	68.94	61.78	636.04	344.150	8.342	-63.200	C.13
17	137.89	58.74	755.371	447.920	9.249	-58.2400	C.13

Table 5.5: Summary of the Drained CTE Test Results

Test #	Initial confining pressure (kPa)	Initial relative density (%)	Ultimate deviatoric stress (kPa)	Ultimate hydrostatic pressure (kPa)	Axial strain (%)	Volumetric strain (%)	Figure
18	137.89	32.33	-88.61	108.350	-13.31	-0.38	C.14
19	137.89	65.71	-97.49	105.390	-6.87	1.40	C.14
20	137.89	93.33	-112.17	100.500	-3.82	1.03	C.14

Table 5.6: Summary of the Undrained CTE Test Results

Test #	Initial confining pressure (kPa)	Initial relative density (%)	Ultimate deviatoric stress (kPa)	Ultimate effective hydrostatic pressure (kPa)	Axial strain (%)	Pore water pressure (kPa)	Figure
21	137.89	30.48	-97.20	20.17	-14.49	85.32	C.15
22	137.89	59.47	-336.4	107.35	-8.230	-81.60	C.15

Table 5.7: Ultimate Failure Data

	Angle of friction		Slopes of the failure lines	
	ϕ'_c	ϕ'_e	M_c	M_c
Loose	30.51	28.250	1.222	1.123
Medium-dense	38.281	33.15	1.561	1.337
Dense	42.870	41.70	1.759	1.709

Chapter 6

PARAMETER IDENTIFICATION

6.1 Introduction

This chapter deals with the identification of the model parameters for the crushed quartz sand, Ottawa sand and Fuji river sand. These parameters are determined from the conventional triaxial compression, CTC, and extension, CTE, tests. In these tests, the loading axes coincide with the principal axes of the anisotropy tensor α. Thus, according to model the material exhibits a cross anisotropy and its transverse isotropy is preserved during shearing. A complete mathematical derivation of the model parameters is presented in Appendix B.

6.2 Model Parameters

The model parameters can be obtained from isotropically consolidated drained triaxial compression and extension tests with volume change measurements. In the compression test, the axial stress is increased to reach the failure state, while in the extension test, the axial stress is reduced to reach the failure state. In order to identify the model parameters, both tests must be performed at the same initial cell

Table 6.1: Measured values of (λ) for crushed quartz sand

State of density	λ
Loose	84.190
Medium-dense	137.980
Dense	214.185

pressure which remains constant throughout the test. As explained in Appendix B, the test results must be presented in the form of graphs, $q - \bar{\epsilon}$ and $P' - \epsilon_v$ where:

1. $q = \sigma_1' - \sigma_3'$
2. $\bar{\epsilon} = \epsilon_1 - \epsilon_3$
3. $P' = \frac{(\sigma_1' + 2\sigma_3')}{3}$.
4. $\epsilon_v = \epsilon_1 + 2\epsilon_3$.

Typical plots of $q - \bar{\epsilon}$ and $P' - \epsilon_v$ are shown in Fig 6.1. The smooth experimental data are approximated by linear segments of constant tangent moduli. Each segment can be viewed as a region bounded by two yield surfaces. Thus, the model consists of a series of nested yield surfaces of which the outermost yield surface is the bounding failure surface. The size of the first yield surface is degenerated to zero. Thus, the pure elastic zone vanishes and the model simulates an elasto-plastic soil behaviour from the start of the stress strain curve.

6.2.1 Isotropic Parameter

Figure 6.2 shows the results of an isotropic compression test carried out on a loose sample of the crushed quartz sand. When the stress point reaches the outermost yield surface, the soil sample is in a normally consolidated state. It was assumed, Prevost(1980), that the isotropic compression test results are plotted as a straight line parallel to the projection of the critical state line in the $lnP' - \epsilon_v$ plane. Thus, the parameter λ is simply determined from Eq 4.55. Table 6.1 shows the values of λ for dense, medium-dense and loose samples of crushed quartz sand.

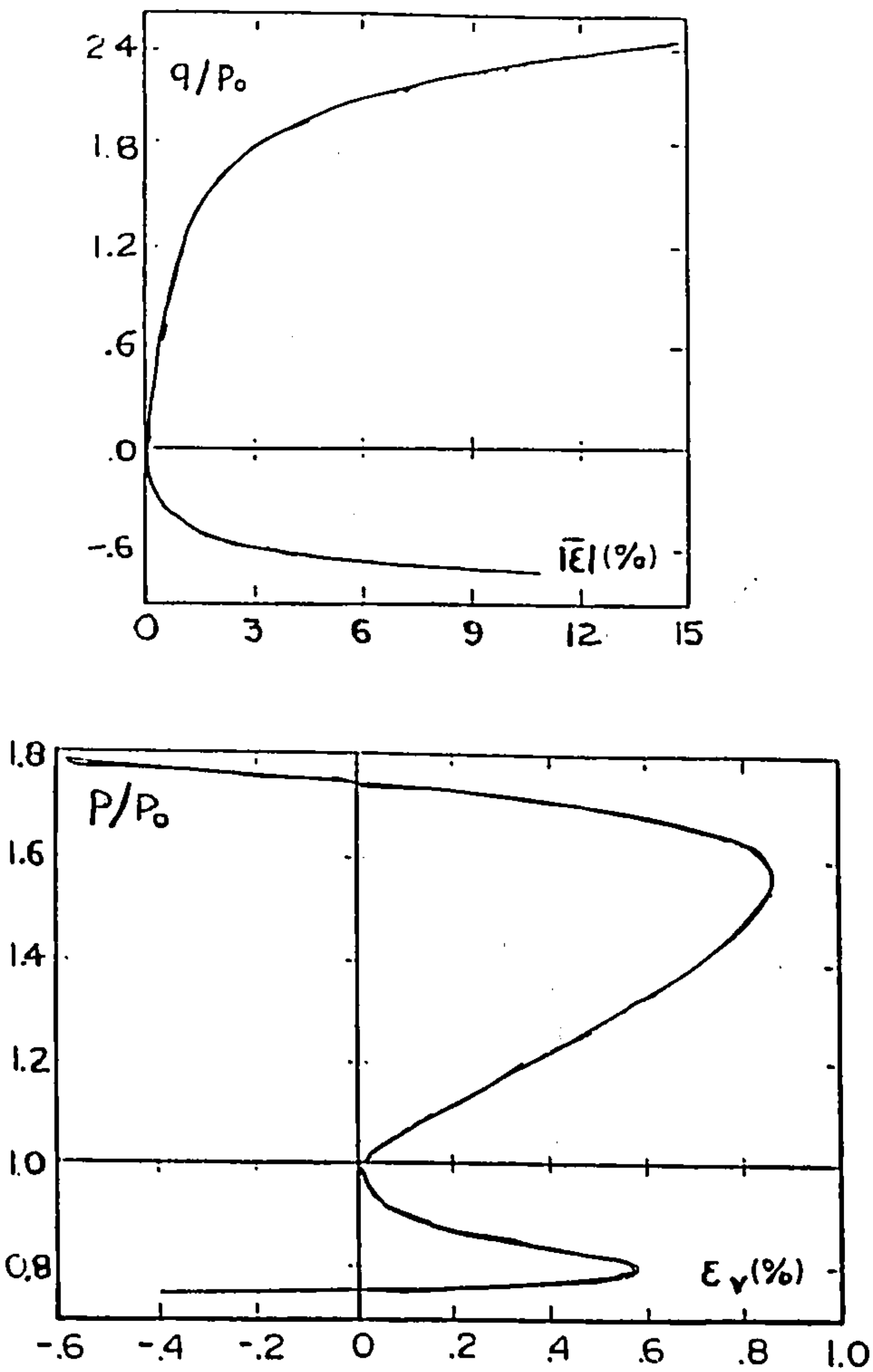

Figure 6.1: Typical Sand Behaviour:

a) Shear stress-strain curve.

b) Volumetric stress-strain curve.

(From Prevost, 1987)

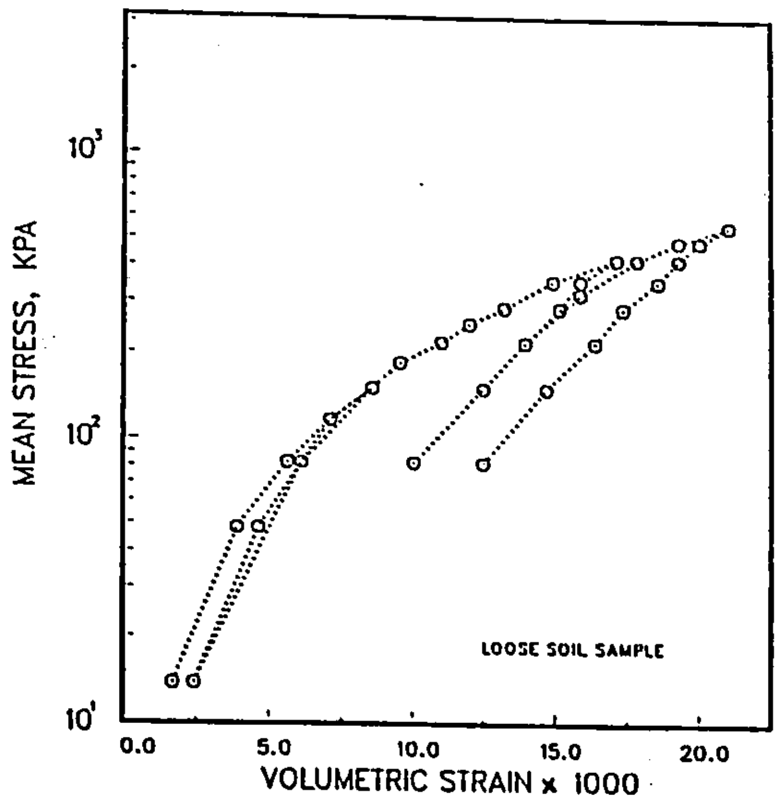

Figure 6.2: Isotropic compression test results, loose soil sample of crushed quartz sand

6.2.2 Elastic Parameters

The first parameters that can be obtained from the data are the initial elastic shear modulus, G_0, and the initial elastic bulk modulus, B_0, corresponding to the reference stress P'_0. These are obtained from the initial gradients of the $q_c - \bar{\epsilon}_c$ and $P' - \epsilon_v$ curves, respectively:

1.$G_0 = (\dot{q}/2\dot{\bar{\epsilon}})_{initial}$

2.$B_0 = (\dot{P}'/\dot{\epsilon}_v)_{initial}$

The computer program, PARAMETER, was used to compute the initial elastic model parameters which are presented in Tables 6.2 to 6.10. The elastic soil non-linearity is introduced through the variation of the parameters G and B during shearing according to Eq 4.53.

6.2.3 Plastic Parameters

The plastic parameters related to each yield surface are listed in Section B.1 of Appendix B. For the simplicity, the plastic parameters are classified into two categories.

1. Geometric parameters: α, β, K, (positions and sizes).

2. Constitutive plastic parameters: B', h, A, (plastic shear modulus, parameter B' and degree of non associativity).

These parameters are determined from the condition that the slopes $\dot{q}/\dot{\bar{\epsilon}}$ are the same in both triaxial compression and extension tests when the stress point reaches a yield surface, f_m. Since the soil behaviour in compression and extension are different, the same tangent modulus is not found for the same shear stress value in compression and extension data, but similar slope may exist at different shear stress levels. For example, when the stress point reaches a yield surface f_m, $q_c \neq q_e$ but $(\dot{q}_c/\dot{\bar{\epsilon}}_c = \dot{q}_e/\dot{\bar{\epsilon}}_e)$

The parameters related to the outermost failure surface are found by noting the points at which the stress-strain curves flatten out in both compression and extension, peak points. The geometric configuration of the outermost yield surface is determined according to the following equations:

1. $M_c = \frac{K^p+3\alpha_q^p}{\beta^p}$.

2. $M_e = \frac{K^p-3\alpha_q^p}{\beta^p}$.

where M_c and M_e are the slopes of the failure lines in $q - P'$ plot.

6.3 Parameter Identification Technique

This section concerns with the technique used to determine the model parameters. As an example, only a loose state of density is considered. The same technique was used for both medium-dense and dense sands.

Having decided on the number of the yield surfaces, NYS, the stress-strain curve, $q - \bar{\epsilon}$ is subdivided into intervals along q axis or $\bar{\epsilon}$ axis, as shown in Fig 6.3. The gradient $\frac{\dot{q}}{\dot{\bar{\epsilon}}}$ or $\frac{\dot{\bar{\epsilon}}}{\dot{q}}$ is obtained for each interval. A search is then made for a point on the extension curve with the same gradient. The two points with matching gradients are then transferred to the $q - P'$ plot and joint to the origin P_0. This defines a yield surfaces in triaxial plane, Fig 6.4. Then, the associated plastic parameters are determined according to Eq B-31 to Eq B-37. If the extension q_e axis (or $\bar{\epsilon}_e$ axis) was subdivided into intervals and the corresponding $\bar{\epsilon}_e$ (or q_e) from its slope, the values obtained for q_e or $\bar{\epsilon}_e$ diverge dramatically from the experimental extension curve.

In here, the stress-strain curves of the extension tests were first fitted with a logarithmic or a hyperbolic function and the values of q_e (or $\bar{\epsilon}_e$) were determined by taking the derivative of the function at a specified points.

During shearing, the geometric parameters vary according to Eq 4.54 while the elastic and plastic parameters vary according to Eq 4.53. Thus, one can imagine set of circular nesting yield surfaces, in $CP' - q$ stress subspace, with initial positions, initial sizes and initial related plastic parameters. During shearing these surfaces expand or contract isotropically depending on the current value of the volumetric strain developed. Their associated parameters vary depending on the current applied hydrostatic stress values.

Table 6.2 shows the initial model parameters obtained for the loose sand. Table 6.3 and Table 6.4 show the model parameters related to the drained CTC and CTE tests of 137.89 kPa of initial confining pressure. The initial model parameters related to the medium-dense and dense sands are represented in Table 6.5 and Table 6.6 respectively. Eleven yield surfaces were used in the calculations of the model parameters related to the crushed quartz sand.

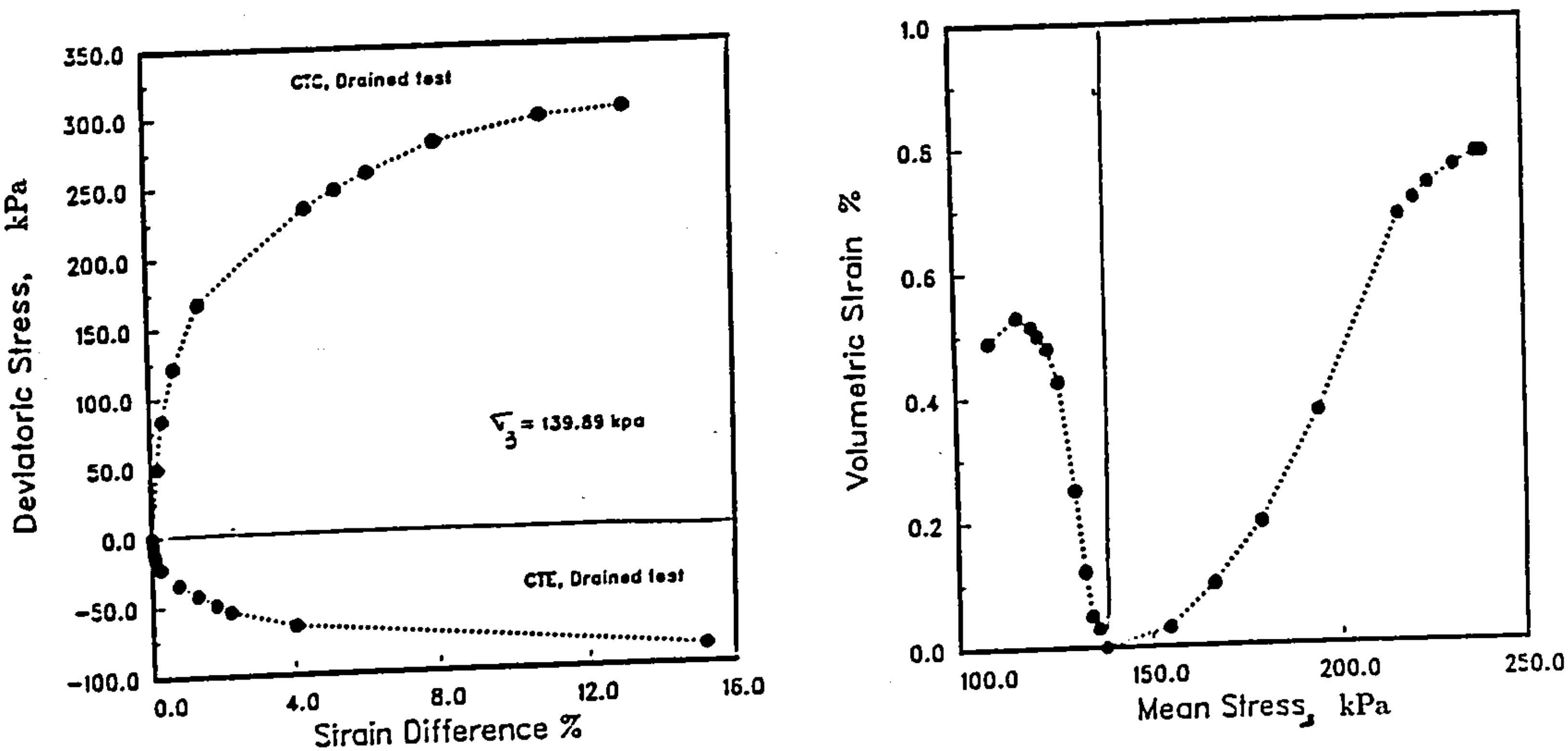

Figure 6.3: Parameter identification, subdivision of the stress-strain curves

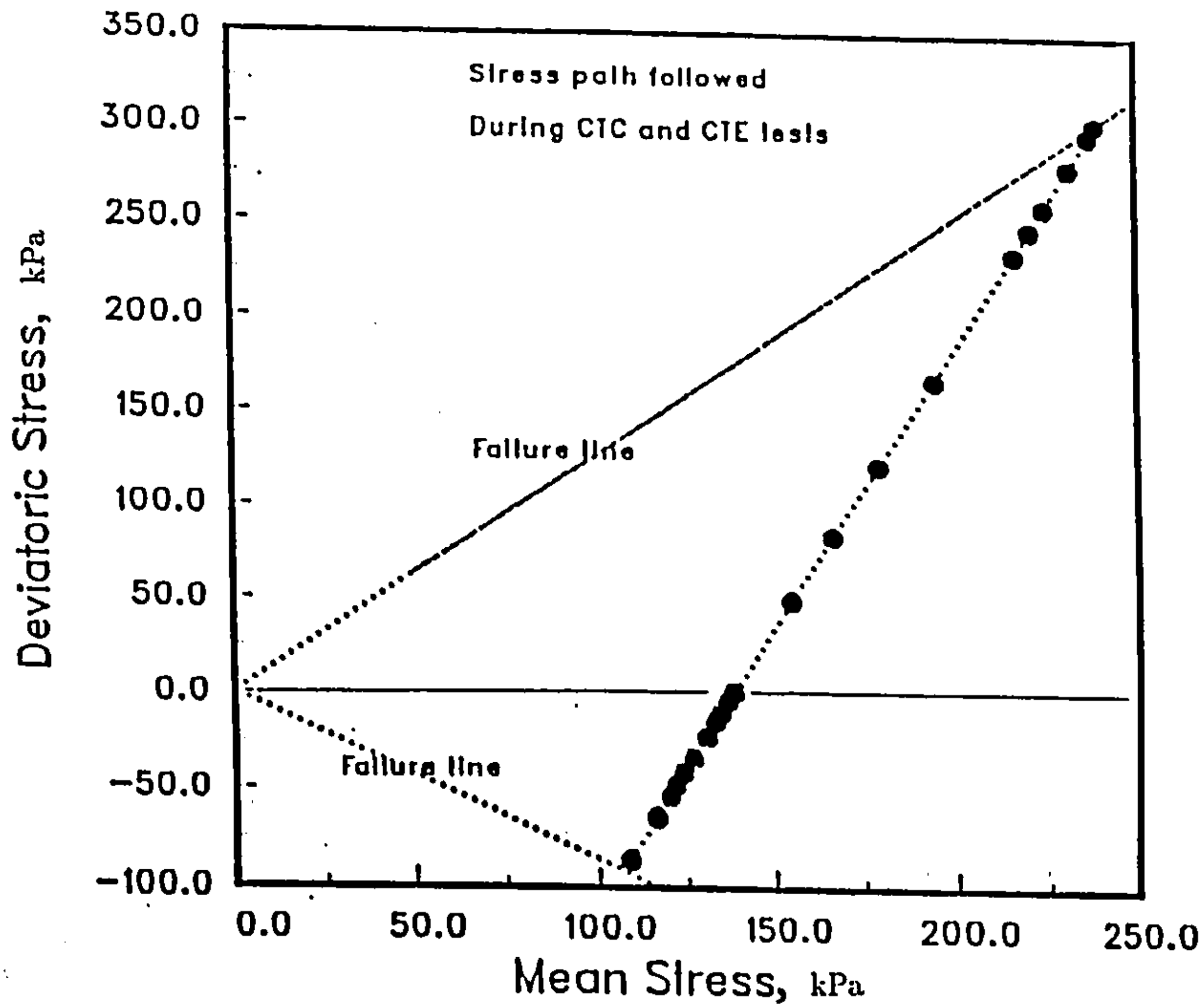

Figure 6.4: Parameter identification, representation of the yield surfaces

6.4 PARAMETER, Computer Code

PARAMETER is a computer program which is used to determine the initial model parameters. The program listing is presented in Appendix B, accompanied with an example of input data and output results for the loose sand.

6.4.1 Flowchart

The determination of the polar angles related to each yield surface is the corner stone in the identification of the model parameters. Since Eq B.30 contains a sign +/- (depending on the sign of the product $tan\phi_c.tan\phi_e$), it will be emphasized on the procedure of solving for ϕ_c and ϕ_e. For the simplicity, the program flowchart is presented in the following form:

1. Read the input data.
2. Determine the elastic parameters.
3. Determine the polar angles associated with each yield surface;

3.1 First solution ($tan\phi_c.tan\phi_e < 0$)

a. $S = \frac{1}{2C}(3\gamma_c \frac{X_c}{Y_c} + 3\gamma_e \frac{X_e}{Y_e})$

b. $T = C\frac{RCE}{1-RCE^2}$

IF $\frac{T-S}{T} > 0$............ GO TO 3.2

Else;........... solve for ϕ_c and ϕ_e

GO TO 3.3

3.2 $S = \frac{1}{2C}(3\gamma_c \frac{X_c}{Y_c} - 3\gamma_e \frac{X_e}{Y_e})$

Solve for ϕ_c and ϕ_e

3.3 Check the overlapping of the yield surfaces.

4. Determine the plastic parameters.
5. Print the output results.

6.4.2 Input Data

The input data required are:
1. Drainage conditions: drained or undrained.
2. Isotropic parameter, λ, noted as (W) in the program.
3. Number of yield surfaces, NYS.
4. Soil type, sand or clay.
5. Initial confining pressure, P_0'.
6. Shear and volumetric stress-strain test results as determined from Section 6.3.

6.4.3 Output Results

The output lists the following:
1. Initial elastic parameters.
2. Polar angles related to each yield surface.
3. Initial geometric configuration of the yield surfaces and their associated initial plastic parameters.

6.5 Ottawa Sand

The drained behaviour of Ottawa sand was considered. The published data of Montreal Workshop (1980) was used to identify the model parameters. The sand, whose gradation is shown in Fig 6.5, was compacted by aerial pluviation up to 1.73 g/ cm^3 ($D_r = 87$) and tested in dry condition. The stress strain curves used for the parameter identification are shown in Fig 6.6 where a CTC and CTE tests under 10 psi of cell pressure are shown. The program output of the initial model parameters is shown in Table 6.7 where nine yield surfaces were involved.

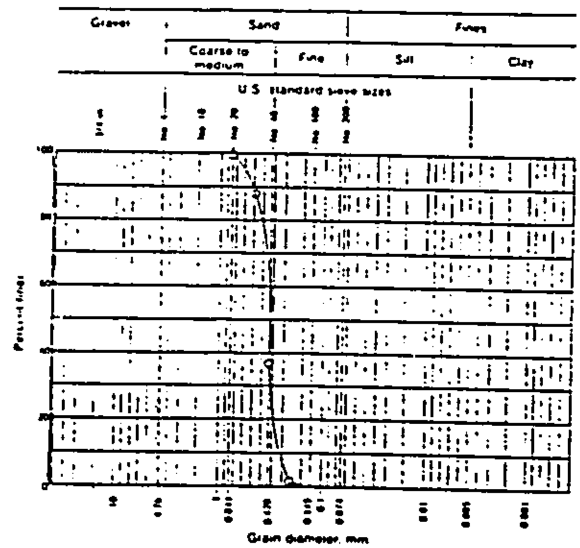

Figure 6.5: Ottawa Sand, grain size distribution.

6.6 Fuji River Sand

Tatsuaka and Ishihara (1974) carried out a series of drained cyclic tests on samples of Fuji River sand. Their data was used to investigate the performance of Prevost's model in simulating the cyclic behaviour of samples subjected to stress reversal from compression to extension and vice versa. The stress strain curves used to identify the model parameters are shown in Fig 6.7. The model parameters are presented in Table 6.8 in which 10 yield surfaces were involved.

6.7 Undrained Model Parameters

In the particular case when $\epsilon_v = 0$, the geometric configuration of the yield surfaces are represented to cover the effective stress path of the isotropically consolidated undrained CTC and CTE tests. The initial sizes and positions of the yield surfaces

remain constant during shearing, $\lambda = 0$. In this case, the model formulation presented in appendix B reduces to;
$Y_e = Y_c = -B$ and $RCE = C\frac{P'_c - P'_e}{q_c - q_e}$.
In which B is the initial elastic undrained bulk modulus determined from $B = A + \frac{2}{3}G$ where A and G are Lame's constants.
The model parameters are determined using the same technique as explained in the drained case. PARAMETER, computer code, was used to calculate the model parameters for the crushed quartz sand. Knowing the polar angles, the model parameters are determined from Eqs B-31 to B-37. Table 6.9 and Table 6.10 show the model parameters for the crushed quartz sand for both loose and medium-dense soils. It should be noted that the initial geometric configuration of the yield surfaces coincide with those related to the test used.

6.8 Predictions of the Model Parameters for Other Tests

The multisurface theory of plasticity combines the isotropic and kinematic hardening rules to model the soil behaviour, Prevost (1977a, 1978, 1986). The hardening rule is expressed by the translation and the expansion/ contraction of the yield surfaces during shearing. Their initial positions and sizes and the associated initial plastic parameters reflect the past stress-strain history of the material.
A set of initial nesting surfaces are ranged in a way to envelope the line of stress-path followed during testing. The stress point moves from one yield surface to another following the loading path. Thus, there is always a set of initial yield surfaces related to each path. At this stage the following question must be asked:
If the initial plastic model parameters represent the stress-strain history of the soil, why Prevost's models employ a set of initial plastic parameters related to each loading path? In other words, does the soil element have a different stress-strain histories related to each stress path followed during testing?
This question can be answered as follows:
The soil element has not different stress-strain histories, but the parameters determined from CTC-CTE tests at low confining pressure do not erase the multi-level soil anisotropy. However, the parameters determined from CTC-CTE tests at high

confining pressure has two major effects:

1. These parameters ignore the volumetric memory of the soil element at low confining pressures.

2. The failure loads will exceed their real values.

It should be noted that the multi-level soil anistropy corresponds to the values of the parameter α at high shear stresses and the volumetric memory corresponds to the initial sizes of the yield surfaces.

Knowing the initial model parameters determined from given CTC-CTE tests, the initial model parameters for other tests can be predicted. The purpose of the computation procedure implemented in the PARAMETER computer code is to find an equivalent initial geometric configuration of a set of nesting surfaces (related to the tests to be predicted) to those determined from the given tests without disturbance of their initial orientations. The procedure involves a variation of the initial elastic and plastic parameters according to the following formula:

$$X_0'' = X_0\left(\frac{PP_0'}{P_0'}\right)^n \tag{6.1}$$

The above formula is similar to Eq 4.53 in which:

$X_0 = G_0, B_0, h_0$ and B_0' .

$X_0'' = G_0'', B_0'', h_0''$ and B_0''.

P_0' is the initial hydrostatic pressure of the given test.

PP_0' is the initial hydrostatic pressure of the test to be predicted.

The initial parameters, G_0, B_0, h_0, and B_0' are the same as defined in Eq 4.53. The superscript, , is used to identify the initial values at a reference PP_0'.

The initial sizes and positions of equivalent yield surfaces are found to be directly dependent on the equivalent stress levels. They expand/ contract uniformly depending on the ratio ($\frac{PP_0'}{P_0'}$) whether it is greater or less than one. The equivalent stress levels correspond to the stresses, q and P' , of the reference PP_0' which have to satisfy the orientation condition.

Table 6.11 shows the predicted initial model parameters of drained CTC-CTE tests under 275.78 kPa of initial hydrostatic pressure (loose sample) using the results shown in Table 6.2 as input data. The initial model parameters for all tests used in this research work, were first predicted as explained above and used as an input data for PREDICTIONS or SIMULATIONS [1]. Thus the model uses a double prediction

[1]PREDICTIONS and SIMULATIONS are computer programs in which the model has been implemented.

Table 6.2: Initial model parameters of loose crushed quartz sand, drained test $\sigma_3 = 137.89kPa$.

G0 = 14119.66 B0 = 55066.69 n = .50 lambda = 84.19

	ALPHA	BETA	K	H	B	A
2	20.98	150.50	27.36	0.54E+06	-.11E+08	0.20
3	58.05	121.18	70.08	0.99E+05	-.84E+05	-4.67
4	65.78	118.53	79.59	0.15E+05	-.92E+04	-2.81
5	66.87	111.09	85.88	0.69E+04	-.25E+04	-1.70
6	60.83	97.58	87.62	0.25E+04	-.12E+04	-1.12
7	54.29	102.23	91.50	0.16E+04	-.54E+03	-0.83
8	55.08	99.32	96.56	0.14E+04	-.50E+03	-0.92
9	58.18	100.27	104.74	0.12E+04	-.40E+03	-0.95
10	56.82	97.89	110.63	0.62E+03	-.24E+03	-0.93
11	49.38	98.24	120.48	0.23E+03	-.37E+02	-0.87

process to simulate the soil behavior.

[1]PREDICTIONS and SIMULATIONS are computer programs in which the model has been implemented.

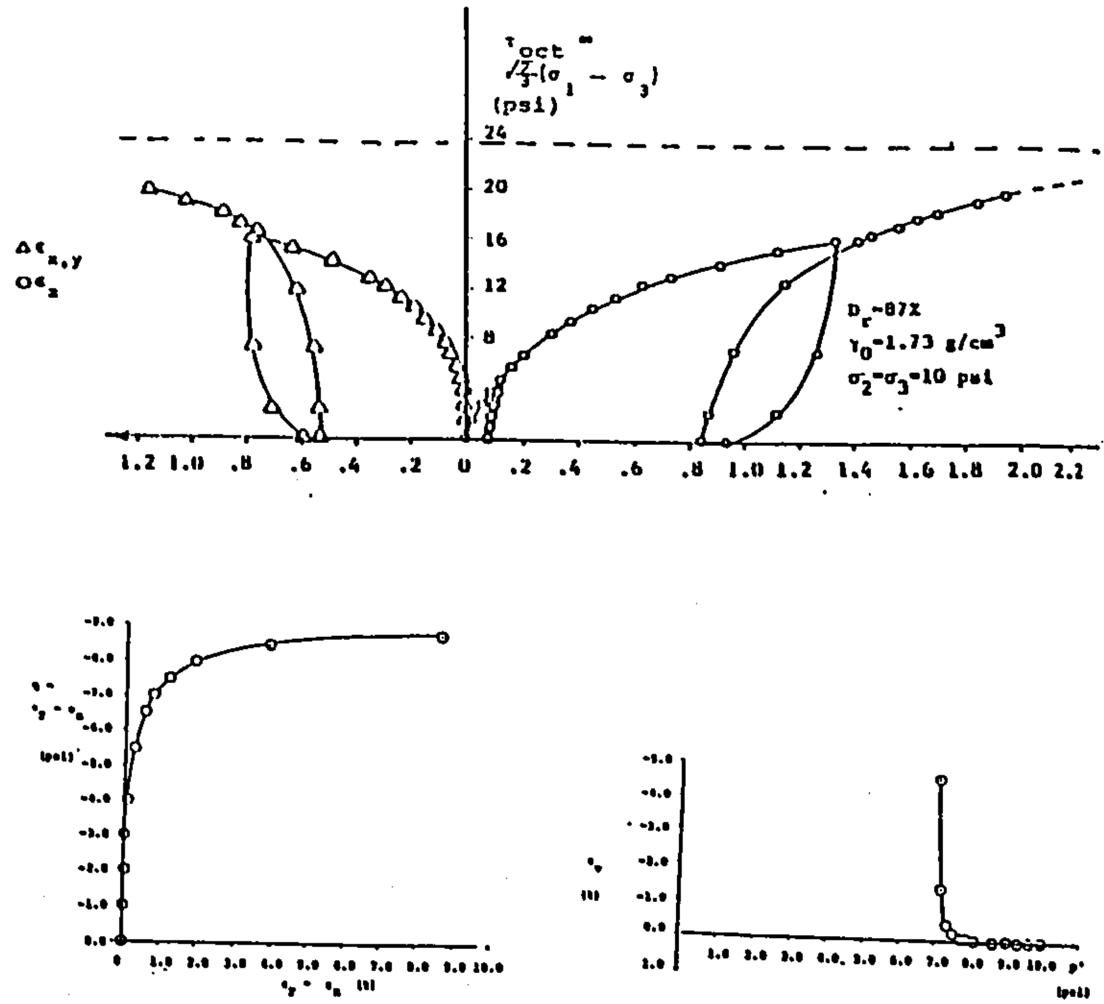

Figure 6.6: Ottawa Sand, stress-strain curves.

.(From Montreal Workshop, 1980)

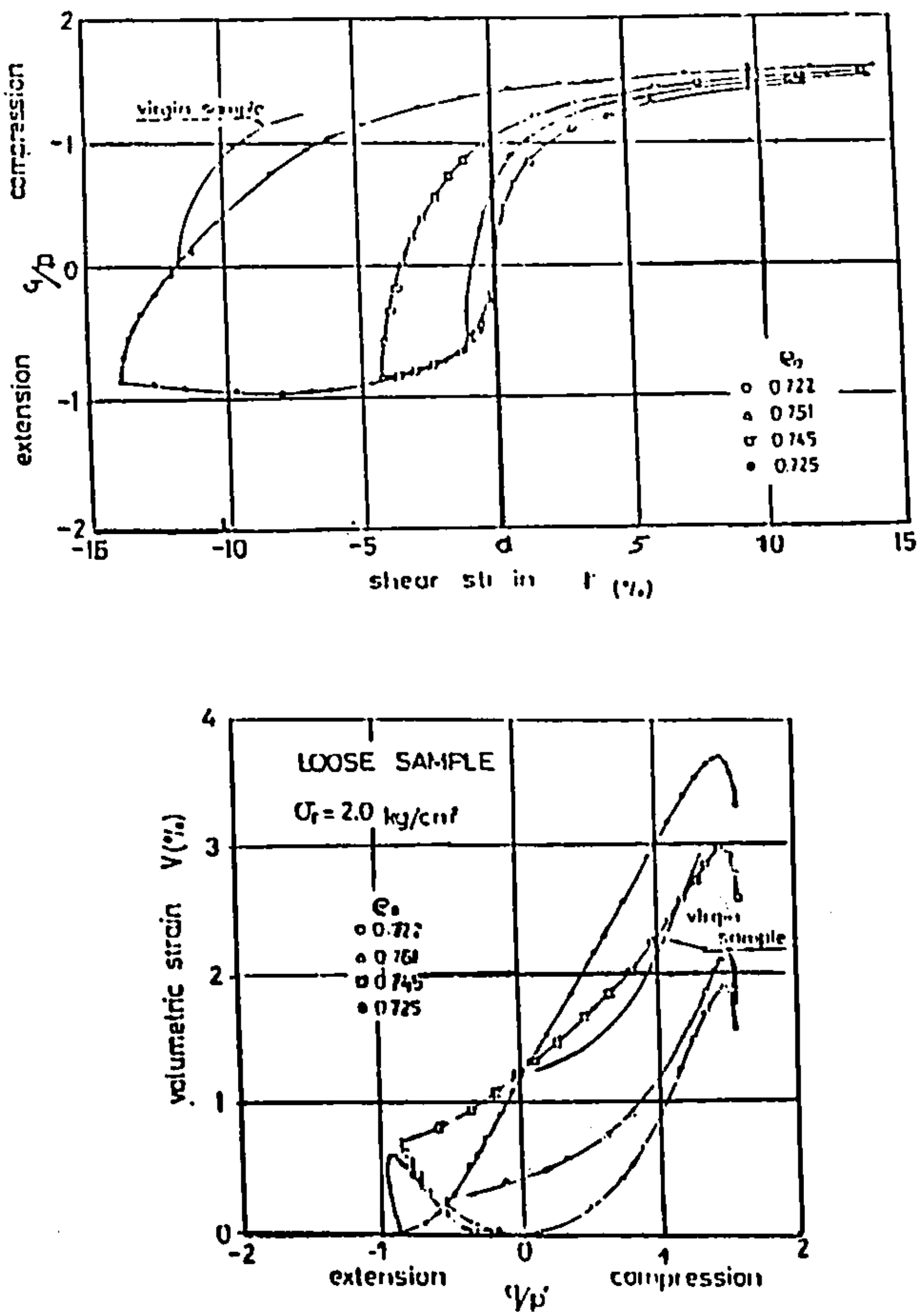

Figure 6.7: Fuji River Sand, stress-strain curves. (From Tatsuka and Ishihara, 1974)

Table 6.3: CTC model parameters of loose crushed quartz sand, drained CTC test $\sigma_3 = 137.89kPa$

G0 = 14119.66 B0 = 55066.69 n = .50 lambda = 84.19

	ALPHA	BETA	Km	Hn	Bn	An
2	21.50	154.35	28.06	0.57E+06	-.11E+08	0.20
3	63.04	131.60	76.11	0.11E+06	-.93E+05	-4.67
4	77.52	139.68	93.79	0.17E+05	-.10E+05	-2.81
5	91.47	151.94	117.47	0.81E+04	-.29E+04	-1.70
6	108.10	173.38	155.71	0.32E+04	-.15E+04	-1.12
7	98.54	185.55	166.08	0.20E+04	-.68E+03	-0.83
8	101.98	183.94	178.84	0.17E+04	-.64E+03	-0.92
9	108.53	187.13	195.45	0.16E+04	-.62E+03	-0.95
10	109.66	188.94	213.51	0.82E+03	-.32E+03	-0.93
11	95.30	189.61	232.53	0.30E+03	-.48E+02	-0.87

Table 6.4: CTE model parameters of loose crushed quartz sand, drained CTC test $\sigma_3 = 137.89kPa$

G0 = 14119.66 B0 = 55066.69 n = .50 lambda = 84.19

	ALPHA	BETA	Km	Hn	Bn	Am
2	21.50	154.35	28.06	0.54E+06	-.11E+08	0.20
3	60.54	126.39	73.10	0.90E+05	-.83E+05	-4.67
4	72.77	131.13	88.05	0.15E+05	-.90E+04	-2.81
5	82.54	137.11	100.00	0.87E+04	-.24E+04	-1.70
6	90.05	144.43	129.71	0.24E+04	-.11E+04	-1.12
7	80.31	151.22	135.35	0.15E+04	-.51E+03	-0.83
8	83.88	151.30	147.10	0.13E+04	-.47E+03	-0.92
9	89.72	154.70	161.59	0.11E+04	-.45E+03	-0.95
10	89.52	154.24	174.30	0.57E+03	-.22E+03	-0.93
11	73.97	147.18	180.47	0.20E+03	-.33E+02	-0.87

Table 6.5: Initial model parameters of medium-dense crushed quartz sand, drained test $\sigma_3 = 137.89kPa$

GO = 31215.00 BO = 34683.32 n = .50 lambda = 137.99

	ALPHA	BETA	K	H	B	A
2	43.21	152.06	62.60	0.45E+06	-.45E+07	0.73
3	111.66	101.45	124.59	0.19E+05	-.11E+05	-4.92
4	101.23	122.79	139.62	0.16E+05	-.91E+04	-1.70
5	105.40	119.43	149.95	0.77E+04	-.25E+04	-1.29
6	122.17	133.56	191.66	0.40E+04	-.14E+04	-1.56
7	184.10	176.69	309.85	0.24E+04	-.65E+03	-1.89
8	350.91	320.69	638.26	0.11E+04	-.22E+03	-1.89
9	542.84	513.14	1016.28	0.63E+03	-.13E+03	-1.81
10	823.03	787.78	1567.99	0.45E+03	-.87E+02	-1.73
11	2144.34	2295.05	4337.96	0.26E+03	-.56E+02	-1.58

Table 6.6: Initial model parameters of dense crushed quartz sand, drained test $\sigma_3 = 137.89kPa$

GO = 40411.28 BO = 14396.55 n = .50 lambda = 214.18

	ALPHA	BETA	K	H	B	A
2	-1.28	120.57	40.36	0.14E+07	-.36E+06	2.29
3	38.06	134.90	59.76	0.36E+06	-.34E+07	-8.45
4	30.05	124.62	97.95	0.13E+06	-.16E+06	-1.50
5	116.48	66.89	152.02	0.36E+05	-.29E+05	-5.71
6	127.54	76.16	145.93	0.17E+05	-.12E+05	-3.29
7	140.85	154.59	229.09	0.49E+04	-.12E+04	-1.59
8	234.55	201.83	371.98	0.35E+04	-.11E+04	-1.74
9	495.02	377.94	837.32	0.19E+04	-.54E+03	-2.04
10	2564.41	1900.73	4603.49	0.89E+03	-.22E+03	-2.22
11	2120.17	2398.47	5168.60	0.41E+03	-.24E+03	-1.16

Table 6.7: Initial model parameters of Ottawa sand, drained test $\sigma_3 = 68.95kPa$

GO = 5208.33 BO = 4274.36 n = .50 lambda = 13.13

	ALPHA	BETA	K	H	B	A
2	1.93	11.50	3.05	0.22E+06	-.11E+07	0.87
3	4.64	10.52	7.70	0.11E+05	-.55E+04	-1.46
4	6.09	12.01	11.72	0.42E+04	-.14E+04	-1.35
5	6.96	12.97	14.85	0.23E+04	-.60E+03	-1.38
6	8.86	13.44	17.59	0.17E+04	-.57E+03	-1.27
7	9.62	14.93	20.81	0.13E+04	-.31E+03	-1.45
8	11.97	15.31	24.06	0.53E+03	-.18E+03	-1.29
9	8.53	17.80	28.20	0.45E+03	-.76E+02	-1.01

Table 6.8: Initial model parameters of Fuji river sand, drained test $\sigma_3 = 196.14kPa$

GO = 15636.01 BO = 14603.37 n = .50 lambda = 10.00

	ALPHA	BETA	K	H	B	A
2	-1.44	206.17	49.48	0.11E+07	-.52E+07	0.87
3	22.14	173.62	121.61	0.30E+05	-.18E+05	-1.91
4	18.33	173.00	156.39	0.12E+05	-.58E+04	-1.50
5	22.10	171.38	191.88	0.72E+04	-.29E+04	-1.46
6	28.92	174.51	216.76	0.40E+04	-.16E+04	-1.28
7	21.84	175.45	226.36	0.14E+04	-.60E+03	-1.06
8	14.92	172.79	243.02	0.13E+04	-.52E+03	-1.04
9	9.92	170.96	256.70	0.96E+03	-.43E+03	-1.02
10	9.85	173.56	266.14	0.60E+03	-.27E+03	-1.04

Table 6.9: Initial model parameters of loose crushed quartz sand, undrained test $\sigma_3 = 137.89 kPa$

GO = 6090.79 BO = 16242.09 n = .50 lambda = 0.00

	ALPHA	BETA	K	H	B	A
2	26.06	148.13	49.27	0.48E+06	-.14E+07	-3.74
3	55.80	131.02	93.75	0.13E+05	-.11E+05	-1.02
4	53.17	124.67	117.37	0.32E+04	-.50E+04	-0.89
5	58.53	119.50	137.68	0.85E+03	-.84E+03	-0.85
6	66.65	118.94	167.86	0.84E+03	-.63E+03	-1.10
7	72.85	121.41	189.66	0.70E+03	-.24E+03	-1.25
8	83.33	131.59	214.46	0.70E+03	-.24E+03	-1.38
9	91.08	133.40	230.77	0.37E+03	-.15E+03	-1.41
10	94.64	135.28	244.72	0.28E+03	-.50E+02	-1.50

Table 6.10: Initial model parameters of medium-dense crushed quartz sand, undrained test $\sigma_3 = 137.89 kPa$

GO = 16025.64 BO = 42735.04 n = .50 lambda = 0.00

	ALPHA	BETA	K	H	B	A
2	65.59	128.98	130.27	0.20E+07	-.20E+07	-1.70
3	110.90	143.78	229.57	0.33E+05	-.19E+05	-1.88
4	88.79	141.57	293.27	0.80E+04	-.43E+04	-1.55
5	99.48	163.41	353.80	0.58E+04	-.35E+02	-1.40
6	83.71	225.19	410.48	0.35E+04	0.19E+05	-1.03
7	145.30	251.20	487.79	0.20E+04	0.80E+04	-1.19
8	178.75	272.34	533.26	0.13E+04	0.42E+04	-1.21
9	194.76	320.08	573.74	0.65E+03	0.42E+04	-1.05
10	222.10	347.13	631.02	0.44E+03	0.84E+03	-1.11

Table 6.11: Predicted initial model parameters of loose crushed quartz sand, drained test $\sigma_3 = 275.78kPa$

G0 = 19968.20 B0 = 77875.94 n = .50 lambda = 84.19

	ALPHA	BETA	K	H	B	A
2	41.93	300.99	54.72	0.76E+06	-.15E+06	0.20
3	116.10	242.35	140.16	0.14E+06	-.12E+06	-4.87
4	131.56	237.05	159.17	0.22E+05	-.13E+05	-2.81
5	133.74	222.17	171.76	0.97E+04	-.35E+04	-1.70
6	121.65	195.11	175.23	0.36E+04	-.17E+04	-1.12
7	108.58	204.46	183.01	0.22E+04	-.76E+03	-0.83
8	110.12	198.64	193.12	0.19E+04	-.71E+03	-0.92
9	116.31	200.55	209.47	0.17E+04	-.68E+03	-0.95
10	113.63	195.79	221.25	0.88E+03	-.34E+03	-0.93
11	88.75	196.48	240.95	0.32E+03	-.52E+02	-0.87

Chapter 7

IMPLEMENTATION OF THE MODEL

7.1 Introduction

The implementation of Prevost's models in computer codes is described in this chapter. A successful computer implementation is necessary to provide proper results for the model to be evaluated accurately. The pressure sensitive and pressure nonsensitive models were coded in two computer programs named PREDICTIONS and SIMULATIONS respectively, Derradji-Aouat and Evgin (1988a, 1988b). The implementation of the models involves integration of the elastic-plastic rate equations using a suitable numerical method. The proposed solution technique, the implementation of the constitutive relations and the flowcharts are presented in this chapter. The input and output samples are given in Appendices F and G respectively.

7.2 Computer Program PREDICTIONS.

The pressure sensitive model was coded in a three dimensional stress driven computer program, where increments of stress were provided as input and the corresponding increments of strains were computed as output.

According to the pressure sensitive model, the stress space is divided by a set of cylindrical yield surfaces. These yield surfaces are not stationary but change sizes and locations during a stress increment. When the stress point goes from a yield surface, f_m, to another one, f_{m+1}, as shown in Fig 7.1, the active yield surface [1] changes size and location depending on the volumetric strain, Eq 4.54. The stress point cannot pass beyond the surface f_{m+1} and goes to the surface $f_{m+i}, (i > 1)$. Otherwise, the plastic parameters of the surfaces f_{m+1} to f_{m+i-1} will not be used in the calculations of the plastic strains, the original piecewise representation of the stress strain curves will be destroyed, and the overlapping of the yield surfaces will occur, Fig 7.2. As a definition, the converged stress increment is the stress increment which captures the active yield surface at its new position. The active yield surface either contracts to state B or expands to state BB, Fig 7.3, depending on the volumetric strains developed in the soil element. In this case, an iterative approach is necessary whereby the strain driven algorithm is performed repeatedly until the convergence to some prescribed tolerance is achieved, i.e 2%. The first iteration is a conservative guess of the plastic volumetric strain increment, i.e $e^{\Delta\epsilon_v^p} = .001$, Derradji-Aouat and Evgin (1988a). The numerical problem, regarding the control of the magnitude of the stress increments, was overcome by introducing an over/under shoot solution technique. For a given stress increment, the stress point may go beyond the yield surface f_{m+1} (overshot), remain inside f_{m+1} (undershot) or capture it at its new position. The stress increments were controlled by solving the update active yield functions for the converged stress increment. Using this solution procedure, a high degree of accuracy was achieved. Figure 7.4 shows a back prediction type of a test carried out on crushed quartz sand of a loose soil sample under 137.89 kPa of initial hydrostatic pressure.

The stress increment may remain on the yield surface f_m, but this situation occurs only in the neutral loading case. The unloading is defined when the component of the stress increment vector, normal to the current yield surface, is directed towards the inside. This can be expressed as follows:

$$Q\dot{\sigma} = \frac{\partial f}{\partial \sigma}\dot{\sigma} = Q'\dot{S} + 3Q''\dot{P} < 0 \tag{7.1}$$

[1] The first yield surface outside the yield surface currently pushed by the stress point is called the active yield surface.

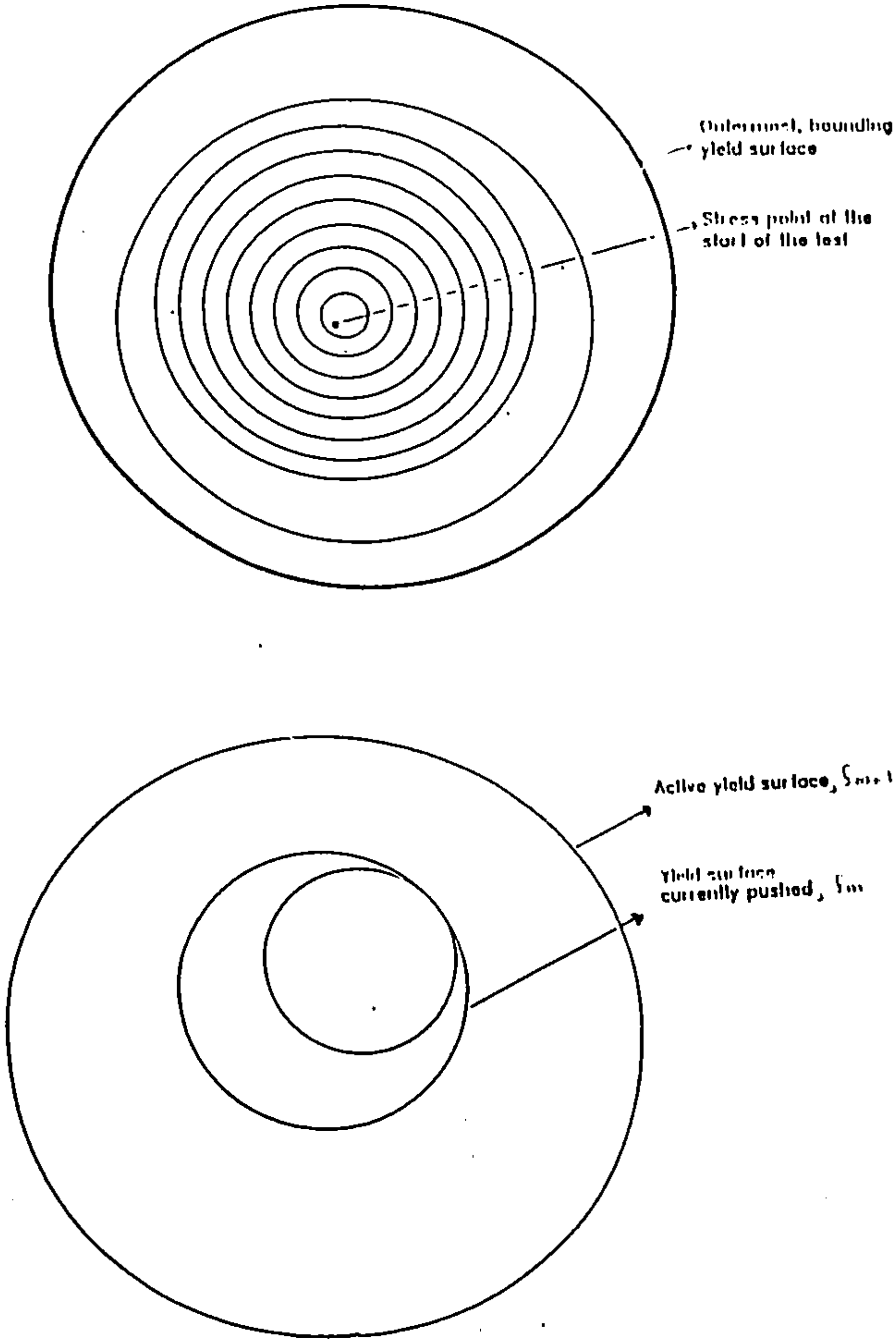

Figure 7.1: Geometric configurations of the yield surfaces

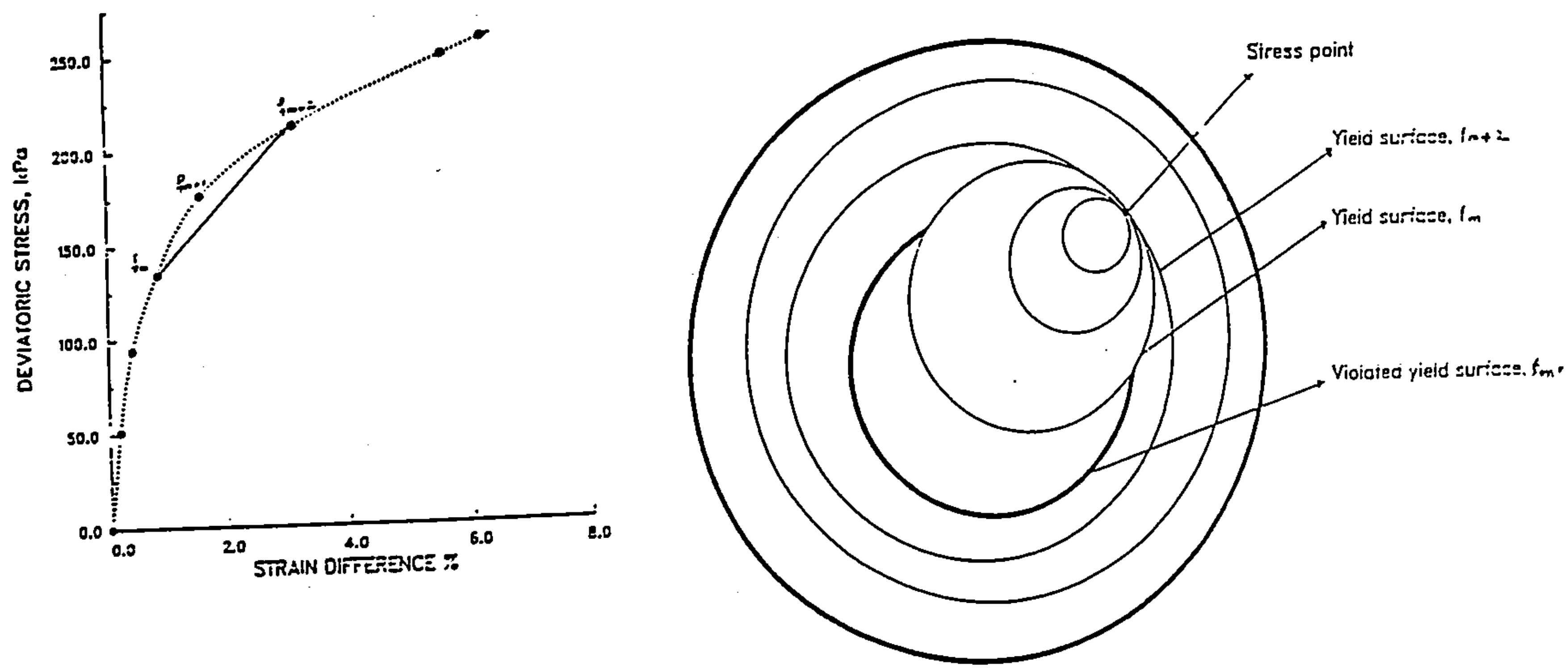

Figure 7.2: Overlapping of the yield surfaces

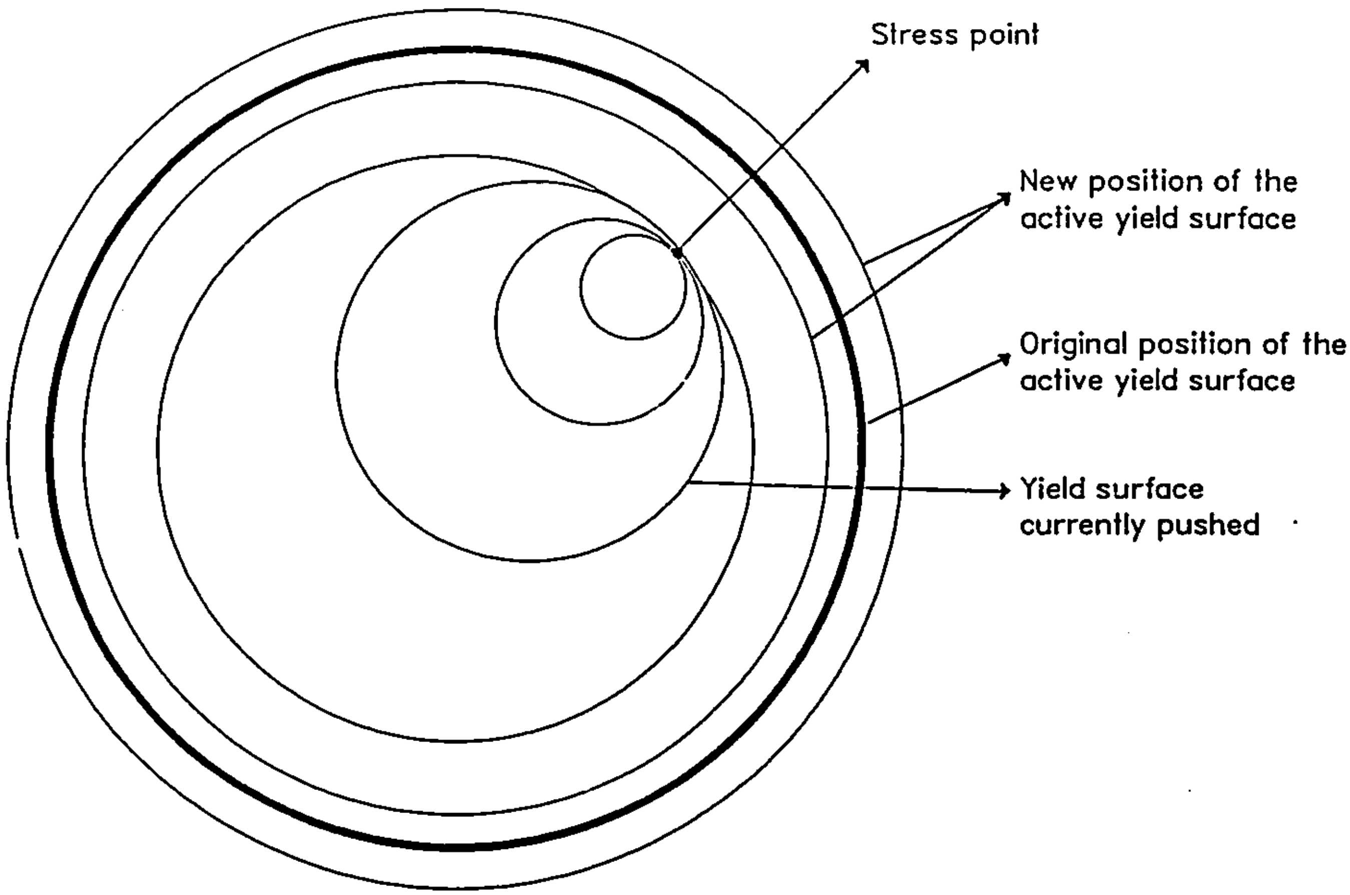

Figure 7.3: Isotropic motion of the active yield surface

At the same time, the vector $Q\dot{\sigma}$ is directed towards the exterior of the first yield surface of a degenerated size which is located at the stress point [2]. Thus, the process of unloading will be regarded as loading in the inverse direction starting from the point of stress reversal. For unloading, a new axes system(X, Y) is used, as shown in Fig 7.5. The initial sizes, positions of the yield surfaces and their associated plastic parameters are those that correspond to the start of the loading from A. The same procedure is valid for the reloading curves using the axes system (XX, YY). Thus, there are three axis systems: one fixed axes system and two moving axis systems related to the monotonic loading, unloading and reloading cases. Figure 7.6 shows the model simulation of the test presented in Fig 7.4 but involving a cycle of loading-unloading-reloading.

For a given converged stress increment, the corresponding strain increments are calculated according to Eq A.1 and Eq A.2. The stress point moves from a yield surface f_m to the active yield surface. The sizes of the inner yield surfaces $f_1 - f_m$ change according to the developed plastic deviatoric strains, Eq 4.37. However, the external yield surfaces $f_{m+1} - f_p$ expand or contract and change their locations depending on the volumetric strain increment, Eq 4.54. Their related plastic parameters vary according to Eq 4.53. The translation of the inner yield surfaces towards the conjugate point is achieved according to Eq 4.33 and Eq 4.36. The direction of translation of the inner yield surfaces is computed by defining the direction of the vector relating the stress point on the current yield surface to its conjugate point on the active yield surface.

For the cyclic loading events, the update sizes and the positions of the yield surfaces must be remembered. This requires a considerable amount of computer storage. The double iteration procedure, for both the converged stress increment and the strain driven algorithm, increases the computer CPU time. An output of the program results related to the test shown in Fig 7.4 is presented in Appendix F where the converged stress increments, update geometric configuration of the yield surfaces and the predicted strain increments are shown.

[2]The first yield surface has a zero size. Always, it is located at the stress point and represents the current stress state.

7.3 Computer Program SIMULATIONS.

Prevost's pressure non-sensitive model was coded in a three dimensional stress driven computer program where increments of total stress were provided as input and the increments of strains corresponding to the converged effective stresses were computed as output, Derradji-Aouat and Evgin (1988b).
Undrained shearing imposes the condition $\epsilon_v = 0$ and Eq A.1 reduces to the form:

$$\dot{P}' = -3P''\frac{B}{H}\frac{Q\dot{\sigma}}{|Q|^2} \tag{7.2}$$

For a given stress increment, the dummy yield surfaces do not change sizes and locations. When the stress point reaches the active yield surface, the value of the effective hydrostatic pressure increment can be defined from the active yield function, Eq 4.39.

$$\dot{P}'(N) = \left(\frac{1}{C^2}(K^2 - \frac{3}{2}(S_{ij}^m - \alpha_{ij}^m)^2)\right)^{\frac{1}{2}} + \beta^m - P'(N-1) \tag{7.3}$$

where the superscript (m) corresponds to the active yield surface f_m. N is the stress increment number.
The converged stress increment is defined as the effective stress increment which satisfy both Eq 7.2 and 7.3. In this case, an iterative approach is necessary whereby the total stress driven algorithm must be performed repeatedly until the convergence is achieved, Derradji-Aouat and Evgin (1988b). In this thesis, the accuracy of 98% was achieved.
The overshoot-undershoot solution technique was introduced depending on whether the stress point goes beyond the active yield surface or remains inside, as explained in Section 7.2. Using this procedure high degree of accuracy can be achieved. Figure 7.7 shows a back prediction of undrained CTC test carried out on loose soil sample of crushed quartz sand. The results shown in Table 6.9 were used as input data.
The computer program SIMULATIONS was restricted to monotonic increasing loading conditions. Under cyclic loading conditions, the pressure non-sensitive model is reduced to a total stress model where the change of the plastic parameters of the inner yield surfaces requires data from static and cyclic simple shear tests, as explained in Chapter 4. Thus, the hardening rule is not needed to be implemented in the program. This reduces the computer storage and CPU time. The examples of input data and output results are presented in Appendix G.

7.4 Program Flowchart

The flowcharts for the computer programs PREDICTIONS and SIMULATIONS will be presented in the following. The control parameters used in the master cards and the variables or constants used in the initialization blocks are defined in the programs manuals, Derradji-Aouat and Evgin (1988a, 1988b).

Flow Chart of the Program SIMULATIONS

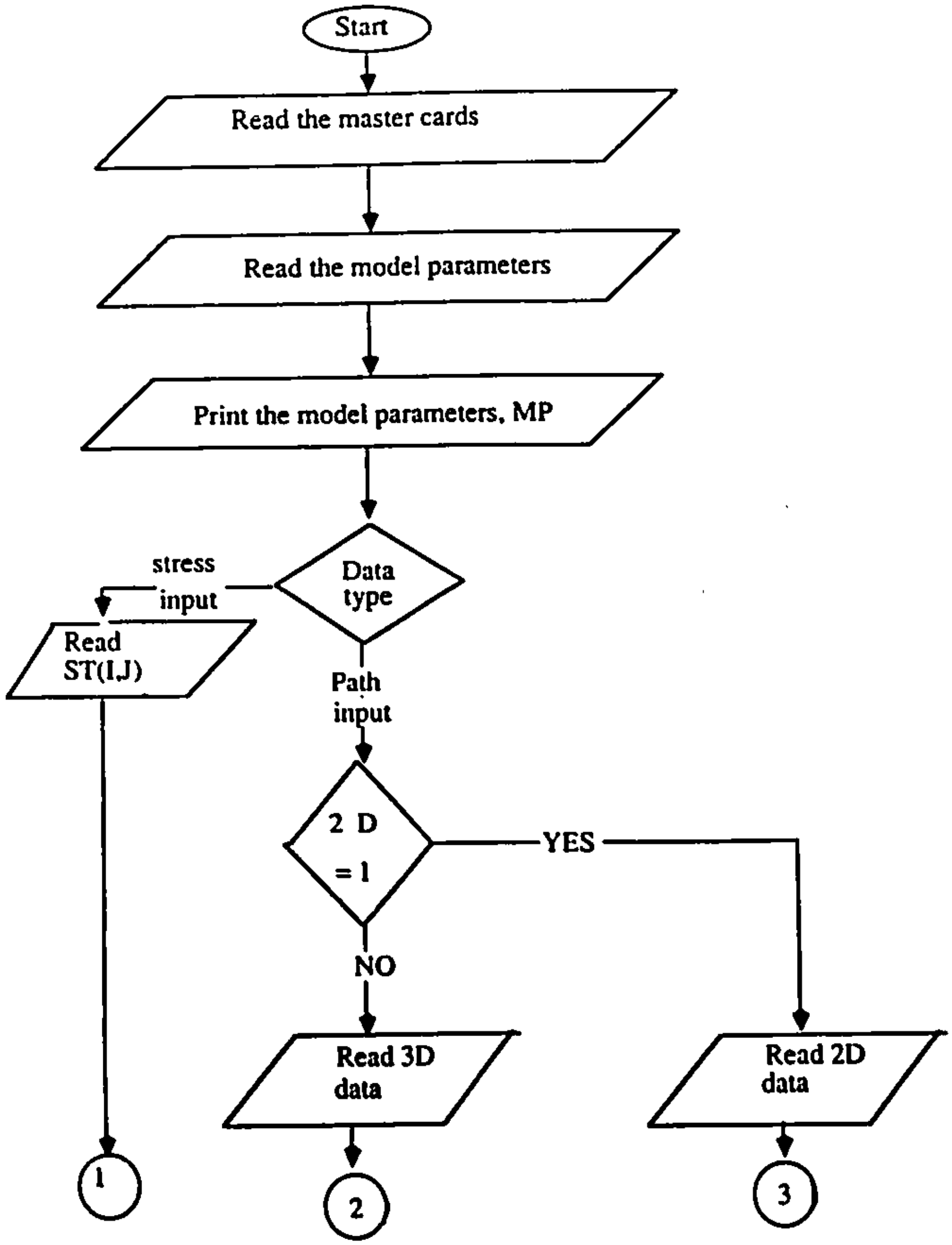

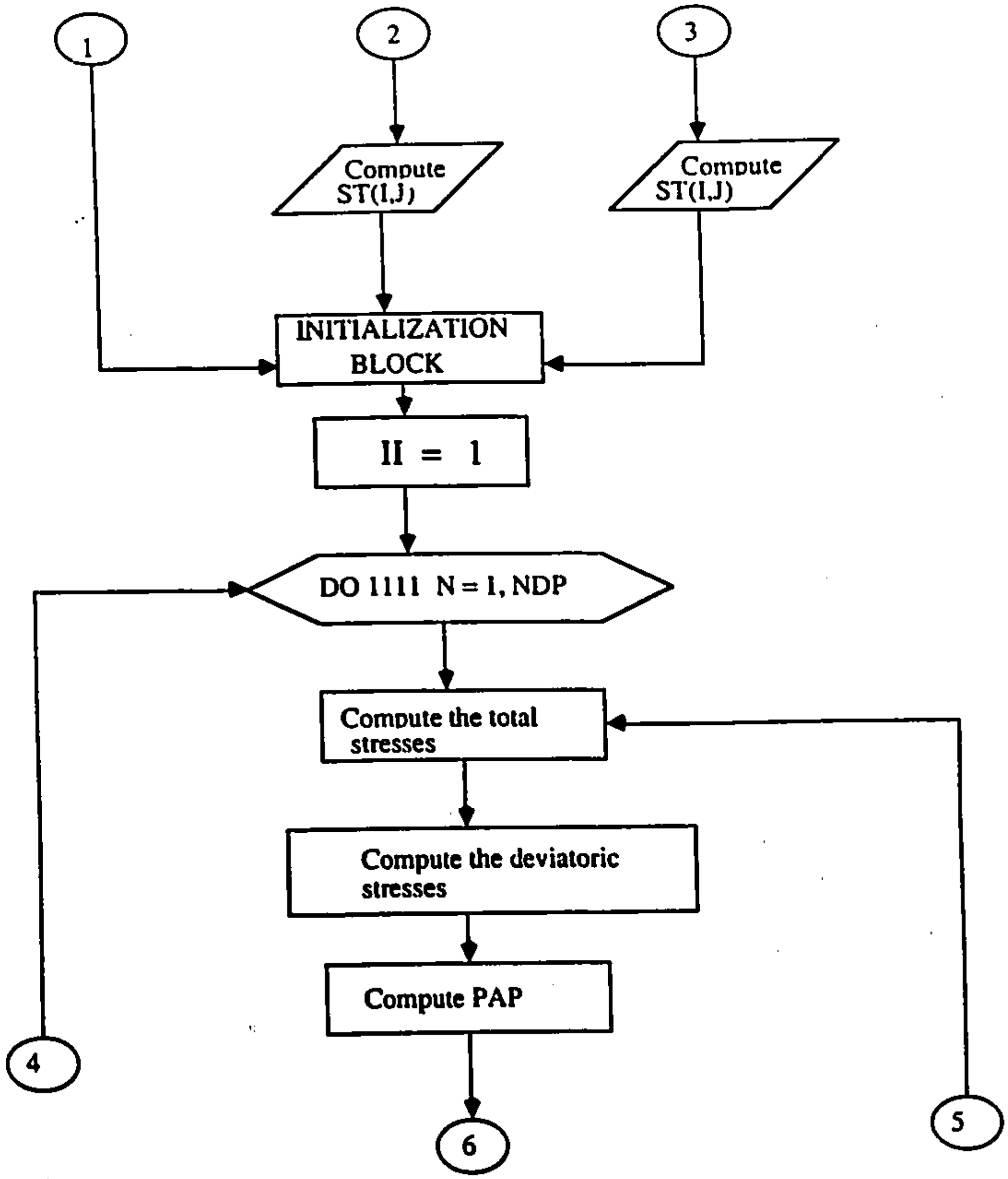
1
2
3
Compute ST(I,J)
Compute ST(I,J)
INITIALIZATION BLOCK
II = 1
DO 1111 N = 1, NDP
Compute the total stresses
Compute the deviatoric stresses
Compute PAP
4
6
5

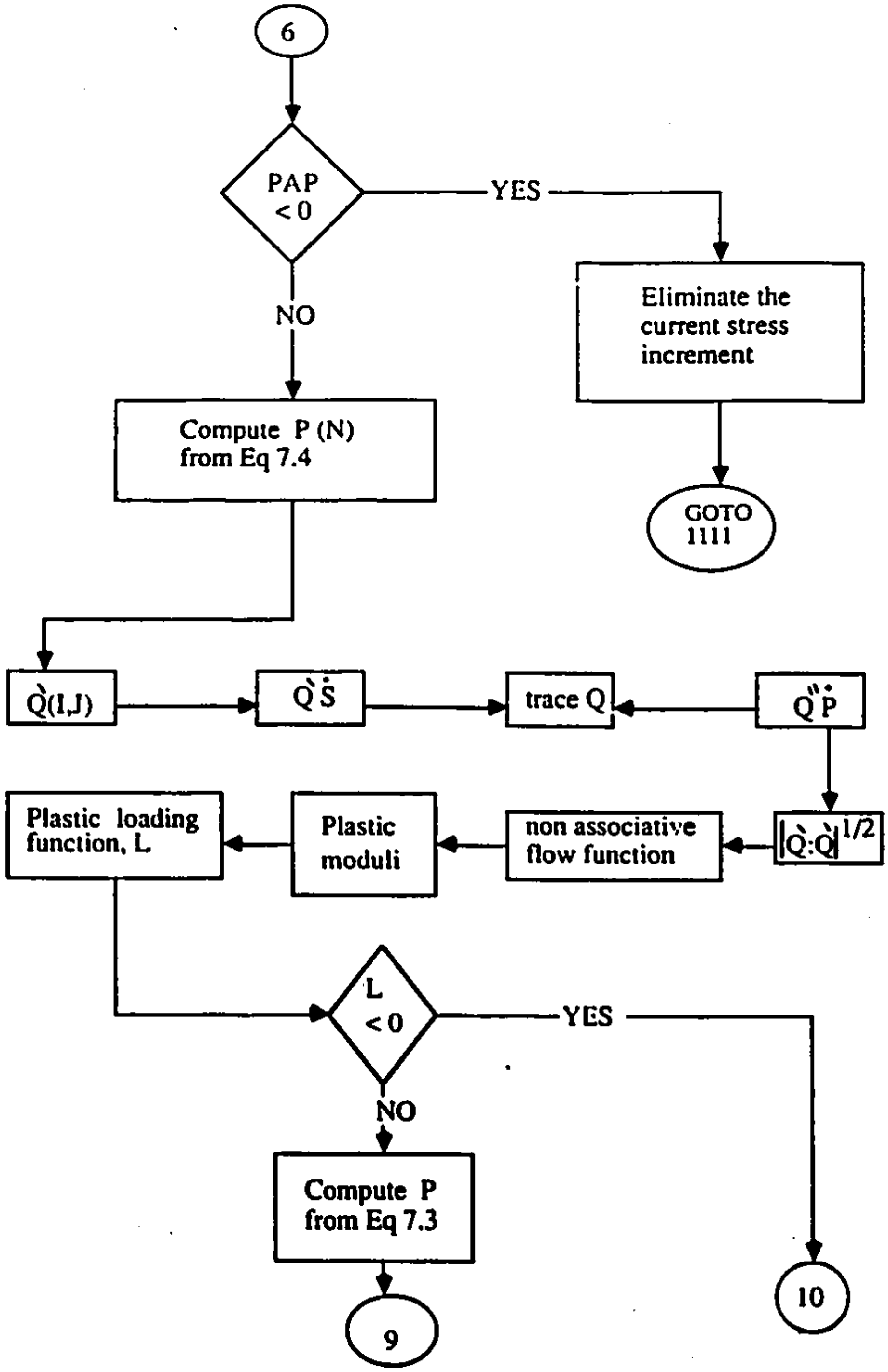
6
PAP
< 0
YES
NO
Eliminate the current stress increment
GOTO 1111
Compute P (N) from Eq 7.4
Q̀(I,J)
Q̀ Ṡ
trace Q
Q̀ Ṗ
|Q̀:Q̀|1/2
non associative flow function
Plastic moduli
Plastic loading function, L
L
< 0
YES
NO
Compute P from Eq 7.3
9
10

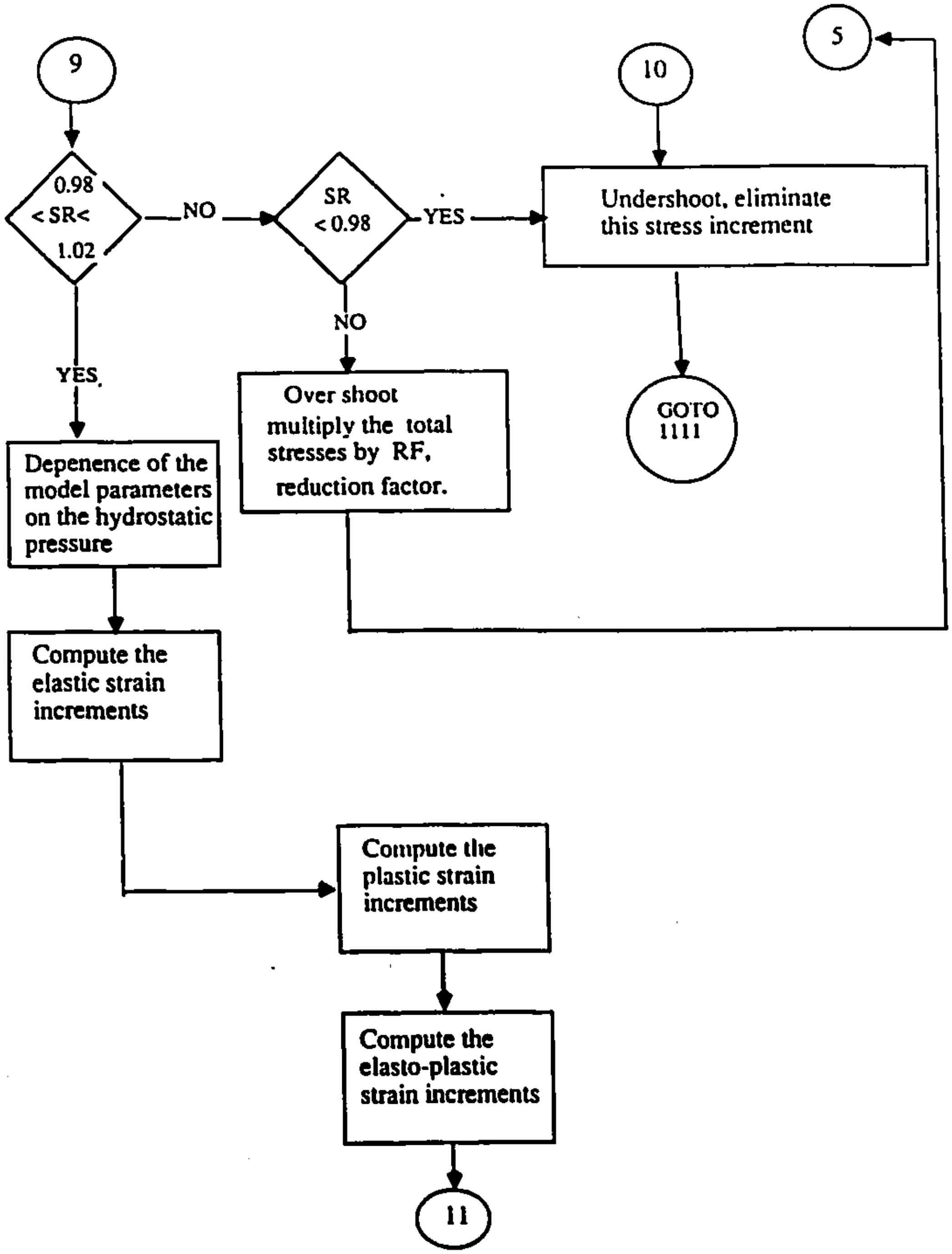
9
0.98 < SR< 1.02
NO
SR < 0.98
YES
10
5
Undershoot, eliminate this stress increment
NO
YES
Over shoot multiply the total stresses by RF, reduction factor.
GOTO 1111
Depenence of the model parameters on the hydrostatic pressure
Compute the elastic strain increments
Compute the plastic strain increments
Compute the elasto-plastic strain increments
11

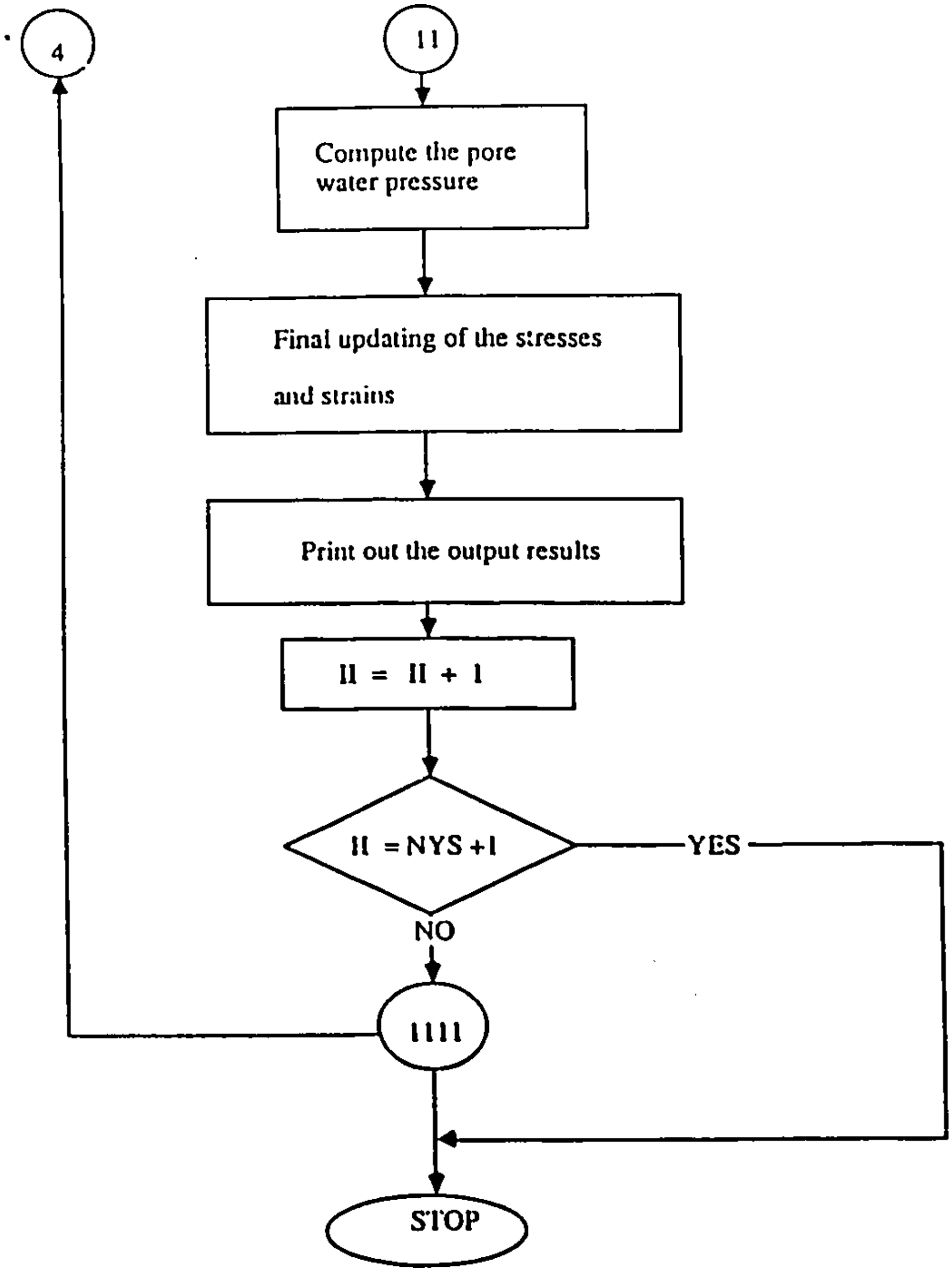
4
11
Compute the pore water pressure
Final updating of the stresses and strains
Print out the output results
II = II + 1
II = NYS + I
YES
NO
1111
STOP

Flow Chart of the Program PREDICTIONS

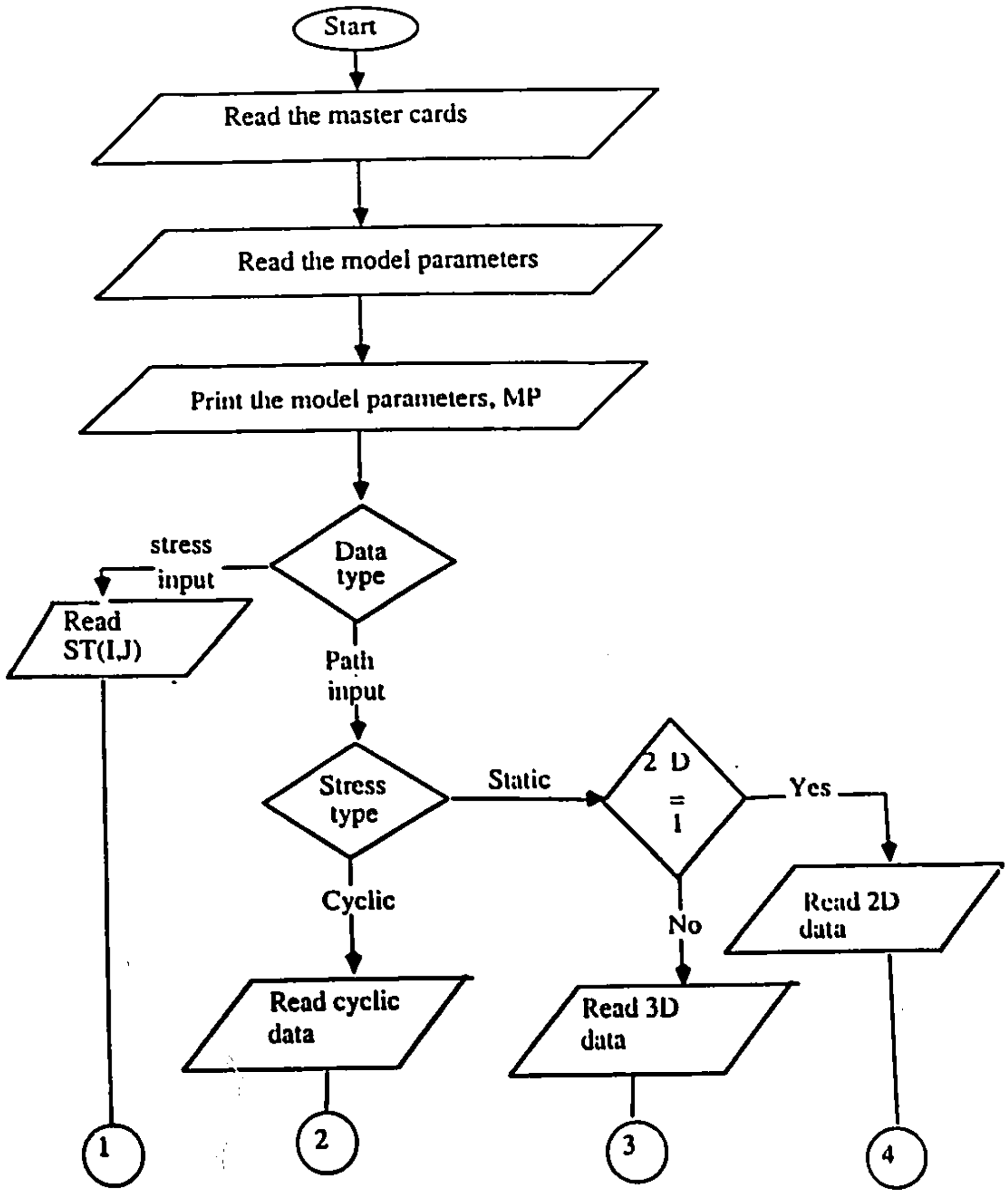

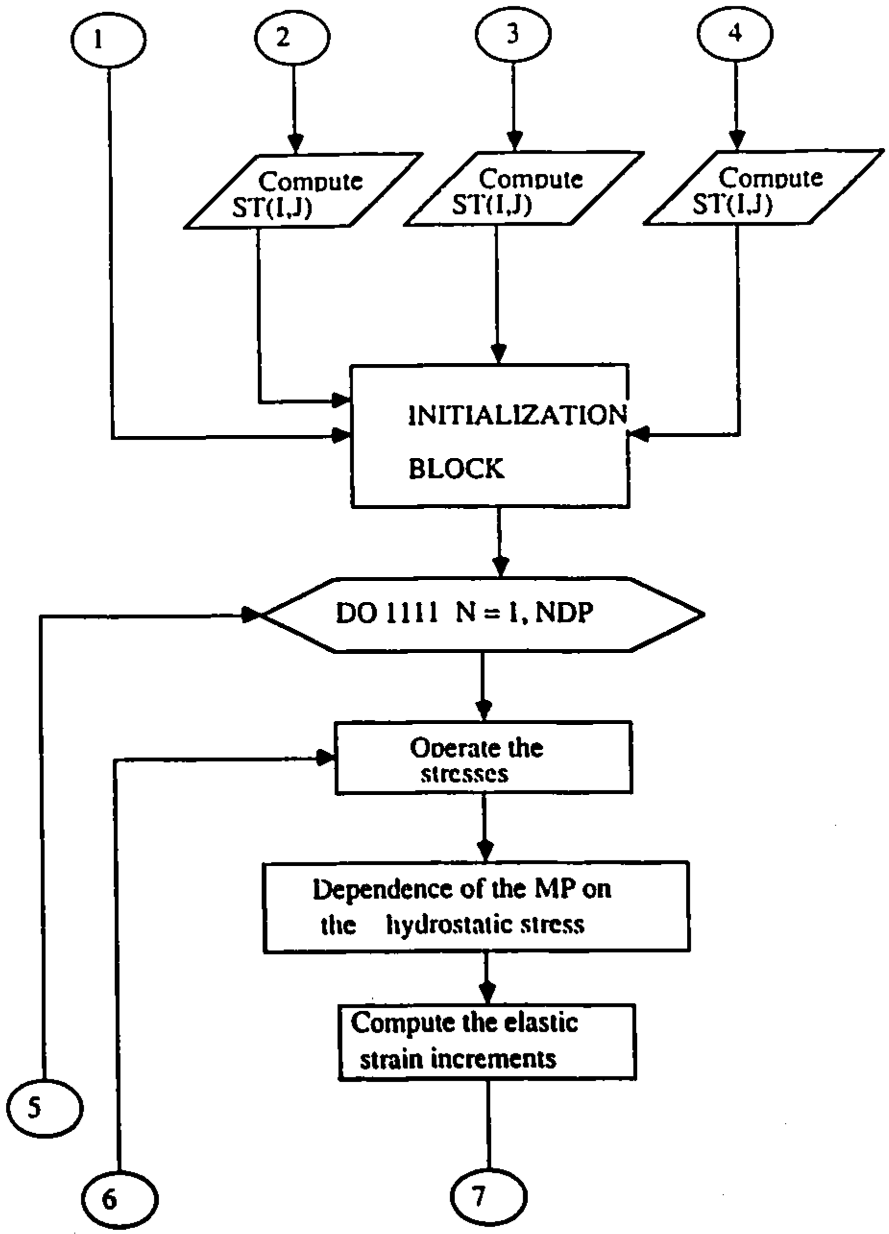
1
2
3
4
Compute ST(I,J)
Compute ST(I,J)
Compute ST(I,J)
INITIALIZATION BLOCK
DO 1111 N = 1, NDP
Operate the stresses
Dependence of the MP on the hydrostatic stress
Compute the elastic strain increments
5
6
7

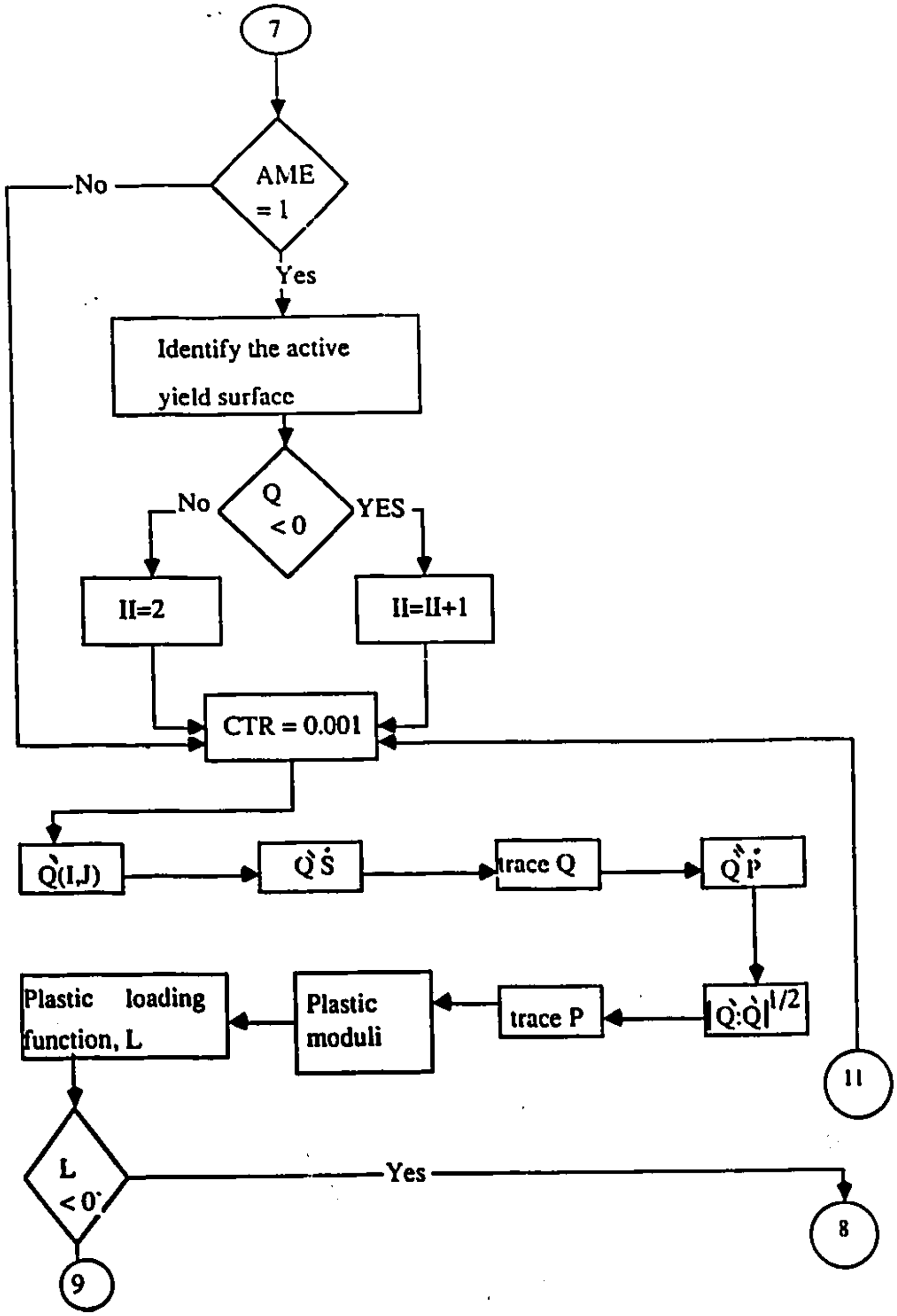
7
AME
= 1
No
Yes
Identify the active
yield surface
Q
< 0
No
YES
II=2
II=II+1
CTR = 0.001
Q(I,J)
Q S
trace Q
Q P
trace P
Plastic
moduli
Plastic loading
function, L
11
L
< 0
Yes
8
9

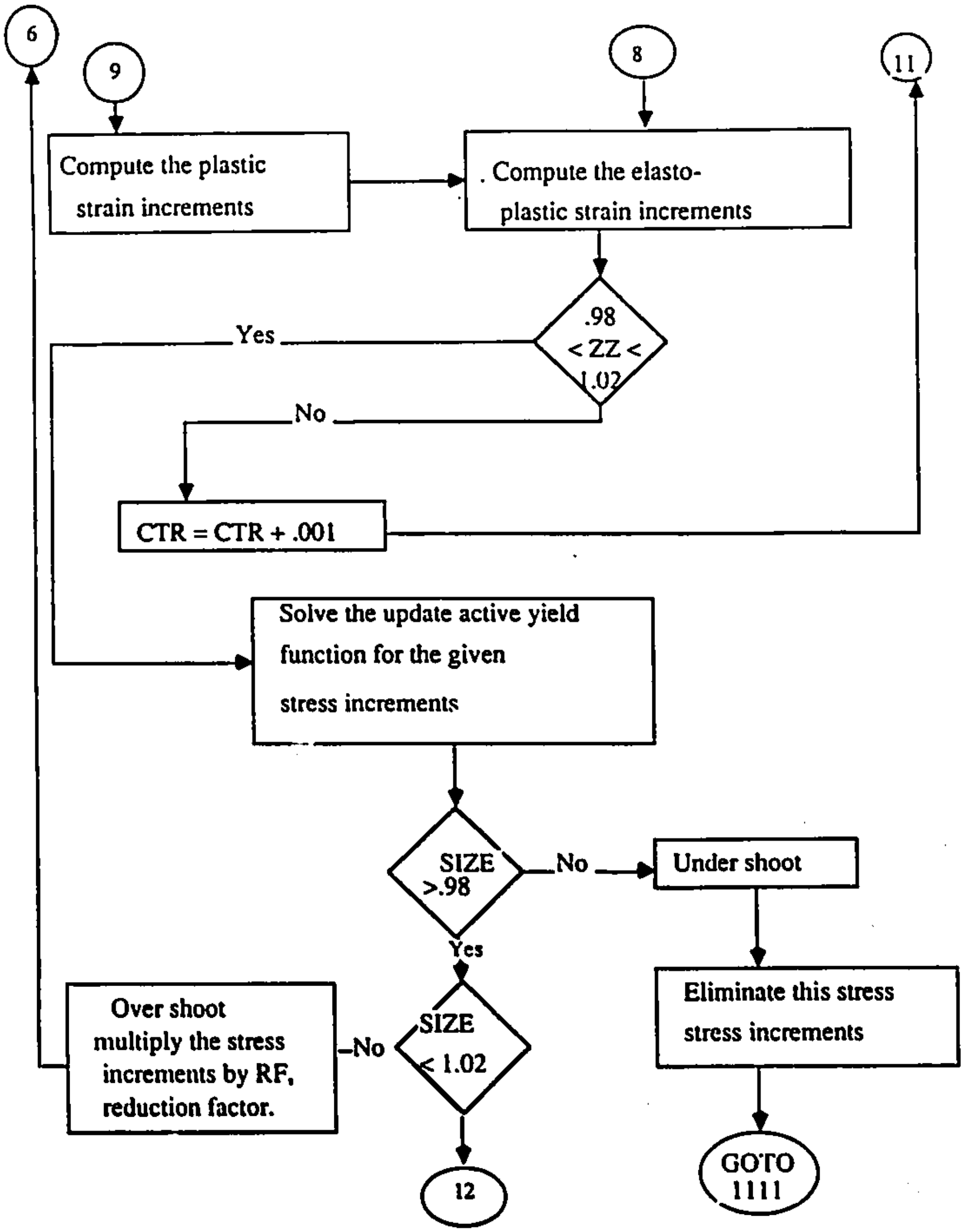
6
9
8
11
Compute the plastic strain increments
. Compute the elasto-plastic strain increments
.98 < ZZ < 1.02
Yes
No
CTR = CTR + .001
Solve the update active yield function for the given stress increments
SIZE >.98
No
Under shoot
Yes
Eliminate this stress stress increments
Over shoot multiply the stress increments by RF, reduction factor.
No
SIZE < 1.02
12
GOTO 1111

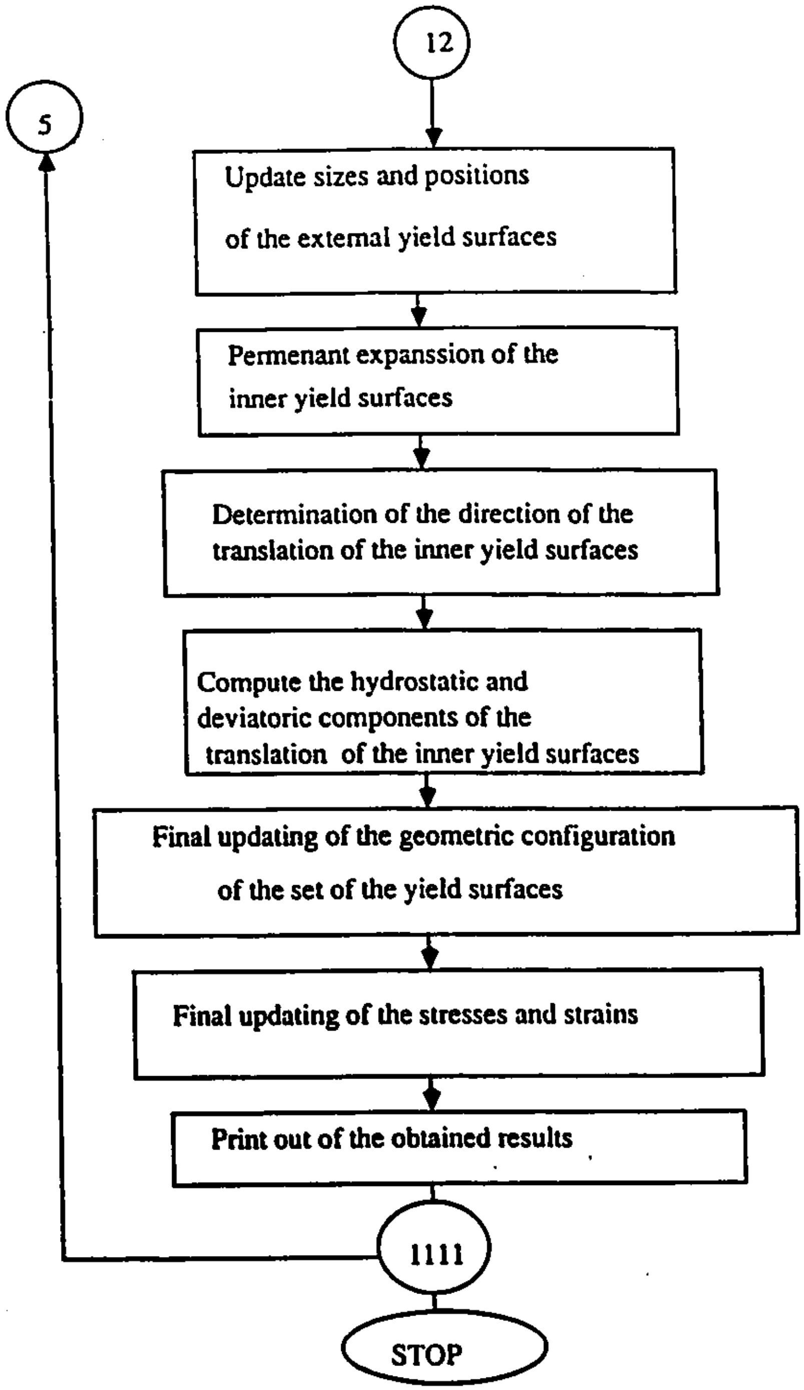

12
5
Update sizes and positions
of the extemal yield surfaces
Permenant expanssion of the
inner yield surfaces
Determination of the direction of the
translation of the inner yield surfaces
Compute the hydrostatic and
deviatoric components of the
translation of the inner yield surfaces
Final updating of the geometric configuration
of the set of the yield surfaces
Final updating of the stresses and strains
Print out of the obtained results
1111
STOP

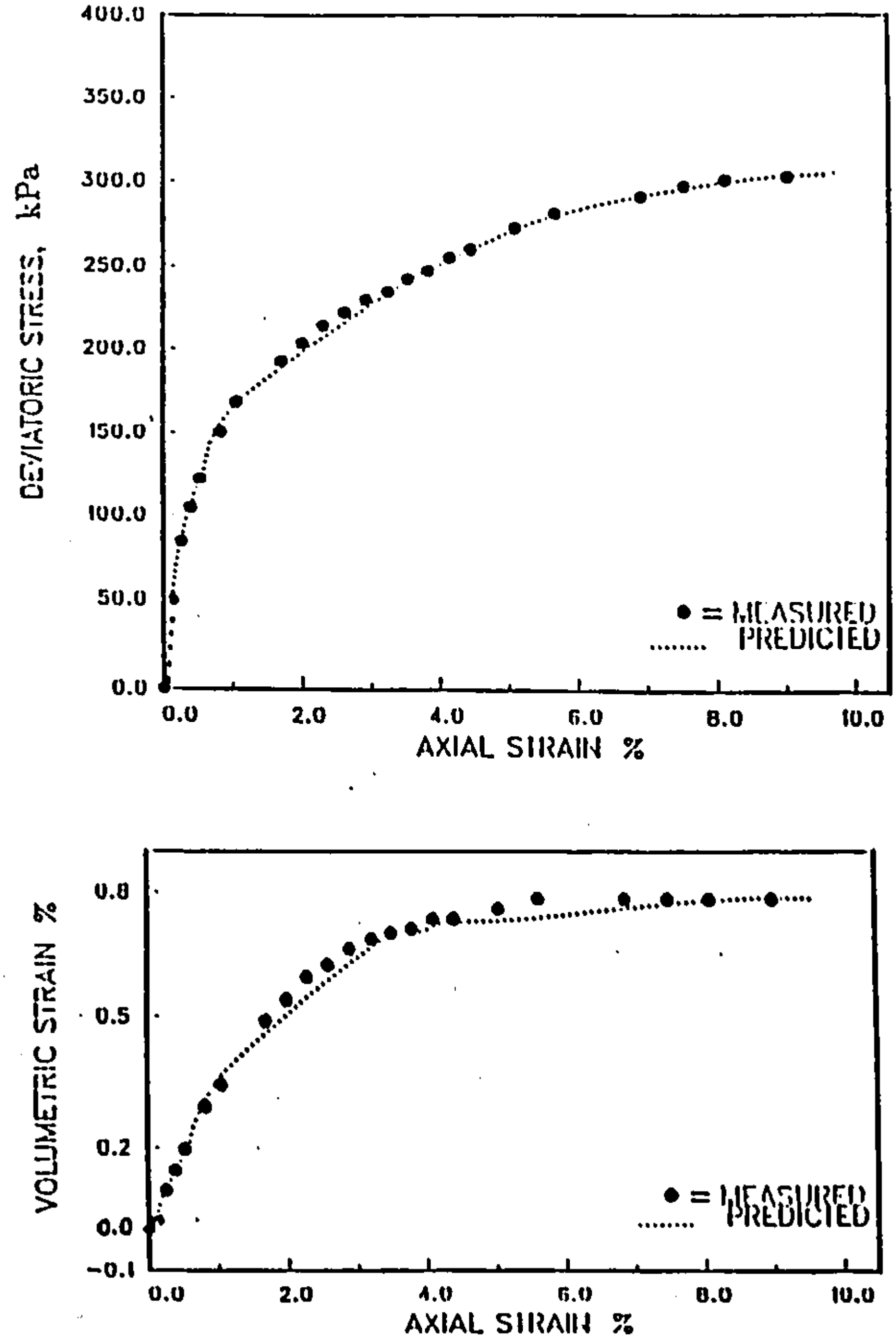

Figure 7.4: Back prediction of drained CTC test, loose sample $\sigma_3 = 137.89$ kPa

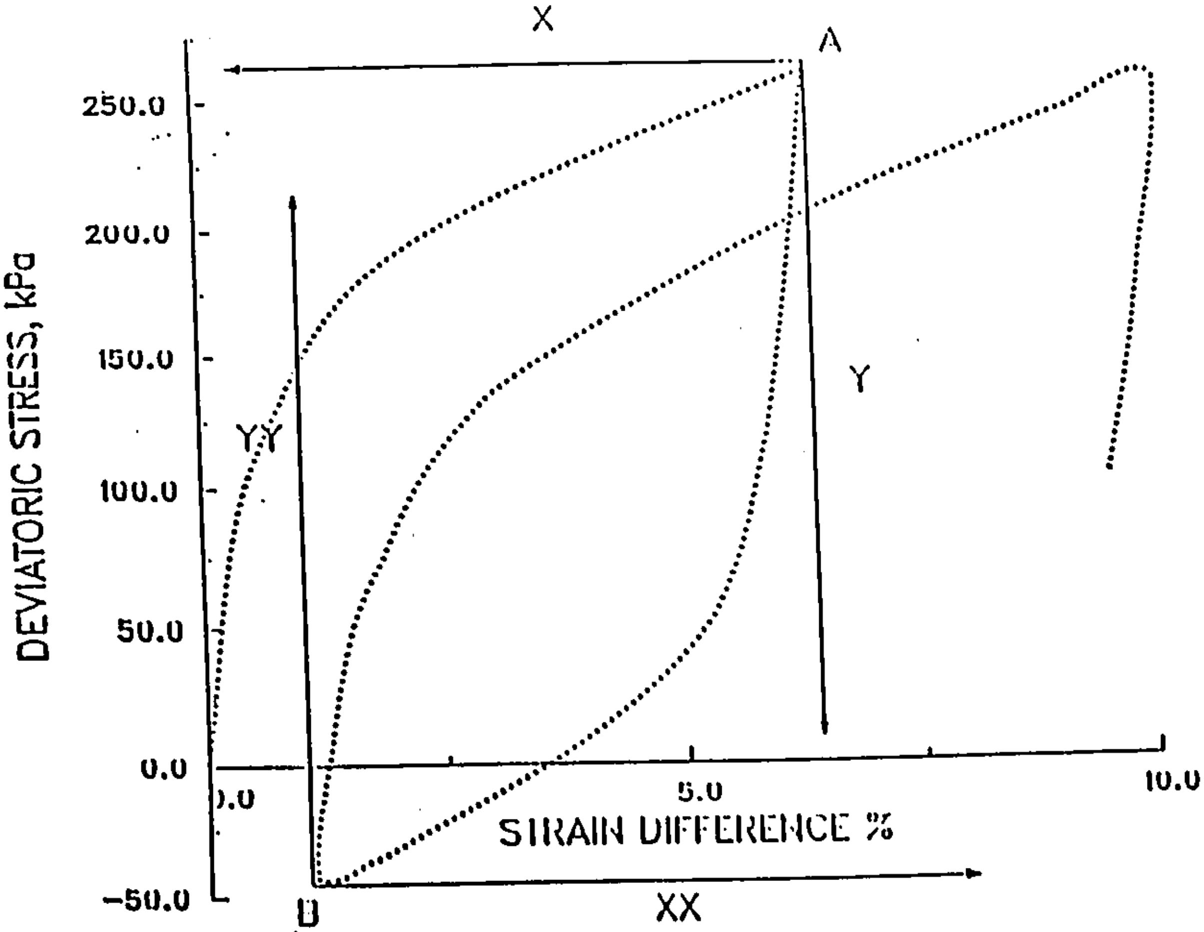

Figure 7.5: Axes systems used in the program PREDICTIONS

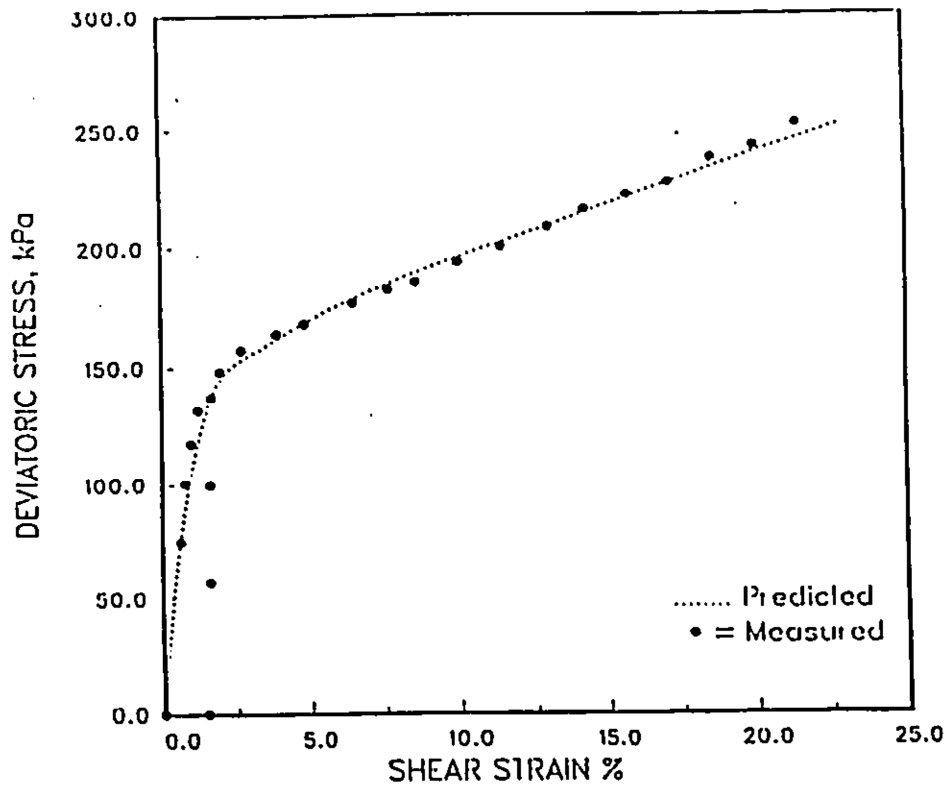

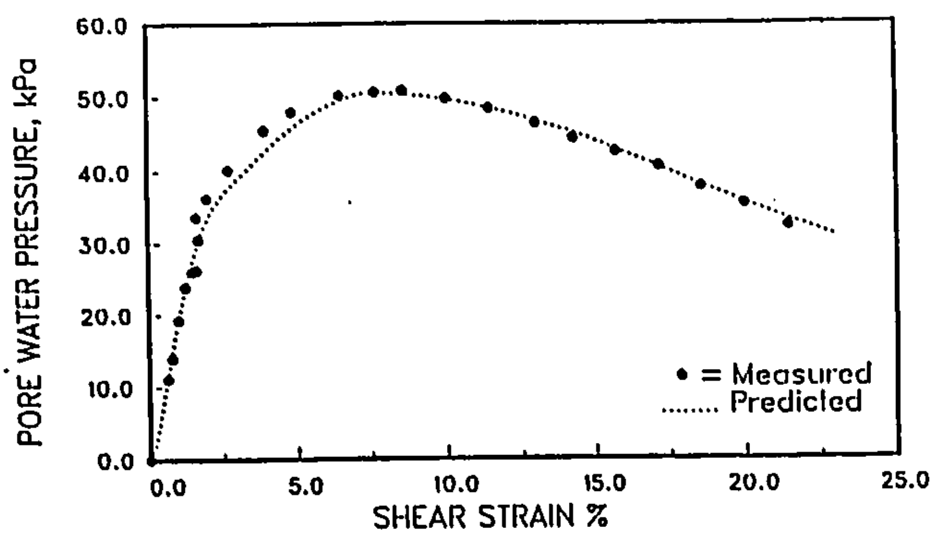

Figure 7.7: Back prediction of undrained CTC test, loose sample $(\sigma_3)_{initial} = 137.89kPa$

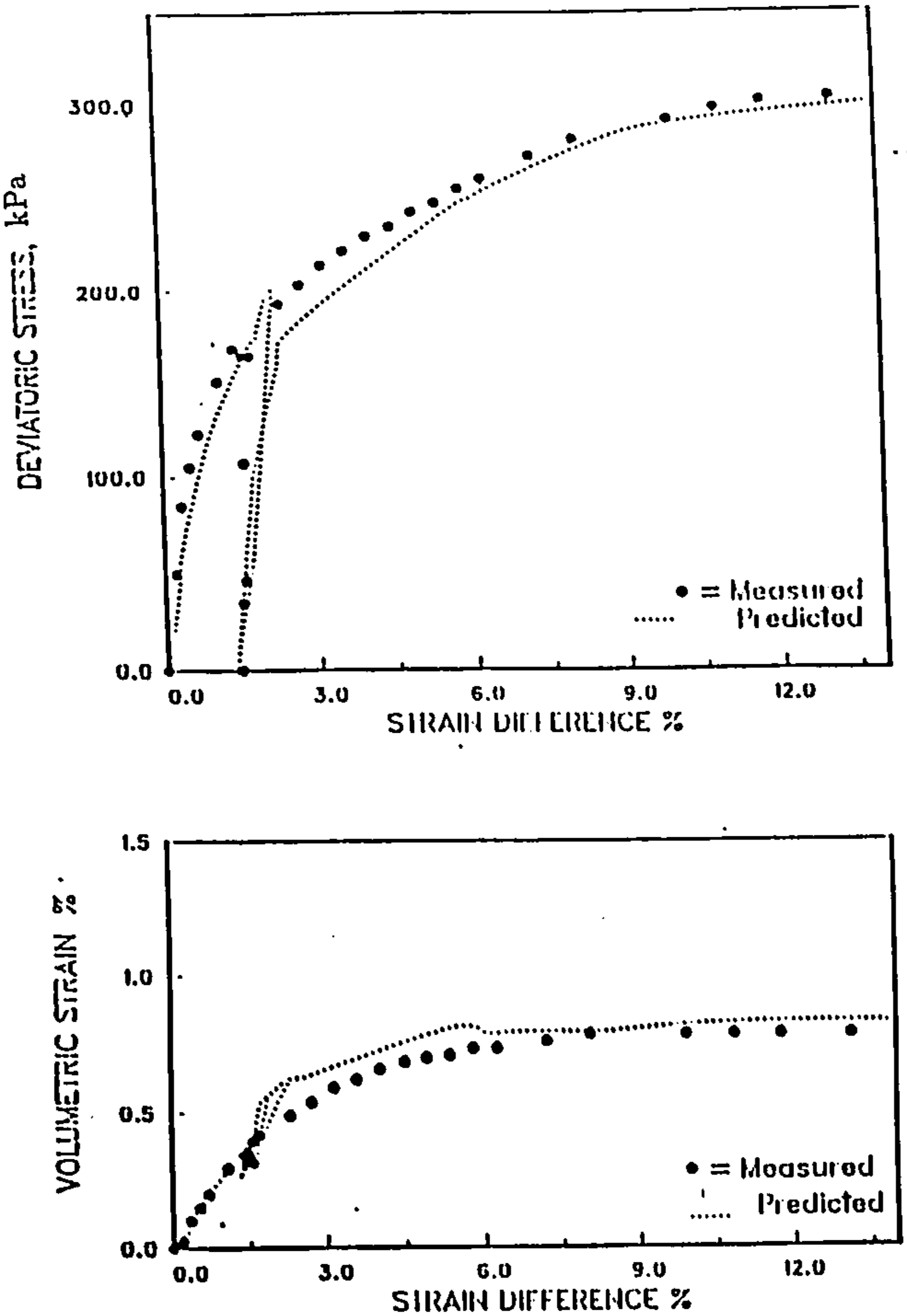

Figure 7.6: Prediction of the test showed in Fig 7.4 involving a cycle of loading unloading reloading

Chapter 8

MODEL SIMULATIONS AND DISCUSSIONS

8.1 Introduction

The purpose of this chapter is to present the model simulations of the laboratory tests. The model predictions were compared to the actual test data to assess the performance of the model. The versatility and accuracy of the model was highlighted with respect to the observed soil behaviour. The stress paths shown in Fig 8.1 were used to generate the data base for model evaluation. Since the laboratory testing program, Chapter 5, was restricted only to the conventional testing in the triaxial plane, the experimental data of Montreal Workshop(1980) was used to generate the model appraisal for complicated stress paths in the three dimensional stress space. Moreover, Tatsuoka and Ishihara's (1974) cyclic tests were used to investigate the response of the model in simulating the observed cyclic behaviour of the soil.

This chapter also includes a general discussions and conclusions to point out the capabilities and the shortcomings of both pressure sensitive and pressure non-sensitive models. A new formulation of the non-associative flow rule function is proposed here to improve the model simulations.

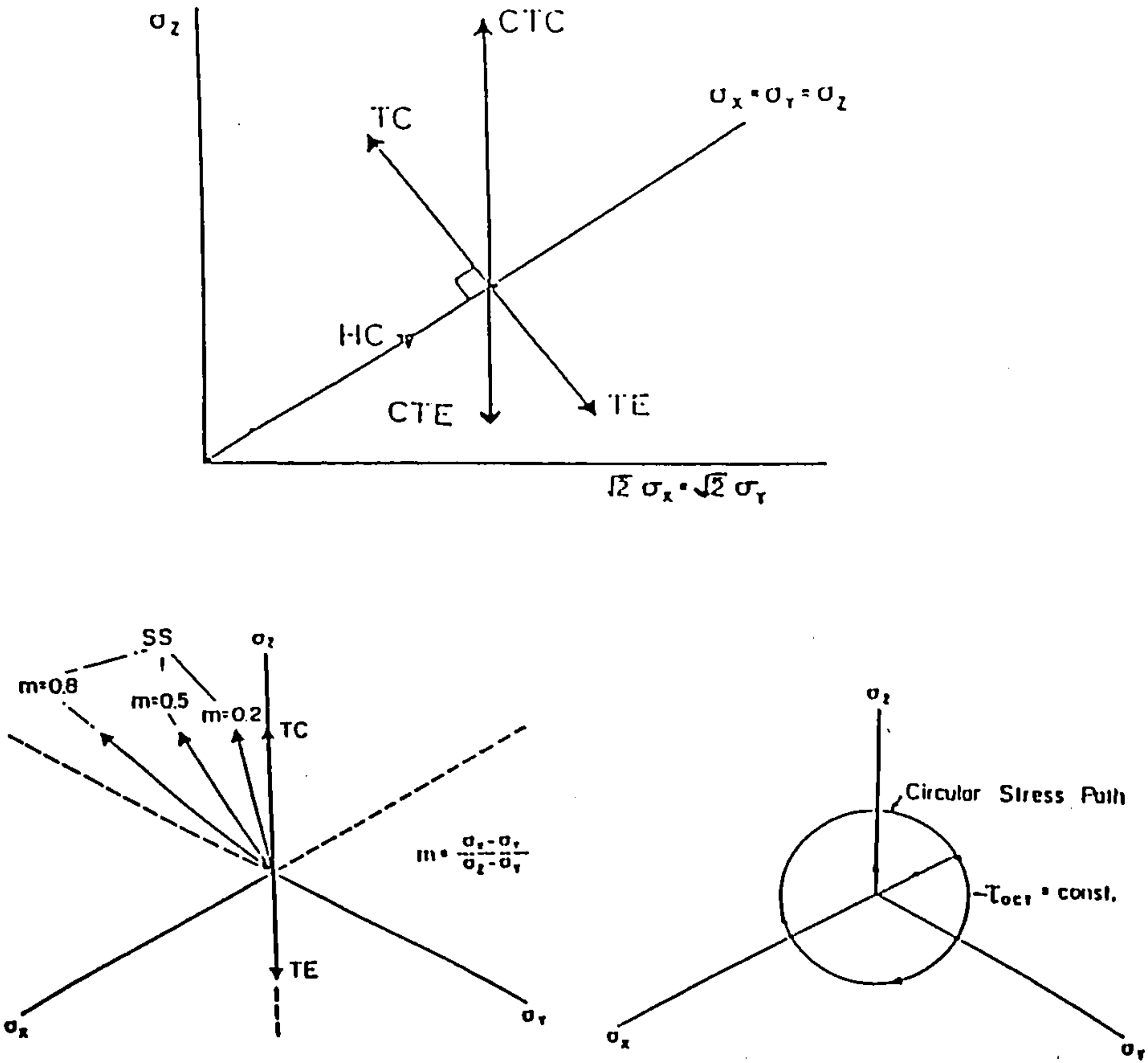

Figure 8.1: Stress paths used for predictions

8.2 Crushed Quartz Sand

The model simulations of the behaviour of crushed quartz sand in various tests are presented next. Note that the tests are numbered according to Table 5.2.

8.2.1 Drained CTC Tests, Loose Samples

Test # 4, $\sigma_3 = 68.95kPa$, Fig D.4
The model underestimated the shear stiffness and strength of the soil. The model predicted increasing compressive volumetric strains whereas the soil tended to dilate. It was believed that such simulation of the volumetric strains is highly influenced by the type of the non-associative flow rule adopted in the model formulation, as it will be explained later. The model overestimated the observed shear strain. This is apparent from the observation of the unloading-reloading cycle. Both predicted and observed curves had unloading from the same deviatoric stress level at which the observed shear strain was less than the predicted value.

Test # 5, $\sigma_3 = 137.89kPa$, Fig D.5
The model predictions of this test were in excellent agreement with the experimental data. However, it should be noted that this test was used for the determination of the initial model parameters. Thus, Fig D.5 shows back prediction of the test and does not represent the performance of the model.

Test # 6, $\sigma_3 = 275.78kPa$, Fig D.6
The predicted shear stress strain curve was in excellent agreement with the observed soil behaviour. However, the model shows less compaction than the observed values. The reason for this is the type of non-associative flow rule adopted.

Test # 7, $\sigma_3 =$ 413.66 kPa, Fig D.7
The predicted shear stress-strain curve agreed well with the experimental values. However, the model underestimated the volumetric strains.

A shortcoming of the model is apparent in its predictions of volumetric strains. Comparisons of predicted volumetric strains of tests #4, #5, #6 and #7 show that the predicted values are very close to each other and they are limited within small

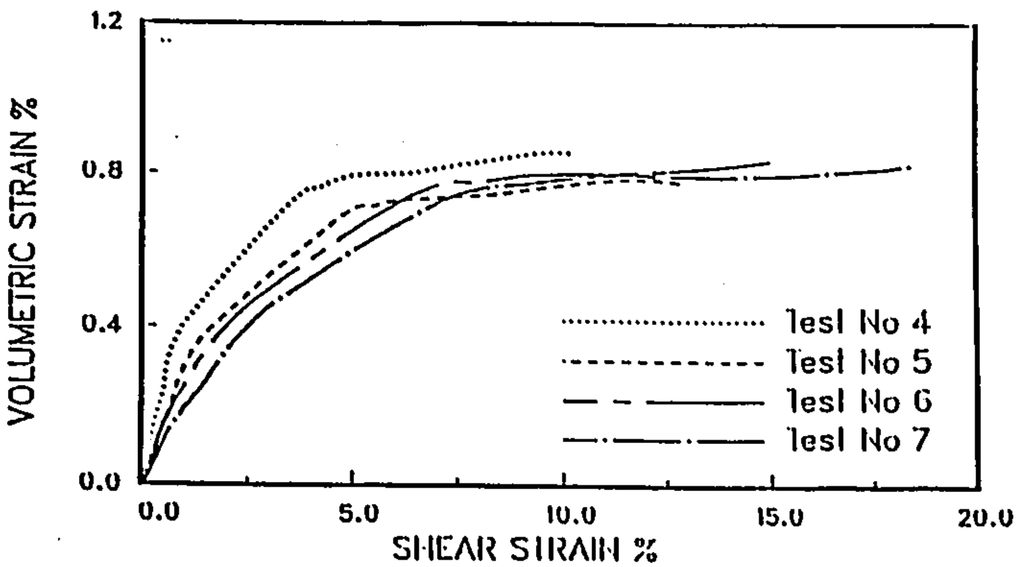

Figure 8.2: Predicted volumetric strains of tests #4, #5, #6 and #7. Volumetric strains versus shear strains curves

range, as shown in Fig 8.2. The predicted volumetric strains of tests #4, #6 and #7 are close to the values of the volumetric strains observed in test # 5. Note that test #5 is the test used originally in the determination of the initial model parameters [1]. In tests #6 and #7, the predicted values of ϵ_v were underestimated, however they were overestimated in test #4. In all cases, the model either overestimated or underestimated the observed volumetric strains trying to match the volumetric strain curve used originally in the determination of the initial model parameters.

8.2.2 Drained CTC Tests, Medium-Dense Samples

Test #8, $\sigma_3 = 68.95kPa$, Fig D.8

The initial stiffness of the soil was modelled well, but the predictions were terminated before the failure load could be defined. The model succeeds in predicting the dilation of the sample. However, the predicted plastic strains were less than the experimental values. The predicted shear stress strain curve agreed well with the observed shear stress strain values up to 80 % of the ultimate load. Thereafter, the predictions were terminated. This can be explained as follows:

The dummy yield surfaces change sizes as a function of the current volumetric strain, Eq 4.54. Thus, they decrease their sizes when dilatancy occurs and the stress point reaches the outermost yield surface before the actual soil failure occurs.

Test #9, $\sigma_3 = 137.89kPa$, Fig D.9

The predictions were in excellent agreement with the experimental values. Again, the model succeeded in simulating the dilatancy of the soil, but the predictions were terminated before the failure load could be defined. This was due to the contraction of the outermost yield surface as dilatancy occurred, as mentioned in the previous test.

Test #10, $\sigma_3 = 275.78kPa$, Fig D.10

The predicted shear stress strain curve agreed well with the observed values. The model was able to predict the observed soil dilatancy, but the volumetric strain versus shear strain curve flattened out trying to match the volumetric strain values used originally in the determination of the initial model parameters, test #9.

[1]The initial model parameters of tests #4, #6 and #7 were predicted from the experimental data of CTC test #5 and CTE test #13.

In all three tests, regarding the medium-dense samples, the predicted shear strain were larger than the observed values during unloading. The experimental results show that the shear stress strain curves drop vertically during loading in the inverse direction, unloading. It was believed that the size and the shape of the sand grains play a major role in such behaviour. Rowe (1962). The multisurface theory of plasticity is not capable of modeling this behaviour for the following reasons:

1. The elastic parameters are not constants.
2. Upon unloading, the soil nonlinearity occurs when the stress point moves from a yield surface f_m to a surface f_{m+1} because the parameters related to these surfaces are different. Moreover, these parameters vary according to the current volumetric strains and the applied hydrostatic pressure.

The nonlinearity of the shear stress strain curve and the soil plasticity are imposed by the concept of the multisurface theory of plasticity, reason #2. Even if it was assumed that the elastic behaviour of the soil is linear and the model parameters are not dependent on the hydrostatic pressure and the volumetric strains, the model still generates a Masing soil behaviour. Therefore, the vertical drop of the shear stress strain curve upon unloading, as it was observed experimentally, cannot be modelled.

8.2.3 Drained CTC Tests, Dense Samples

Test #11, $\sigma_3 = 68.95kPa$, Fig D.11

The predicted values of the shear stress strain curve and the volumetric strain versus shear strain curve agreed well with the experimental values. Two remarks can be made:

1. The predictions were terminated well before the failure load could be reached. This is due to the contraction of the outermost yield surface when dilatancy occurs.
2. The unloading-reloading cycle observed in the experimental data is missing in the predicted curve. The reason of this will be explained during the discussion of the next test.

Test #12, $\sigma_3 = 137.89kPa$, Fig D.12

In this test, the predicted shear stress strain curve and the volumetric response of

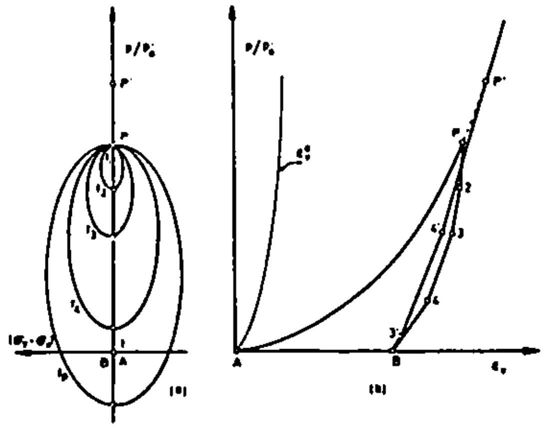

Figure 8.3: Isotropic compression test, field of yield surfaces.
(From Prevost, 1978).

the soil agreed well with the observed soil behaviour.
In classical theory of plasticity the loading must occur from a yield surface. The reasons for this are explained in Chapter 2. The deviatoric stress level [2] of 280 kPa was found to be bounded between two yield surfaces. Unloading from that stress level was not possible, as it was explained in Chapter 7. The same situation occurred during the predictions of the stress path test, test # 23. The predicted curves were the same as the predictions of test # 12 and the model simulations were ended during the first loading path, path 1-2 Fig C.9.

8.2.4 Isotropic Compression Tests

For cohesionless soil samples prepared in the laboratory, $\alpha_{ij} = 0$, Prevost (1979b). The yield surfaces are initially centered along P axis and tangent to each other at the origin of the (q - P) stress subspace. During the virgin consolidation, the stress point moves along P axis and translates the inner yield surfaces, as shown in Fig 8.3. All inner yield surfaces increase their sizes the same amount as expressed by Eq 4.37. Upon loading in the inverse direction (swelling), the stress point travels

[2]A deviatoric stress level at which the unloading occurs

backwards along P axis. The yield surfaces decrease their sizes isotropically, $\dot{\epsilon}_v^p < 0$. The model parameters were obtained by combining the experimental virgin consolidation and swelling curves, Prevost (1979b). Since the effect of the shear stress anisotropy does not exist, the constitutive equation A.1 reduces to the following form:

$$\dot{\epsilon}_v = (\frac{1}{B'} + \frac{1}{H})\dot{P} \tag{8.1}$$

In which $H = h + B'$ and $H = h - B'$ are the plastic bulk modulus associated with the virgin consolidation and swelling curves [3].

Tests #1, #2 and #3, Figs D.1, D.2, and D.3

The model predictions were in excellent agreement with the experimental values. The parameters were obtained by combining the virgin consolidation and swelling curves of isotropic compression tests, Fig C.1, C.2 and C.3. The model was then used to predict the same tests using these parameters. The back prediction procedure is the reason for achieving such high accuracy in the model simulations.

8.2.5 Drained CTE Tests

Test #18, $\sigma_3 = 137.89kPa$, Fig D.13

The model predictions were in excellent agreement with the experimental results. Both the shear and volumetric soil behaviour were modelled well. The initial stiffness of the soil was a little higher than the observed value. The reason of this is attributed to the computation of the elastic shear modulus in which its initial value was determined from the corresponding compression test (test # 5) and not from the extension curve, as explained in Chapter 6.

Test #19, $\sigma_3 = 137.89kPa$, Fig D.14

The initial stiffness was modelled well. The predicted values of the shear stress strain curve agreed with the experimental curve until the ultimate shear strength was reached, 100 %. Then, the predictions were terminated. The observed strain softening could not be predicted. It is believed that either one of the following two reasons is behind the termination of the model predictions.

[3]The polar angles associated with the virgin consolidation and swelling curves are equal to ±90° respectively.

1. Inability of the model to simulate the progressive failure of the soil after the ultimate value of the shear strength has been reached, strain softening.
2. Influence of the curve fitting procedure adopted for the extension tests to allow for the determination of the initial model parameters satisfying the slope condition, as explained in Chapter 6.
The first reason suggests that the capabilities of the model to simulate the strain softening have to be checked. This will be highlighted in Chapter 9, Section 9.2. The second reason is explained within the framework of the discussion of the next test, test #20.

Test #20, $\sigma_3 = 137.89kPa$, Fig D.15
The model predictions agreed well with the experimental values up to the ultimate shear strength of the soil. Then, the predictions were terminated. The determination of the initial model parameters requires that the slope condition has to be satisfied. Since the soil behaviour in extension and compression are different, the model parameters are not those related to the extension or compression curves, but a combination of the two. The softening observed in extension curve, test # 20, is not observed in the corresponding compression curve, test # 12. This provides non consistency of combining the two tests to allow for the determination of the initial model parameter related to the outermost yield surface. Consequently, it disturbs the model simulations at failure stages. More details regarding the inaccuracy of the model in defining the failure loads will be given later.

8.2.6 Undrained CTC Tests, Loose Samples

Test #13, $\sigma_3 = 137.89kPa$, Fig D.16
The predicted shear stress strain curve agreed well with the experimental values. The model simulated successfully the initial stiffness of the soil and the hardening of the stress-strain curve as the load increased. The response of the pore water pressure was modelled well. The model showed the ability of predicting the positive pore water pressure change as the sample tended to compress.

Test #14, $\sigma_3 = 275.78kPa$, Fig D.17
The model predictions were in good agreement with the experimental data. The initial stiffness and the failure load were underestimated slightly. This effects the

computed values of the elastic bulk modulus, as explained previously in Chapter 6. Consequently, there was a slight difference between the computed and measured pore water pressure values.

Test #15, $\sigma_3 = 413.66kPa$, Fig D.18
The difference between the observed and predicted curves in test # 14 became more clear as the initial confining pressure increased from 275.78 kPa (test # 14) to 413.66 kPa (test # 15). Regarding test # 15, the model underestimated the initial stiffness of the soil and overestimated the failure load. Also, the pore water pressure was underestimated. The reasons for this are explained later.

8.2.7 Undrained CTC Tests, Medium-Dense Samples

Test #16, $\sigma_3 = 68.95kPa$, Fig D.19
The predicted shear stress strain curve agreed well with the experimental values up to the shear stress level at which unloading occurred. In general, the model showed reasonable predictions of the shear stress strain curve. However, the response of the pore water pressure and the failure load were underestimated.

Test #17, $\sigma_3 = 137.89kPa$, Fig D.20
The model predictions of this test were in excellent agreement with the experimental values. The model simulated successfully the development of the positive pore water pressure at the initial stage of shearing and the negative pore water pressure as the sample tended to dilate.

8.2.8 Undrained CTE Tests

Test #21, $\sigma_3 = 137.89kPa$, Fig D.21
The predicted shear stress strain curve agreed well with the experimental values, at least up to 80 % of the shear strength of the soil. Then, the predictions were ended before the actual soil failure occurred. The model succeeded to simulate the initial stiffness of the soil and the gradual increase of the pore water pressure as the load continued. Since the model did not capture the failure load, the predictions of the pore water pressure were ended well before the observed soil failure.

Test #22, $\sigma_3 = 137.89kPa$, Fig D.22
The model simulated the initial soil stiffness properly. As the shear stress level increased, the model overestimated the observed shear stress strain curve and the predictions were terminated before the actual soil failure occurred.

The comparisons presented in Sections 8.2.6, 8.2.7 and 8.2.8 suggest that Prevost's pressure non-sensitive model describes the undrained soil behaviour reasonably well. The model simulates satisfactorily the prepeak shear stress strain curves, at least up to 80 % of the shear strength of the soil. However, the model suffers from a setback in simulating the failure loads in some cases, as it will be discussed in Section 8.3. In general, the differences between the predicted and observed undrained soil behaviour are thought to be due mainly tc the following reasons.

1. The experimental pore water pressure versus shear strain curves are not used in the determination of the initial model parameters. As the loading process continues, the pore water pressure was computed from Eq 4.47, Chapter 4, which is directly dependent on the current values of the elastic bulk modulus, the plastic modulus and the elastic shear modulus. For other tests different than the CTC-CTE tests used for the identification of the initial model parameters, the values of H, B and G have to be predicted using Eq 6.1. Thus, the predictions of the pore water pressure passes through a series of predictions and computations of the model parameters which may reduce the accuracy of the model simulations.

2. The loading unloading and reloading affect the predictions. A cycle of loading, unloading and reloading was performed for each test, which could not be predicted for the reasons explained in Chapter 4 and Chapter 7. This effects the observed soil behaviour because the stress strain curves obtained from monotonic shearing tests are different than those obtained from shear tests where cycles of loading unloading are included. This is due to the differences in change of the soil density in the tests with cycles of loading-unloading compared to the monotonic shearing tests, as explained in Chapter 5. It should be noted that Prevost's models do not take into account the change of the soil density as loading continues. The model formulations are independent of the current soil density.

3. Necking of the soil specimen, observed in the undrained CTE tests, is another

reason for the differences between the observed and predicted curves. Some inaccuracies may be introduced in the experimental procedure by the non-uniform deformation conditions which are developed in the soil sample at large shear strain levels due to necking of the specimen.

8.3 Discussions and Conclusions

The following discussions and conclusions were based on comparisons made between the model simulations and the test results of crushed quartz sand.

8.3.1 Pressure Sensitive Model

Prevost's pressure sensitive model was used to predict the drained CTC-CTE tests presented in Chapter 5. The model simulations were compared with the experimental values. The conclusion was that the model succeeded to simulate the shear stress strain curves. The initial stiffness of the soil was modelled well and the shear stress strain curves agreed with the experimental values at least up to 80 % of the soil shear strength. However, the model suffers from inaccuracies in its simulations of the failure loads. In some of the predictions, the model overshot or undershot the observed strength of the soil. The reasons for this were investigated. The parameters controlling the motion of the outermost yield surface and the technique used in the determination of the initial model parameters are the main reasons for the model of not being able to capture the failure loads. In addition, possibly the shape of the yield surface has contributed in these inaccuracies, Prevost (1987).
As it was pointed out previously, the outermost yield surface contracts or expands depending on whether the soil element exhibits contractive or expansive behaviour. A theoretical investigation was conducted to study the influence of the parameter λ, in Eq 4.54, on the simulated soil behaviour. A series of predictions of drained CTC test were performed for the loose sample of Fuji river sand. The experimental data of this sand was given in Fig 6.7. The values of the parameter λ were varied between 0 and 100. Figure 8.5 shows the test results together with the model simulations for each value of λ. As λ increased, the predicted shear stress strain curves varied within a very small range. It was observed that the failure load was highly

underestimated for $\lambda = 100$. For $\lambda = 50$, the model overestimated the shear strain at failure state. The failure load was captured exactly for $\lambda = 0$, Fig 8.6.

Tables 8.3, 8.4, and 8.5 show the initial model parameters of Fuji river sand for $\lambda = 0$, 50, and 100 respectively. It can be seen from Table 8.5 that the initial model parameters for $\lambda = 100$ are not realistic because there is a high degree of overlapping of the initial yield surfaces. For example, the initial size of the yield surface # 8 is much larger than the initial sizes of the yield surfaces # 9 and # 10. Such overlapping was due to the fact that the value of the parameter λ was not consistent with the other input data given to the computer program PARAMETER. In other words, the past soil stress history and its memory were not computed properly. This inconsistency of the initial model parameters effects the model simulations. Often, the convergence conditions required in PREDICTIONS for certain yield surfaces can never be met and, as a result, divergence occurs. In the case shown in Fig 8.6, the last computed results are those related to the yield surface f_{p-1}. They are not related to the outermost yield surface f_p.

Table 8.4 show the initial model parameters for $\lambda = 50$. The overlapping of the yield surfaces occurred. However, the degree of error of the computed initial model parameters was negligible compared to the previous case where $\lambda = 100$. In this case, the convergence conditions in PREDICTIONS were satisfied, but the inaccuracies observed in the initial model parameter influenced the predicted curves and model either overshot or undershot the failure loads, as shown in Fig 8.5.

Table 8.3 shows the initial model parameters when the influence of the isotropic parameter does not exist, $\lambda = 0$. The model simulated accurately the shear stress strain curve and the failure load was defined exactly. However, the model showed very poor predictions of the volumetric strain. This has led to the following questions.

1. Why did the model simulate accurately the shear stress-strain curve and poorly the volumetric strains when $\lambda = 0$?

2. Is this accurate predictions of the shear stress-strain curve and the failure load were obtained because the multisurface theory of plasticity was originally developed for metals where $\lambda = 0$?

Answers for these two questions are not available at this point because the answers have to consider not only the effect of the isotropic parameter, but also the effect of the shape of the yield surface and the effect of the assumption made for the motion of the outermost yield surface, Eq 4.37. On the basis of the results shown

in Fig 8.5, it is highly recommended that more research has to be done to assess the performance of the multisurface theory of plasticity in defining the failure loads for soils.
The contribution of the technique used in the determination of the initial model parameters to the unstable behaviour of the model in defining the failure loads will be highlighted within the discussion of the performance of the pressure non-sensitive model in simulating the undrained soil behaviour. Section 8.3.2.

A shortcoming of the model is clear in its predictions of the volumetric strains. The reason for this was believed to be related to the type of the non-associative flow rule used in the model formulation. It was found that when the stress point reaches a given yield surface f_m, the numerical values of the function $(3P''/K)^m$ are the same for given series of tests [4]. This means that the strain increment ratio, SVR, is constant regardless of the intensity of the applied stresses.

$$SVR = \dot{\bar{\epsilon}}/\dot{\epsilon}_v \tag{8.2}$$

This statement will be substantiated by using the following example:
Let's consider the series of drained CTC tests carried out on loose soil samples of crushed quartz sand, tests # 4, #5, #6 and #7. Remember that test # 5 was originally used for the identification of the initial model parameter. When the stress point reaches the yield surface #5, in test #5, the strain increment ratio ($\dot{\bar{\epsilon}}/\dot{\epsilon}_v$) is the same as if the stress point reaches the yield surface # 5 in tests #4, #6, and #7, as shown in Table 8.1. Similar statement is valid for the remaining yield surfaces. This means that the same ($\bar{\epsilon}$ versus ϵ_v) plot is obtained in all four tests, as shown in Fig 8.2. Also, Table 8.2 shows that the value of the function of $(3P''/K)$ is constant in all tests. By combining Eqs A.1, A.2, B.4 and B.5, the following equation can be obtained:

$$\left(\frac{3P''}{K}\right)^m = 2C\cos\phi_m + A_m\sqrt{6}\cos\phi_m|\tan\phi_m| \tag{8.3}$$

From Eq 8.3, it is clear that the same value of the function $(3P''/K)$ was obtained to fulfil the orientation condition, Chapter 6. In other words, the value of $(3P''/K)^m$ is constant because both the polar angle and the degree of non-associativity are constant parameters. Consequently, the initial overlapping of the yield surfaces was avoided. In order to avoid such inconvenience, the following improvements of the

[4]Note that P'' is the projection of the vector normal to the plastic potential surface onto the hydrostatic axis and K is the current size of the given yield surface f_m.

Table 8.1: Computed Strain Ratio Related to f_5

Yield surfaces # ....f_5, Degree of non-associativity............$A_5 = -1.70$
Polar angle..........................$\alpha_5 = (40.71)^\circ$

Test #	H_0 (kPa)	G_0 (kPa)	B_0 (kPa)	$\dot{q}$ (kPa)	$\dot{P}$ (kPa)	$\dot{\bar{\epsilon}}$ (%)	$\dot{\epsilon}_v$ (%)	$\dot{\bar{\epsilon}}/\dot{\epsilon}_v$
4	3510	9984.10	38938.00	23.03	7.67	0.5650	0.1354	4.17
5	5000	14119.66	55066.69	40.06	15.34	0.7944	0.1904	4.17
6	6640	19968.20	77875.94	92.12	30.68	1.1828	0.2836	4.17
7	8740	24455.95	95378.19	138.46	46.02	1.3651	0.3272	4.17

model are suggested:

1. The volumetric strain rate equation should be made a function of the current soil density or the current soil porosity to reflect the gradual increase of the relative density as the hydrostatic pressure increases. This can be accomplished by multiplying Eq A.1 by η [5]. In other words, multiplying the hydrostatic component of the non-associative flow rule function by the current soil porosity. In this case, the initial soil porosity, η_0, will be viewed as an additional initial model parameter. Its variation, during shearing, can be made a function of the current hydrostatic pressure, by analogy to Eq 4.53. In this case, the effect of the current soil porosity can be introduced into the flow rule function and Eqs 4.22 and 4.23 will be:

$$P' = Q' \tag{8.4}$$

$$P'' = \left(Q'' + A_m(Q' : Q')^{\frac{1}{2}}\right)\eta \tag{8.5}$$

where η is the current soil porosity, $\eta_0 < \eta < \eta_{max}$.

The advantage of this procedure is not only to simulate more accurately the observed volumetric strains for a given set of tests, but also to include the change of the soil density as loading continues for a single test. For a given cyclic test, the loose sample gradually becomes denser as the number of cycles increases, Tatsuoka and Ishihara (1974). The model as it was proposed by Prevost (1986), does not consider the change of the soil density as the number of cycles increases. It was found that for each cycle, the model produces the same amount of volumetric strain, Chapter

[5] η is the current soil porosity.

Table 8.2: Computed Flow rule Values Related to f_5

Test #	α (kPa)	β (kPa)	Size (kPa)	Deviatoric stress (kPa)	Hydrostatic stress (kPa)	$3P''$ (kPa)	$\frac{3P''}{K}$
4	45.73	75.97	58.73	84.04	96.96	34.88	0.594
5	91.47	151.94	117.47	168.08	193.92	69.77	0.594
6	182.92	303.88	234.94	336.16	387.84	139.55	0.594
7	274.38	455.82	352.41	504.24	581.76	209.33	0.594

9. This has led to the following statement:
As the number of cycles increases, the model produces ever increasing volumetric strains. According to the model, if a loose soil sample was subjected to cyclic loading condition, the sample conserves its initial density and the volumetric strain never converges to a limiting value. More details of this are given in Chapter9.

2. Another possibility to avoid the shortcoming observed in the volumetric strain predictions is to allow the rotation of the initial yield surfaces when their initial geometric configuration is predicted from given CTC-CTE tests. Simply, the condition of conservation of the orientation will not be respected. During shearing, the initial orientation of the yield surfaces must be conserved to avoid the overlapping and conserve the validity of Prevost's hardening rule presented in Chapter 4. This can be accomplished by assuming a variable degree of non-associativity and not a constant parameter. However, this suggestion complicates the computation of the initial model parameters when they are predicted for other tests.

8.3.2 Pressure Non-Sensitive Model

The capabilities of the pressure non sensitive model for describing the undrained soil behaviour was highlighted by comparing the test results presented in Chapter 5 with the predicted curves. It was shown that the model was able to predict the shear stress-strain-pore water pressure curves properly. However, some inaccuracies in the model predictions were observed. The model was not able to capture the failure loads of a number of tests and the predictions were ended before the failure load could be defined. The reason for this is strictly related to the concept used for the determination of the initial model parameters. In order to satisfy the same slope condition, the extension shear stress strain curves were expressed by mathematical functions, as explained in Chapter 6. In most cases, if the ultimate shear strength of the soil in compression was reached at a given shear strain level, the soil shear strength in extension will not necessary be reached at same shear strain level. The compression ultimate shear stress was used to identify the initial geometric configuration of the outermost yield surface. The corresponding extension shear stress was computed to satisfy the slope condition which may or may not correspond to the ultimate value. Thus, the initial geometric configuration of the outermost yield surface may not correspond to the ultimate value of the extension shear stress strain curve. This limits the ability of the model in capturing the actual failure loads, but it captures the maximum extension shear stress used in the determination of the initial model parameters and the model predictions will be ended when the stress point reaches the outermost yield surface. The model predictions of tests # 21 and # 22 were plotted together with the fitted curves used in the determination of the initial model parameters. The model predictions were 100 % matching the fitted curves, as shown in Fig 8.7. This proves that the model simulations are highly effected by the procedure of the determination of the initial model parameters. Thus, it is recommended that more research has to be done to investigate the possibility of eliminating the slope condition.

It should be noted that the pressure non-sensitive model is not able to simulate the softening of the soil after the peak strength has been reached. When the stress point reaches the outermost yield surface, the sample is considered to be failed, because the plastic moduli related to the outermost yield surface is equal to zero during all stages of shearing, $\lambda = 0$ in Eq 4.20. Thus, it is recommended that the model should include a parameter to be able to model the softening of the undrained shear stress strain curve after the soil shear strength has been reached.

8.4 Ottawa Sand

The experimental data used in this Section were collected from the proceedings of the Workshop on **Limit Equilibrium, Plasticity and Generalized Stress-**

Strain in Geotechnical Engineering, held at McGill University, Montreal, Canada (Yong and Ko, 1980). The tests had been conducted on prismatic samples of Ottawa sand in a cubical testing device under stress controlled conditions. The samples were first consolidated under equal all around pressure, then tested dry.
Prevost's model was used to predict the stress paths shown in Fig 8.4. The objective was to check the ability of the model to simulate the behaviour of soils subjected to three dimensional stress actions. In this case, the soil looses its initial transverse isotropy and becomes totally anisotropic material. This is due to the fact that the increments of the anisotropic tensor α, Eq 4.36, depend of the deviatoric stress increments. Since the values of the lateral deviatoric stress increments, $\dot{S}_x$, $\dot{S}_y$, are different, the increments of the component of α are also different, $\dot{\alpha}_x \neq \dot{\alpha}_z$.

Triaxial Compression, TC Test, Fig D.23 .
In a true triaxial testing device, the sample was subjected to 103.5 kPa of initial hydrostatic stress. Then, the lateral stresses were reduced while the vertical stress was increased such that the hydrostatic stress remained the same. The test was carried out in such a way that BB, stress ratio, remains constant:

$$BB = \frac{\sigma_2 - \sigma_3}{\sigma_1 - \sigma_3} \tag{8.6}$$

Thus, the variation of the principal stresses could be obtained by solving three non-linear system of equations:

$$\sigma_1 = \frac{3P + (BB-2)\sigma_3}{BB+1}, \quad \sigma_2 = \frac{3P + (1-2BB)\sigma_3}{BB+1} \tag{8.7}$$

σ_3 was obtained by knowing σ_1, σ_2 and BB value.
Figure D.23 shows both the experimental and the predicted shear stress strain curves. The model underestimated the shear strength of the soil. The failure loads were not captured and the sample failed before the actual failure occurred. However, the initial stiffness of the soil was modelled well and the predicted shear stress strain curves were in excellent agreement with the experimental values up to 80 %.

Triaxial Extension, TE Test, Fig D.24.
In this test, the lateral stresses were increased while the vertical stress was reduced such that the stress ratio BB remained constant. The sample was first subjected to 103.5 kPa of initial hydrostatic stress, then sheared with constant mean pressure.
Figure D.24 shows both the experimental and the predicted shear stress strain curves. The model underestimated the shear strength of the soil. The predictions

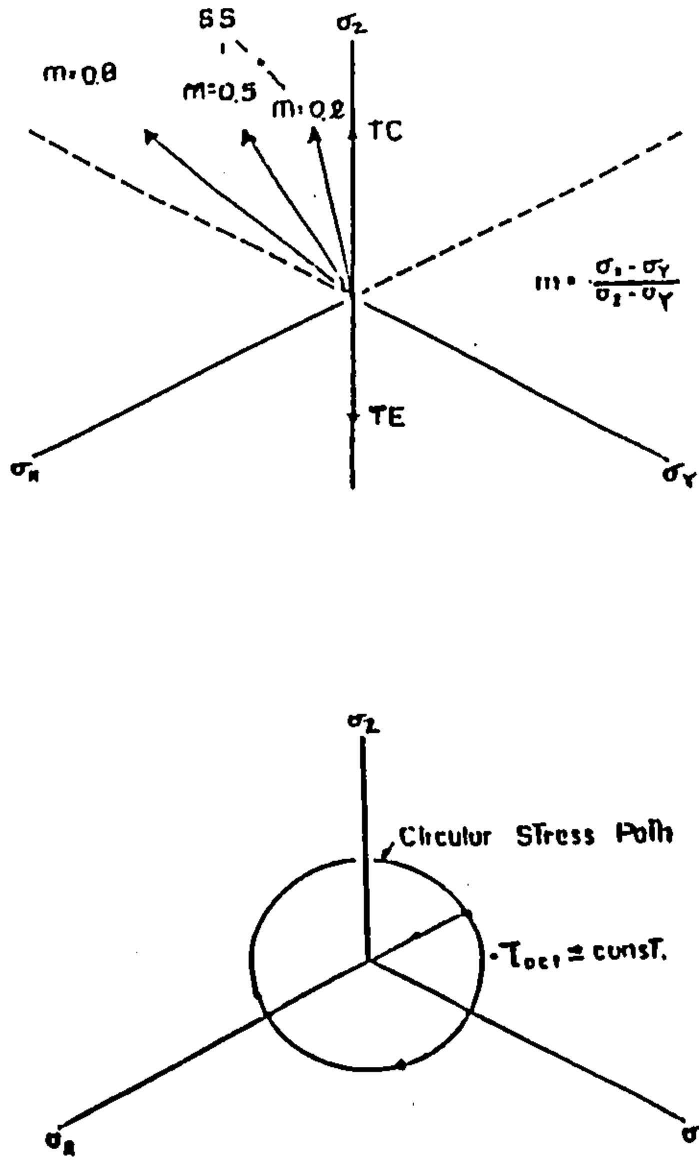

Figure 8.4: Stress paths used for predictions of the behaviour of Ottawa sand.

agreed well with the experimental values up to 80 %.
By comparing the experimental and the predicted shear stress strain curves for both TC and TE tests shown in Figs D.23 and D.24, it is clear that the predicted curves diverge from the experimental values at failure stages. The model missed to capture the failure loads and the shear strength of the soil was underestimated. The initial stiffnesses were modelled well and the predicted curves agreed with the observed soil stress strain curves up to 80%.

Simple Shear Stress Path, SS Test, constant mean pressure = 34.5 kPa, Figs D.25, D.26 and D.27 .
The simple shear stress path test was conducted in the octehedral plane. One of the lateral stresses was kept constant. The other lateral stress was decreased and the vertical stress was increased by the same amount such that the ratio BB was kept constant and the mean pressure was the same throughout the test.
Figures D.25, D.26 and D.27 show the experimental and the model predictions of the shear stress strain curves. The model succeeds to simulate this test. The failure loads were captured. The initial stiffness was modelled well. The predicted shear stress strain curves were in excellent agreement with the observed values.

Simple Shear Stress Path, SS Test, constant mean pressure = 137.9 kPa, Fig D.28, D.29 and D.30 .
Figures D.28, D.29, and D.30 show the test results plotted together with the model predictions. Accept for the comparison shown in Fig D.28, the model predictions agree well with the experimental values. The reasons for the divergence of the predicted curve from the test results, shown in Fig D.28, are not clear. However, it is believed that the experimental results of the plot $\sigma_1 - \sigma_2$ versus $\epsilon_1 - \epsilon_3$ are not consistent with the two other plots shown in Figs D.29 and D.30.

8.4.1 Conclusions

The following conclusions were based on the comparisons between of the model predictions of the observed behaviour of Ottawa sand.

1. The model is capable of predicting accurately the shear behaviour of soils in

complicated stress path tests. Although the model predictions agreed well with the experimental values, the failure loads were not captured occasionally. The initial stiffnesses were modelled well and the predicted shear stress strain curves agreed with the experimental values up to 80 %, at least, in all cases.

2. From the theory view point, the model cannot reproduce the circular stress path test. The reason for this is very clear. The stress point moves along the same yield surface f_m, and the stress increment vector is tangential to the yield surface. For this neutral loading case, the model does not produce plastic strains, see Chapter 2. Thus, the model simulates linear elastic soil behaviour in which $\epsilon_v = 0$ if the mean pressure is kept constant during testing. Otherwise the model simulates nonlinear elastic soil behaviour

8.5 Fuji River Sand

Tatsuoka and Ishihara (1974) conducted a series of drained cyclic tests on saturated loose samples of Fuji River sand. The tests were carried out by changing the axial load from extension to compression and vice versa. The confining pressure was kept constant. The test results show that the soil exhibits hysteretic behaviour and accumulates strains. The shear stress strain hysteresis loops decrease their sizes gradually as the number of cycles increases. Also, the tendency of the soil for compaction reduces as the number of cycles increases. Eventually, the sample reaches a high density where further compaction is not possible, Tatsuoka and Ishihara (1974). In this thesis, this characteristic behaviour of soil where the volumetric strains reach an ultimate constant value is called the shake down aspect.

The computer program, PREDICTIONS, was used to predict the results of a drained cyclic test carried out on loose soil sample of Fuji river sand under initial confining pressure of 196.14 kPa. Figure D.31 shows the model predictions of the first 4 cycles together with the test results. It is obvious that the model succeeds to simulate the hysteretic soil behaviour and the accumulative strains. However, it reproduced larger shear strain than observed experimentally and fails in reproducing the shake down aspect. Whereas the experimental volumetric strains converge towards a limiting value, the model predicts ever increasing volume change.

8.5.1 Discussions and Conclusions

The following discussions and conclusions were based on the comparisons between the model predictions of the observed cyclic behaviour of Fuji river sand.

With respect to the inability of the model to simulate the shake down aspect, a theoretical investigation was carried out to study the influence of Prevost's flow rule on the model simulations. It was observed that the shape of the q versus $3P''$ plot has the same shape for each cycle, as shown in Fig 8.8a. If each function $(3P'')^m$ was normalized with respect to the current sizes K^m, a linear plot of the function (q versus $3P''/K$) could be obtained. In the test shown in Fig D.31, the values of the functions $(3P'')_4$ related to the yield surface # 4 were normalized with respect to the current size, K_4. the resulted plot of the function (q versus $(3P''/K)$) is presented in Fig 8.8b where linear relation can be observed. Note that the curved plot A-B in Fig 8.8b is related to the primary loading before any stress reversal occurred. After the first cycle was completed, the model produced the same amount of the plastic volume change at the end of each cycle. As it is shown in Fig 8.9, the model produced almost 5 % of plastic volumetric strain in cycles # 2, # 3 and #4. It will be shown in Chapter 9 that as the number of cycles increases, the model produced ever increasing volume change. At the end of each cycle, the model reproduces the same amount of volumetric strain. There is no upper limit for the predicted volume change to converge.

Table 8.3: $\lambda = 0$. Initial model parameters of loose Fuji river sand, drained test, $\sigma_3 = 196.14kPa$

GO = 15636.01 BO = 14603.37 n = .50 lambda = 0.00

	ALPHA	BETA	K	H	B	A
2	-0.86	208.78	49.51	0.12E+07	-.67E+07	0.87
3	23.87	178.22	125.87	0.29E+05	-.18E+05	-1.98
4	20.79	180.28	164.48	0.11E+05	-.56E+04	-1.56
5	25.53	181.98	205.25	0.71E+04	-.29E+04	-1.51
6	35.50	189.54	238.37	0.39E+04	-.16E+04	-1.35
7	31.30	194.88	256.45	0.14E+04	-.56E+03	-1.17
8	27.01	195.65	281.00	0.13E+04	-.47E+03	-1.18
9	25.29	197.18	302.71	0.92E+03	-.38E+03	-1.18
10	27.53	201.80	317.20	0.57E+03	-.23E+03	-1.21

Table 8.4: $\lambda = 50$. Initial model parameters of loose Fuji river sand, drained test, $\sigma_3 = 196.14kPa$

GO = 15636.01 BO = 14603.37 n = .50 lambda = 50.00

	ALPHA	BETA	K	H	B	A
2	-4.60	196.04	50.30	0.96E+06	-.25E+07	0.87
3	15.13	156.33	106.72	0.31E+05	-.18E+05	-1.63
4	9.40	146.80	128.53	0.12E+05	-.61E+04	-1.25
5	10.79	134.92	147.15	0.75E+04	-.31E+04	-1.26
6	8.93	125.80	149.77	0.44E+04	-.19E+04	-0.97
7	-4.12	116.42	141.24	0.15E+04	-.82E+03	-0.59
8	-15.48	106.95	142.31	0.14E+04	-.85E+03	-0.49
9	-25.78	99.37	142.66	0.10E+04	-.91E+03	-0.38
10	-29.42	98.40	144.09	0.63E+03	-.71E+03	-0.35

Table 8.5: $\lambda = 100$. Initial model parameters of loose Fuji river sand, drained test, $\sigma_3 = 196.14 kPa$

G0 = 15636.01   B0 = 14603.37   n = .50   lambda = 100.00

	ALPHA	BETA	K	H	B	A
2	-11.32	184.01	54.26	0.88E+06	-.13E+07	0.87
3	6.00	137.26	92.41	0.29E+05	-.14E+05	-1.26
4	-0.02	119.84	102.19	0.13E+05	-.60E+04	-0.93
5	0.98	100.30	106.79	0.77E+04	-.31E+04	-1.00
6	-5.73	84.38	97.48	0.45E+04	-.24E+04	-0.58
7	-19.01	71.72	85.99	0.16E+04	-.31E+04	-0.02
8	-28.28	-564.80	-1331.90	0.60E+02	-.11E+02	-27.31
9	-36.63	-175.24	483.30	0.14E+03	-.32E+02	-9.81
10	-40.69	-126.67	371.96	0.12E+03	-.28E+02	-7.42

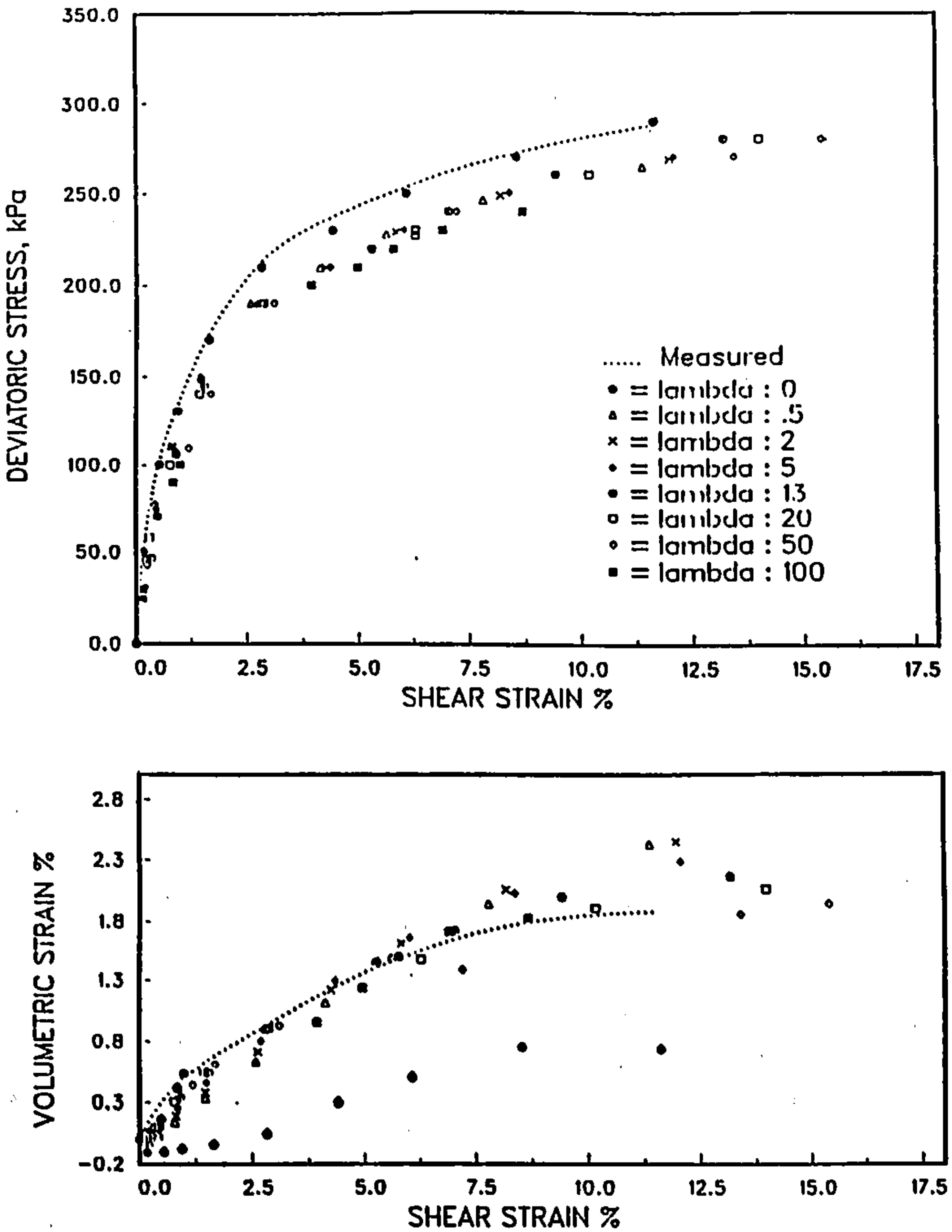

Figure 8.5: Drained CTC test, comparison of predicted and measured stress strain curves, loose sample of Fuji river sand, $\sigma_3 = 196.14kPa$.

a) Shear stress strain curves.

b) Volumetric strain versus shear strain curves.

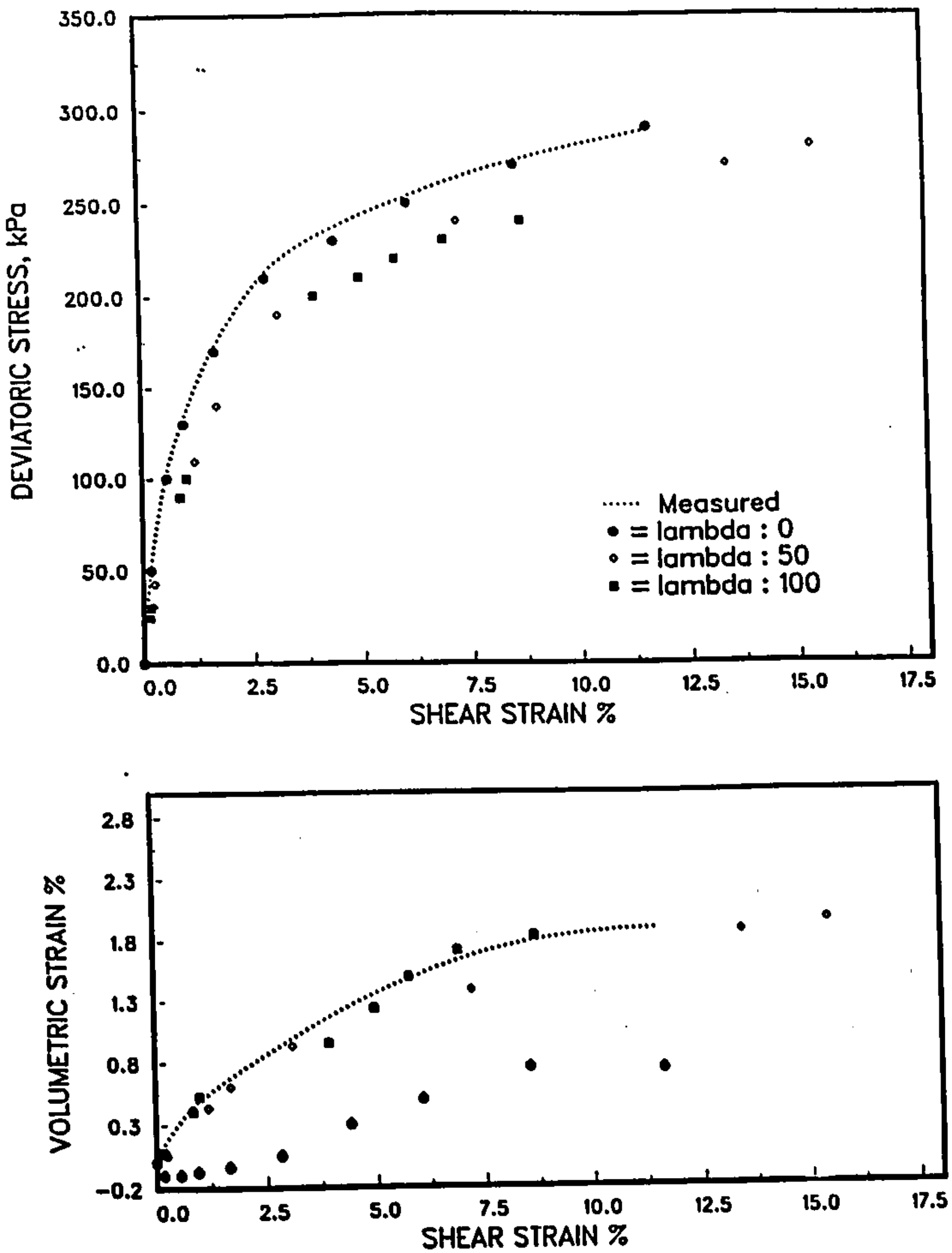

Figure 8.6: Drained CTC test, comparison of predicted and measured stress strain curves, loose sample of Fuji river sand, $\sigma_3 = 196.14kPa$.

a) Shear stress strain curves.

b) Volumetric strain versus shear strain curves.

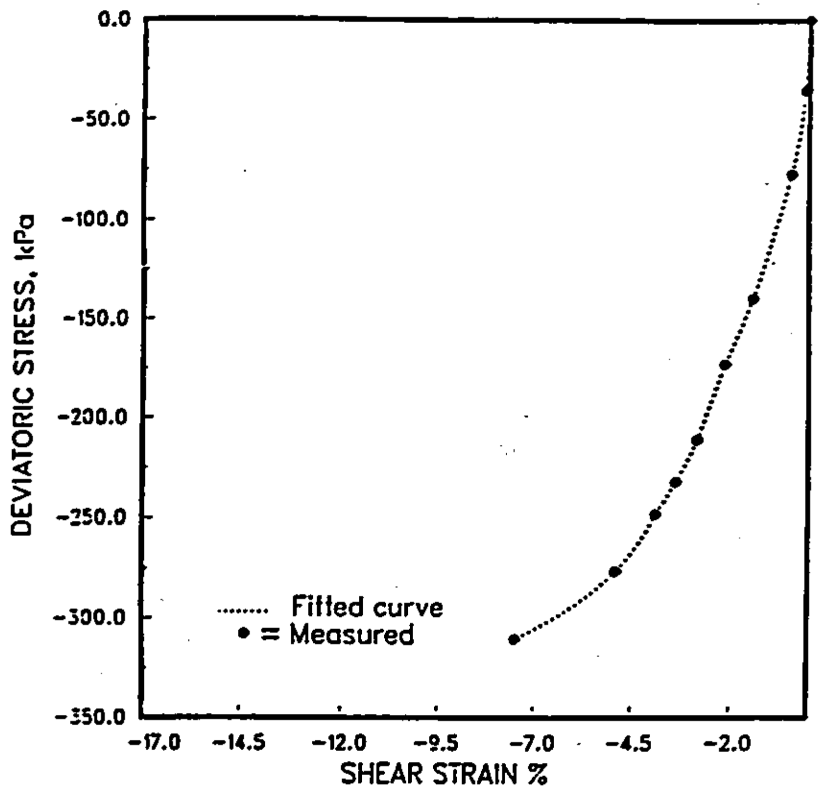

(a)

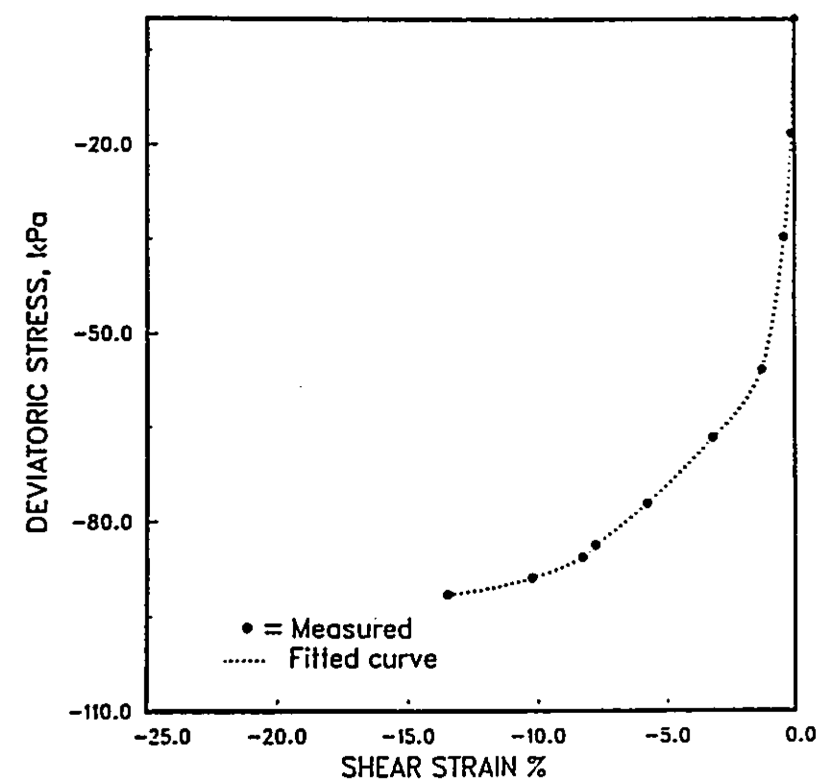

(b)

Figure 8.7: Undrained CTE tests, comparison of predicted and fitted stress strain curves.
a) Loose sample of crushed quartz sand, $(\sigma_3)_{initial} = 137.89kPa$.
b) Medium-dense sample of crushed quartz sand, $(\sigma_3)_{initial} = 137.89kPa$.

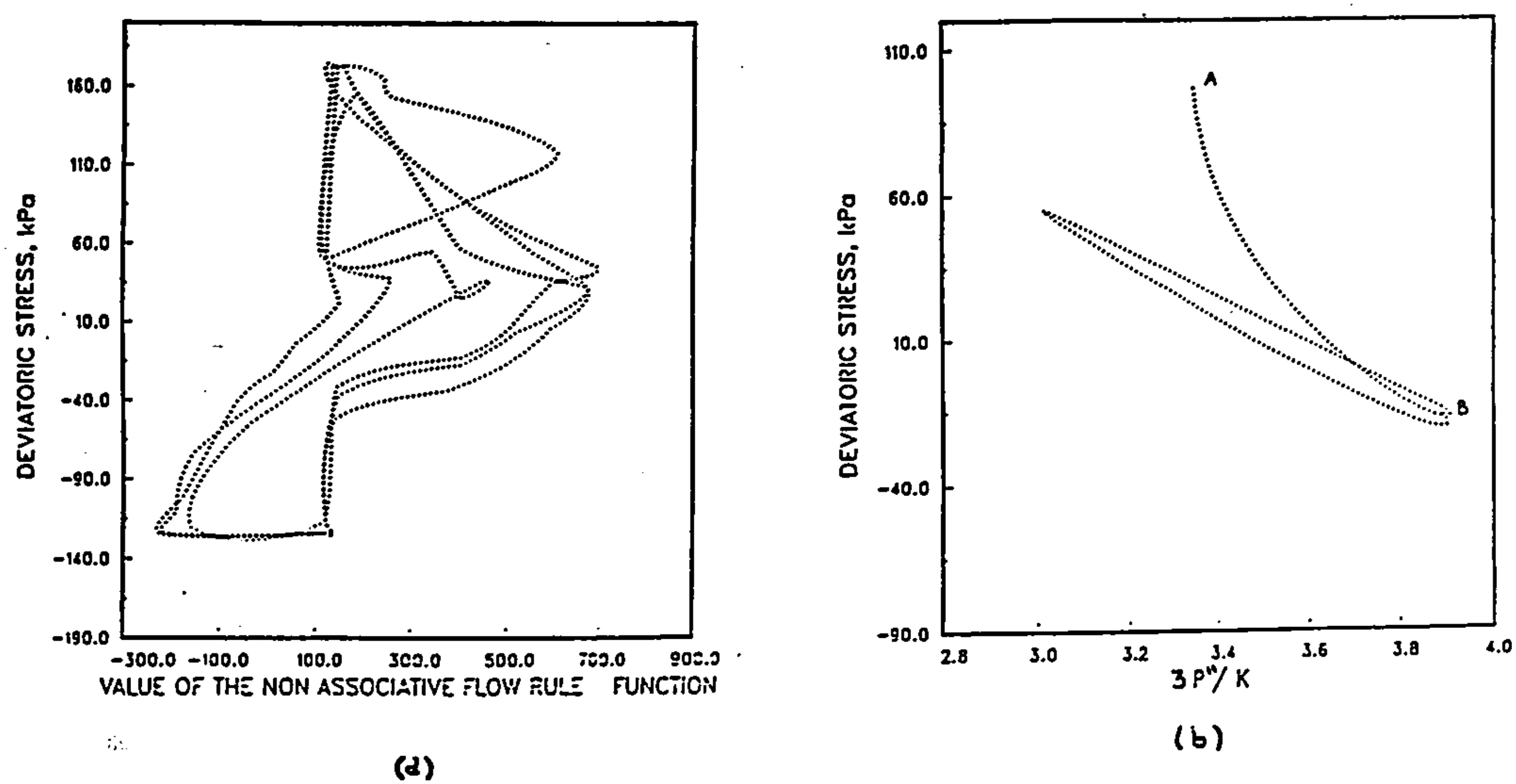

Figure 8.8: Drained cyclic test, Fuji river sand.

Deviatoric stress non-associative flow function relationships.

a) Variation of the non-associative flow function.

b) Variation of the normalized non-associative flow function.

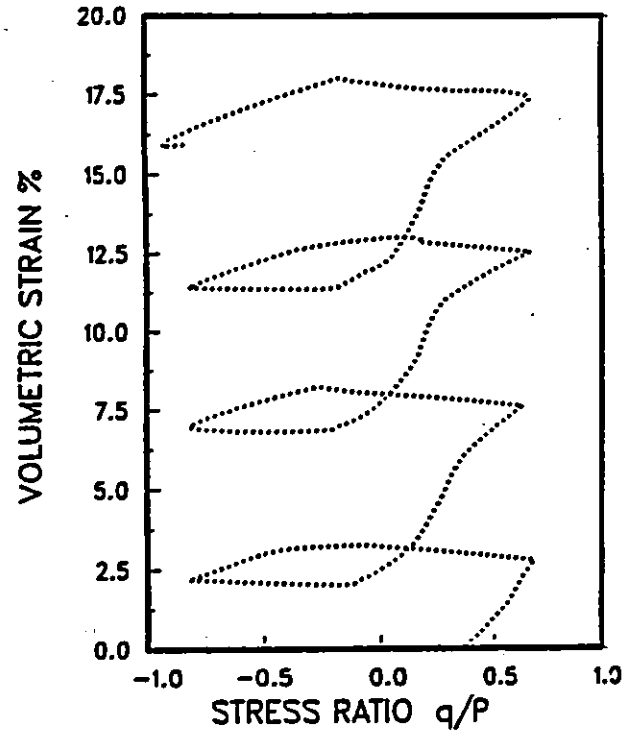

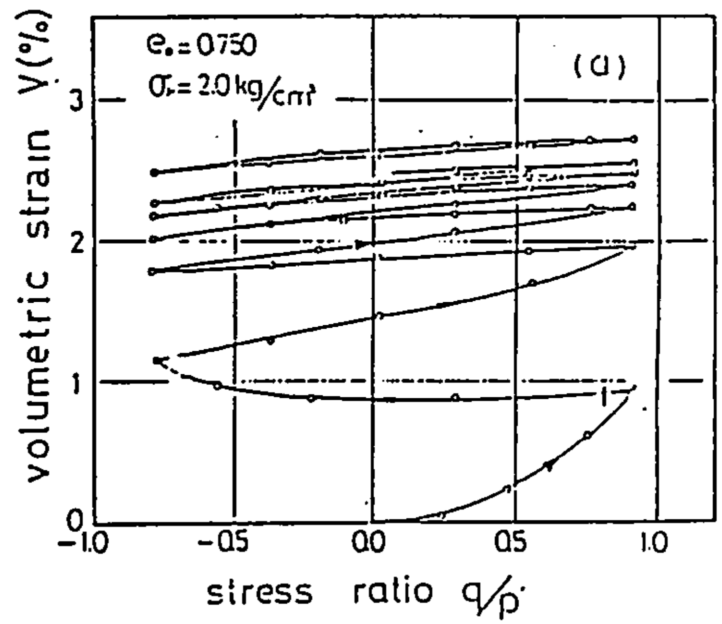

Figure 8.9: Drained cyclic test, comparison of predicted and measured volumetric strain curves, loose sample of Fuji river sand, $\sigma_3 = 196.14 kPa$.

Chapter 9

AN EVALUATION OF THE ADDITIONAL CAPABILITIES OF THE MODEL

9.1 Introduction

This chapter presents the results of a theoretical investigation which was conducted to study the ability of the model to simulate:

1. Strain softening,
2. Shakedown,
3. Behaviour of sand subjected to small and large amplitude cyclic loading.

9.2 Softening of the Stress Strain Curve

Hardening or softening of the material is modelled by changing the value of plastic modulus, H_p. The model uses an associative flow rule for the outermost yield surface. The plastic modulus related to the outermost yield surface was given according to Eq 4.20. It should be noted that Eq 4.20 was based on the assumptions discussed in section 4.3. When the stress point reaches the outermost yield surface, the plastic modulus increases or decreases towards zero depending on whether the soil exhibits softening or hardening, as shown in Fig E.1.

For the purpose of investigating the ability of the model in simulating the softening of the soil, the computer program, PREDICTIONS, was used to predict the behaviour of a dense soil sample of crushed quartz sand subjected to monotonically increasing loading. The test was carried out on a 4 inch diameter by 8 inch high cylindrical sample, Rahman (1974). The sample was sheared in dry conditions under $\sigma_3 = 344.7kPa$. The test results are presented in Fig E.2 together with the model simulation. The experimental data showed a softening behaviour of the soil after reaching the peak of the stress strain curve at 7% of axial strain. The model prediction is in excellent agreement with the experimental data up to the peak value. Then, the model shows negligible hardening of the stress strain curve which is not observed in the test results. An investigation was conducted to study the variation of the plastic moduli related to the outermost yield surface as the loading process continued. It was found that the variation of the plastic moduli, H_p, is small compared to what is observed experimentally. Indeed, the plastic moduli decreases and drops below zero, then increases towards zero. However, this situation occurs after reaching 30% of the axial strain, as shown in Fig E.3. Thus, the model is not capable to simulate the softening of the material at observed axial strain level.

9.3 Shakedown

Loose soil samples compact during cyclic loading. The rate for compaction reduces as the number of cycles increases. Eventually, the sample reaches a high density and further compaction does not occur, Tatsuoka and Ishihara (1974). This is called shakedown, Prevost(1987).

For the purpose of investigating the ability of Prevost's model in simulating the shakedown, a constant amplitude of cyclic load was provided as input data for the computer program PREDICTIONS. The input data shown in Fig E.4 was provided as follows:

From a spherical stress state of 137.89 kPa, a loose sample of the crushed quartz sand was subjected to a sinusoidal cyclic excitation by increasing the axial stress to 337.89 kPa, then reducing it to 137.89 kPa. In other words, the deviatoric stress varied between 0 and 200 kPa in a sinusoidal manner as a function of time.

The program output shows that the model simulates the hysteretic behaviour of the soil and the shear strains accumulate as the number of cycles increases, Fig E.5. Figure E.6 shows the predicted volumetric strains. No indication is observed regarding the ability of the model in simulating the shakedown phenomenon. The volumetric strain versus shear strain plot, Fig E.6, shows that the volumetric strains keep increasing monotonically. Even during the 10^{th} cycle, the model produces volumetric strain increments similar to those observed during the start of the cyclic loading. The predictions could be improved if the plastic volumetric strain rate equation was made a function of the current relative density or the current soil porosity. This statement can be explained as follows:

Within the framework of multisurface theory of plasticity, in a cyclic loading case, the stress varies between prescribed limits. The stress point translates only a certain number of yield surfaces and the remaining yield surfaces are not dragged by the stress point. In the case shown in Fig E.5, only the first five yield surfaces were subjected to translations and expansions. The remaining yield surfaces did not experience any kinematic hardening. In here, the translated yield surfaces are called the activated yield surfaces and the remaining yield surfaces are called the dummy yield surfaces because they are not involved in the computations of the plastic strains.

The difference between Eqs 9.1 and 9.2 is the type of non-associative flow rule adopted in the model formulation, Eqs 4.22 and 4.23.

$$\epsilon_v^p = \frac{1}{H} 3P'' \frac{Q.\sigma}{|Q|^2} \tag{9.1}$$

$$e^p = \frac{1}{H} Q' \frac{Q.\sigma}{|Q|^2} \tag{9.2}$$

Since the model simulations are reasonable for shear stress strain curves, the inability of the model to simulate the shakedown phenomenon can attributed to Eq 9.1. Thus, the effect of relative density should be introduced into the formulation of the non-associative flow rule.

9.4 Small Amplitude Cyclic Loading

The initial geometric configuration of the yield surfaces is not centered with respect to the hydrostatic axis, P, because:

1. The model uses stress induced anisotropy.
2. The stress strain characteristics in compression and extension are not the same. The stress level which is required to reach the 2^{th} yield surface in compression may correspond to the 4^{th} (or more) yield surface in extension. The amplitude of the cyclic loading must be provided in a such way that the stress level reaches at least the 2^{th} yield surface in compression. Otherwise, the model simulates an elastic behaviour in compression during the first cycle. During the 2^{th} cycle, the model simulates an elasto-plastic soil behaviour in compression because the 2^{th} yield surface was dragged when the stress point goes to the extension portion of the stress space.

In order to evaluate the model for small amplitude cyclic loading, the following input data was used:

From a spherical stress state of 137.89 kPa, a loose sample of crushed quartz sand was subjected to a sinusoidal cyclic excitation by increasing the axial stress to 257.89 kPa, then reducing it to 97.89 kPa in a sinusoidal manner, as shown in Fig E.7. During the 1^{st} cycle, the number of activated yield surfaces in compression(4 yield surfaces) is less than the number of activated yield surfaces in extension (7 yield surfaces), for the reasons given above. Thus, the 1^{st} cycle can be considered as a disturbance of the initial geometric configuration of the yield surfaces and the real cyclic model simulation starts from point A, as shown in Fig E.8. Figure E.9 shows the model simulation of the shear stress strain curve for a large number of cycles. Again the model succeeds in simulating the hysteretic soil behaviour and the accumulative strains. Figure E.10 shows the volumetric response of the soil sample. No indication is observed regarding the ability of the model in simulating the shakedown phenomenon. The inability of the model to simulate the shakedown phenomenon is demonstrated in Fig E.11 by plotting the volumetric stress-strain curve. The model fails to simulate the convergence of the volumetric strains to a steady state as the number of cycles increases.

It should be noted that small amplitude cyclic loading does not erase the anisotropy induced by the previous loading history because the stress state does note reach the dummy yield surfaces.

9.5 Large Amplitude Cyclic Loading

The ability of the model in simulating the behaviour of sand subjected to a large amplitude cyclic loading is analyzed here. With the objective of activating all the existing yield surfaces and erasing any previous anisotropy, accept for the outermost yield surface, a large amplitude cyclic loading was provided as input data for the computer program, PREDICTIONS. The cyclic load shown in Fig E.12 was applied as follows:

From a spherical stress state of 137.89 kPa, a loose sample of crushed quartz sand was subjected to a sinusoidal cyclic excitation by increasing the axial stress to 397.89 kPa, then reducing it to 87.89 kPa in a sinusoidal manner. The model succeeds in simulating the hysteretic behaviour and the accumulative shear strains, Fig E.13. Starting from the first cycle, the yield surfaces reach their limiting sizes and the model simulates the soil behaviour in almost a kinematic manner, i.e the hardening is introduced only through the translation of the yield surfaces. This conclusion is obtained from Fig E.14 in which the volumetric strain at 6 % of the shear strain was 0.72 % and at 50 % of the shear strain was 1.1 %. Since, the change of volumetric strain is relatively small compared to the change of shear strain , the influence of the isotropic hardening rule is very limited. The kinematic hardening had major influence on the results. The model continues to reproduce almost the same amount of shear strain for each cycle. The sample never fails as long as the stress level remains inside the outermost yield surface. The volumetric response of the sample is shown in both Fig E.14 and Fig E.15 in which the shakedown phenomenon is not is observed.

9.6 Variable Amplitude Cyclic Loading

The model simulations of the behaviour of sand sample subjected to mixed amplitude cyclic loading, from small to large amplitude or vice versa, is presented here. The input data shown in Fig E.16 was provided to the computer program as follows;

From spherical stress state of 137.89 kPa, a loose sample of crushed quartz sand was subjected to a cyclic excitation by increasing and decreasing the axial stress in a sinusoidal manner, as shown in Fig E.16. The program output, Fig E.17, show that the transition from the a small to a large amplitude of the cyclic loading disturbs the trend of the developed volumetric strain curve. It seems that the volumetric strain-shear strain curve is, somehow, a combination of the two previous cases.

9.7 Conclusion Regarding the Cyclic Simulations

A shortcoming of the model is apparent in the volumetric response, Fig E.10, E.11, E.14, E.15 and E.17. Whereas the experimental work show that the volumetric strain converge toward a limiting value, Tatsuoka and Ishihara (1974), the model predicts ever increasing volumetric strain change with each cycle. [1] This is shown by studying the response of the model for both a small and a large amplitude of cyclic loading. It can be concluded that the model is unable to predict the shake-down phenomenon. However, the model succeeds in simulating the hysteretic soil behaviour and the accumulative shear strains as the number of cycles increases.

The ability of Prevost's model in simulating the cyclic behaviour of the soil plays an important role in solving complex Geotechnical Engineering problems. In the literature, a large number of elasto-plastic soil models were published. However, they cannot be applied to cyclic loading condition. For example, cap models by Roscoe and Bruland (1968), DiMaggio and Baladi (1971), Baladi and Rohani (1979). These cap models have been based on the classical theory of plasticity using isotropic hardening alone, see Chapter 3. The most obvious limitations of these models are:

1. They do not adequately model the stress induced anisotropy.
2. They are not applicable to cyclic loading conditions.

Similar limitations apply to other models, Lade and Duncan (1975), Griffiths, Molenkamp and Smith (1982). It may be argued that isotropic hardening rules are adequate for situations in which only monotonically increasing loading occurs. However, it is unlikely that such restrictions can be met in every geotechnical problem.

[1] The same conclusion was reached by Prevost (1987) for his new model which was based on the same concept as the model in question.

Chapter 10

CONCLUSIONS AND RECOMMENDATIONS

The following conclusions have been drawn on the basis of comparisons between the model simulations and the actual test data.

10.1 Conclusions Regarding the Pressure Sensitive Model

1. The initial soil stiffness was modelled well and the predicted shear stress strain curves agreed with the experimental values, at least up to 80 % of the ultimate load.

2. In some predictions, the model overshot or undershot the observed strength of the soil. The concept used for the contraction or expansion of the outermost yield surface and the parameter identification technique were the main reasons for the model of not being able to capture the actual failure loads.

3. A shortcoming of the model is apparent in its predictions of the volumetric strains. One reason for this was believed to be the type of non-associative flow rule used by the model. It is suggested that the volumetric strain rate equation should

be made a function of the current relative density to reflect its gradual change as the loading process continues. This suggestion was made on the basis of comparisons between the static test results with the model predictions, and also the predicted and observed cyclic behaviour of both Fuji river sand and crushed quartz sand subjected to small and large amplitude cyclic loading.

4. The model is capable of simulating accurately the shear behaviour of soil in complicated stress path tests in three dimensional stress space.

5. The model is able to simulate the strain softening. However, because of the inaccuracies in its definition of the failure loads, the model reproduced the softening of the shear stress strain curve at a larger shear strain level than the observed value. It was found that the variation of the plastic modulus related to the outermost yield surface is very small compared to what is observed experimentally. Indeed, the value of the plastic modulus related to the outermost yield surface dropped below zero, then increases towards zero. However, this situation occurred at a very large shear strain level.

6. Under cyclic loading conditions, the model is unable to predict the shake-down phenomenon. Whereas the experimental volume change of loose samples converged towards a limiting value, the model simulated ever increasing volume change. This was demonstrated by studying the response of the model for small, large and variable amplitude of cyclic loading. On the other hand, the hysteretic soil behaviour and the accumulative shear strains were simulated successfully as the number of cycles increased.

10.2 Conclusions Regarding the Pressure Non-Sensitive Model

1. The capabilities of the pressure non-sensitive model for describing the observed undrained soil behaviour was evaluated by comparing the test results with the predicted curves. It was shown that the model was able to predict the shear stress-strain-pore water pressure response properly. However, there are some inaccuracies in the model predictions. For example, the model was not able to capture the failure

loads of a number of tests and the predictions were terminated before the actual failure load could be defined. The model predictions of the pore water pressure were in agreement with the observed values. The model was able to predict the positive pore water pressure at initial stages of shearing, then negative pore water pressure as the sample tended to dilate.

2. The pressure non-sensitive model is not able to simulate the softening of the shear stress strain curve after the peak strength has been reached. When the stress point reaches the outermost yield surface, failure occurs, because the plastic modulus related to the outermost yield surface is equal to zero during all stages of shearing.

3. Under cyclic loading conditions, the pressure non-sensitive model reduces to total stress model in which the generation of the pore water pressure is ignored. Moreover, the identification of the hardening parameters is based on a curve fitting procedure of the static and cyclic simple shear tests. Thus, the accuracy of the model simulations depends highly on the accuracy achieved by the curve fitting procedure of the experimental data.

10.3 General Conclusions

In the following, the term Prevost's model will correspond to both pressure sensitive and pressure non-sensitive models at the same time.

1. Prevost's model can be considered as one of the most complicated and sophisticated soil models existing in the field of geotechnical engineering. The model tends to be a general theory applicable for both sand and clay. Its formulation includes both drained and undrained situations. Thus, the model is academically elegant, but unlikely to be favoured by the practicing engineers. This is due to the model complexity.

2. The determination of the initial model parameters was based on a curve fitting procedure using the extension tests data. It was shown that the accuracy of the model simulations was directly related to the accuracy of the fitted extension curve.

3. The initial elastic model parameters are determined from the compression stress strain-volume change curves. These parameters are assumed to be the same for both

compression and extension cases. This assumption effects the model simulations of the initial soil stiffness for extension tests, because the soil behaviour in compression and extension are different.

4. The model uses lines for failure in compression and extension. These lines have a constant slopes. The model does not consider curved failure lines to reflect the gradual reduction of the peak friction angle as the mean pressure increases.

5. The model involves a large number of parameters. These parameters are variables and interconnected. This complicates both the model implementation in computer programs and the computation procedure for the model simulations. For the cyclic events, the update geometric configuration of the yield surfaces must be remembered. This requires a considerable amount of computer storage and increases the CPU time.

6. The model can be considered as a powerful tool to simulate the cyclic shear stress strain behaviour of soil. This may play very important role in solving complex boundary value problems.

7. The multisurface theory of plasticity represents a more versatile and powerful tool for describing the constitutive behaviour of soils than it seems to be recognized.

10.4 Recommendations

1. It is highly recommended that further research has to be done to investigate the following aspects:
1.a. The possibility of reducing the number of the model parameters and simplifying the constitutive relations. These will reduce the computations cost and minimize the complexity of the model implementation in computer programs.

1.b. The effect of the assumption made for the motion of the outermost yield surface, Eq 4.37. This allows for a better understanding of the inaccuracies of the model in its predictions of the failure loads.

1.c. The effect of the shape of the yield surface on the model simulations of the volumetric deformation behaviour of soil.

2. It is recommended that a certain softening parameter should be used to model the softening of the shear stress versus shear strain behaviour in an undrained case.

3. It was suggested that the model formulation should be made a function of the current relative density of the soil.

REFERENCES

ANSAL, A.M., 1977 An endochronic constitutive law for normally consolidated clay. Ph.D. dissertation, Northwestern University. Faculty of Engineering, Department of Civil Engineering, 199 p.

ATKINSON, J.H. and BRANSBY, P.L. , 1977. The mechanics of soils, *An introduction to the critical state soil mechanics.*
McGRAW Hill., London, 375 p.

BAZANT, Z.P. and KRIZEK, R.J., 1976. Endochronic constitutive law for liquefaction of sand. American Society of Civil Engineers, ASCE Journal of the Engineering Mechanics Division., Vol 102, EM 2, pp. 225 - 238.

BISHOP, A.W. and HENKEL, D.J., 1962. The measurement of soil properties in the triaxial test. A. EDWARD., Publishers., London., 228 p.

CALLADINE, C.R., 1969. Engineering Plasticity. Pergamon press., 1^{st}*edition*, Oxford., 318 p.

CHEN, W.F. and BALADY, G.Y., 1985. Soil plasticity, *Theory and implementation.* Elsevier, Amsterdam., 231 p.

DERRADJI-AOUAT, A. and EVGIN, E. , 1988. Evaluation of Prevost's pressure sensitive model. An internal report, Department of Civil Engineering, University of Ottawa., Canada., 259.p

DERRADJI-AOUAT, A. and EVGIN, E. , 1988. Computer implementation of Prevost's pressure non-sensitive model. An internal report, Department of Civil Engineering, University of Ottawa., Canada., 60.p

DESAI, C.S. and SIRIWARDANE, H.J., 1984. Constitutive laws for engineering materials *with emphasis on geologic materials.* Prentice-Hall. inc., 468 p.

DESAI, C.S., 1971. Nonlinear analyses using spline functions. American Society of Civil Engineers, ASCE Journal of the Soil Mechanics and Foundation Division., Vol. 97, SM 10, pp. 1461 - 1479.

DRUCKER, D.C., 1950. Some implications of work-hardening and ideal plasticity. Quarterly of Applied Mathematics. Vol. 7, No 4, pp. 411 - 418.

DUNCAN, J.M. and CHANG, C.Y. , 1970. Nonlinear analysis of stresses and strains in soils. American Society of Civil Engineers, ASCE Journal of Soil Mechanics and Foundation Engineering, Vol. 96, SM 5, pp. 1629 - 1653.

HILL, R., 1950. Mathematical theory of plasticity.
Oxford clearendon press., 355 p.

IWAN, W.D., 1967. On a class of models for the yielding behaviour for the continuous and composite systems. Journal of Applied Mechanics Transitions., Vol. 34, No E3, pp. 612 - 617.

KO, H.Y. and SCOTT, R.F. , 1967. Deformation of sand in shear. American Society of Civil Engineers, ASCE Journal of Soil Mechanics and Foundation Division. Vol. 93, SM 3, pp. 137 - 156.

KURDAZE, V.D., GEGLIA, T.G., BASHELEISHVILI, M.O. and BURCHULADZE, T.V., 1979. Three dimensional problems of elasticity and thermoelasticity. H. A. LAUWERIER. and W. T. KOITER, Editors., Amsterdam., 929 p.

LADE, P.V. and DUNCAN, J.M., 1967 Stress path dependent behaviour of cohesionless soils. American Society of civil Engineers, ASCE Journal of the Geotechnical Engineering division. Vol. 102, GT 1, pp. 51 - 68

MROZ, Z., 1967. On the description of anisotropic work-hardening. Journal of the Mechanics and Physics of Solids, london, Vol. 15, pp. 163 - 1175.

MROZ, Z., 1978. An anisotropic hardening model for soils and its application to cyclic loading. International Journal for Numerical and Analytical Methods in Geomechanics. Vol. 2, pp. 203 - 221.

MROZ, Z. , NORIS, V.A. and ZIENKIEWICZ, O.C., 1979. Application of an anisotropic hardening model in the analysis of elasto-plastic deformation of soils. Geotechnique, Vol. 29, No 1, pp. 1 - 34.

PHILIPS, A. and SIERAKOWSKI, R.L., 1965. On the concept of the yield surface. Acta Mechanica, Vol. 1, pp. 29 - 35.

PRAGER, A.W., 1949. Recent development in mathematical theory of plasticity. Journal of Applied Physics. Vol 20, No 3, pp. 235 - 241.

PRAGER, A.W., 1956. A new method of analyzing stresses and strains in work-hardening plastic solids. American Society of Mechanical Engineers, ASME Journal of Applied Mechanics devision, No 56, APM 34, pp. 493 - 496.

PREVOST, J.H., 1977. Mathematical modelling of monotonic and cyclic undrained clay behaviour. International Journal for the Numerical and Analytical Methods in Geomechanics. Vol. 1., pp. 195 - 216

PREVOST, J.H. and HOEG, K., 1977. Plasticity model for undrained stress-strain behaviour. Proceedings of the 9^{th} International Conference on Soil Mechanics and Foundation Engineering., Tokyo., Vol. 1., pp. 255 - 261

PREVOST, J.H., 1978. Plasticity theory of soil stress strain relations. American Society of Civil Engineers, ASCE Journal of the Engineering Mechanics Devision. Vol. 104, EM 5, pp. 1177 - 1194.

PREVOST, J.H., 1979. Anisotropy undrained stress strain behaviour of clays. American Society of Civil Engineers, ASCE Journal of the Geotechnical Engineering Devision. Vol. 104, GT 8, pp. 1075 - 1090.

PREVOST, J.H., 1979. Mathematical modelling of soil stress strain strength behaviour. Proceedings of the 3^{th} International Conference on Numerical Methods in Geomechanics., Aachen 2-6 april 1979. , pp. 347 - 361

PREVOST, J.H., 1979. Undrained shear tests on clays. American Society of Civil Engineers, ASCE Journal of the Geotechnical Engineering Devision. Vol. 105, GT 1, pp. 49 - 63.

PREVOST, J.H. and HUGH, T.J.R., 1981. Finite element solution of elastic-plastic boundary value problems. American Society of Civil Engineers, ASME Journal of Applied Mechanics Devision. Vol. 48, No 81, APM 17., pp. 69 - 74.

PREVOST, J.H., 1981. Nonlinear anisotropic stress-strain strength behaviour of soils. American Society for Testing Materials., Symposium on Laboratory Shear Strength of Soils. R. N. YONG and F. C. TOWSEND, Editors. Special Technical Publications, ASTM, STP 740. pp. 431 - 455

PREVOST, J.H., CUNY, B. and SCOTT, R.F., 1981 Offshore gravity structures *centrifugal modelling.* American Society of Civil Engineers, ASCE Journal of the Geotechnical Engineering Devision. Vol. 107, GT 2, pp. 125 - 141.

PREVOST, J.H., AHMED, M.A. and SARA, J.L., 1985 Nonlinear dynamic analyses of an earth dam. American Society of Civil Engineers, ASCE Journal of the Geotechnical Engineering. Vol. 111, No 7, pp. 882 - 897.

PREVOST, J.H., AHMED, M.A. and WAEIL, A.E., 1985 Nonlinear hysteretic dynamic response of soil systems. American Society of Civil Engineers, ASCE Journal of Engineering Mechanics., Vol. 111, No 5, pp. 696 - 713.

PREVOST, J.H., 1986 Constitutive equations for pressure sensitive soils, *theory, numerical implementation and examples.* Geotechnical Modelling in Engineering Practice. Chapter 14. pp. 331 - 349. R. DUNGAR and J. A. STUDER., Editors. boston., 400 p.

RAHMAN, M.G., 1974 Bearing capacity and settlement of circular footing on sand. M. A. Sc. thesis, University of ottawa, Faculty of Engineering, Department of Civil Engineering, 194 p.

ROSCOE, K.H. and POOROOSHASB, H.B., 1963 A theoretical and experimental study in triaxial compression tests on normally consolidated clays. Geotechnique., Vol 13., No 1., pp. 12 - 28.

ROSS, B.C. and HASSAN, F., 1974 Nonlinear stress-strain formulation for soils. American Society of Civil Engineers, ASCE Journal of the Geotechnical Engineering Devision. Vol. , GT 9, pp. 993 - 1008

SCOTT, R.F., 1985 Plasticity and constitutive relations in soil mechanics. American Society of Civil Engineers, ASCE Journal of Geotechnical Engineering Devision. Vol. 111, No5, pp. 563 - 605

SEED, H.B. and LEE, K.L., 1967 Undrained strength characteristics of cohesionless soils. American Society of Civil Engineers, ASCE Journal of Soil Mechanics and Foundation Engineering Devision. Vol. 93, SM6, pp. 333 - 360

SOLOMON, L., 1968 Elasticite linear. Masson et C^{ie} editeurs., Paris., 742 p.

TATSUOKA, F. and ISHIHARA, K., 1974. Drained deformation of sand under cyclic stresses reversing direction. Japanese Society of Soil Mechanics and Foundation Engineering. Mechanics Devision. Vol. 14, No 3., pp. 69 - 74.

TERZAGHI, K., 1943 Theoretical soil mechanics. John Wiley and sons, Inc., New York, N. Y., 600p.

VIJAY, K.K. and TIEN, H.W., 1976 Stress strain behaviour of sand. American Society of Civil Engineers, ASCE Journal of the Geotechnical Engineering Devision. Vol. 102, GT 4, pp. 303 - 321

YONG, R.N. and SELIG, E.T., 1980. Application of plasticity and generalized stress-strain in Geotechnical Engineering. Proceedings of the symposium on limit equilibrium and generalized stress strain applications in Geotechnical Engneering. *held in conjunction with the 1980 ASCE annual convention and exposition., Hollywood., Florida. October 27-31,* 351.p

YONG, R.K. and KO, H.Y., 1980. *Proceedings of the Workshop on* **Limit equilibrium, plasticity and generalized stress-strain in Geotechnical Engineering.** McGill University., Canada, May 28-30., 871.p

Appendix A

GENERAL STRESS STRAIN RELATIONS

The general elasto-plastic stress-strain relations of Prevost can be written as follows:

$$\dot{\epsilon}_v = \frac{\dot{P}'}{B} + \frac{1}{H} 3P" \frac{Q\dot{\sigma}}{|Q|^2} \tag{A.1}$$

$$\dot{e} = \frac{\dot{S}}{2G} + \frac{1}{H} Q' \frac{Q\dot{\sigma}}{|Q|^2} \tag{A.2}$$

These constitutive equations can be inverted:

$$\dot{S} = 2G\dot{e} - \frac{4G^2}{H} Q' X \tag{A.3}$$

$$\dot{P} = B\dot{\epsilon}_v - 2G\frac{B}{H} 3P" X \tag{A.4}$$

In which:

$$X = \frac{Q'\dot{\epsilon} + \frac{B}{2G} 3Q"\dot{\epsilon}_v}{|Q'|^2(1 + \frac{2G}{H}) + 3(Q")^2 + 9(\frac{B}{H})Q"P"} \tag{A.5}$$

In a more general form, the constitutive relation for the finite deformations was given by Prevost (1986):

$$C : \dot{\epsilon} = \dot{\sigma}' \tag{A.6}$$

In which:

$\dot{\sigma}'$ is the effective Cauchy stress tensor.

$\dot{\epsilon}$ is the rate of deformation tensor.

Prevost (1986) proposed the following C tensor:

$$C = E - \frac{1}{H + Q : E : P}(E : P)(Q : E) \tag{A.7}$$

In which:

H is the plastic modulus, see Eq 4.5

Q and P are symmetrical 2^{nd} order tensor, see Eq 4.9 and 4.10.

E is a 4^{th} order tensor of the elastic moduli.

$$E = A\delta_{ab}\delta_{bc} + G(\delta_{ac}\delta_{bd} + \delta_{ad}\delta_{bc}) \tag{A.8}$$

A and G are Lame's constants, δ_{ab} = Kronecker delta.

Since $f = \frac{3/}{2}(S_{ij} - \alpha_{ij})^2 + C^2(P - \beta)^2 = K^2$, the values of Q' and Q'' are expressed as follows:

$$Q' = 3(S_{ij} - \alpha_{ij}) \tag{A.9}$$

$$Q'' = 3(P - \beta) = \frac{1}{3}tr(Q) \tag{A.10}$$

and

$$P' = Q' \tag{A.11}$$

$$P'' = \frac{1}{3}tr(P) = tr(Q) + A_m(Q' : Q')^{\frac{1}{2}} \tag{A.12}$$

$|Q|^2$ in Eqs A.1 and A.2 takes the form:

$$|Q|^2 = \frac{gradf}{|gradf|} = |Q'|^2 + 3|Q''|^2 = 6K^2 \tag{A.13}$$

Taking into consideration Eqs 4.9 and 4.10, the following expression may be obtained

$$Q : E : P = Btr(P)tr(Q) + 2G(P' : Q') \tag{A.14}$$

Eq A.6 will have the following general form:

$$\dot{\sigma}' = 2G\dot{\epsilon} + (3BP''\delta)\frac{2GQ'\dot{\epsilon} + 3BQ''\dot{\epsilon}_v}{H + 2GQ'' : Q' + B3Q''3P''} \tag{A.15}$$

Where $B = A + \frac{2G}{3}$ is the bulk modulus.

Appendix B

MODEL PARAMETERS

B.1 List of the Model Parameters

The formulation of Prevost's model involves the following set of elastic and plastic parameters.

a. **Elastic parameters:**
1. G elastic shear modulus.
2. B elastic bulk modulus.

b. **Plastic parameters:**
1. α and β are the center coordinates of the yield surface.
2. K is the size of the yield surface.
3. h is the plastic shear modulus.
4. A is the degree of non-associativity.
5. B' is a plastic parameter in which $(h + B')$ is the plastic bulk modulus.

c. **Isotropic parameter:** λ

Note that each yield surface requires a new set of plastic parameters. Thus, the total number of parameters is ($6 \times NYS + 3$) in which NYS is the number of the yield surfaces and 3 corresponds to the elastic parameters and the isotropic parameter.

B.2 Laboratory Tests Needed

A complete determination of the model parameters require the following data:

1. Experimental stress strain curves for both triaxial compression and extension tests originating from a common mean effective stress P_0', given in the form:

Compression	q_c versus $\bar{\epsilon}_c$	P_c versus ϵ_v^c .
Extension	q_e versus $\bar{\epsilon}_e$	P_e versus ϵ_v^e .

in which $\bar{\epsilon}$ is the strain difference :

$$\bar{\epsilon} = \epsilon_y - \epsilon_x \tag{B.1}$$

2. Experimental data of an isotropic compression test.

B.3 Parameter Identification

The initial model parameters are determined from the condition that the slope, $\frac{\dot{q}}{\dot{\epsilon}}$, of both triaxial compression and extension curves are the same when the stress point reaches a yield surface f_m.
The initial elastic parameters G_0 and B_0 are determined from the steepest slopes observed in the (q_c versus $\bar{\epsilon}_c$) and (P_c versus ϵ_v^c) plots respectively.

When the stress point reaches the yield surface f_m Fig B.1, the following relations may be obtained:

$$q = \alpha + K \sin\phi \tag{B.2}$$

$$P = \beta + \frac{K}{C} \cos\phi \tag{B.3}$$

From Eqs A.1, A.2, B.2 and B.3 the following stress strain relation can be derived:

$$\frac{\dot{\bar{\epsilon}}}{\dot{q}} = \frac{1}{2G} + \frac{1}{H} \sin\phi\,(\sin\phi + C\gamma\cos\phi) \tag{B.4}$$

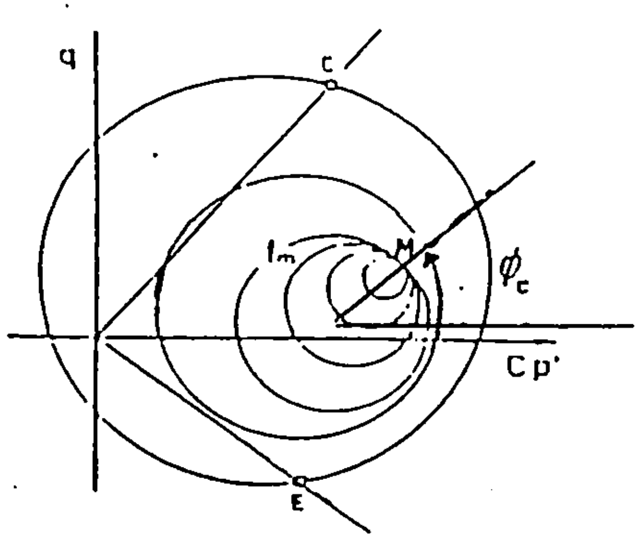

Figure B.1: Geometric representation of the polar angle ϕ.
(From Prevost, 1986)

$$\frac{\dot{\epsilon}_v}{\dot{P}} = \frac{1}{B} + \frac{1}{H}\left(2C\cos\phi + A\sqrt{6}\cos\phi|\tan\phi|\right)\frac{1}{3\gamma}(\sin\phi + C\gamma\cos\phi) \qquad \text{(B.5)}$$

in which :
$\epsilon_v = \epsilon_y + 2\epsilon_x$.
$\bar{\epsilon} = \epsilon_y - \epsilon_x$.
$\gamma = \frac{p'}{q}$.
ϕ is called the polar angle formed at the center of a given yield surface f_m, between the current stress point on this surface and the horizontal axis through the yield surface center which is parallel to the CP' axis in the transformed plot, Fig B.1.

B.3.1 Determination of the Polar Angle

From Fig B.1 one derives the following equations:

$$q_c = \alpha + K\sin\phi_c \qquad \text{(B.6)}$$

$$P_c = \beta + \frac{K}{C}\cos\phi_c \qquad \text{(B.7)}$$

$$q_e = \alpha + K\sin\phi_e \qquad \text{(B.8)}$$

$$P_e = \beta + \frac{K}{C}\cos\phi_e \tag{B.9}$$

Note that the subscripts c and e are used to identify the compression and the extension tests respectively.
Since the model parameters α, β and K depend on the volumetric strain, Eqs B.6, B.7, B.8 and B.9 will be:

$$\sin\phi_c = \frac{q_c - \alpha_0 e^{\lambda\epsilon_v^c}}{K_0 e^{\lambda\epsilon_v^c}} \tag{B.10}$$

$$\sin\phi_e = \frac{q_e - \alpha_0 e^{\lambda\epsilon_v^e}}{K_0 e^{\lambda\epsilon_v^e}} \tag{B.11}$$

$$\cos\phi_c = C\frac{P_c - \beta_0 e^{\lambda\epsilon_v^c}}{K_0 e^{\lambda\epsilon_v^c}} \tag{B.12}$$

$$\cos\phi_e = C\frac{P_e - \beta_0 e^{\lambda\epsilon_v^e}}{K_0 e^{\lambda\epsilon_v^e}} \tag{B.13}$$

From Eqs B.10, B.11, B.12 and B.13 one gets:

$$\sin\phi_c - \sin\phi_e = \frac{q_c e^{\lambda\epsilon_v^e} - q_e e^{\lambda\epsilon_v^c}}{K_0 e^{\lambda(\epsilon_v^c+\epsilon_v^e)}} \tag{B.14}$$

$$\cos\phi_c - \cos\phi_e = \frac{C}{K_0}\left(\frac{P_c e^{\lambda\epsilon_v^e} - P_e e^{\lambda\epsilon_v^c}}{e^{\lambda(\epsilon_v^c+\epsilon_v^e)}}\right) \tag{B.15}$$

Let $RCE = \frac{\cos\phi_c - \cos\phi_e}{\sin\phi_c - \sin\phi_e}$, RCE can be determined from Eqs B.14 and B.15:

$$RCE = C\frac{P_c - P_e e^{\lambda(\epsilon_v^c-\epsilon_v^e)}}{q_c - q_e e^{\lambda(\epsilon_v^c-\epsilon_v^e)}} \tag{B.16}$$

Eq B.16 can be written in the following form:

$$\frac{1}{\tan\phi_c} + \frac{1}{\tan\phi_e} + \left(\frac{2RCE}{1-RCE^2}\right)\left(\frac{1}{\tan\phi_c}\frac{1}{\tan\phi_e} - 1\right) = 0 \tag{B.17}$$

Since the model parameters G, B, h and B' depend on the mean effective stress, the stress strain relations in Eqs B.4 and B.5 will be:

$$\left(\frac{P'}{P'_0}\right)^n \frac{\dot{\epsilon}}{\dot{q}} - \frac{1}{2G_0} = \frac{1}{H_0} sin\phi(\sin\phi + C\gamma\cos\phi) \tag{B.18}$$

$$\left(\frac{P'}{P'_0}\right)^n \frac{\dot{\epsilon}_v}{\dot{P}} - \frac{1}{B_0} = \frac{1}{H_0}(\sin\phi + C\gamma\cos\phi)\frac{1}{3\gamma}(2C\cos\phi + A\sqrt{6}\cos\phi|\tan\phi|) \tag{B.19}$$

in which :

$$H_0 = h_0 + B_0\cos\phi \tag{B.20}$$

Let's consider the following transformations:

$$\left(\frac{P'}{P'_c}\right)^n \frac{\dot{\varepsilon}}{\dot{q}} - \frac{1}{2G_0} = \frac{1}{X} \tag{B.21}$$

$$\left(\frac{P'}{P'_0}\right)^n \frac{\dot{\epsilon}_v}{\dot{P}} - \frac{1}{B_0} = \frac{1}{Y} \tag{B.22}$$

$$T = (\sin\phi + C\gamma\cos\phi) \tag{B.23}$$

Thus, Eqs B.18 and B.19 can be written as follows:

$$\frac{1}{X_c} = \frac{1}{H_0}\sin\phi_c T_c \tag{B.24}$$

$$\frac{1}{Y_c} = \frac{1}{H_0}\frac{T_c}{3\gamma_c}\left(2C\cos\phi_c + A\sqrt{6}\cos\phi_c|\tan\phi_c|\right) \tag{B.25}$$

$$\frac{1}{X_e} = \frac{1}{H_0}\sin\phi_e T_e \tag{B.26}$$

$$\frac{1}{Y_e} = \frac{1}{H_0}\frac{T_e}{3\gamma_e}\left(2C\cos\phi_e + A\sqrt{6}\cos\phi_e|\tan\phi_e|\right) \tag{B.27}$$

From Eqs B.24, B.25, B.26 and B.27 one gets:

$$\frac{1}{\tan\phi_c} = \frac{1}{2C}\left(3\gamma_c\frac{X_c}{Y_c} \pm A\sqrt{6}\right) \tag{B.28}$$

$$\frac{1}{\tan\phi_e} = \frac{1}{2C}\left(3\gamma_e\frac{X_e}{Y_e} \pm A\sqrt{6}\right) \tag{B.29}$$

Note that the sign (+) is used when $tan\phi < 0$ and the sign (-) is used when $tan\phi > 0$.
Adding Eq B.28 and B.29 one gets:

$$\frac{1}{\tan\phi_c} \pm \frac{1}{\tan\phi_e} = \frac{1}{2C}\left(3\gamma_c\frac{X_c}{Y_c} \pm 3\gamma_e\frac{X_e}{Y_e}\right) \tag{B.30}$$

The sign (+) is used when the product $(\tan\phi_c \tan\phi_e) < 0$.
Thus, the two Eqs B.17 and B.30 provide the solution for $tan\phi_c$ and $tan\phi_e$.

B.3.2 Initial Model Parameters

Knowing ϕ_c and ϕ_e the parameters can be obtained .
1. degree of non associativity :

$$A = \frac{1}{\sqrt{6}}\frac{1}{\tan\phi_c}\left(3\gamma_c\frac{X_c}{Y_c}\tan\phi_c - 2C\right) \tag{B.31}$$

2. initial sizes of the yield surfaces :

$$K_0 = \frac{q_c e^{-\lambda \epsilon_v^c} - q_e e^{-\lambda \epsilon_v^e}}{\sin \phi_c - \sin \phi_e} \tag{B.32}$$

3. Initial positions of the yield surfaces :

$$\alpha_0 = q_c e^{-\lambda \epsilon_v^c} - K_0 \sin \phi_c \tag{B.33}$$

$$\beta_0 = P_c e^{-\lambda \epsilon_v^c} - \frac{K_0}{C} \cos \phi_c \tag{B.34}$$

4. Initial value of the parameter B':

$$B_0' = \frac{X_c \sin \phi_c T_c - X_e \sin \phi_e T_e}{\cos \phi_c - \cos \phi_e} \tag{B.35}$$

5. initial plastic shear modulus :

$$h_0 = X_c \sin \phi_c T_c - B_0' \cos \phi_c \tag{B.36}$$

6. Initial plastic moduli :

$$H_0 = h_0 + B_0' \cos \phi_c \tag{B.37}$$

B.4 Undrained Model Parameters

In an undrained case, $\epsilon_v = 0$, the model parameters are determined from the condition of the equal slopes of both compression and extension triaxial curves when the stress point reaches a yield surface f_m. Knowing ϕ_c and ϕ_e, the model parameters are determined from Eqs B.31 to B.37 with the condition that $\epsilon_v^c = \epsilon_v^e = 0$.

B.5 Computer Program PARAMETER

In the following, PARAMETER listing and examples of input data and output results are presented. The control parameters used in the master cards are defined in the manual presented at the beginning of the program listing.

B.5.1 Example of Input Data

In the following, the compression and extension test results used for the determination of the model parameters, correspond to the test shown in Fig 7.4, are presented as an example of input data:

```
FILE: PARAMETE DATA      *   UNIV D'/OF OTTAWA CMS

1,84.193,11,1,137.89, 137.89
 0.     ,   137.89 , 0.          ,  0.
49.56   ,   154.41 , 0.000300    ,   0.001755
84.43   ,   166.03 , 0.000980    ,   0.00336
122.07  ,   178.58 , 0.001950    ,   0.006915
168.08  ,   193.92 , 0.003720    ,   0.01431
234.69  ,   216.12 , 0.006830    ,   0.0449
247.33  ,   220.33 , 0.007080    ,   0.053505
259.06  ,   224.24 , 0.007320    ,   0.062535
280.10  ,   231.26 , 0.007410    ,   0.080565
297.28  ,   236.98 , 0.007810    ,   0.108625
303.    ,   238.89 , 0.00781     ,   0.131095
 0.     ,   137.89 , 0.         ,  0.
-5.00   ,   136.22 , 0.00030    , -0.000177
-10.50  ,   134.49 , 0.00050    , -0.000430
-15.20  ,   132.82 , 0.00120    , -0.00091
-22.50  ,   130.39 , 0.0025     , -0.00230
-34.00  ,   126.56 , 0.00466    , -0.00734
-42.00  ,   123.89 , 0.00465    , -0.01280
-49.00  ,   121.56 , 0.0050     , -0.0182
-54.00  ,   119.89 , 0.00515    , -0.0224
-65.00  ,   116.22 , 0.0054     , -0.04037
-87.        108.69 , 0.0048     , -0.1518
```

B.5.2 Example of Output Results

In the following, the results of the data shown in Section B.5.1 are presented as an example of output results:

```
                         MODEL PARAMETERS
                         ****************

          CONTROL INFORMATION
          -------------------

      Test type.................. 1
           Drained CTC test........1
           Undrained CTC test......2
      SOIL TYPE.................. 1
           SAND .....................1
           CLAY .....................2
      NUMBER OF YIELD SURFACES...  11
      VOLUMETRIC EXPONENT.........  84.19
      INITIAL MEAN PRESSURE.........137.89
```

INPUT COMPRESSION TEST DATA

Q	P	EPY	EPX	EPV	EPY-EPX
0.00	137.89	0.0000	0.0000	0.0000	0.0000
49.56	154.41	0.1270	-0.0485	0.0300	0.1755
84.43	166.03	0.2567	-0.0793	0.0980	0.3360
122.07	178.58	0.5260	-0.1655	0.1950	0.6915
168.08	193.92	1.0780	-0.3530	0.3720	1.4310
234.69	216.12	3.2210	-1.2690	0.6830	4.4900
247.33	220.33	3.8030	-1.5475	0.7080	5.3505
259.06	224.24	4.4130	-1.8405	0.7320	6.2535
280.10	231.26	5.6180	-2.4385	0.7410	8.0565
297.28	236.98	7.5020	-3.3605	0.7810	10.8625
303.00	238.89	9.0000	-4.1095	0.7810	13.1095

INPUT EXTENSION TEST DATA

QE	PE	EPY	EPX	EPV	EPY-EPX
0.00	137.89	0.0000	0.0000	0.0000	0.0000
-5.00	136.22	-0.0018	0.0159	0.0300	-0.0177
-10.50	134.49	-0.0120	0.0310	0.0500	-0.0430
-15.20	132.82	-0.0207	0.0703	0.1200	-0.0910
-22.50	130.39	-0.0700	0.1600	0.2500	-0.2300
-34.00	126.56	-0.3340	0.4000	0.4660	-0.7340
-42.00	123.89	-0.6983	0.5817	0.4650	-1.2800
-49.00	121.56	-1.0467	0.7733	0.5000	-1.8200
-54.00	119.89	-1.3217	0.9183	0.5150	-2.2400
-65.00	116.22	-2.5113	1.5257	0.5400	-4.0370
-87.00	108.69	-9.9600	5.2200	0.4800	-15.1800

POLAR ANGLES

	compression degrees	extension degrees
2	89.72	-70.82
3	16.32	-76.40
4	28.36	-87.66
5	40.71	262.27
6	54.39	253.01
7	63.62	244.64
8	61.44	244.60
9	61.38	242.80
10	61.49	242.44
11	63.28	243.11

INITIAL MODEL PARAMETERS

G0 = 14119.66   B0 = 55066.69   n = .50   lambda = 84.19

	ALPHA	BETA	K	H	B	A
2	20.96	150.50	27.36	0.54E+06	-.11E+08	0.20
3	58.05	121.18	70.08	0.99E+05	-.84E+05	-4.67
4	65.78	118.53	79.59	0.15E+05	-.92E+04	-2.81
5	66.87	111.09	85.88	0.69E+04	-.25E+04	-1.70
6	60.83	97.56	87.62	0.25E+04	-.12E+04	-1.12
7	54.29	102.23	91.50	0.16E+04	-.54E+03	-0.83
8	55.06	99.32	96.56	0.14E+04	-.50E+03	-0.92
9	58.16	100.27	104.74	0.12E+04	-.48E+03	-0.95
10	56.82	97.89	110.63	0.62E+03	-.24E+03	-0.93
11	49.38	98.24	120.48	0.23E+03	-.37E+02	-0.87

CTC, MODEL PARAMETERS

GO = 14119.66 BO = 55066.69 n = .50 lambda = 84.19

	ALPHA	BETA	Km	Hm	Bm	Am
2	21.50	154.35	28.06	0.57E+06	-.11E+08	0.20
3	63.04	131.60	76.11	0.11E+06	-.93E+05	-4.67
4	77.52	139.68	93.79	0.17E+05	-.10E+05	-2.81
5	91.47	151.94	117.47	0.81E+04	-.29E+04	-1.70
6	108.10	173.38	155.71	0.32E+04	-.15E+04	-1.12
7	98.54	185.55	166.08	0.20E+04	-.68E+03	-0.83
8	101.98	183.94	178.84	0.17E+04	-.64E+03	-0.92
9	108.53	187.13	195.45	0.16E+04	-.62E+03	-0.95
10	109.66	188.94	213.51	0.82E+03	-.32E+03	-0.93
11	95.30	189.61	232.53	0.30E+03	-.48E+02	-0.87

CTE, MODEL PARAMETERS

GO = 14119.66 BO = 55066.69 n = .50 lambda = 84.19

	ALPHA	BETA	Km	Hm	Bm	Am
2	21.50	154.35	28.06	0.54E+06	-.11E+08	0.20
3	60.54	126.39	73.10	0.98E+05	-.83E+05	-4.67
4	72.77	131.13	88.05	0.15E+05	-.90E+04	-2.81
5	82.54	137.11	106.00	0.67E+04	-.24E+04	-1.70
6	90.05	144.43	129.71	0.24E+04	-.11E+04	-1.12
7	80.31	151.22	135.35	0.15E+04	-.51E+03	-0.83
8	83.88	151.30	147.10	0.13E+04	-.47E+03	-0.92
9	89.72	154.70	161.59	0.11E+04	-.45E+03	-0.95
10	89.52	154.24	174.30	0.57E+03	-.22E+03	-0.93
11	73.97	147.16	180.47	0.20E+03	-.33E+02	-0.87

B.5.3 PARAMETER Listing

```
C
C                          PARAMETER  listing
C
C-----------------------------------------------------------------------
C
C  Parameter is a computer code which allows the determination of
C  Prevost's model parameters from  conventioanl triaxial compression
C  and extension tests. The program incorporates drained and
C  undrained versions for both sand and clay. Using the test results
C  of a given CIC-CIE tests, the program permits the predictions
C  of the initial model parameters for any other tests.
C
C
C                               INPUT DATA
C                               **********
C   Input 1
C   -------      CD - Drainage conditions  Drained CIC test - 1
C                                          Undrained CIC test - 2
C                ST - Soil type  Sand - 1
C                                Clay - 2
C                NYS - Number of yield surfaces
C
C                W - Isotropic parameter, Lambda
C
C                PO - Initial confining pressure
C
C                HPP- Initial confining pressure of the predicted test
C
C
C   Input 2                     -------
C   -------      Input of the triaxial compression test results
C                QC  -  Deviatoric stress
C                PC  -  Hydrostatic stress
C                EPD -  Deviatoric strain
C                EPV -  Volumetric strain
C
C
C   Input 3                     -------
C   -------      Input of the triaxial extension test results
C                QE    -  Deviatoric stress
C                PE    -  Hydrostatic stress
C                EPDE  -  Deviatoric strain
C                EPVE  -  Volumetric strain
C
C
C
C-----------------------------------------------------------------------
C
      INTEGER I,J,NYS,ST,CT,CD,CTR
      REAL*8 W,C,M,L,PO,GO,BO,HPP
      DIMENSION QC(20),PC(20),EPX(20),EPY(20),EPZ(20),EPV(20),EPD(20)
      DIMENSION DQC(20),DPC(20),RC(20),DEPD(20),DEPV(20)
      DIMENSION QE(20),PE(20),EPXE(20),EPYE(20),EPZE(20),EPVE(20)
      DIMENSION EPDE(20),DQE(20),DPE(20),RE(20),DEPDE(20),DEPVE(20)
      DIMENSION X1(20),X2(20),X3(20),X4(20),X5(20),X6(20)
      DIMENSION XC1(20),YC1(20),XE1(20),YE1(20)
      DIMENSION XC(20),YC(20),XE(20),YE(20)
      DIMENSION A(20),RCE(20),RCE1(20),RCE2(20),T(20),S(20),S1(20)
      DIMENSION A1(20),TS(20),TS1(20),DEL1(20),DEL2(20),U(20),V(20)
      DIMENSION A2(20),OC(20),OE(20),TC(20),TE(20)
      DIMENSION DE(20),RR(20),AD(20),GI(20),AO(20),UA(20),TT(20),AH(20)
      DIMENSION BM(20),PH(20),AM(20),XK(20),TT1(20)
      DIMENSION ALPO(20),BETO(20),ALP(20),BET(20),OK(20)
      DIMENSION ALPE(20),BETE(20),XKE(20)
      DIMENSION EBM(20),EPH(20),PBM(20),PPH(20)
```

```
      DIMENSION U1(20),V1(20),SS(20),AHH(20)
C
C-----------------------------------------------------------------------
C              1.   Control Input
C-----------------------------------------------------------------------
      WRITE(6,9777)
 9777 FORMAT('1',//35X,' MODEL PARAMETERS         ',3X/35X,19('*')//)
C
      WRITE(6,9998)
 9998 FORMAT(//19X,'CONTROL INFORMATION',3X/19X,19('-')/)
C
      C=3/(2**.5)
      READ(5,*) CD,W,NYS,ST,PO,HPP
C
      WRITE(6,1000) CD,ST,NYS,W,HPP
 1000 FORMAT(/15X,'Test type',18('.'),I3/20X,'Drained CTC test',
     18('.'),'1',2X/20X,'Undrained CTC test',6('.'),'2',2X/3X,
     212X,'SOIL TYPE',18('.'),I3/20X,'SAND    ',20('.'),'1',
     32X/20X,'CLAY ',21('.'),'2',3X,
     4/15X,'NUMBER OF YIELD SURFACES',3('.'),I5/15X,
     5'VOLUMETRIC EXPONENT',9('.'),F8.2/15X,'INITIAL MEAN PRESSURE',
     69('.'),F6.2)
C
C-----------------------------------------------------------------------
C          2.   Compression  Test Data
C-----------------------------------------------------------------------
C
      WRITE(6,9997)
 9997 FORMAT(//19X,' INPUT COMPRESSION TEST DATA',1X/19X,29('-'),
     11X//10X,'Q',10X,'P',9X,'EPY',8X,'EPX',8X,'EPV',8X,
     2'EPY-EPX',2X/5X,73('.'))
      DO 10 I=1,NYS
      READ(5,*) QC(I),PC(I),EPV(I),EPD(I)
      EPY(I)=(EPV(I)+2*EPD(I))/3
      EPX(I)=EPY(I)-EPD(I)
C
      WRITE(6,1010) QC(I),PC(I),EPY(I)*100,EPX(I)*100,EPV(I)*100,EPD(I)
     1*100
 1010 FORMAT(5X,2(F9.2,2X),F9.4,2X,F9.4,3X,F9.4,3X,F9.4)
   10 CONTINUE
C
      DO 11 I=2,NYS
      DQC(I)=QC(I)-QC(I-1)
      DPC(I)=PC(I)-PC(I-1)
      RC(I)=DPC(I)/DQC(I)
      DEPD(I)=EPD(I)-EPD(I-1)
      DEPV(I)=EPV(I)-EPV(I-1)
   11 CONTINUE
C
C-----------------------------------------------------------------------
C          3.   Extension  Test Data
C-----------------------------------------------------------------------
C
      WRITE(6,9996)
 9996 FORMAT(//19X,' INPUT EXTENSION  TEST DATA ',1X/19X,29('-'),
     11X//10X,'QE',9X,'PE',8X,'EPY',7X,'EPX',9X,'EPV',
     29X,'EPY-EPX',2X/5X,73('.'))
C
      DO 15 I=1,NYS
      READ(5,*) QE(I),PE(I),EPVE(I),EPDE(I)
      EPYE(I)=(EPVE(I)+2*EPDE(I))/3
      EPXE(I)=EPYE(I)-EPDE(I)
C
      WRITE(6,1020) QE(I),PE(I),EPYE(I)*100,EPXE(I)*100,EPVE(I)*100,
     1EPDE(I)*100
 1020 FORMAT(5X,2(F9.2,2X),F9.4,2X,F9.4,3X,F9.4,3X,F9.4)
   15 CONTINUE
C
```

```
      DO 16 I=2,NYS
      DQE(I)=QE(I)-QE(I-1)
      DPE(I)=PE(I)-PE(I-1)
      RE(I)=DPE(I)/DQE(I)
      DEPDE(I)=EPDE(I)-EPDE(I-1)
      DEPVE(I)=EPVE(I)-EPVE(I-1)
   16 CONTINUE
C
C-----------------------------------------------------------------------
C         4.   Elastic Parameters
C-----------------------------------------------------------------------
C
      AN=1.
      IF(ST.EQ.1) AN=.5
      ZE=(HPP/PO)**AN
      GO=.5*ZE*(QC(2)/EPD(2))
      IF(CD.EQ.2) GOTO 122
      BO=ZE*DPC(2)/EPV(2)
      GOTO 113
C122  BO=8*ZE*GO/3
  122 BO=8*GO/3
  113 M=1/(2*GO)
      L=1/BO
C
C-----------------------------------------------------------------------
C         5.   Polar Angles
C-----------------------------------------------------------------------
C
      WRITE(6,1901)
 1901 FORMAT('1',24X,'POLAR ANGLES',2X/24X,13('-'),1X)
      WRITE(6,1902)
 1902 FORMAT(19X,'compression',10X,'extension',4X/14X,
     15X,'degrees',14X,'degrees',2X/13X,38('-')/)
C
      DO 20 I=2,NYS
C
C
C  5.1 Transformation of the stress-strain relations
C      ---------------------------------------------
C
      AN=1.
      IF(ST.EQ.1) AN=.5
C
      X1(I)=( PC(I)/(PO) )**AN
      X2(I)=DEPD(I)/(ZE*DQC(I))
      X3(I)=DEPV(I)/(ZE*DPC(I))
      X4(I)=( PE(I)/(PO) )**AN
      X5(I)=DEPDE(I)/(ZE*DQE(I))
      X6(I)=DEPVE(I)/(ZE*DPE(I))
      XC1(I)=X1(I)*X2(I)-M
      XC(I)=1/XC1(I)
      YC1(I)=X1(I)*X3(I)-L
      YC(I)=1/YC1(I)
      XE1(I)=X4(I)*X5(I)-M
      XE(I)=1/XE1(I)
      YE1(I)=X4(I)*X6(I)-L
      YE(I)=1/YE1(I)
C
      A(I)=EXP(W*(EPV(I)-EPVE(I)))
      A1(I)=EXP(W*(EPV(I)))
      A2(I)=EXP(W*(EPVE(I)))
C
      RCE1(I)=PC(I)-PE(I)*A(I)
      RCE2(I)=QC(I)-QE(I)*A(I)
      RCE(I)=C*RCE1(I)/RCE2(I)
C
C  5.2 Solve for the polar angles
C      ---------------------------
```

```
C
      T(I)=2*RCE(I)/(1-RCE(I)*RCE(I))
      S(I)=((3*RC(I)*XC(I)/YC(I))+(3*RE(I)*XE(I)/YE(I)))/(2*C)
      SS(I)=(T(I)-S(I))/(T(I))
      IF(SS(I).GT.0) GOTO 50
C
C  5.2.1   First solution
C
C
      CTR=1
      TS(I)=T(I)*S(I)
      DEL1(I)=(TS(I)**2)-4*T(I)*(T(I)-S(I))
      U1(I)=(TS(I)+SQRT(DEL1(I)))/(2*T(I))
      V1(I)=(T(I)-S(I))/(T(I)*U1(I))
C
      IF(U1(I).GT.0) GOTO 61
      GOTO 66
   61 IF(V1(I).LT.0) GOTO 55
C
   66 U1(I)=(TS(I)-SQRT(DEL1(I)))/(2*T(I))
      V1(I)=(T(I)-S(I))/(T(I)*U1(I))
      GOTO 55
C
C  5.2.2    2nd solution
C
C
   50 CTR=2
      S1(I)=((3*RC(I)*XC(I)/YC(I))-(3*RE(I)*XE(I)/YE(I)))/(2*C)
      TS1(I)=T(I)*S1(I)
      DEL2(I)=SQRT((2-TS1(I))**2 + 4*T(I)*(T(I)+S1(I)))
      U1(I)=(-2+TS1(I)+DEL2(I))/(2*T(I))
      V1(I)=-S1(I)+U1(I)
C
      IF(U1(I).GT.0) GOTO 62
      GOTO 67
   62 IF(V1(I).GT.0) GOTO 55
C
C  5.2.3    Check for overlaping
C
C
   67 U1(I)=(-2+TS1(I)-DEL2(I))/(2*T(I))
      V1(I)=-S1(I)+U1(I)
      IF(U1(I).GT.0.) GOTO 55
      CTR=3
      U1(I)=(-2+TS1(I)+DEL2(I))/(2*T(I))
      V1(I)=-S1(I)+U1(I)
C
C  5.2.4 Angular transformation
C
C
   55 BB=180/3.141592654
C
      OC(I)=ATAN(1/U1(I))
      OE(I)=ATAN(1/V1(I))
      IF(CTR.EQ.1) GOTO 13
      IF(CTR.NE.3) GOTO 77
      OC(I)=OC(I)
      OE(I)=OE(I)
      GOTO 13


   77 OC(I)=OC(I)
      OE(I)=3.141592654+OE(I)

   13 IF(CTR.EQ.1) OC(I)=1.5708-OC(I)
C
C  5.3      Print out of the polar angles
C
```

```
C
      WRITE(6,3) I,OC(I)*BB,OE(I)*BB
    3 FORMAT(10X,I5,4X,F7.2,14X,F7.2)
C
C
C  5.4 Elimination of the effect of volumetric strains
C
C
      AO(I)=OC(I)*EXP(-W*EPV(I))
      UA(I)=OE(I)*EXP(-W*EPVE(I))
      TT(I)=PC(I)*EXP(-W*EPV(I))
C
      FOM = (HPP/PO)
C
C-----------------------------------------------------------------------
C        6.   Plastic Parameters
C-----------------------------------------------------------------------
C
C     6.1. INITIAL SIZES OF THE YIELD SURFACES
C
      RR(I)=SIN(OC(I))-SIN(OE(I))
      OK(I)=( AO(I)-UA(I))/(RR(I) )
C
C     6.2. INITIAL POSITIONS OF THE YIELD SURFACE
C
      ALPO(I)=FOM*( AO(I)-OK(I)*SIN(OC(I)) )
      BETO(I)=FOM*(TT(I)-(OK(I)/C)*COS(OC(I)))
C
      OK(I)=FOM*( OK(I) )
C
      TC(I)=SIN(OC(I))+C*RC(I)*COS(OC(I))
      TE(I)=SIN(OE(I))+C*RE(I)*COS(OE(I))
C
C     6.3. PLASTIC BULK MODULUS
C
      DE(I)=COS(OC(I))-COS(OE(I))
      AH(I)=(XC(I)*SIN(OC(I))*TC(I))-(XE(I)*SIN(OE(I))*TE(I))
      BM(I)=AH(I)/DE(I)
C
C     6.4. PLASTIC SHEAR MODULUS
C
      PH(I)=(XC(I)*SIN(OC(I))*TC(I)-BM(I)*COS(OC(I)))

C
C     6.5. DEGREE OF NON-ASSOCIATIVITY
C
      AD(I)=3*RC(I)*XC(I)*TAN(OC(I))/YC(I)
      GI(I)=1/(ABS(TAN(OC(I))))
      AM(I)=(1/(6**.5))*GI(I)*(AD(I)-2*C)
C
      AHH(I)=PH(I)+BM(I)*COS(OC(I))
   20 CONTINUE
C***********************************************************************
C
C                 7.  PRINT OUT OF THE MODEL PARAMETERS
C
C***********************************************************************
C
C
C                  7.1    INITIAL MODEL PARAMETERS
C
C
      WRITE(6,9900)
 9900 FORMAT(//,30X,'INITIAL MODEL PARAMETERS',4X/29X,26('-')//)
C
      WRITE(6,9990) GO,BO,AN,W
 9990 FORMAT(9X,'GO = ',F9.2,5X,'BO = ',F9.2,5X,'n = ',F3.2,5X,
     1'lambda = ',F8.2,5X/)
```

```
      WRITE(6,9905)
 9905 FORMAT(8X,'ALPHA',10X,'BETA',10X,' K      ',4X,'  H     ',6X,' B   ',
     17X,'  A   ',3X/3X,75('-'),3X/)
C
      DO 500 I=2,NYS
      WRITE(6,600) I,ALPO(I),BETO(I),OK(I),PH(I),BM(I),AM(I)
  500 CONTINUE
  600 FORMAT(I5,2X,F7.2,5X,2(F8.2,6X),2(E8.2,4X),F9.2)
C
      IF(CD.EQ.2) GOTO 9999
      IF(PO.NE.HPP) GOTO 9999
C
C                 7.2   MODEL PARAMETERS, CTC test
C
      WRITE(6,9300)
 9300 FORMAT('1',//,30X,' CTC, MODEL PARAMETERS',4X/10X,
     119X,24('-')//)
C
      WRITE(6,9990) G0,B0,AN,W
C
      WRITE(6,9915)
 9915 FORMAT(8X,'ALPHA',10X,'BETA',10X,' Km     ',4X,'  Hm    ',6X,' Bm ',
     17X,'  Am ',3X/3X,75('-'),3X/)
      DO 510 I=2,NYS
      ALP(I)=ALPO(I)*A1(I)
      BET(I)=BETO(I)*A1(I)
      XK(I)=OK(I)*A1(I)
      PBM(I)=BM(I)*X1(I)
      PPH(I)=PH(I)*X1(I)
      WRITE(6,600) I,ALP(I),BET(I),XK(I),PPH(I),PBM(I),AM(I)
  510 CONTINUE
C
C                 7.3   MODEL PARAMETERS, CTE test
C
      WRITE(6,9400)
 9400 FORMAT(//,30X,' CTE, MODEL PARAMETERS',4X/10X,
     119X,24('-')//)
C
      WRITE(6,9990) G0,B0,AN,W
C
      WRITE(6,9915)
C
      DO 511 I=2,NYS
      ALPE(I)=ALPO(I)*A2(I)
      BETE(I)=BETO(I)*A2(I)
      XKE(I)=OK(I)*A2(I)
      EBM(I)=BM(I)*X4(I)
      EPH(I)=PH(I)*X4(I)
      WRITE(6,600) I,ALPE(I),BETE(I),XKE(I),EPH(I),EBM(I),AM(I)
  511 CONTINUE
C
 9999 STOP
      END
```

Appendix C

LABORATORY TESTING

This Appendix presents the results of laboratory tests discussed in Chapter 5. In the figures, all stresses are effective. Compressive stresses and expansive volumetric strains are indicated as positive.

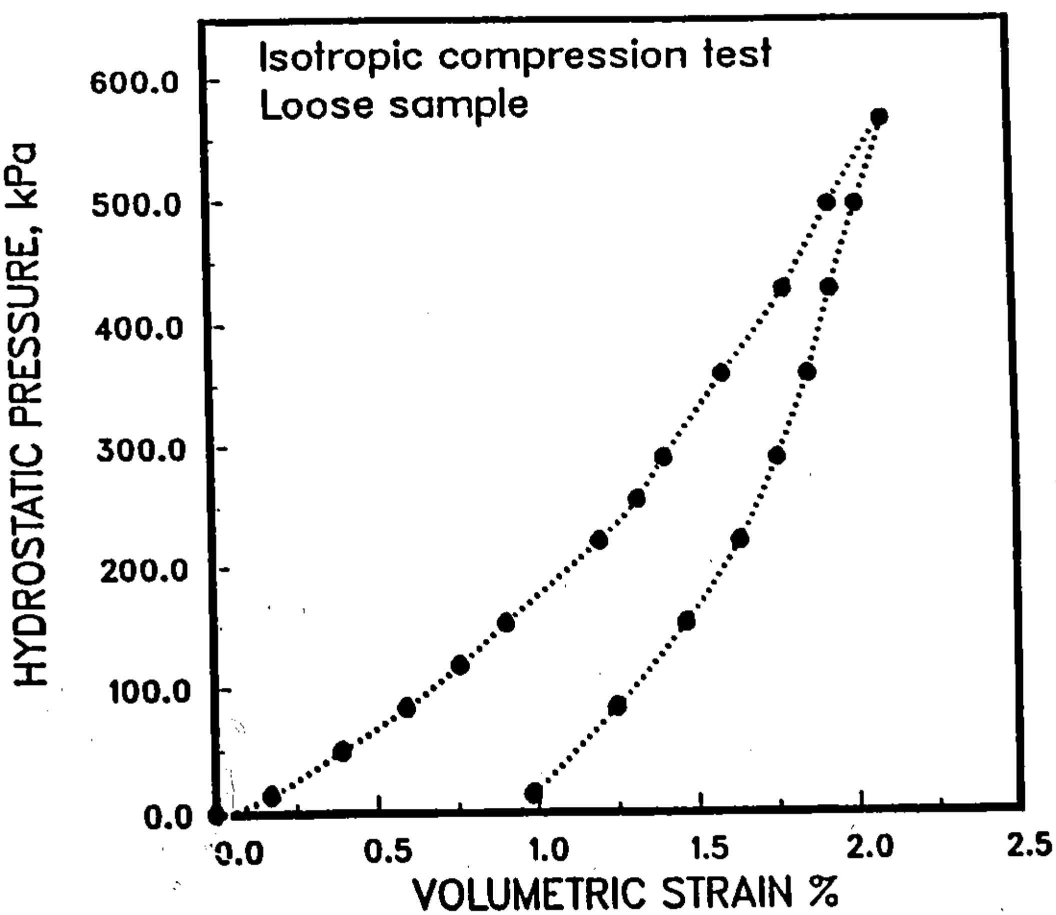

Figure C.1: Isotropic compression test, loose soil sample.

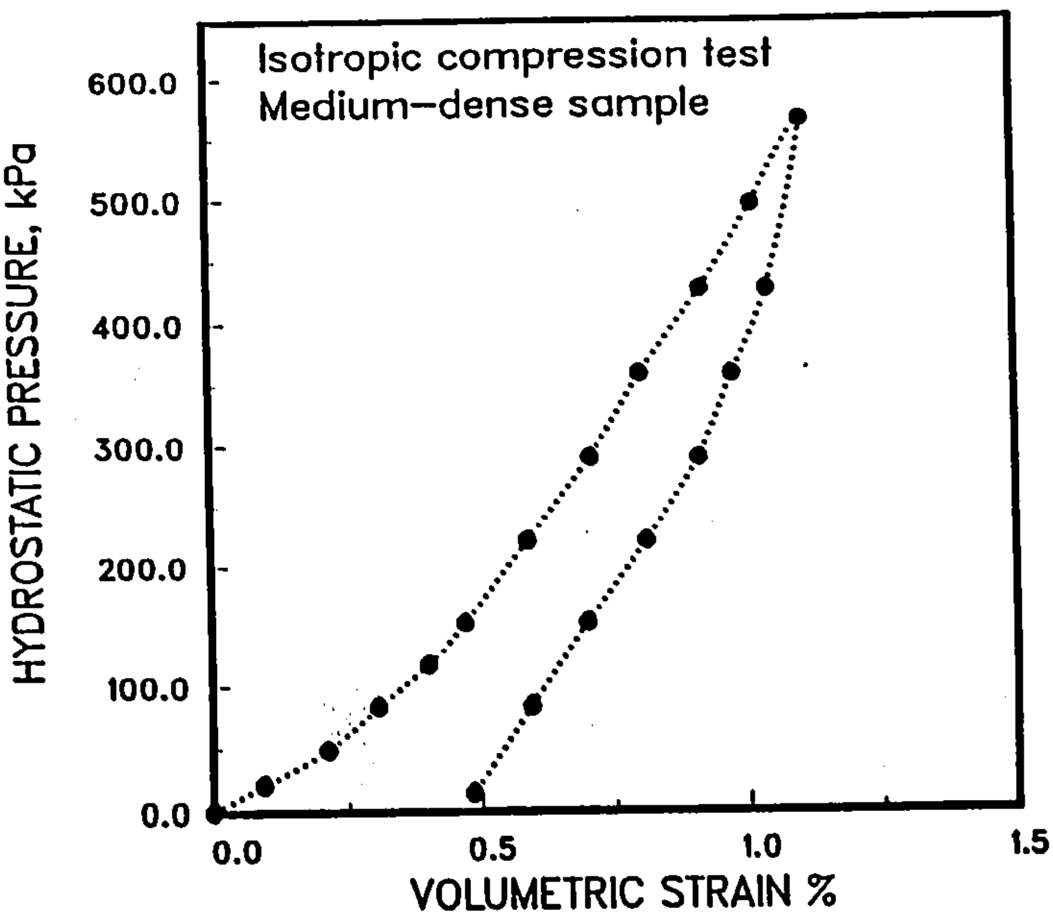

Figure C.2: Isotropic compression test, medium-dense soil sample.

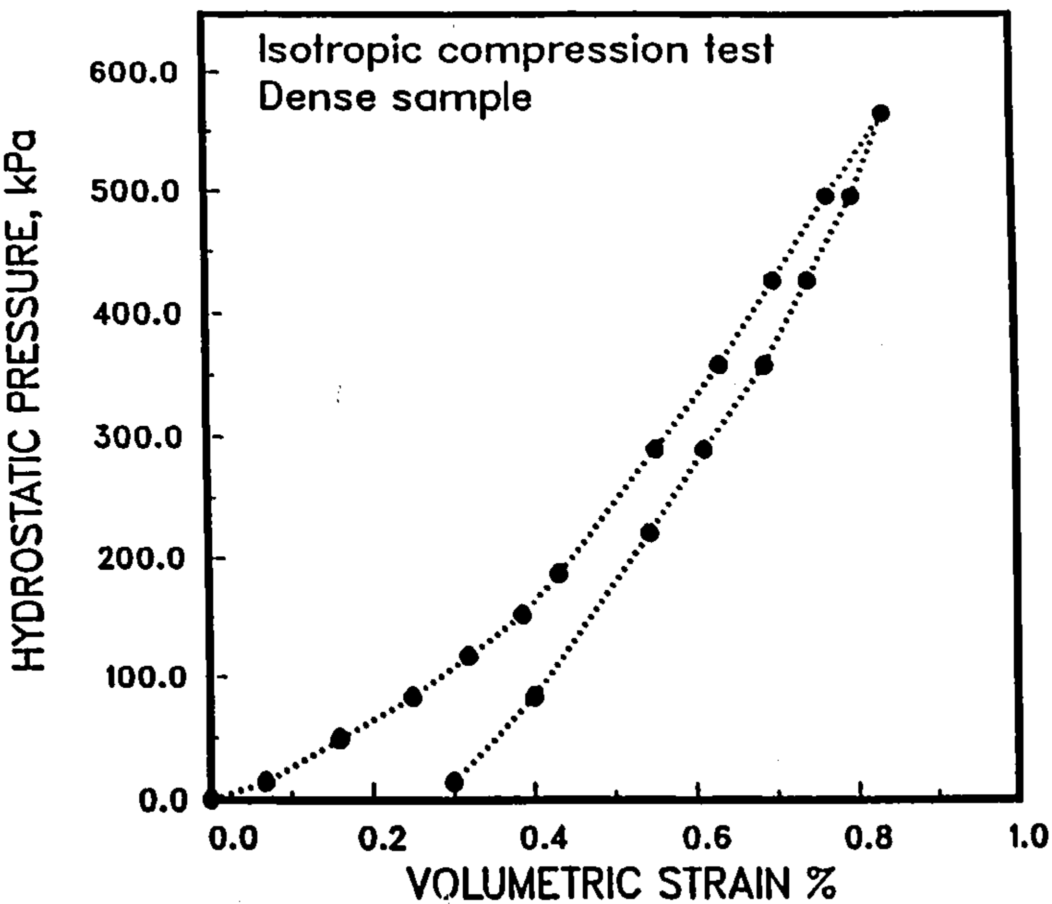

Figure C.3: Isotropic compression test, dense soil sample.

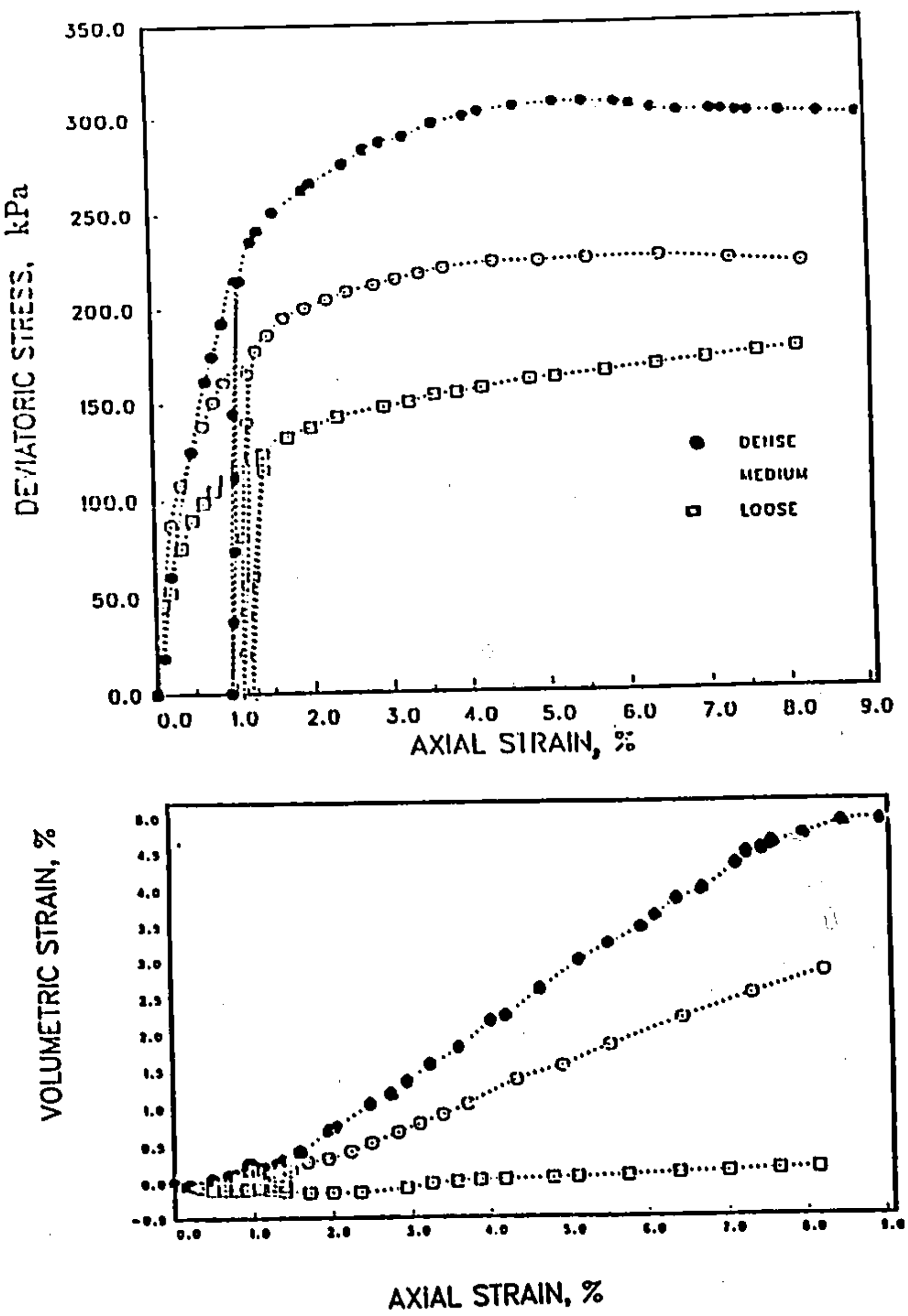

Figure C.4: Drained CTC tests, effect of the initial density, $\dot{\sigma}_3 = 68.94$. kPa

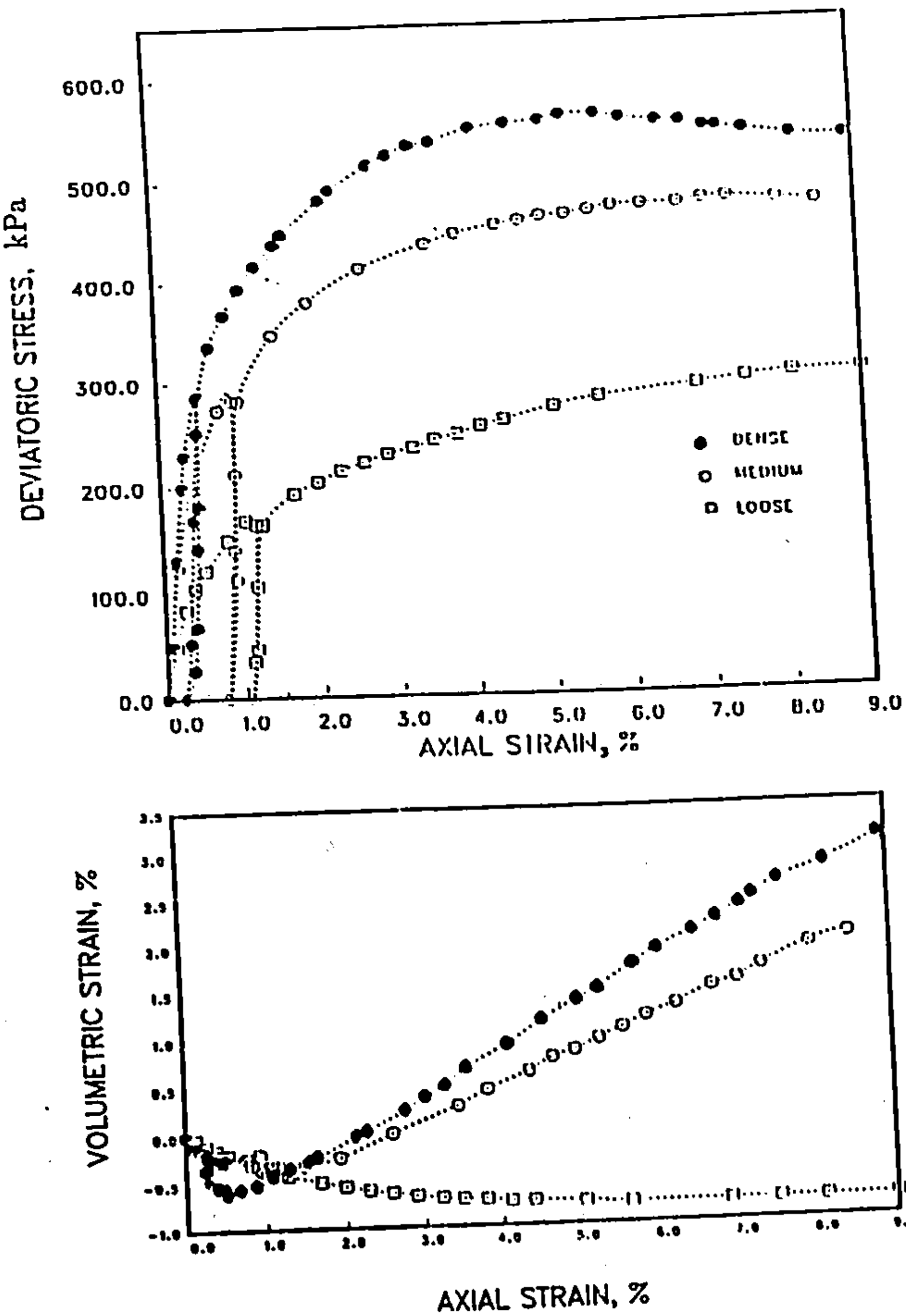

Figure C.5: Drained CTC tests, effect of the initial density, $\sigma_3 = 137.8kPa$

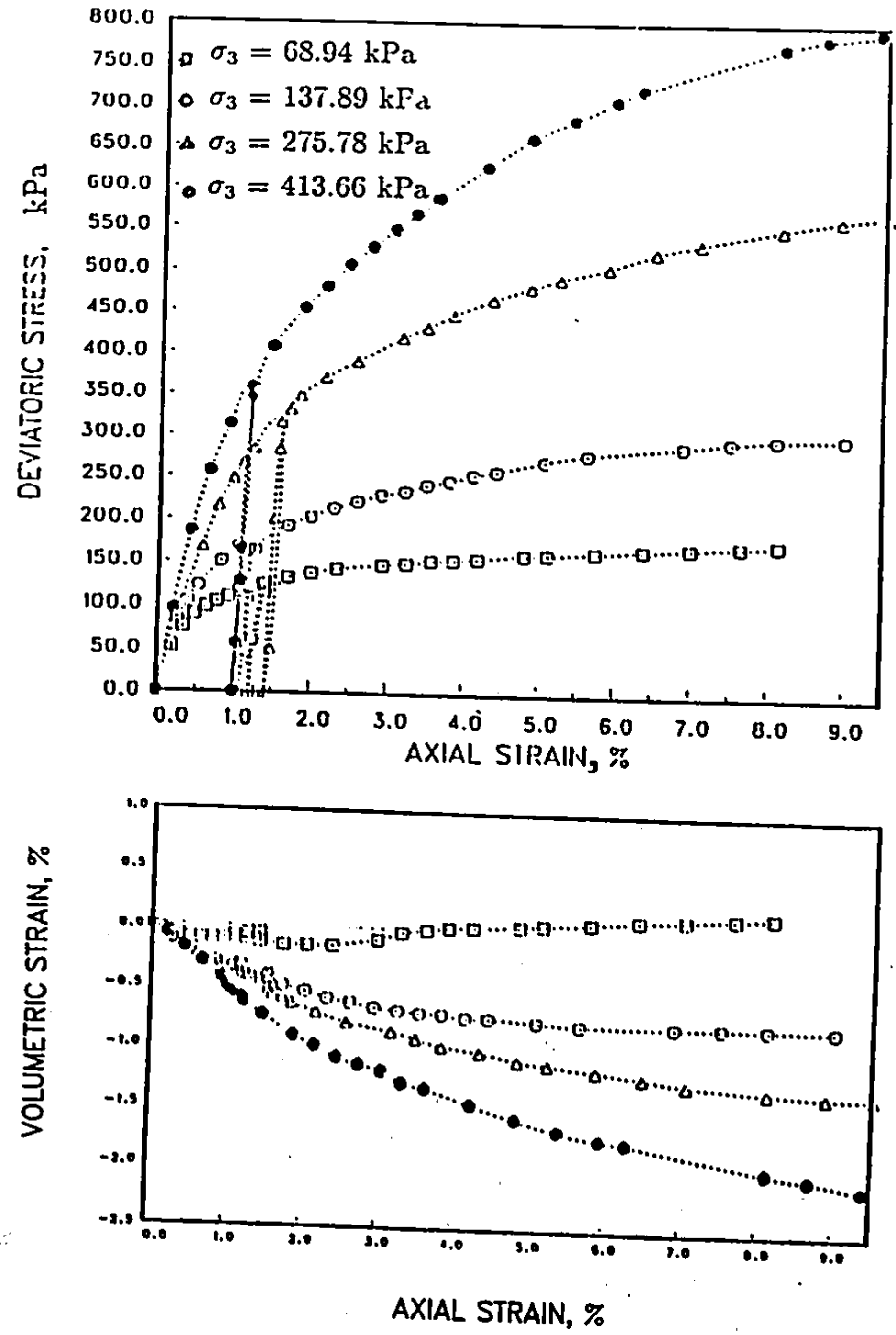

Figure C.6: Drained CTC tests, loose soil samples.

a) Shear stress-strain curves.

b) Axial strain-volumetric strain curves.

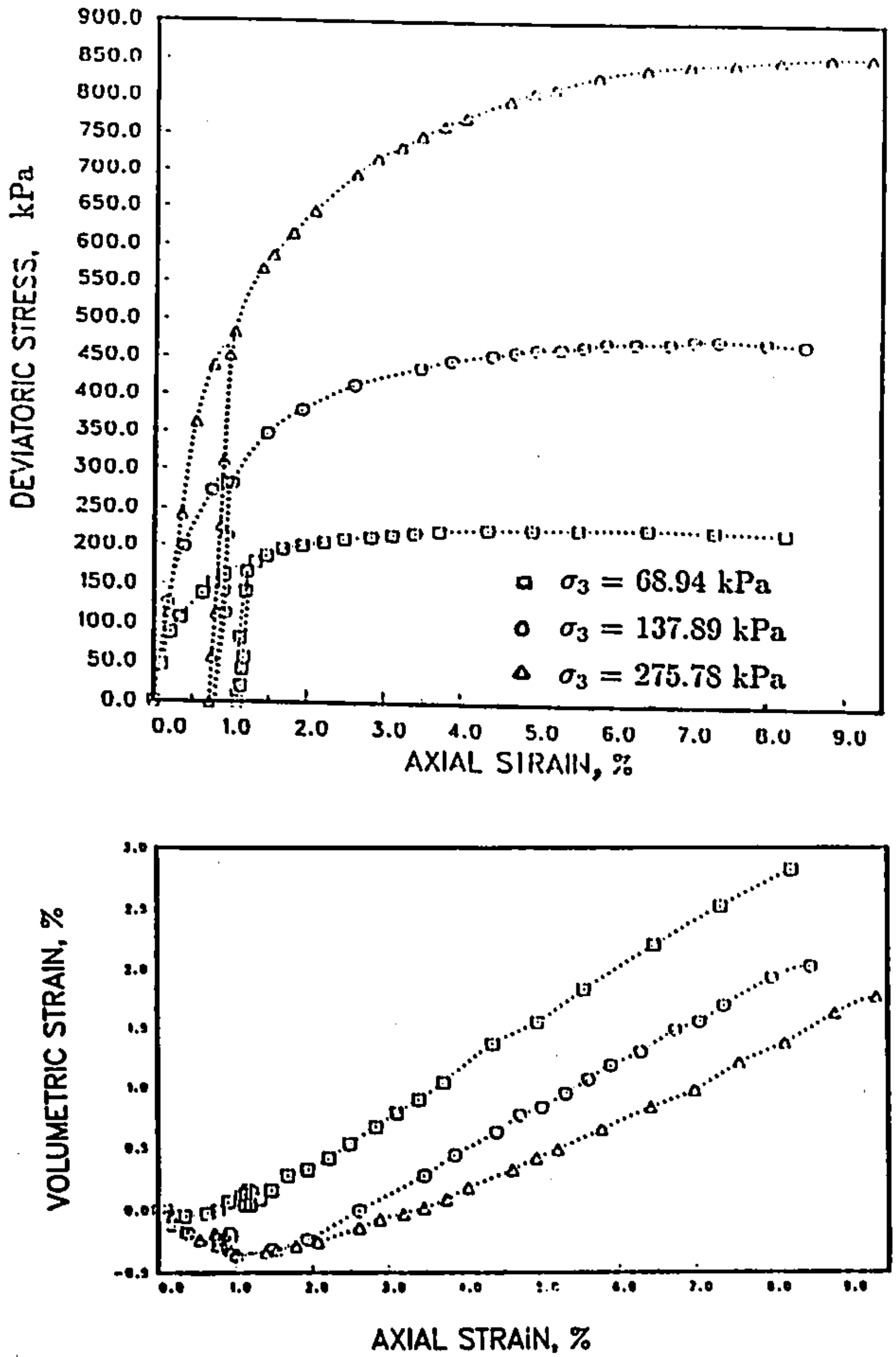

Figure C.7: Drained CTC tests, medium-dense soil samples.

a) Shear stress-strain curves.

b) Axial strain-volumetric strain curves.

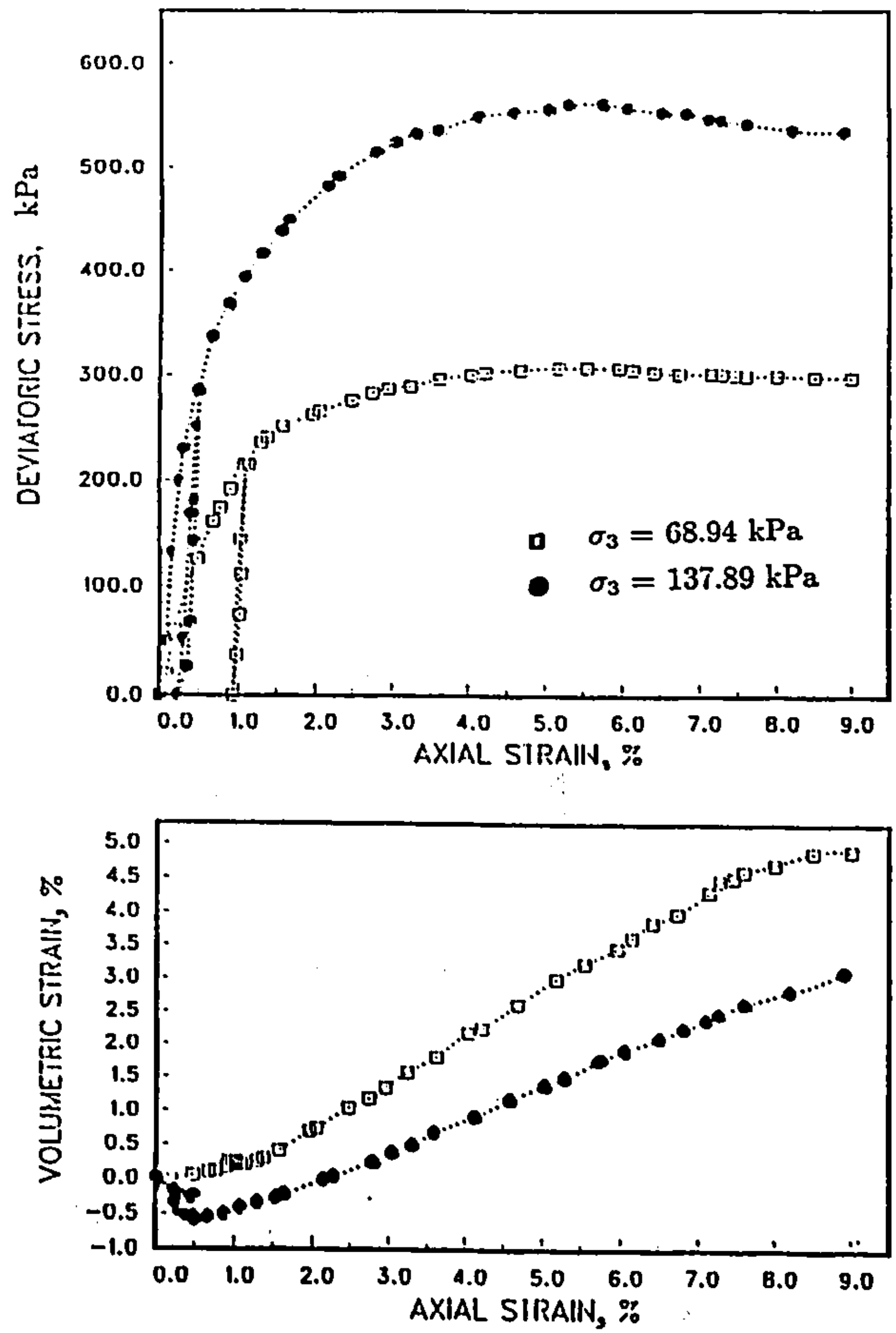

Figure C.8: Drained CTC tests, dense soil samples.
a) Shear stress-strain curves.
b) Axial strain-volumetric strain curves.

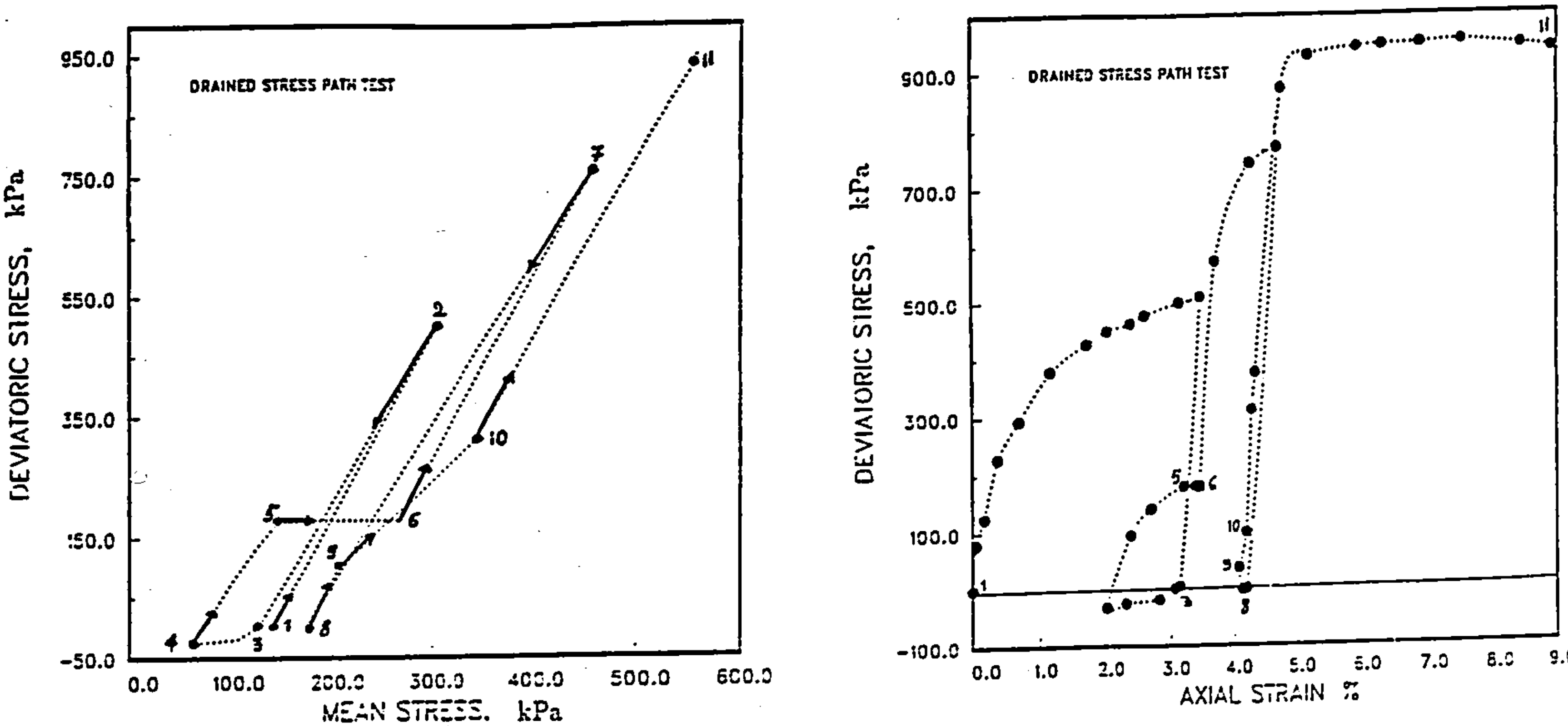

Figure C.9: Drained stress path test.
a) Path followed in ($q - P'$) stress subspace.
b) Shear stress-strain curve.

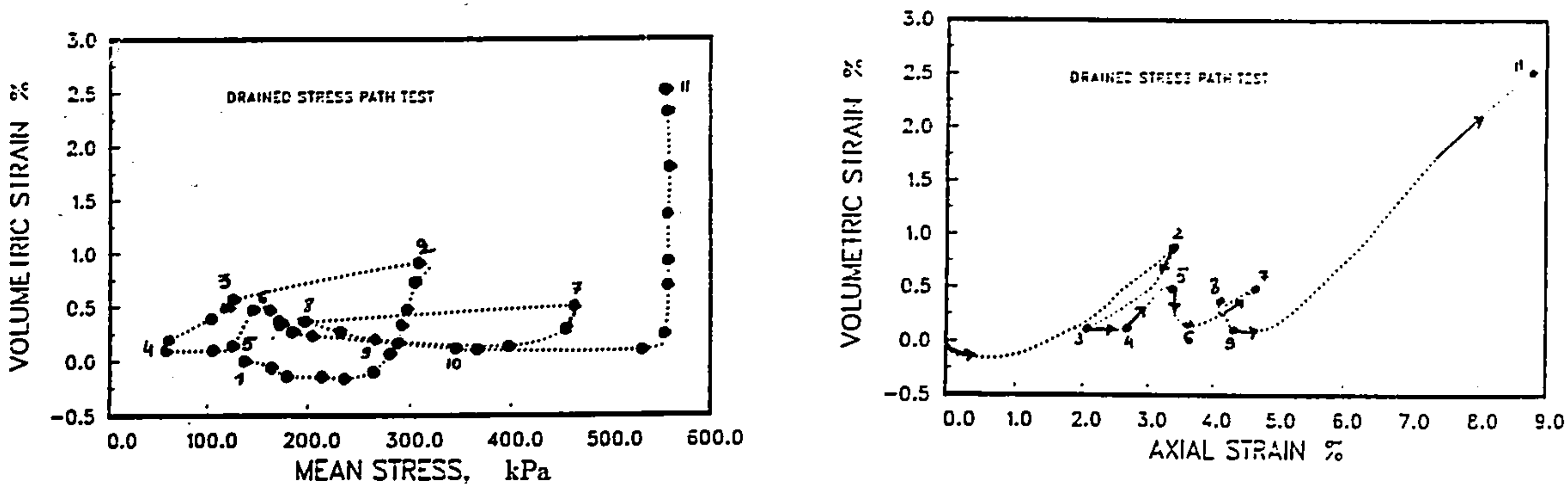

Figure C.10: Drained stress path test.
a) Volumetric stress-strain curve.
b) Axial strain-volumetric strain curve.

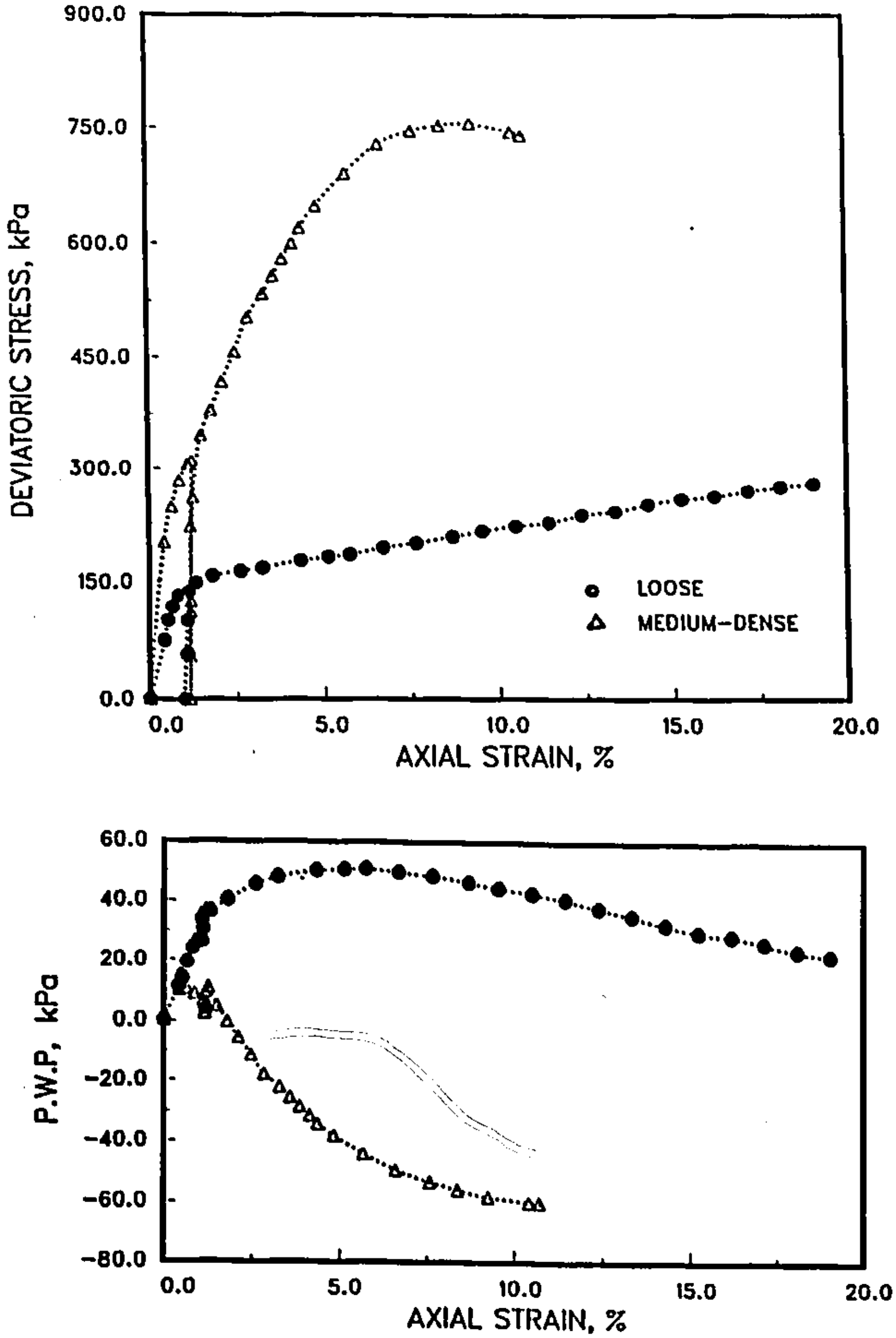

Figure C.11: Undrained CTC tests, effect of the initial density, $\sigma_3' = 137.89$ kPa

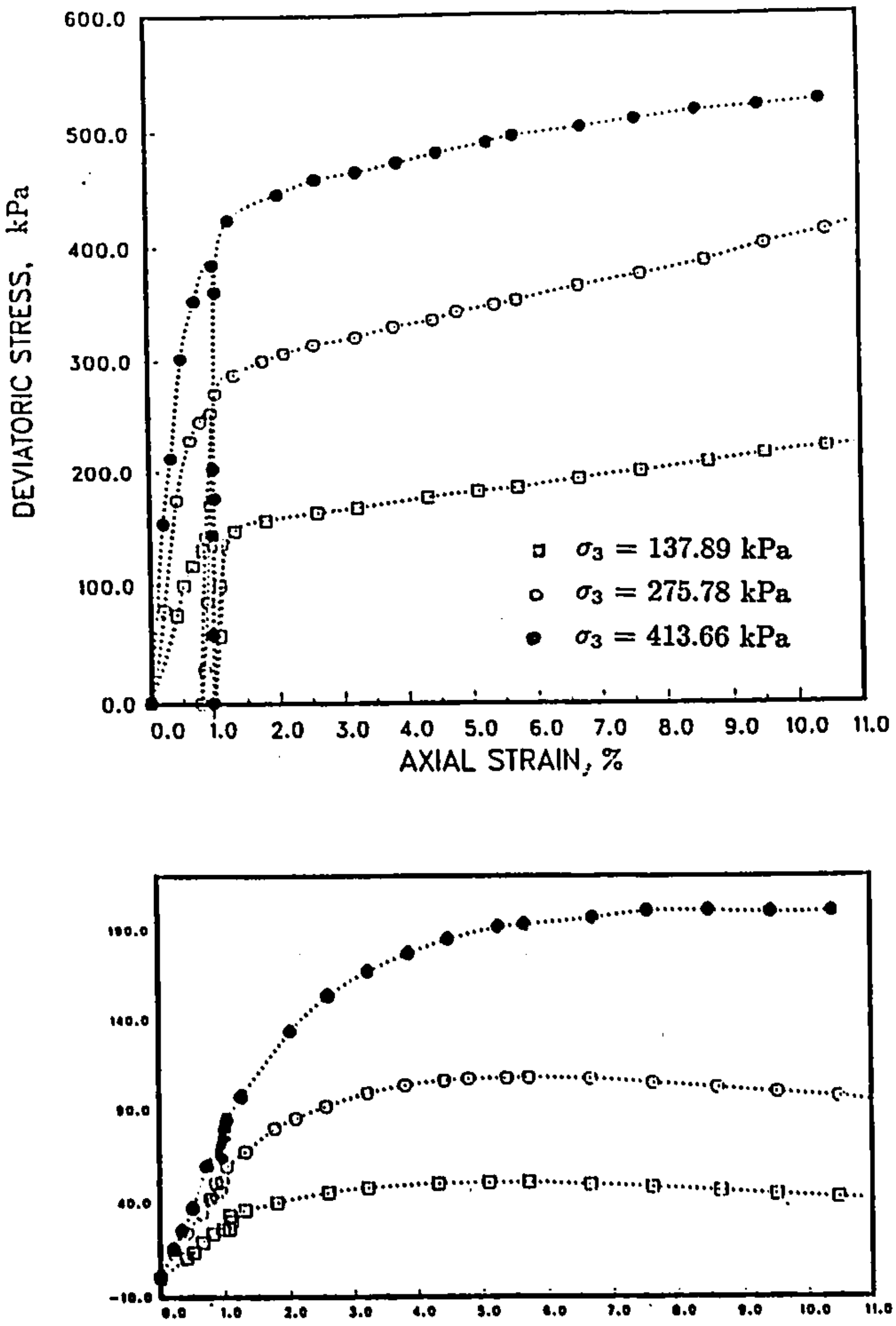

Figure C.12: Undrained CTC tests, loose soil samples.

a) Shear stress-strain curves.

b) Axial strain-Pore water pressure curves.

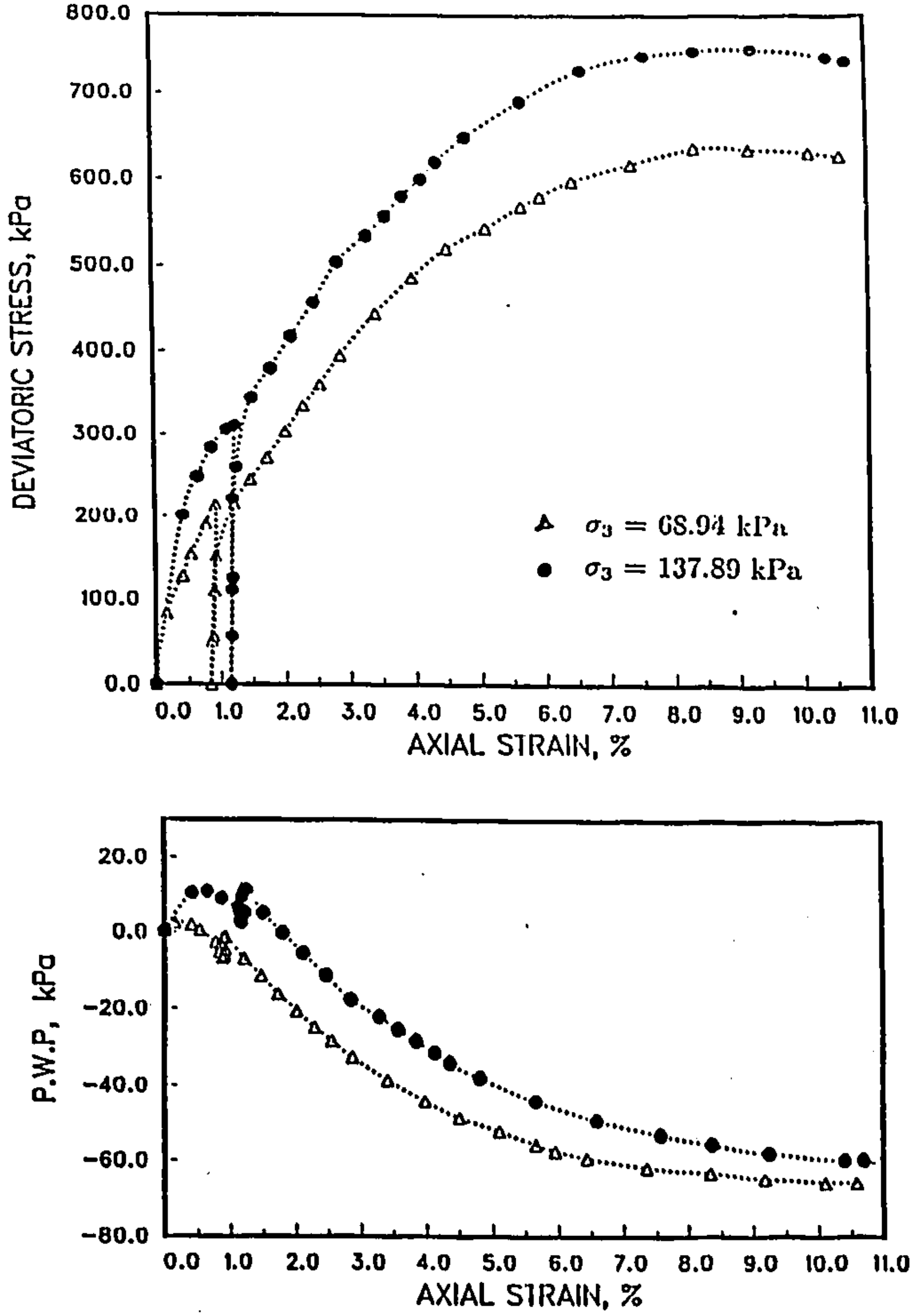

Figure C.13: Undrained CTC tests, medium dense soil samples.

a) Shear stress-strain curves.

b) Axial strain-pore water pressure curves.

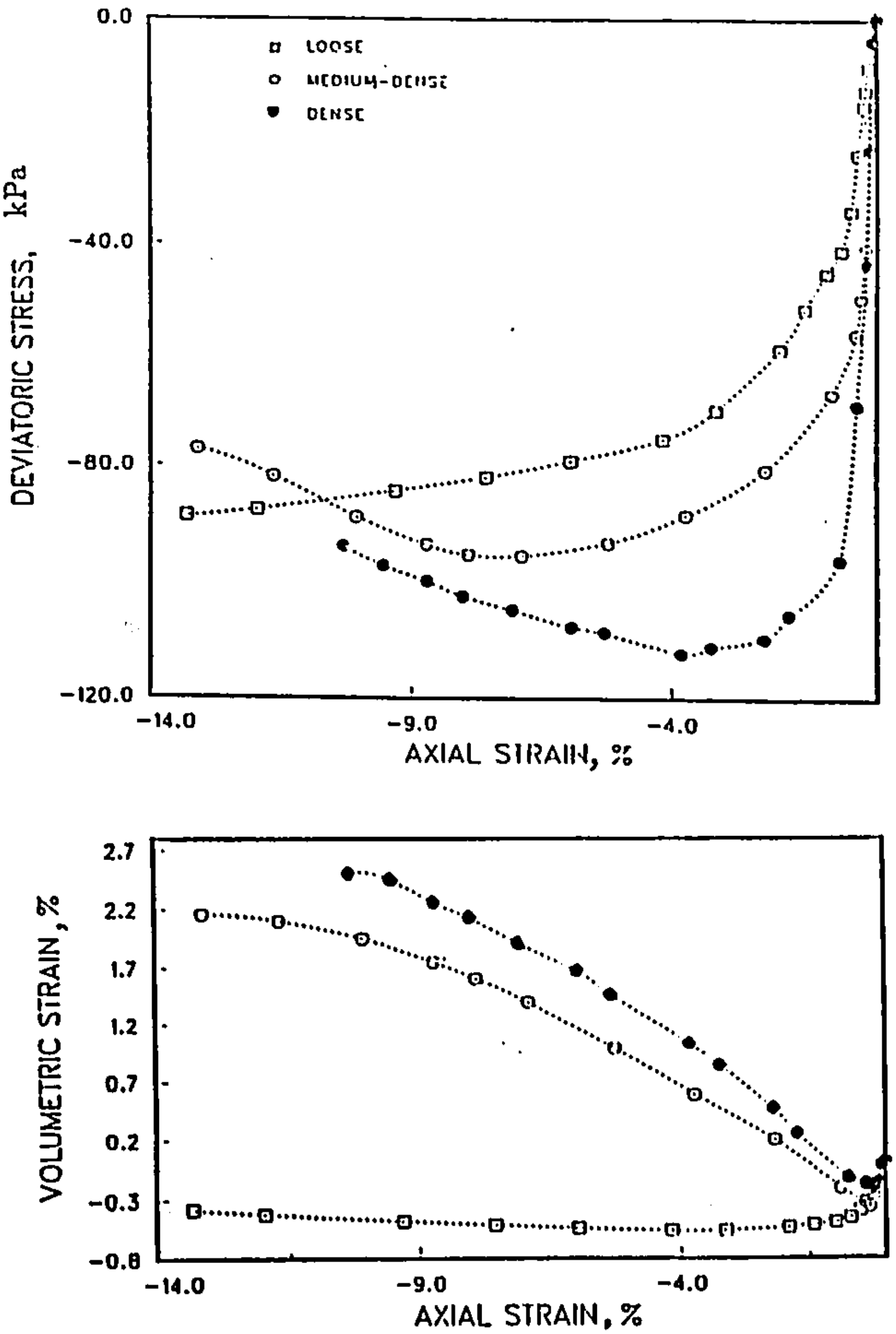

Figure C.14: Drained CTE tests, effect of the initial density, σ_3 = 137.89 kPa

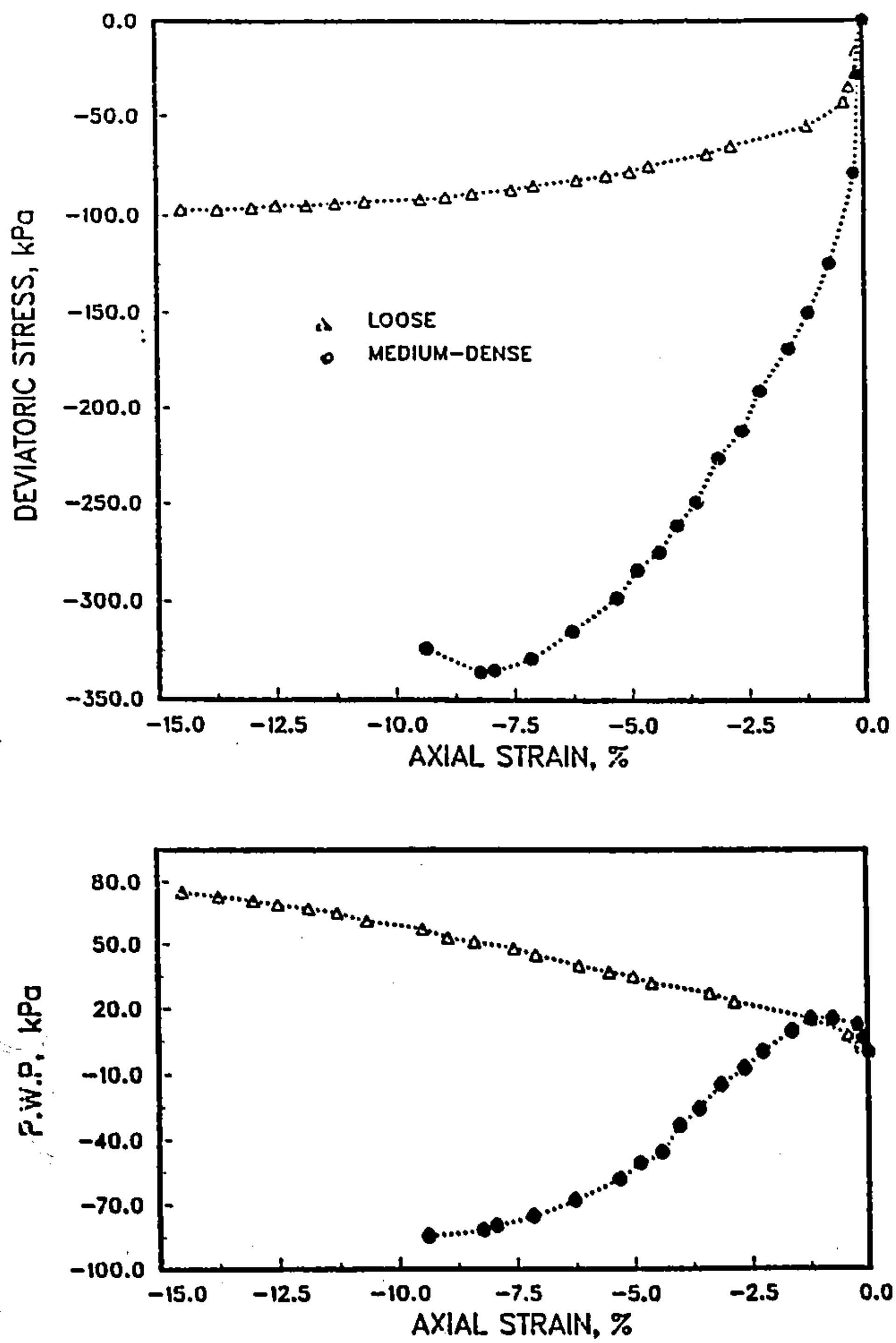

Figure C.15: Undrained CTE tests, effect of the initial density, $\sigma_3' = 137.89$ kPa

Appendix D

MODEL SIMULATIONS

The purpose of this Appendix is to present the figures corresponding to the model predictions discussed in Chapter 8. Each figure includes the experimental data indicated with full circles and the model predictions with dotted lines.

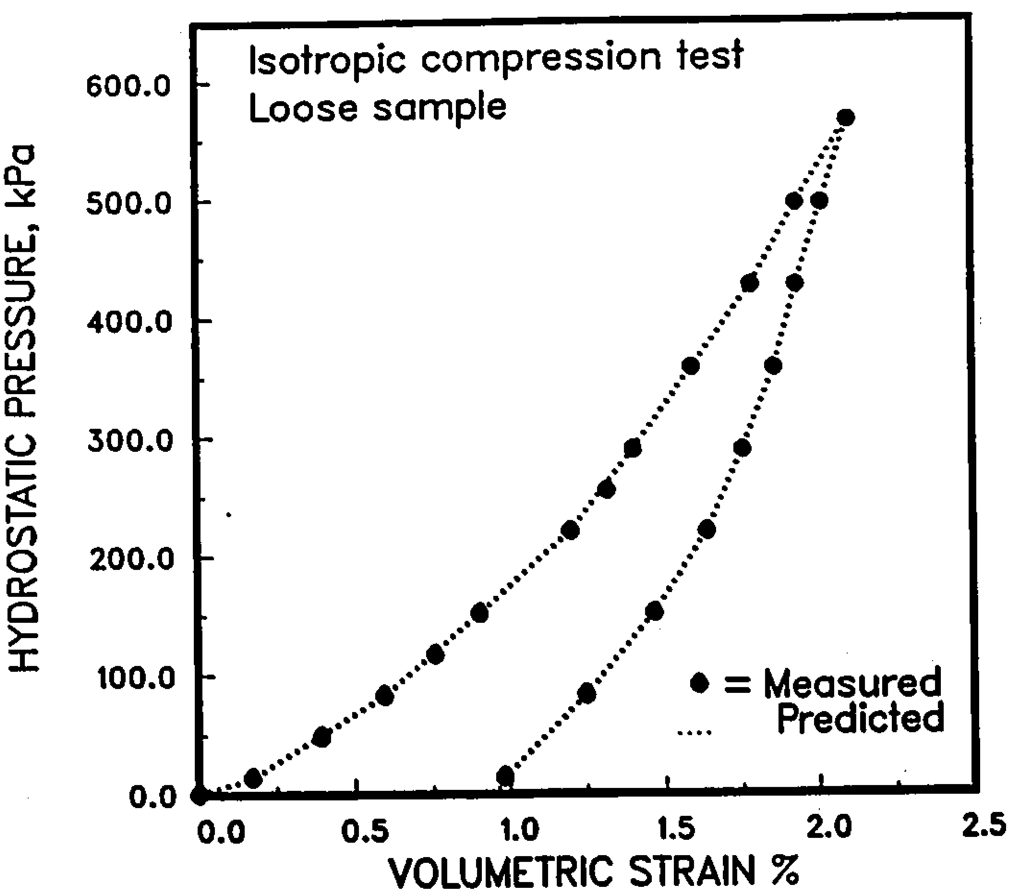

Figure D.1: **Hydrostatic pressure versus volumetric strain,** test # 1. Comparison of predicted and measured volumetric stress strain curves, loose sample of crushed quartz sand.

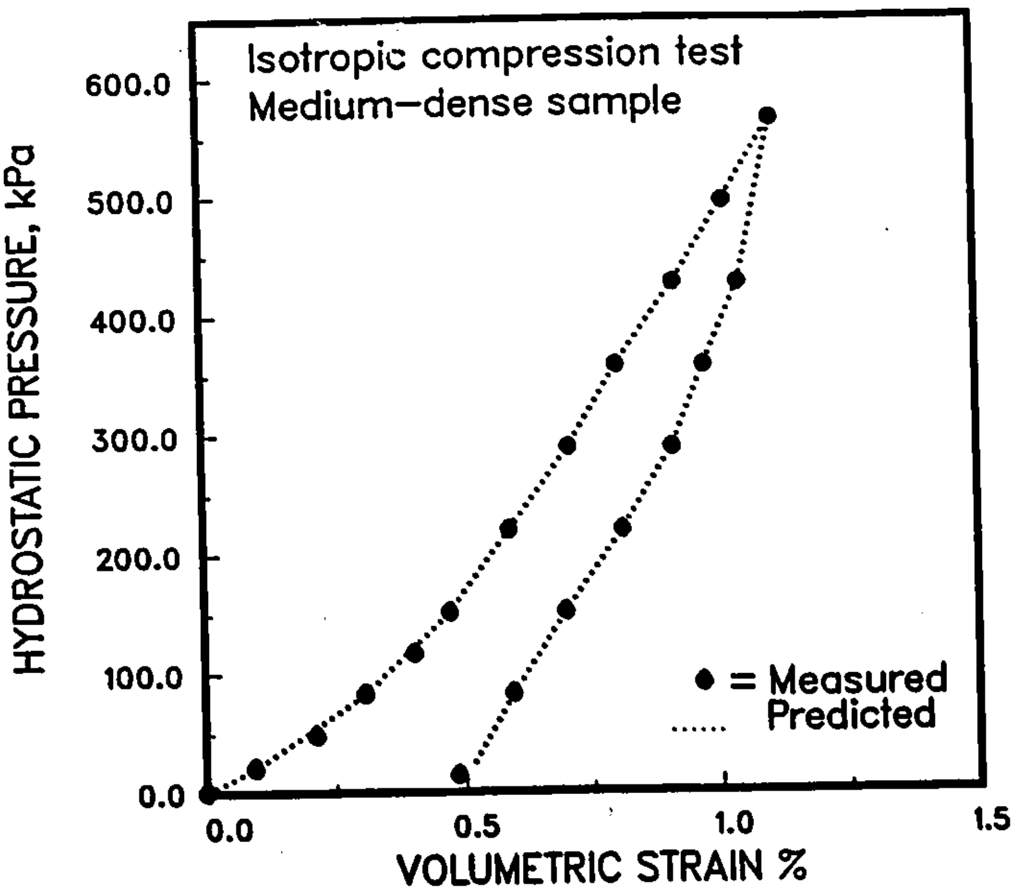

Figure D.2: **Hydrostatic pressure versus volumetric strain**, test # 2. Comparison of predicted and measured volumetric stress strain curves, medium-dense sample of crushed quartz sand.

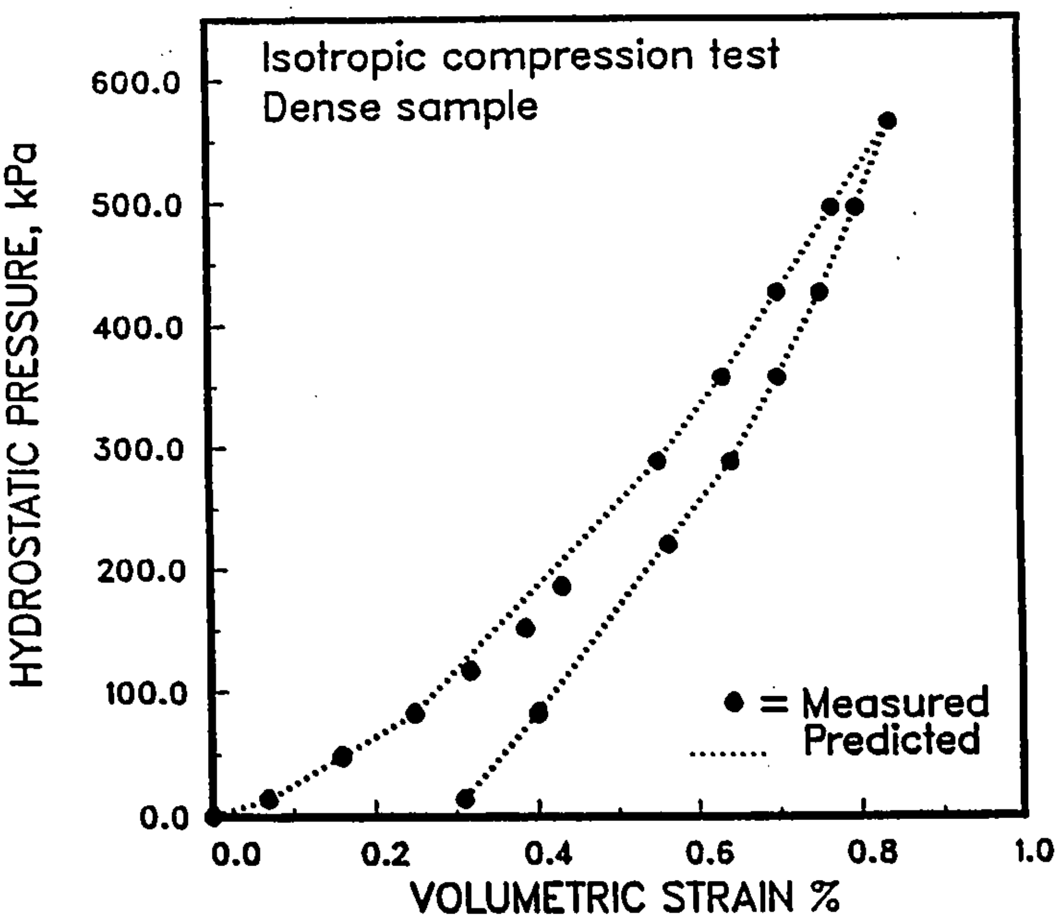

Figure D.3: **Hydrostatic pressure versus volumetric strain, test # 3. Comparison of predicted and measured volumetric stress strain curves, dense sample of crushed quartz sand.**

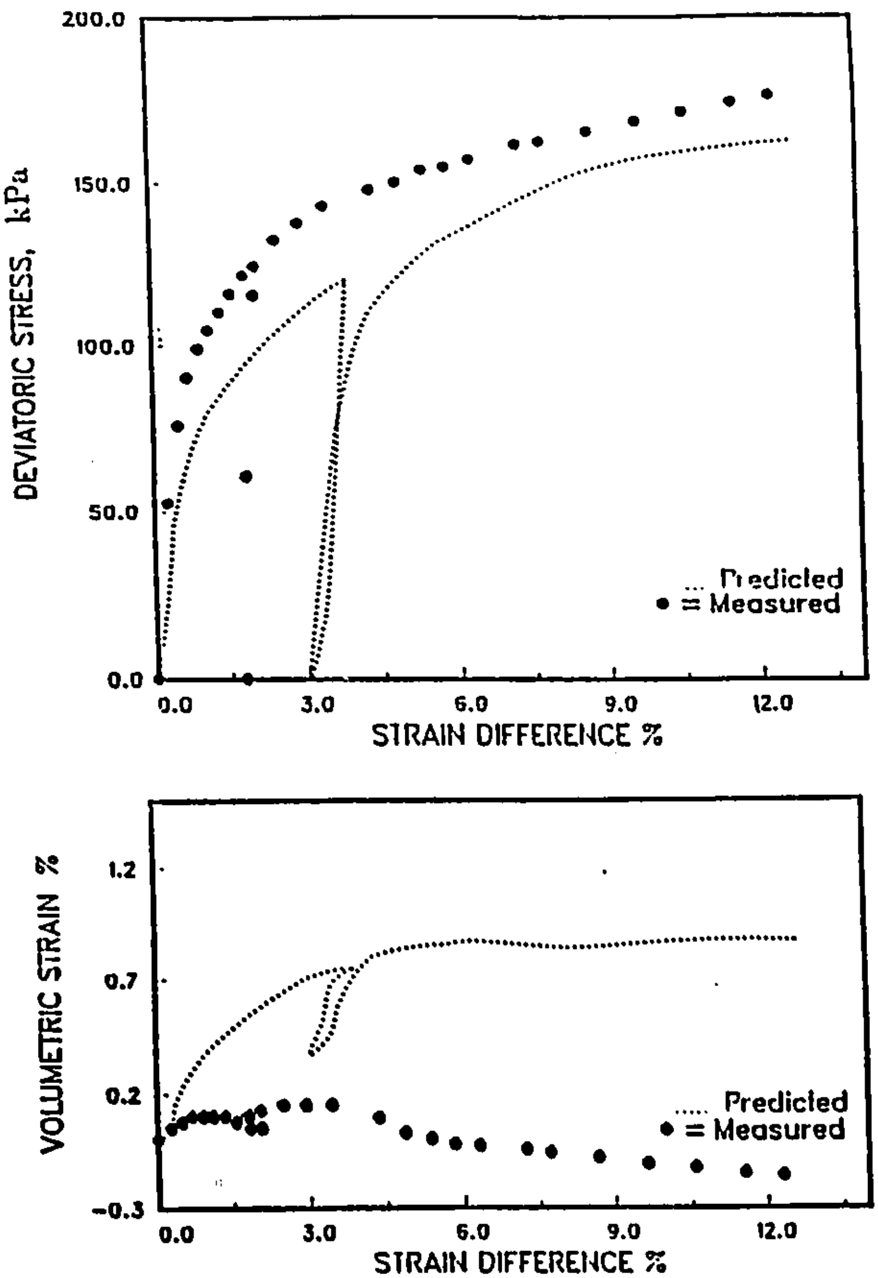

Figure D.4: Drained CTC test #4.
Comparison of predicted and measured stress strain curves , loose sample of crushed quartz sand, $\sigma_3 = 68.95kPa$.

a) Shear stress strain curves.

b) Volumetric strain versus shear strain curves.

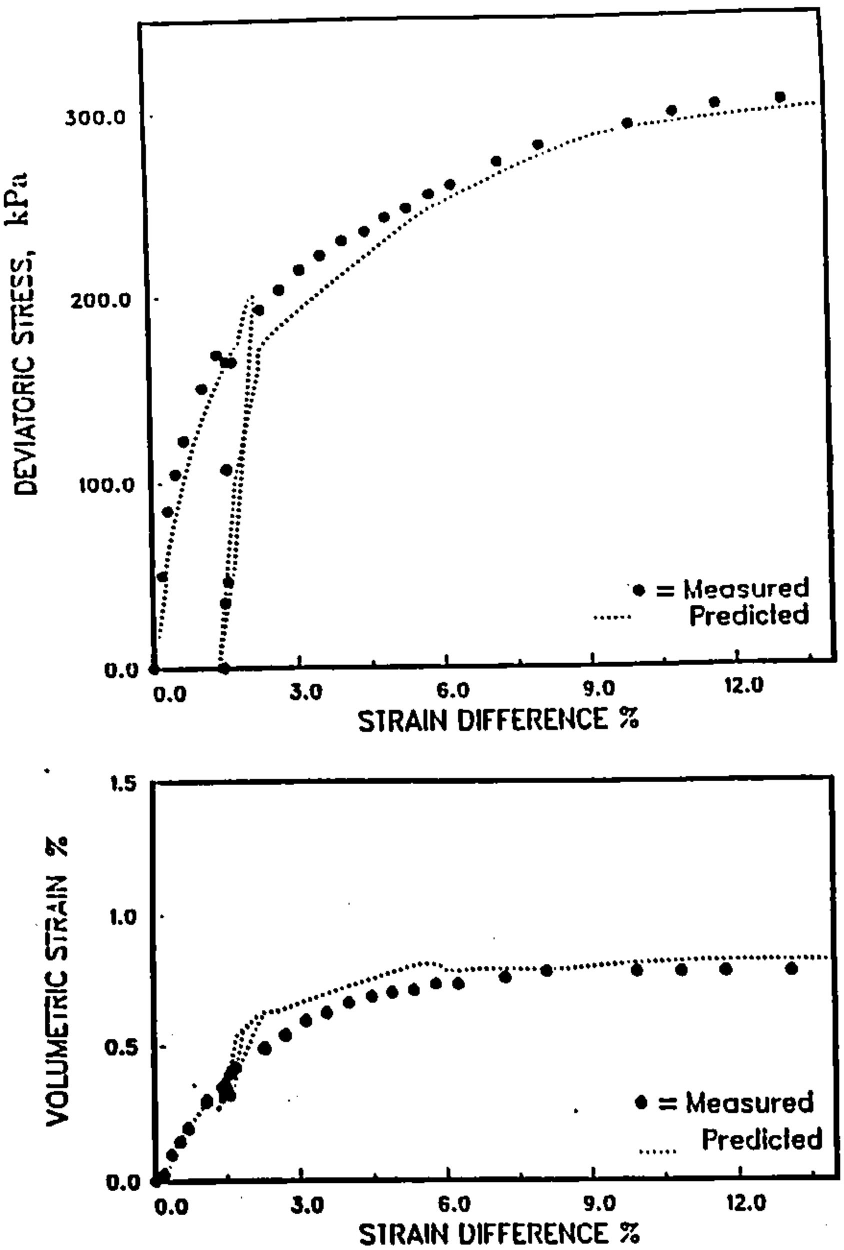

Figure D.5: Drained CTC test #5.

Comparison of predicted and measured stress strain curves , loose sample of crushed quartz sand, $\sigma_3 = 137.89 kPa$.

a) Shear stress strain curves.

b) Volumetric strain versus shear strain curves.

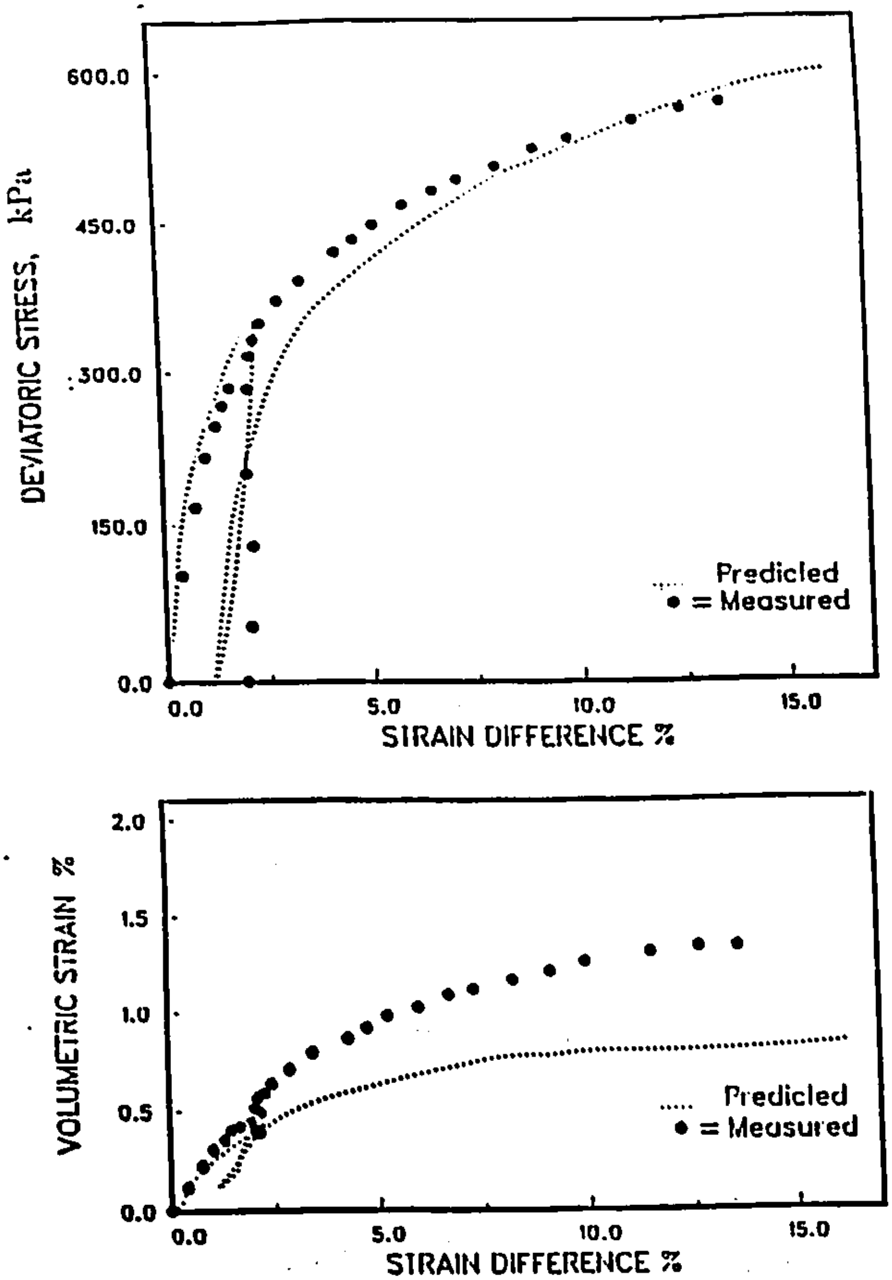

Figure D.6: Drained CTC test #6.

Comparison of predicted and measured stress strain curves , loose sample of crushed quartz sand, $\sigma_3 = 275.78kPa$.

a) Shear stress strain curves.

b) Volumetric strain versus shear strain curves.

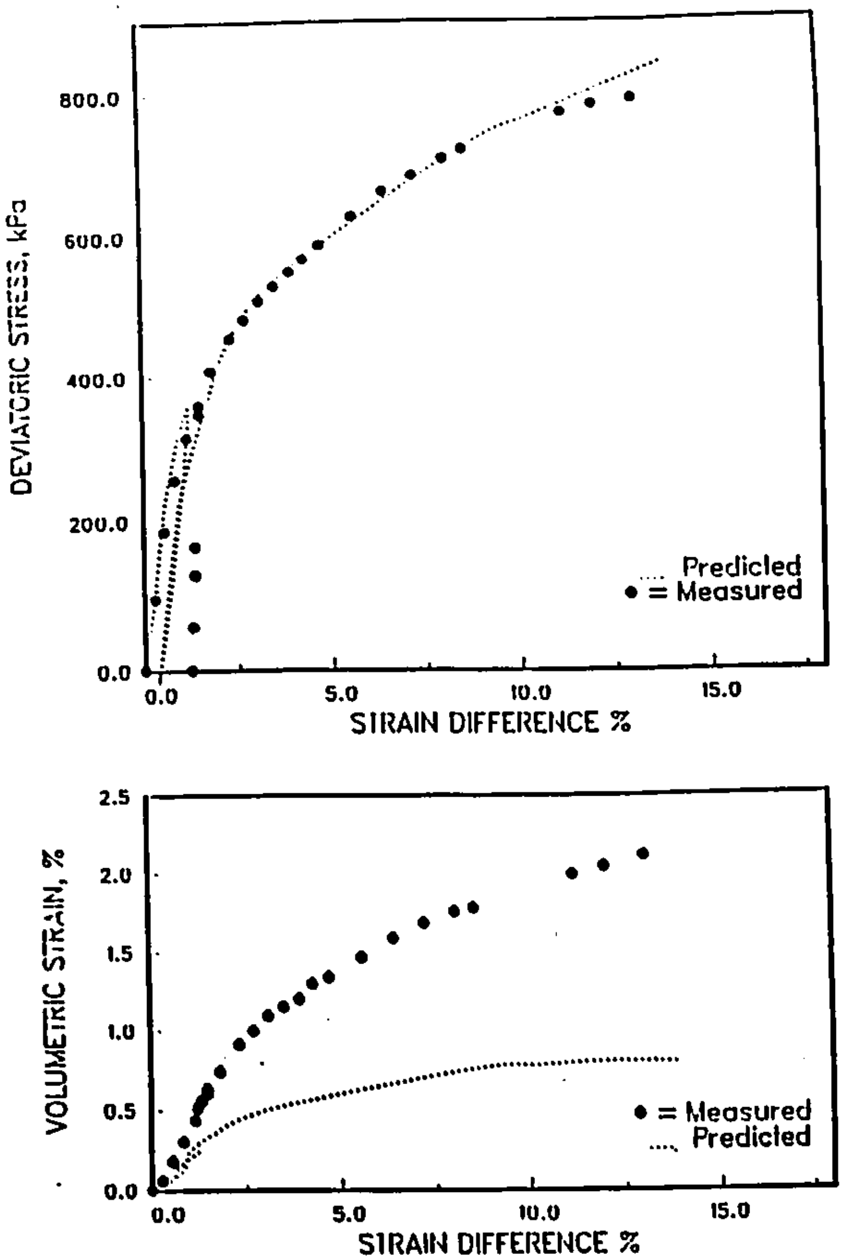

Figure D.7: Drained CTC test #7.

Comparison of predicted and measured stress strain curves , loose sample of crushed quartz sand, $\sigma_3 = 413.66 kPa$.

a) Shear stress strain curves.

b) Volumetric strain versus shear strain curves.

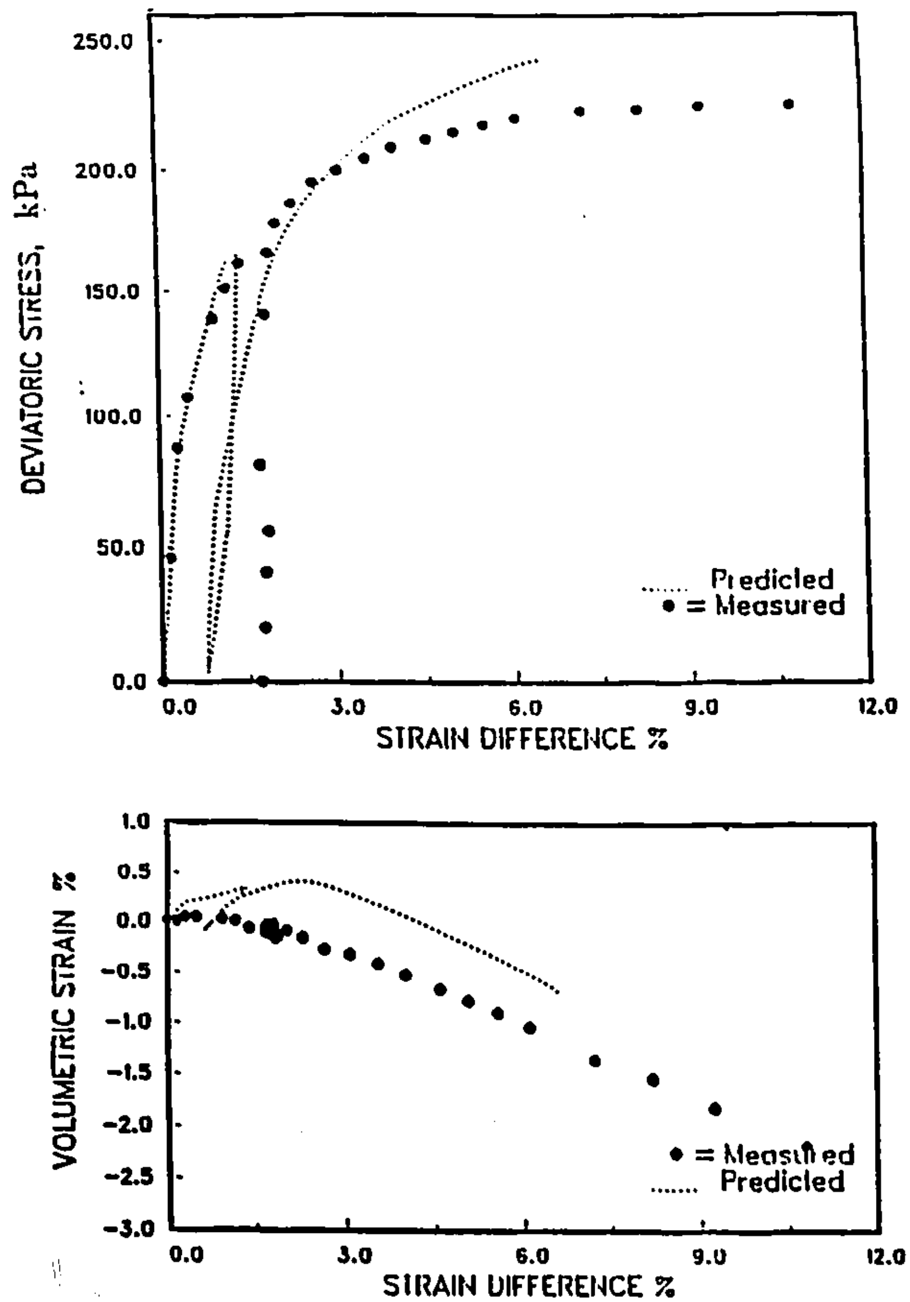

Figure D.8: Drained CTC test #8.

Comparison of predicted and measured stress strain curves, medium-dense sample of crushed quartz sand, $\sigma_3 = 68.95kPa$.

a) Shear stress strain curves.

b) Volumetric strain versus shear strain curves.

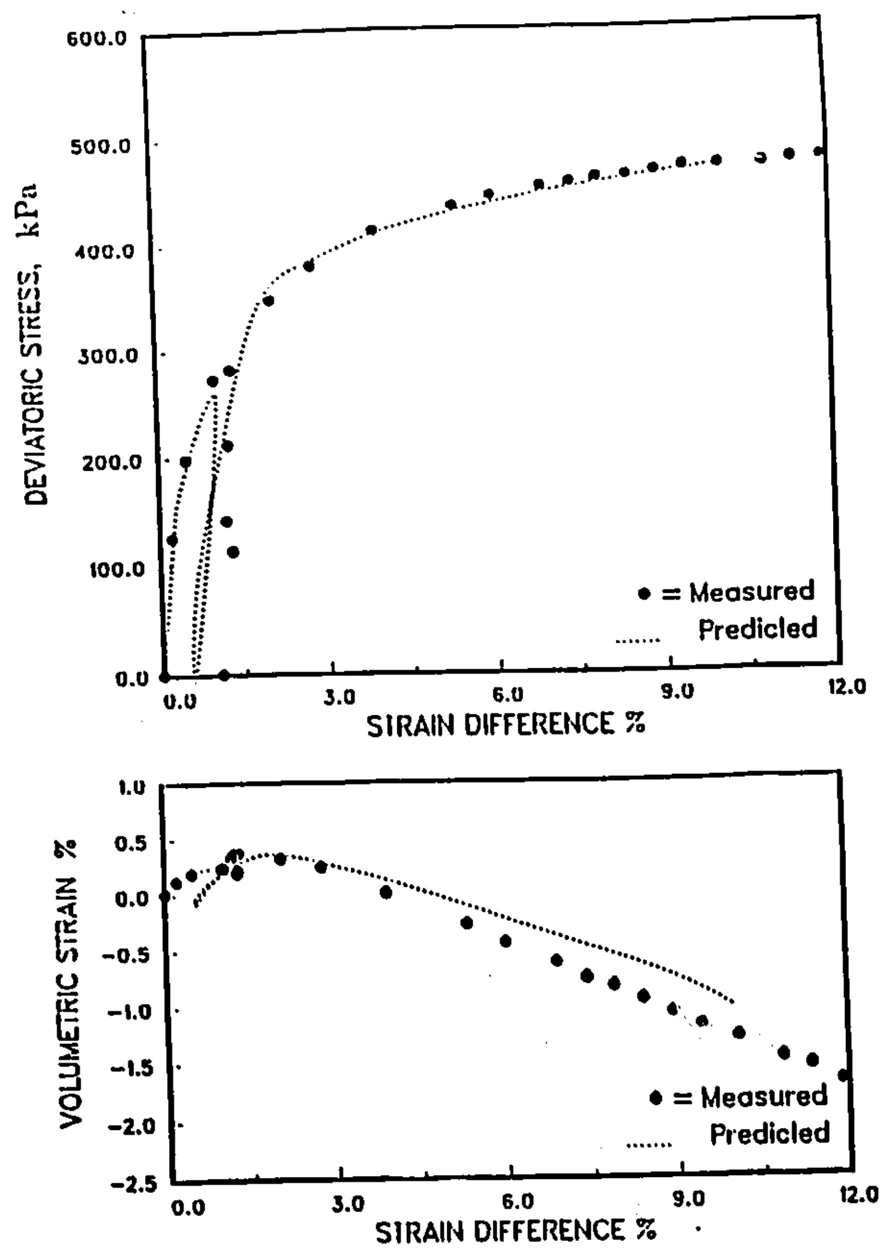

Figure D.9: Drained CTC test #9.
Comparison of predicted and measured stress strain curves, medium-dense sample of crushed quartz sand, $\sigma_3 = 137.89 kPa$.

a) Shear stress strain curves.

b) Volumetric strain versus shear strain curves.

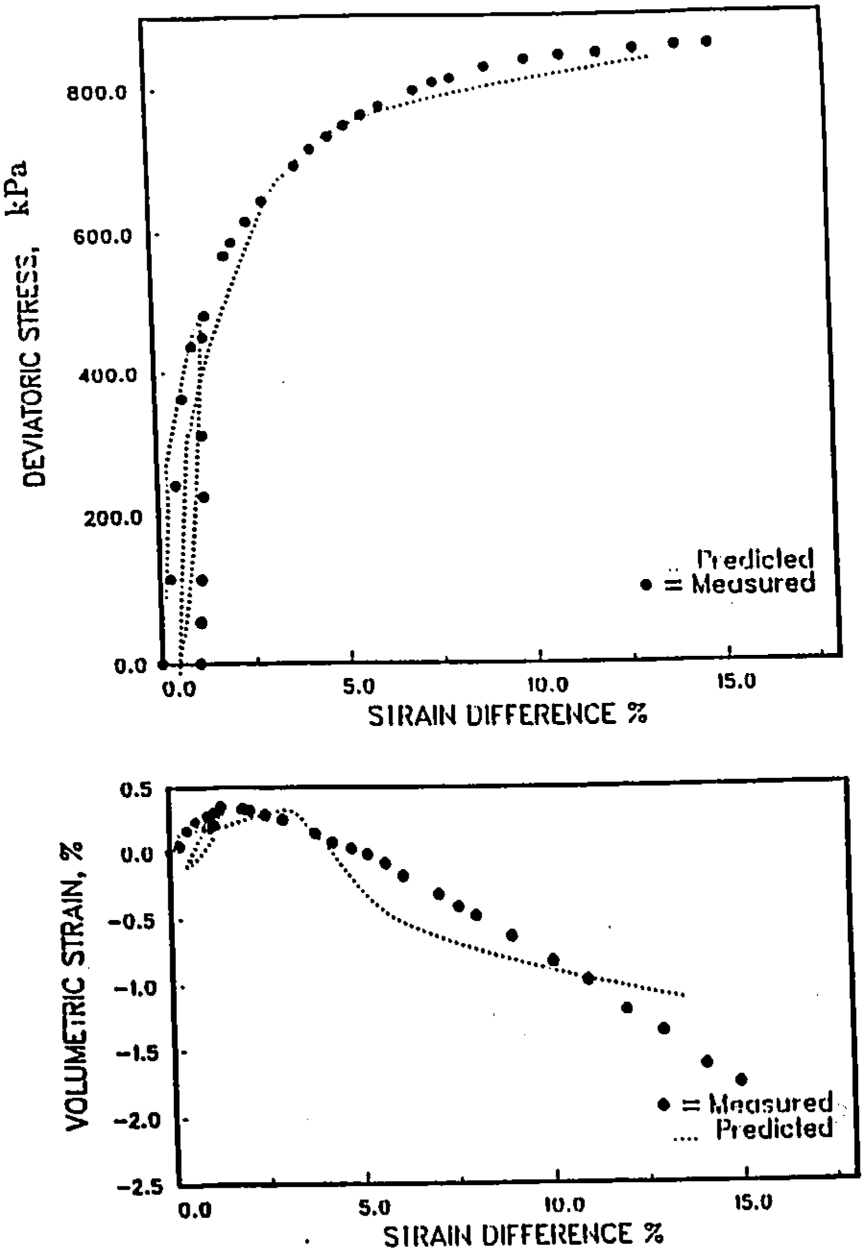

Figure D.10: Drained CTC test #10.

Comparison of predicted and measured stress strain curves, medium-dense sample of crushed quartz sand, $\sigma_3 = 275.78kPa$.

a) **Shear stress strain curve.**

b) **Volumetric strain versus shear strain curves.**

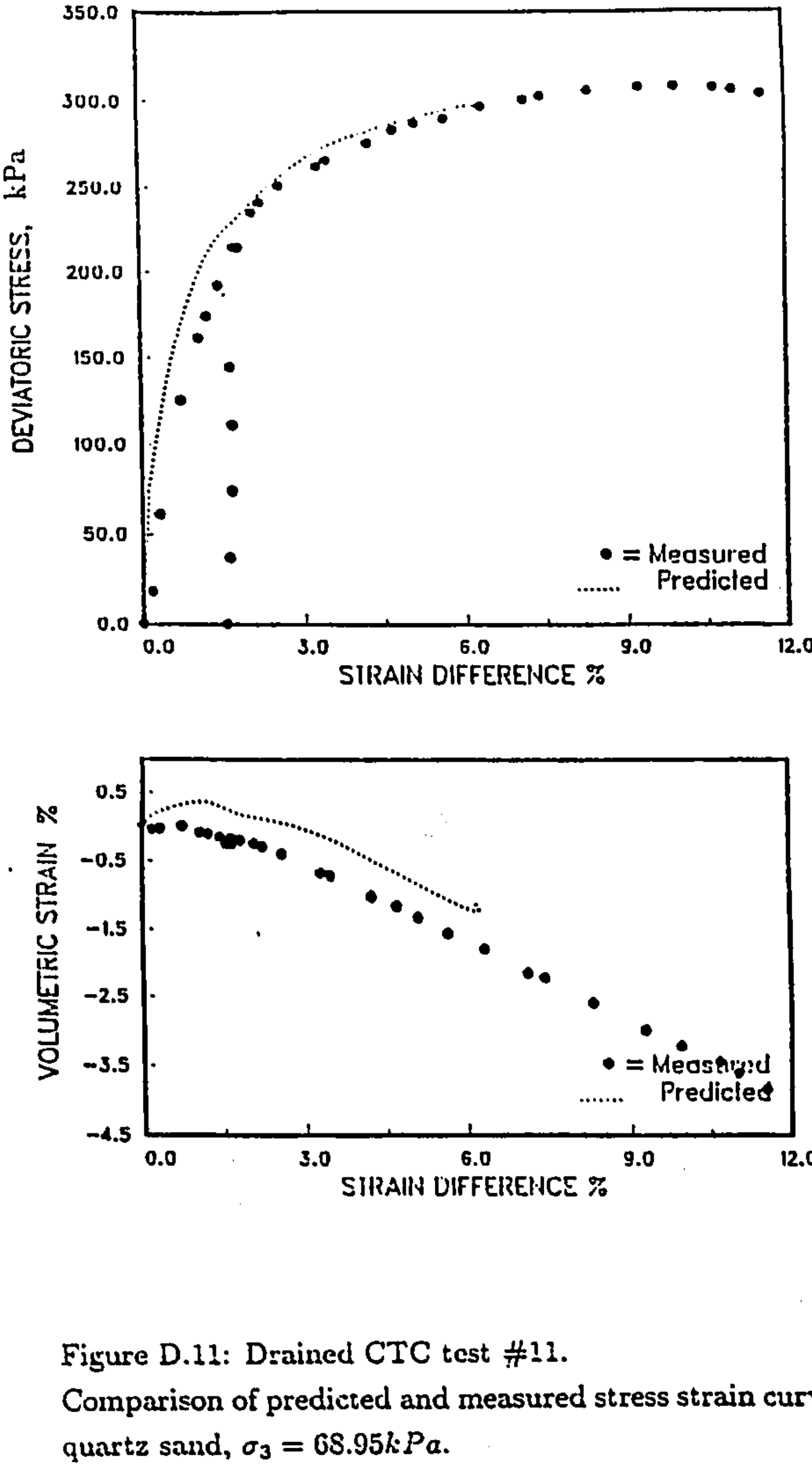

Figure D.11: Drained CTC test #11.
Comparison of predicted and measured stress strain curves, dense sample of crushed quartz sand, $\sigma_3 = 68.95kPa$.

a) Shear stress strain curves.

b) Volumetric strain versus shear strain curves.

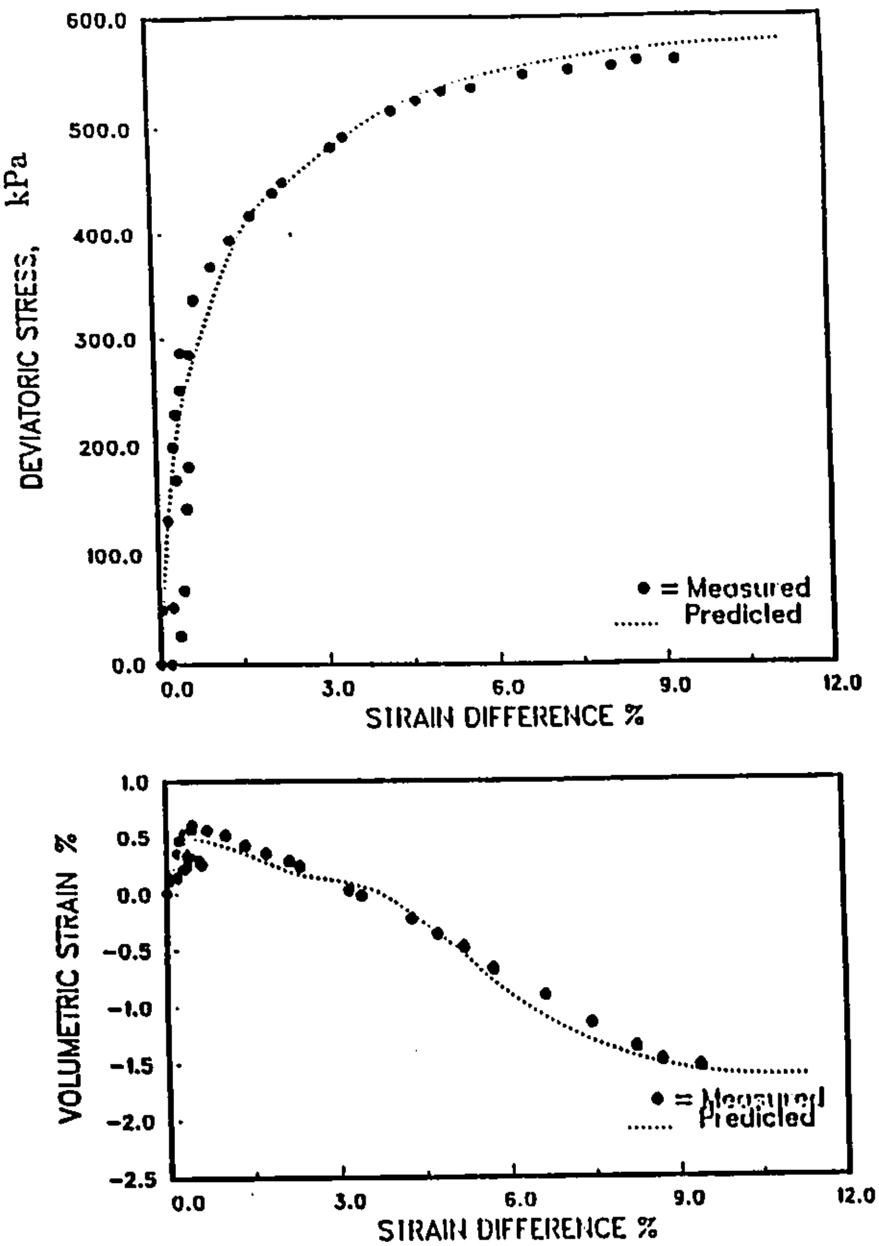

Figure D.12: Drained CTC test #12.
Comparison of predicted and measured stress strain curves, dense sample of crushed quartz sand, $\sigma_3 = 137.89 kPa$.

a) Shear stress strain curves.

b) Volumetric strain versus shear strain curves.

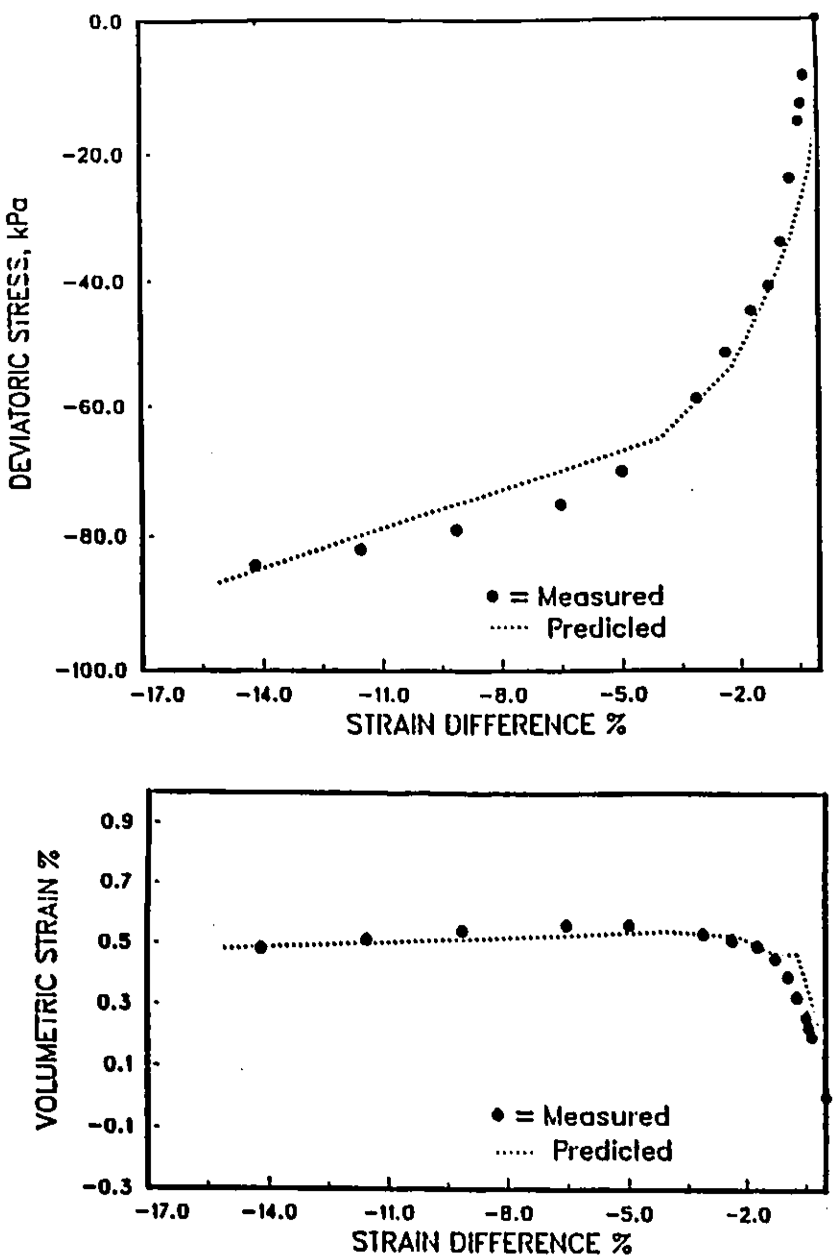

Figure D.13: Drained CTE test #18.

Comparison of predicted and measured stress strain curves, loose sample of crushed quartz sand, $\sigma_3 = 137.89 kPa$.

a) **Shear stress strain curves.**

b) **Volumetric strain versus shear strain curves.**

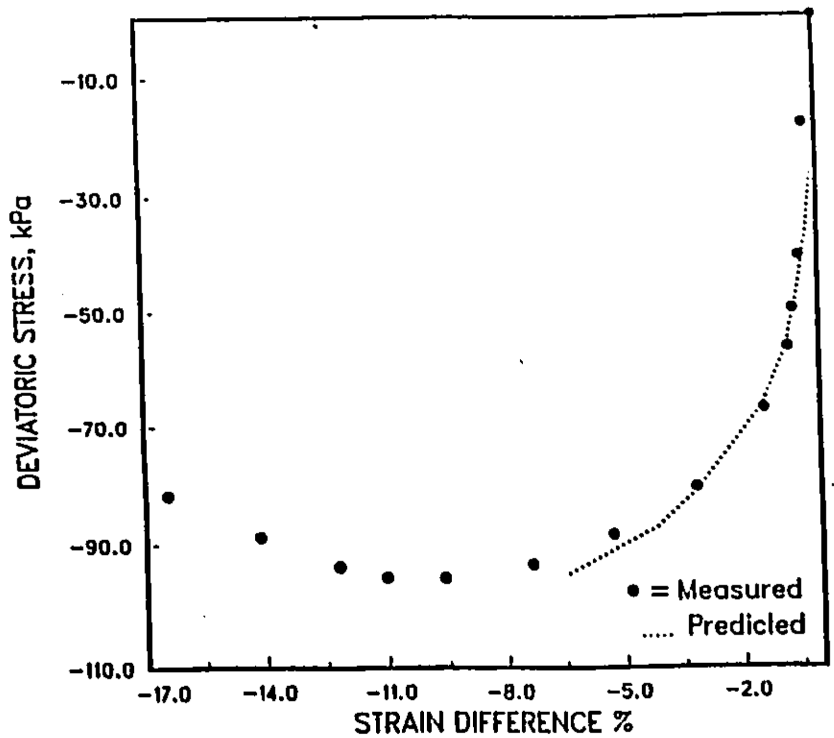

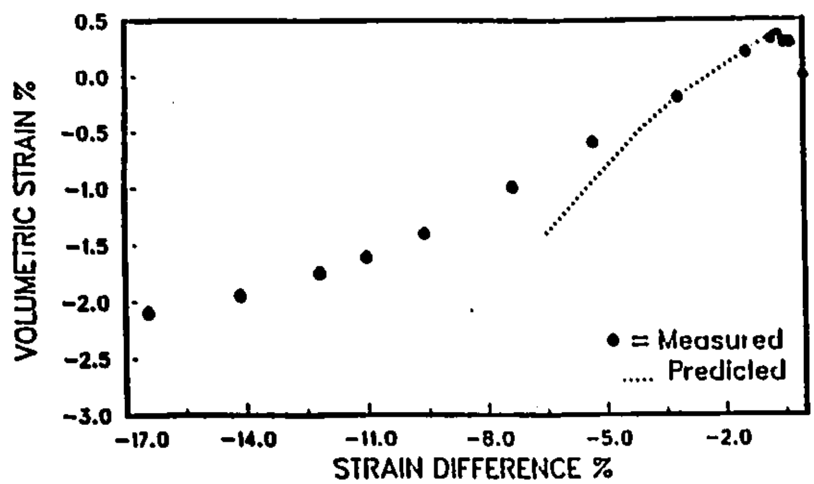

Figure D.14: Drained CTE test #19.
Comparison of predicted and measured stress strain curves, medium-dense sample of crushed quartz sand, $\sigma_3 = 137.89 kPa$.

a) Shear stress strain curves.

b) Volumetric strain versus shear strain curves.

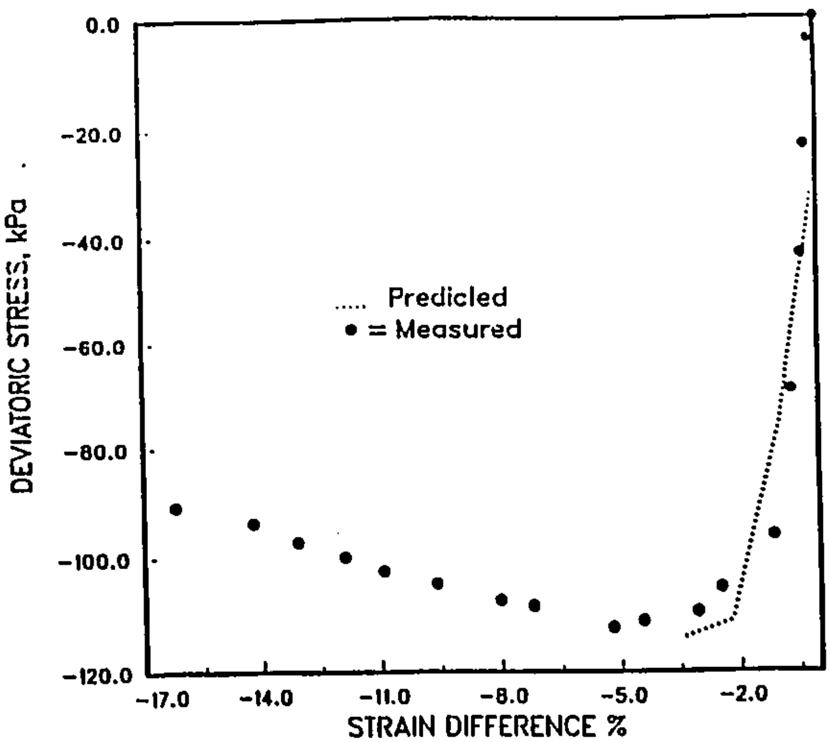

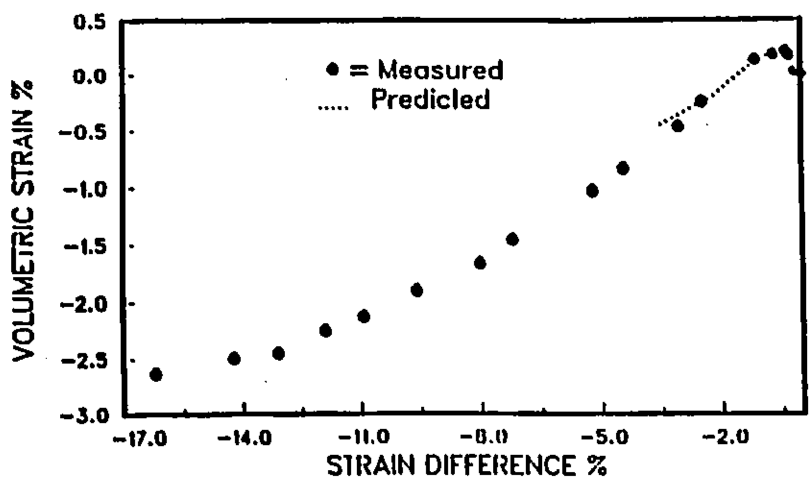

Figure D.15: Drained CTE test #20.

Comparison of predicted and measured stress strain curves, dense sample of crushed quartz sand, $\sigma_3 = 137.89 kPa$.

a) Shear stress strain curves.

b) Volumetric strain versus shear strain curves.

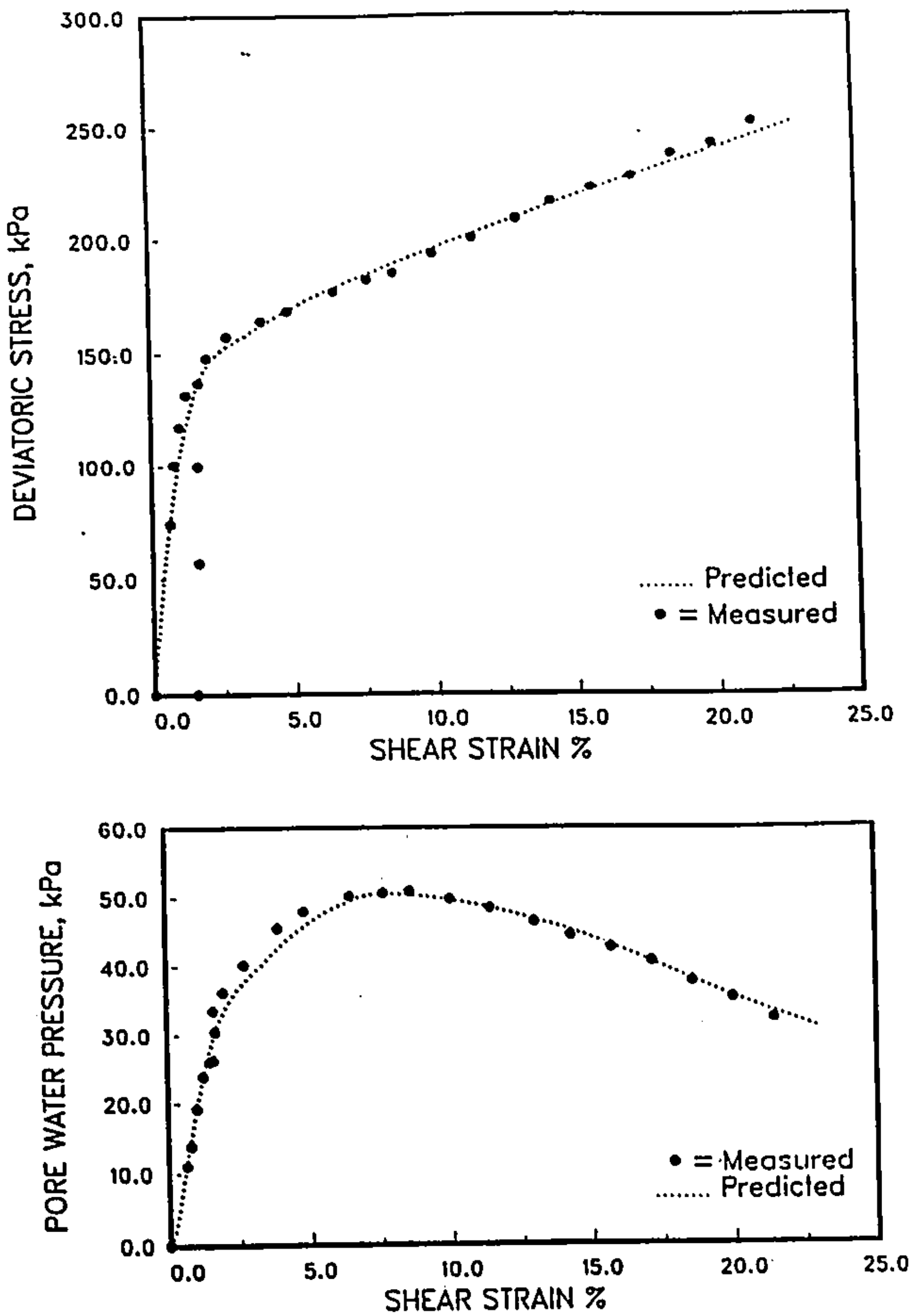

Figure D.16: Undrained CTC test #13.

Comparison of predicted and measured stress strain pore water pressure curves, loose sample of crushed quartz sand, $(\sigma_3)_{initial} = 137.89kPa$.

a) Shear stress strain curves.

b) Pore water pressure versus shear strain curves.

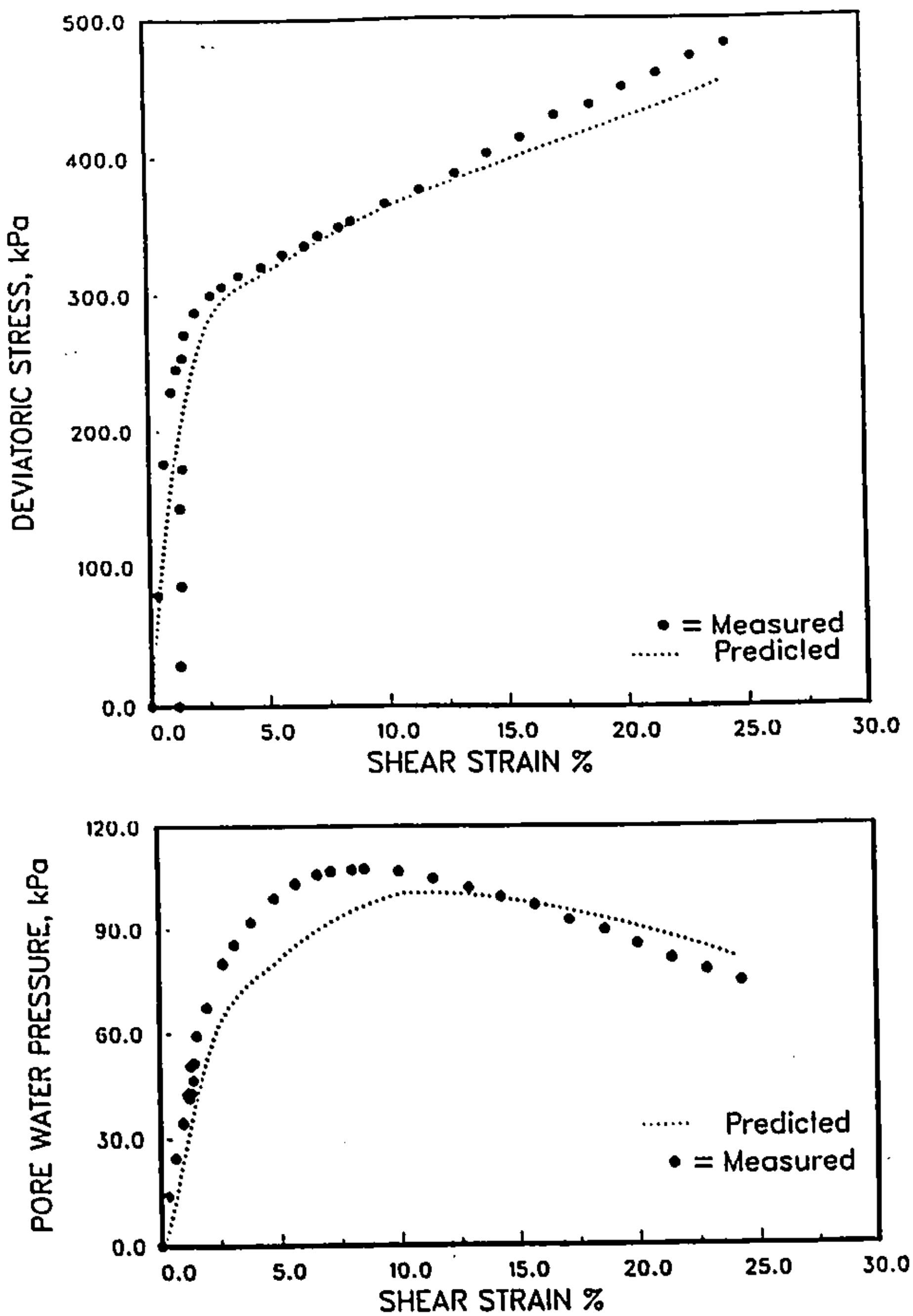

Figure D.17: Undrained CTC test #14.
Comparison of predicted and measured stress strain pore water pressure curves, loose sample of crushed quartz sand, $(\sigma_3)_{initial} = 275.78kPa$.

a) Shear stress strain curves.

b) Pore water pressure versus shear strain curves.

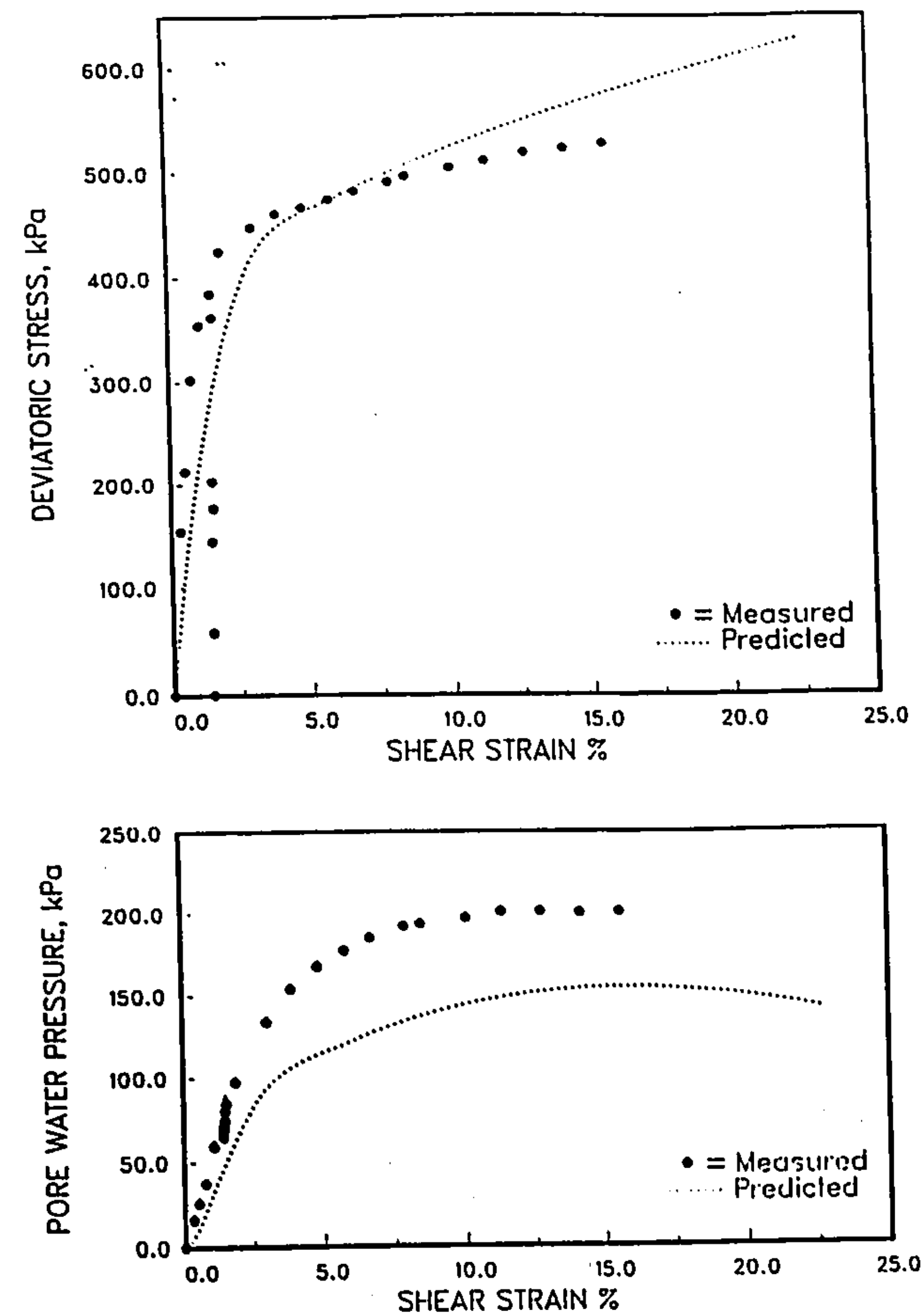

Figure D.18: Undrained CTC test #15.

Comparison of predicted and measured stress strain pore water pressure curves, loose sample of crushed quartz sand, $(\sigma_3)_{initial} = 413.66kPa$.

a) Shear stress strain curves.

b) Pore water pressure versus shear strain curves.

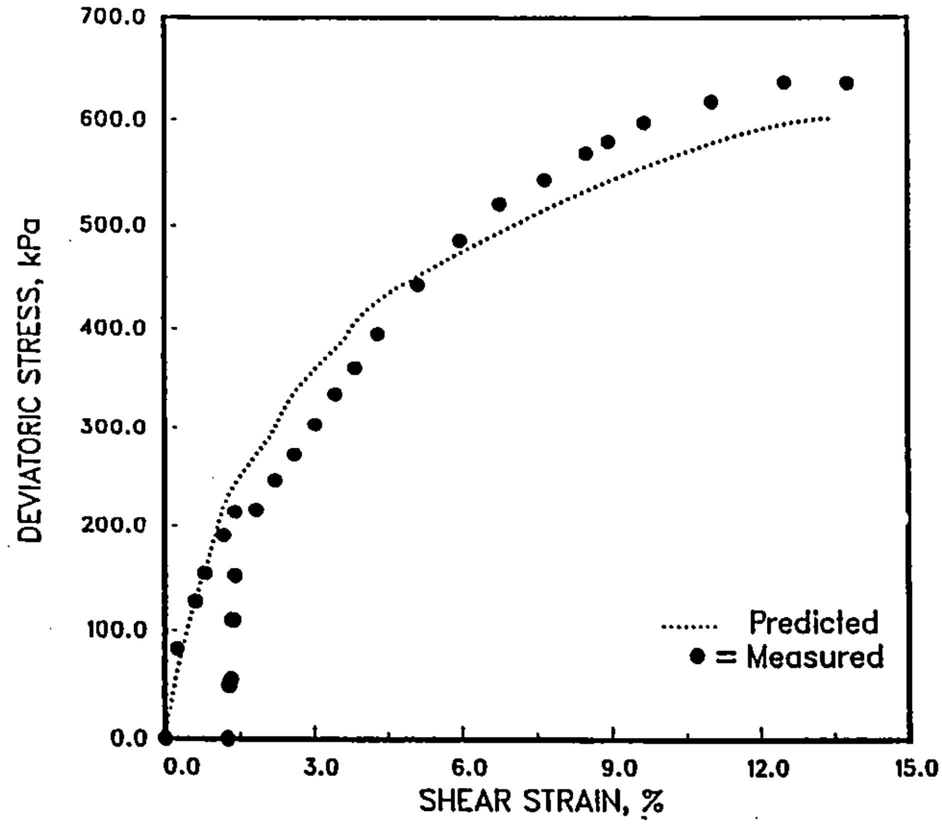

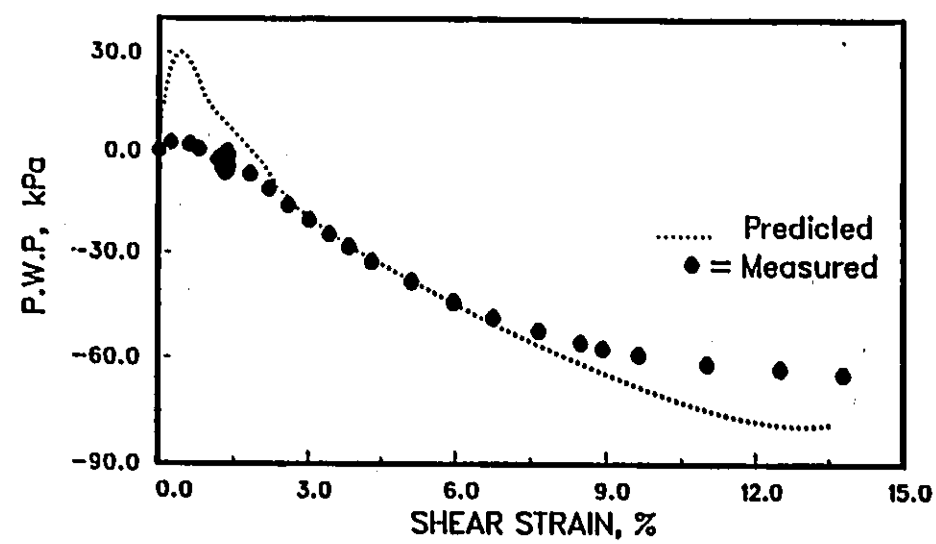

Figure D.19: Undrained CTC test #16.
Comparison of predicted and measured stress strain pore water pressure curves, medium-dense sample of crushed quartz sand, $(\sigma_3)_{initial} = 68.95 kPa$.
a) Shear stress strain curves.
b) Pore water pressure versus shear strain curves.

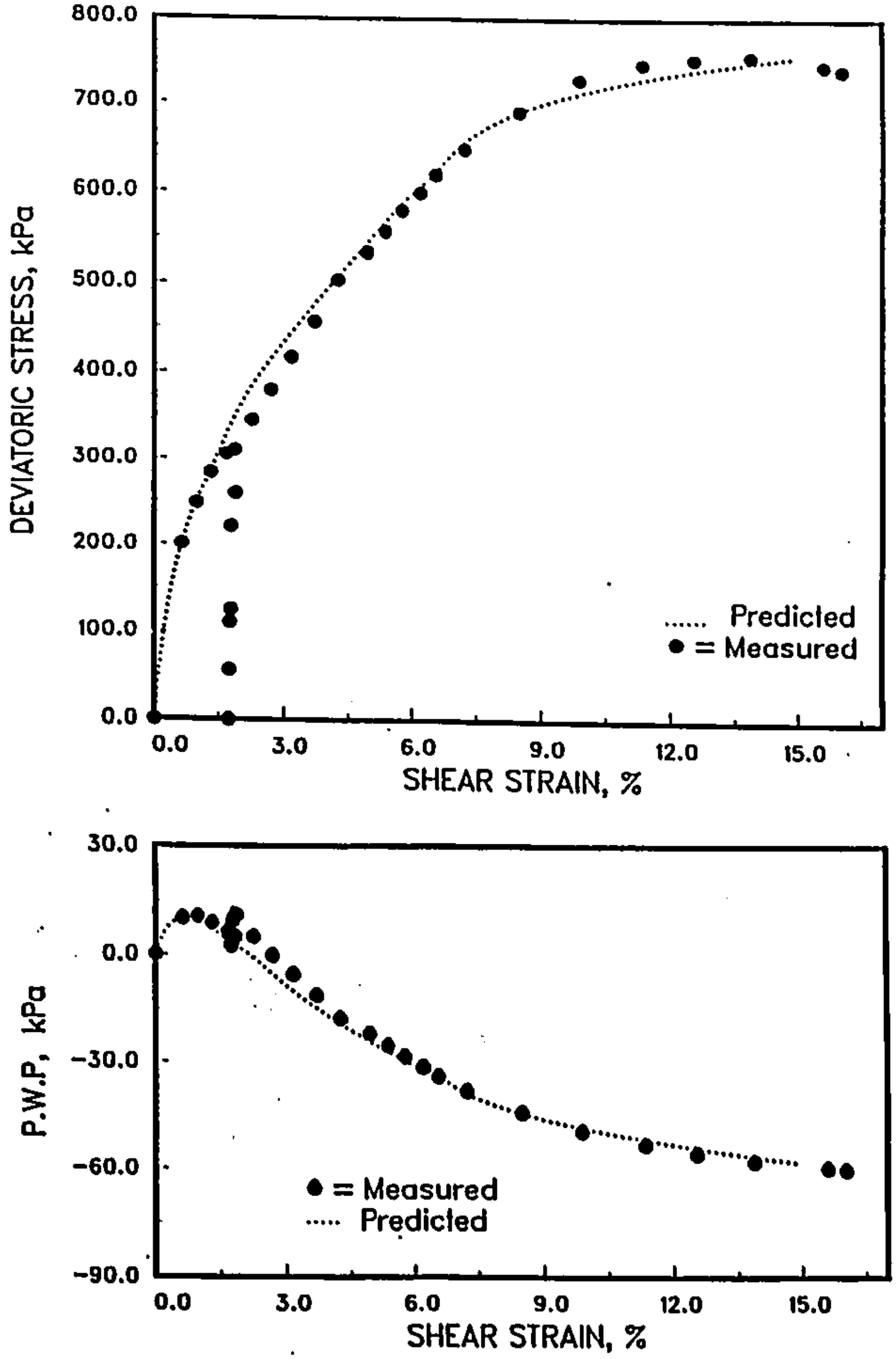

Figure D.20: Undrained CTC test #17.

Comparison of predicted and measured stress strain pore water pressure curves, medium-dense sample of crushed quartz sand, $(\sigma_3)_{initial} = 137.89 kPa$.

a) Shear stress strain curves.

b) Pore water pressure versus shear strain curves.

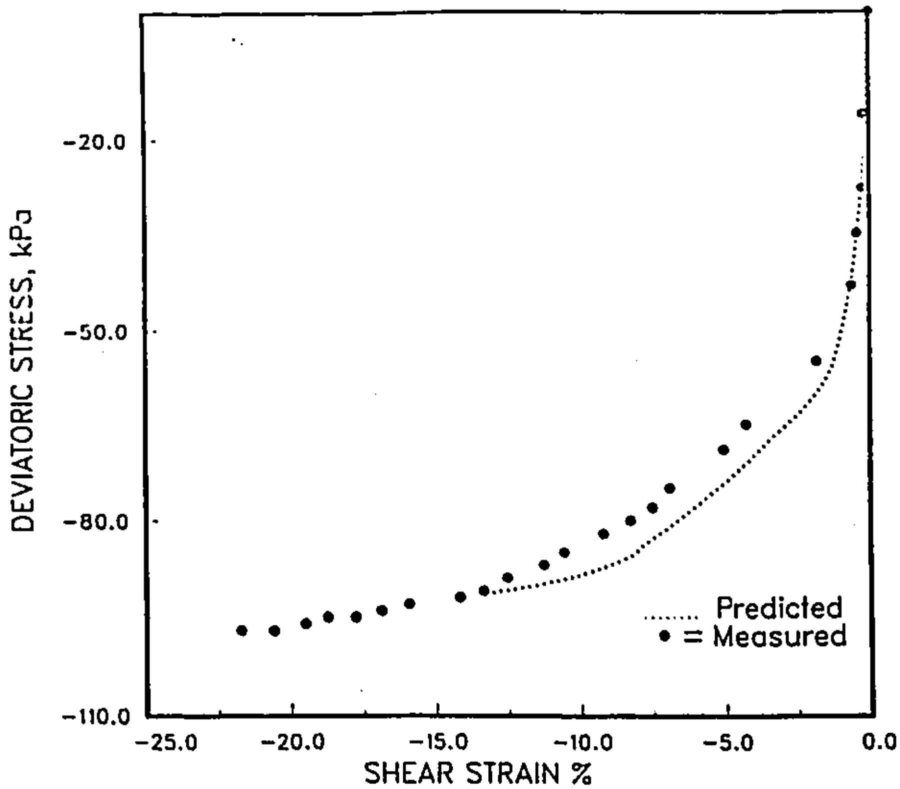

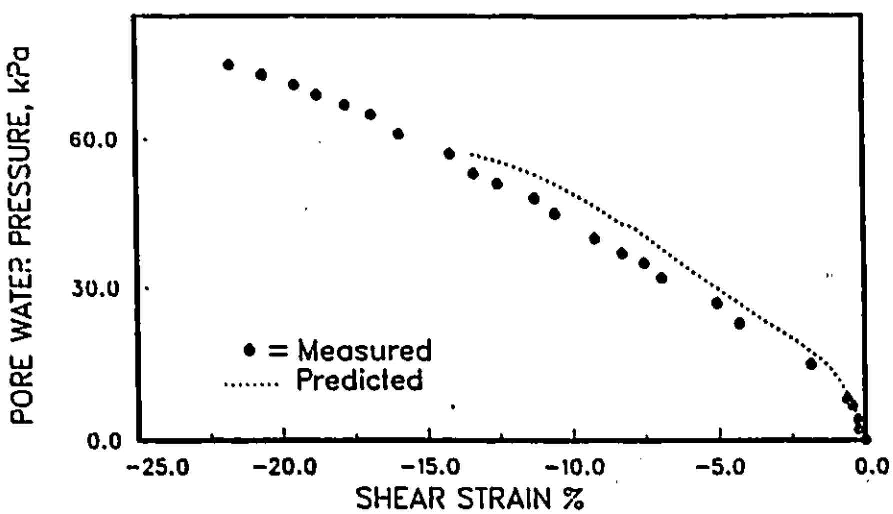

Figure D.21: Undrained CTE test #21.
Comparison of predicted and measured stress strain pore water pressure curves, loose sample of crushed quartz sand, $(\sigma_3)_{initial} = 137.89kPa$.
a) **Shear stress strain curves.**
b) **Pore water pressure versus shear strain curves.**

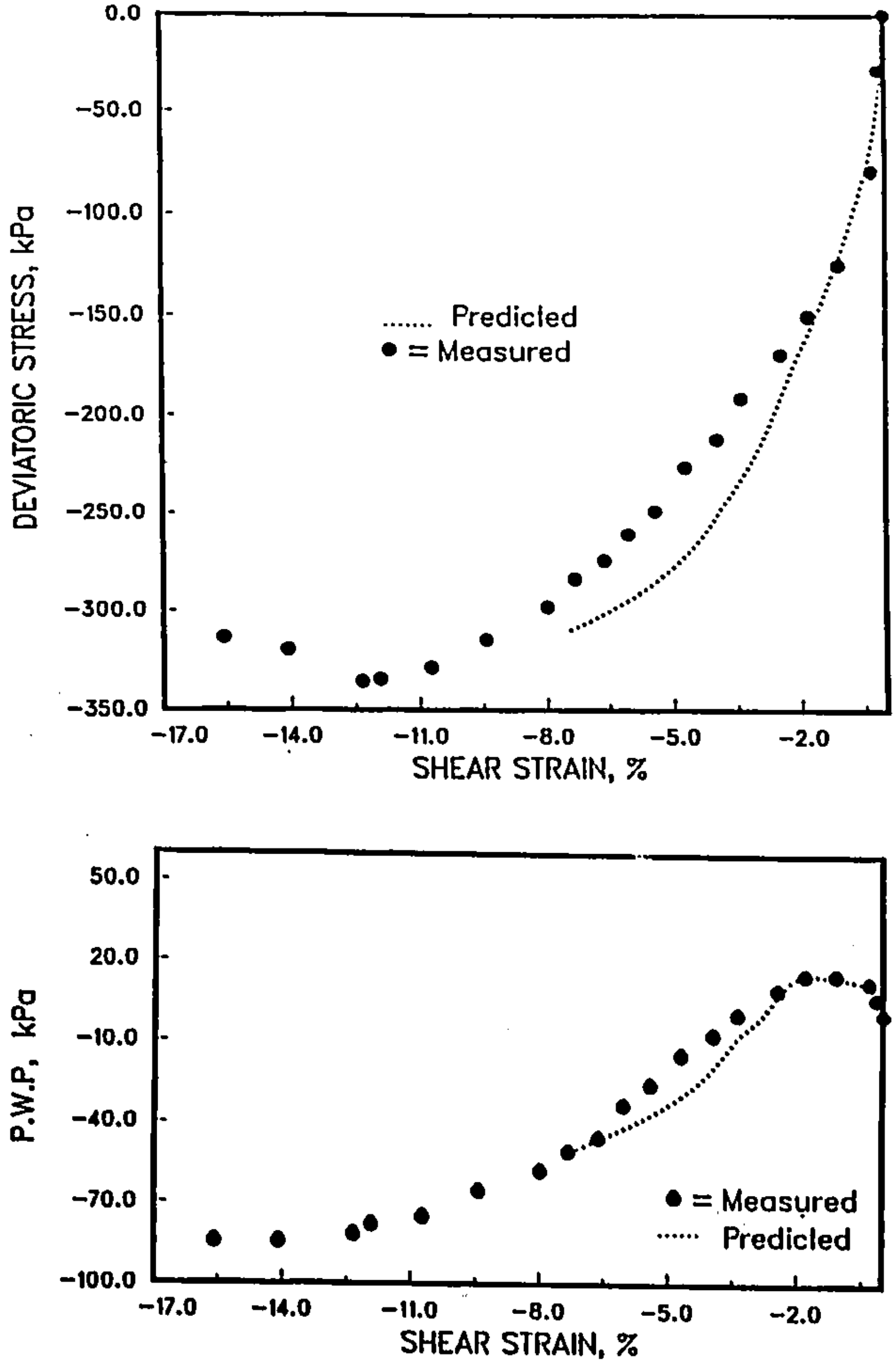

Figure D.22: Undrained CTE test #22.

Comparison of predicted and measured stress strain pore water pressure curves, medium-dense sample of crushed quartz sand, $(\sigma_3)_{initial} = 137.89kPa$.

a) Shear stress strain curves.

b) Pore water pressure versus shear strain curves.

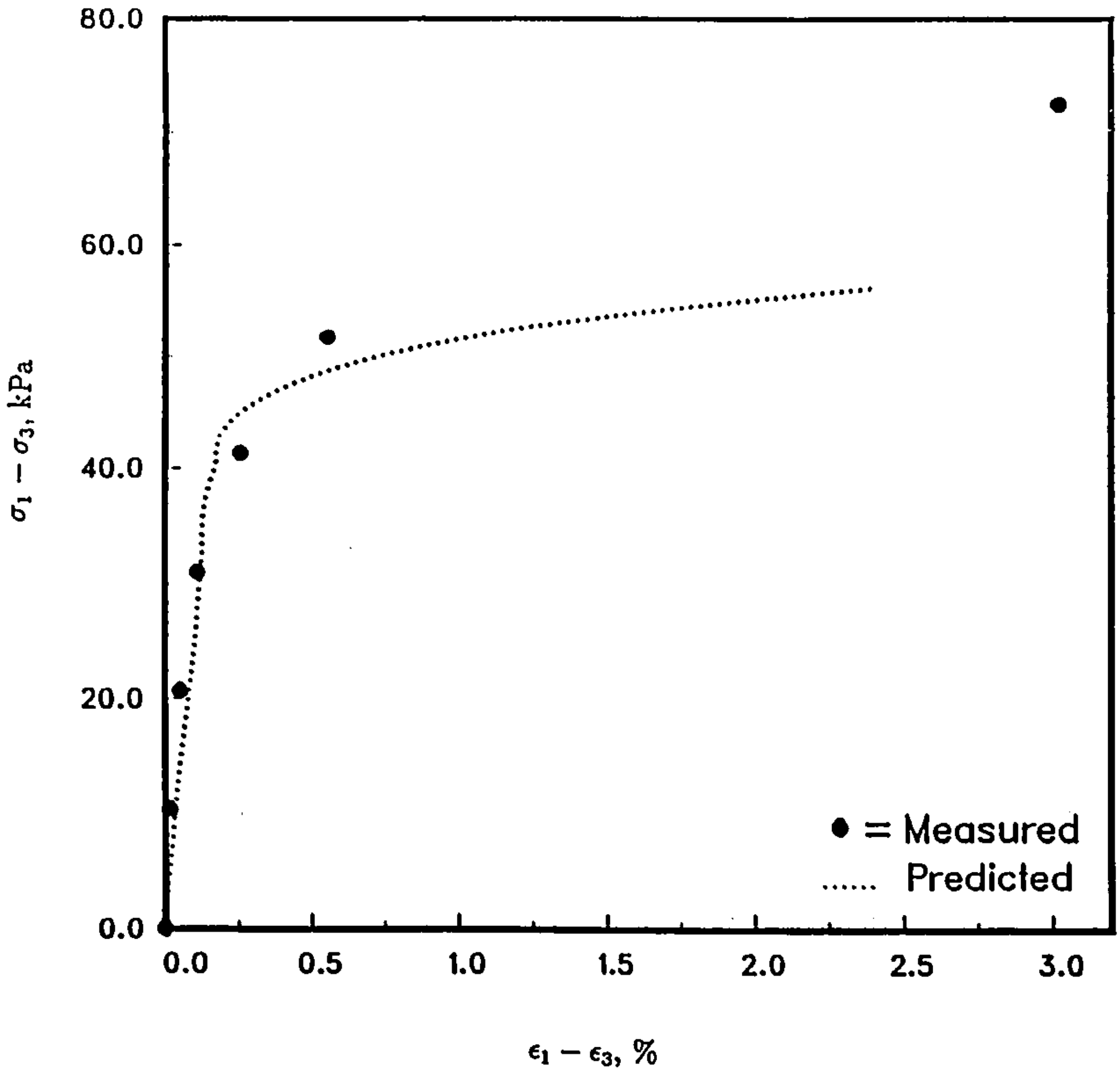

Figure D.23: Ottawa sand, TC test, constant mean pressure = $34.5kPa$. Comparison of predicted and measured shear stress strain curves. $\sigma_1 - \sigma_3$ versus $\epsilon_1 - \epsilon_3$

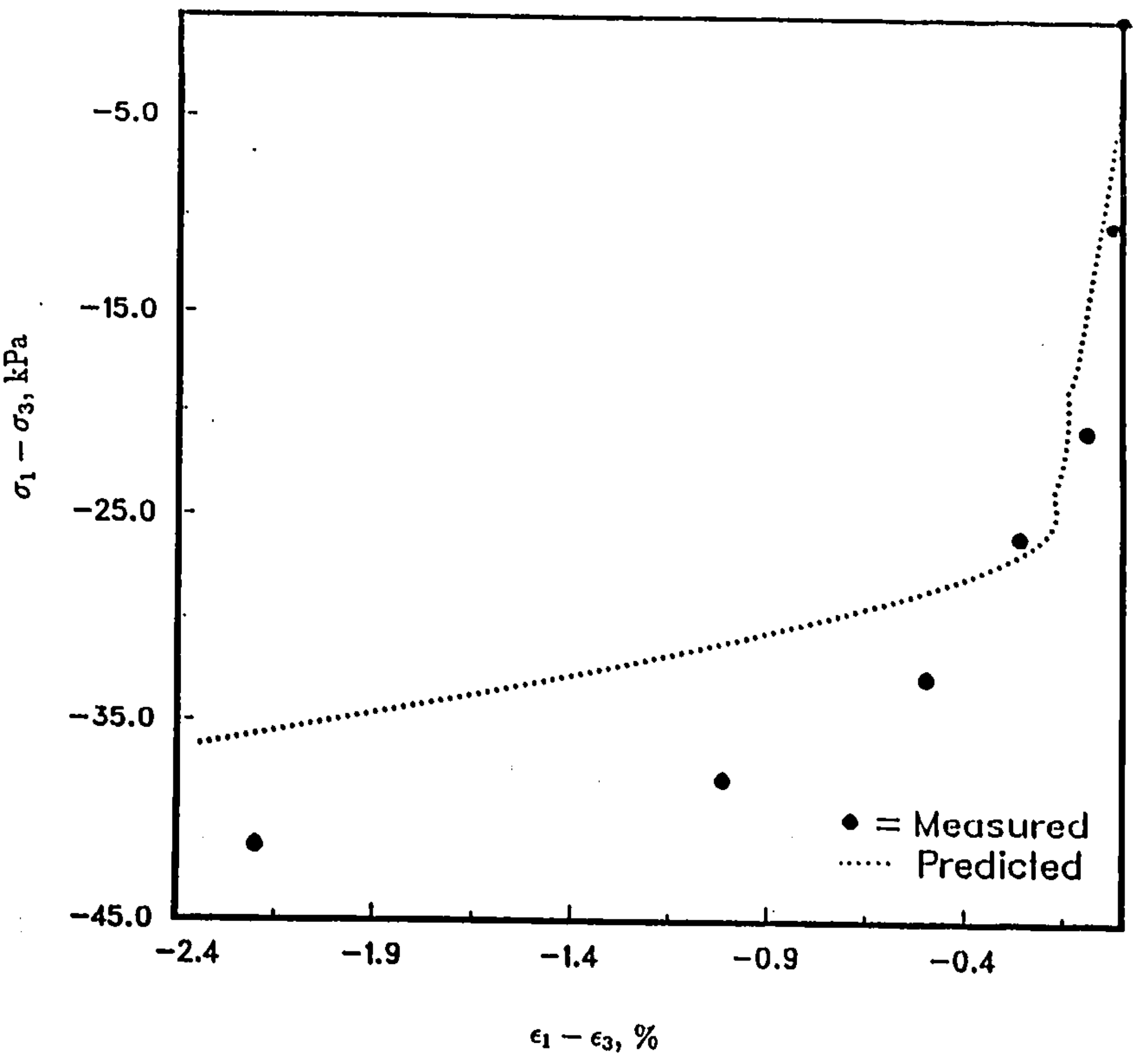

Figure D.24: Ottawa sand, TE test, constant mean pressure = $34.5kPa$. Comparison of predicted and measured shear stress strain curves. $\sigma_1 - \sigma_3$ versus $\epsilon_1 - \epsilon_3$

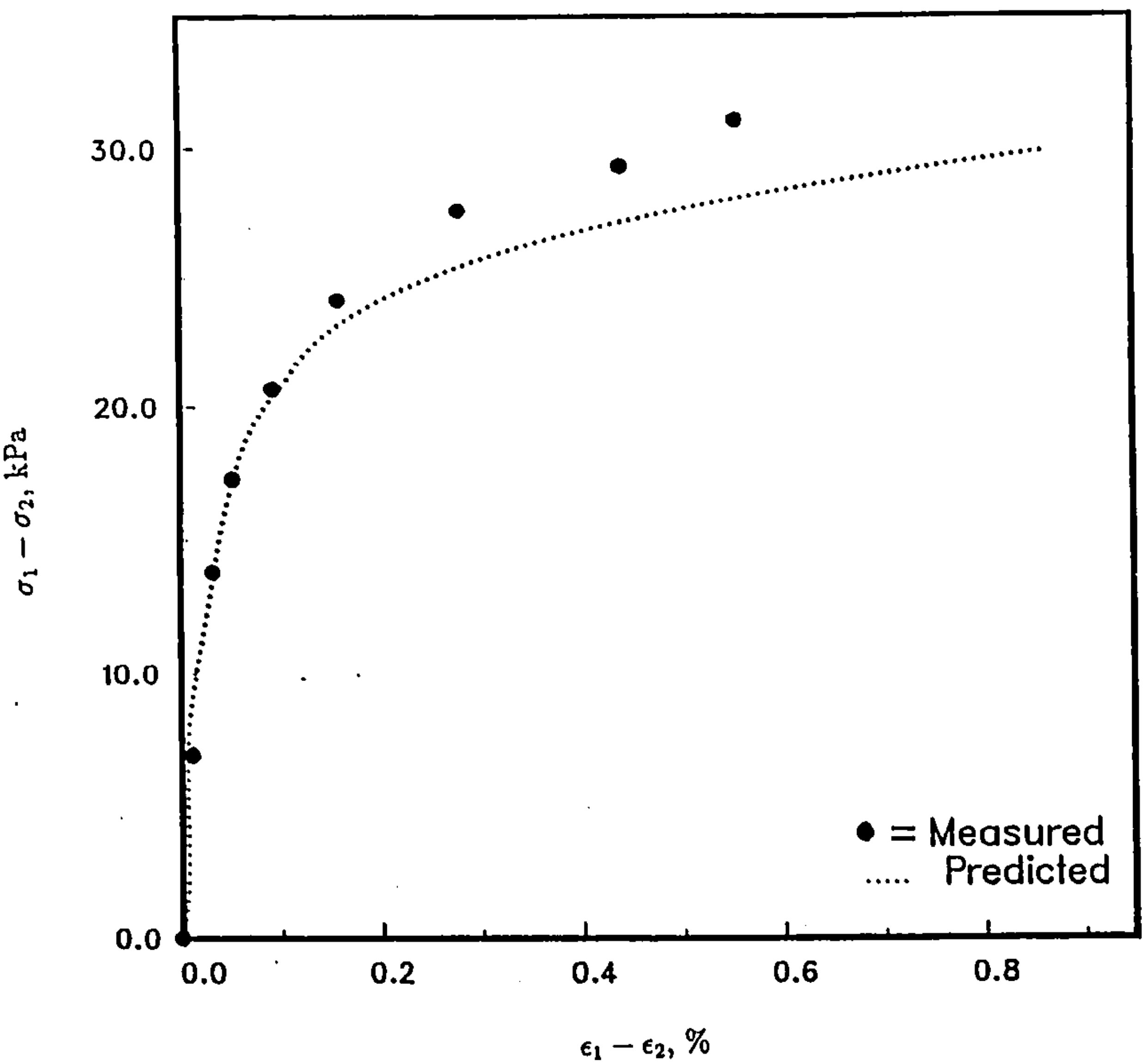

Figure D.25: Ottawa sand, SS test, constant mean pressure = $34.5kPa$. Comparison of predicted and measured shear stress strain curves. $\sigma_1 - \sigma_2$ versus $\epsilon_1 - \epsilon_2$

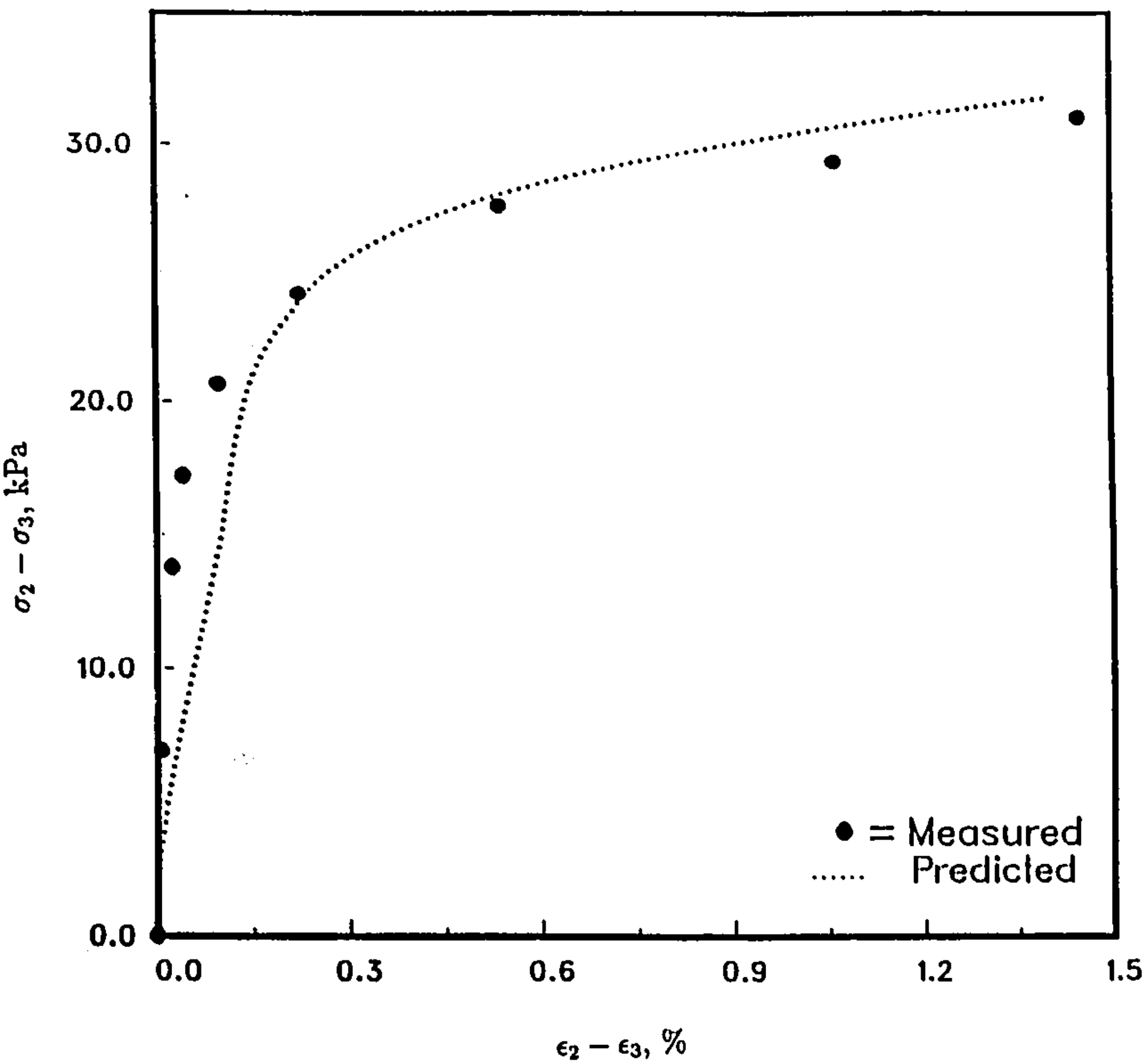

Figure D.26: Ottawa sand, SS test, constant mean pressure = $34.5kPa$. Comparison of predicted and measured shear stress strain curves. $\sigma_2 - \sigma_3$ versus $\epsilon_2 - \epsilon_3$

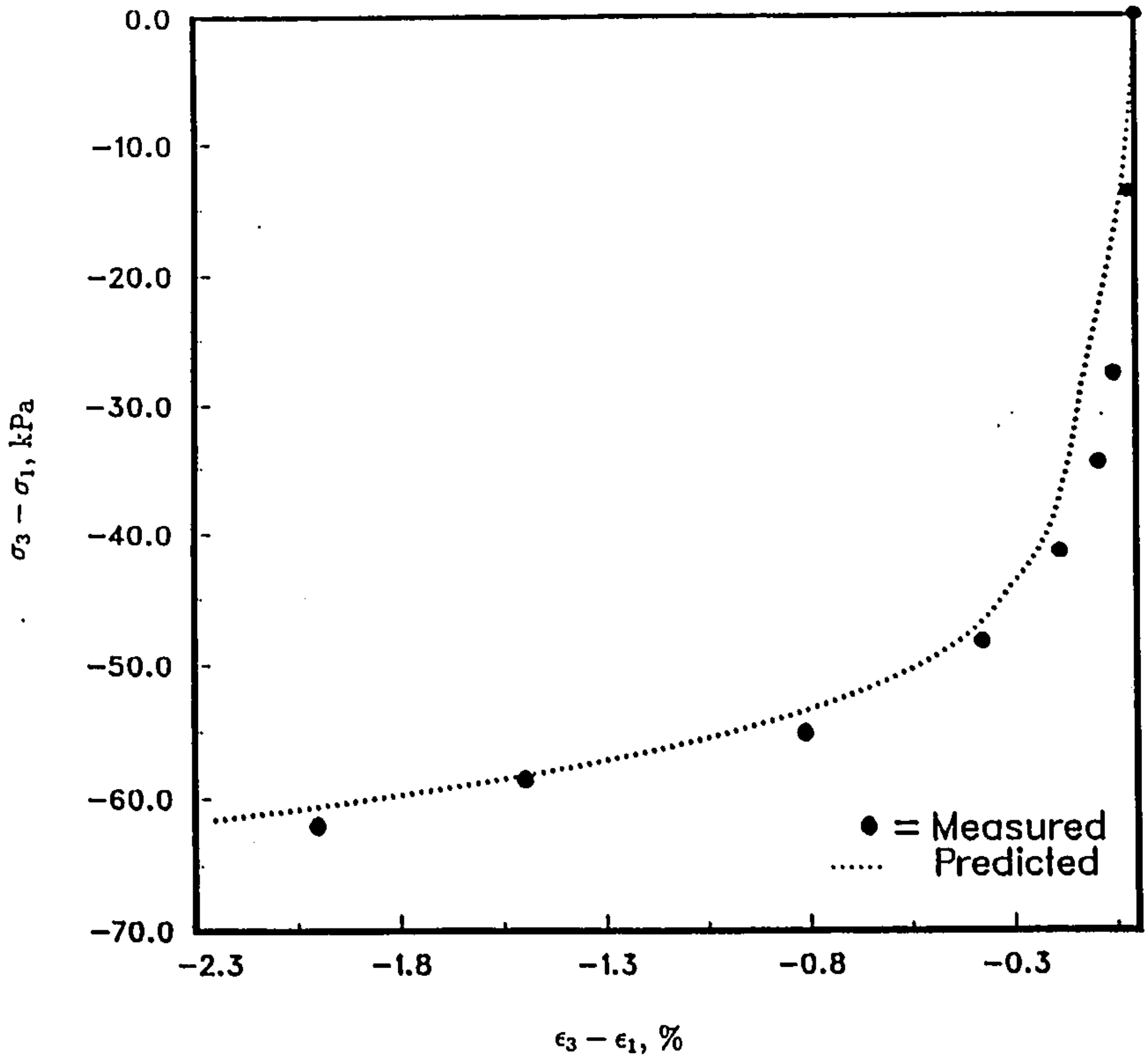

Figure D.27: Ottawa sand, SS test, constant mean pressure = $34.5kPa$. Comparison of predicted and measured shear stress strain curves. $\sigma_3 - \sigma_1$ versus $\epsilon_3 - \epsilon_1$

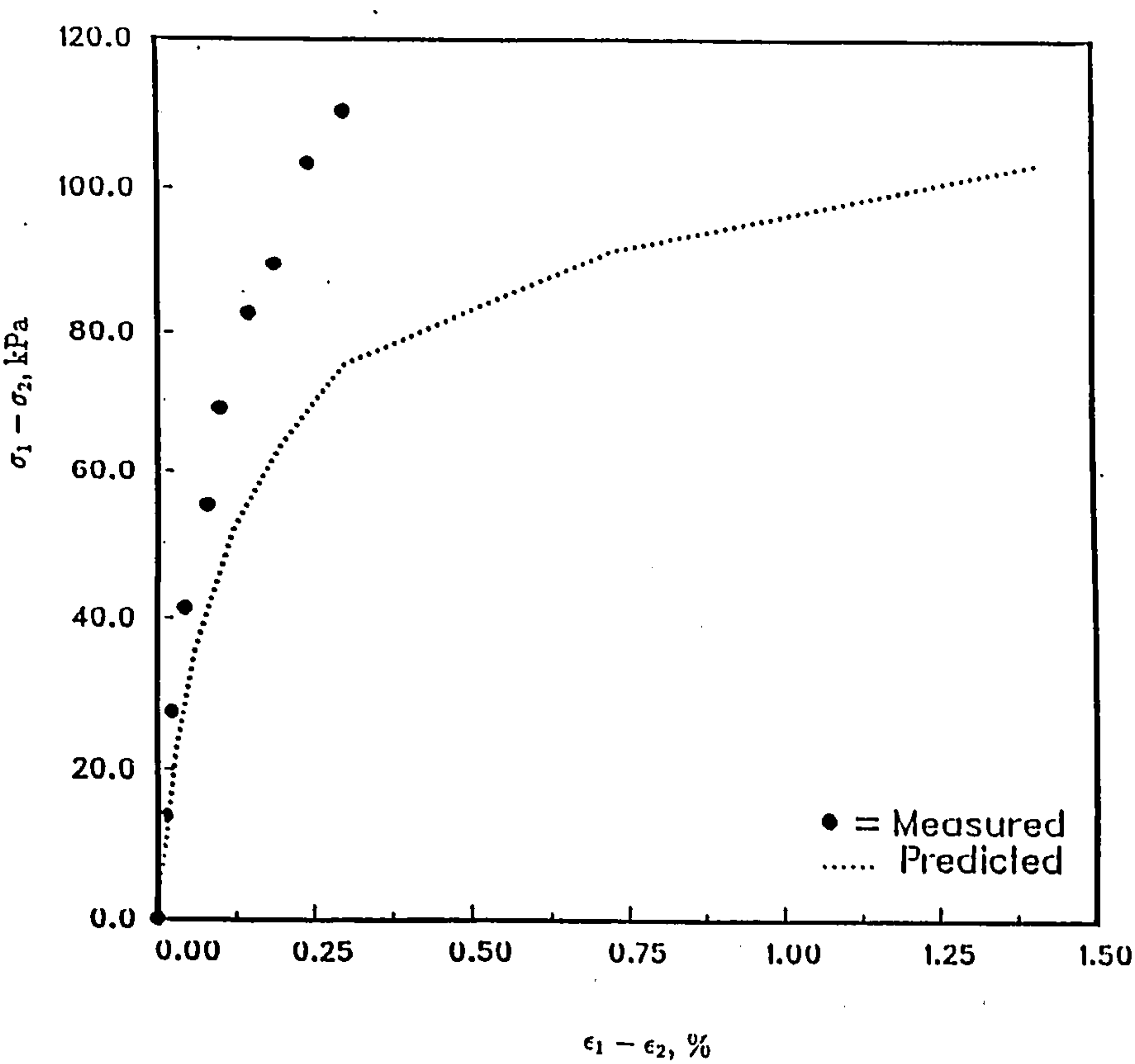

Figure D.28: Ottawa sand, SS test, constant mean pressure = $137.89 kPa$. Comparison of predicted and measured shear stress strain curves. $\sigma_1 - \sigma_2$ versus $\epsilon_1 - \epsilon_2$

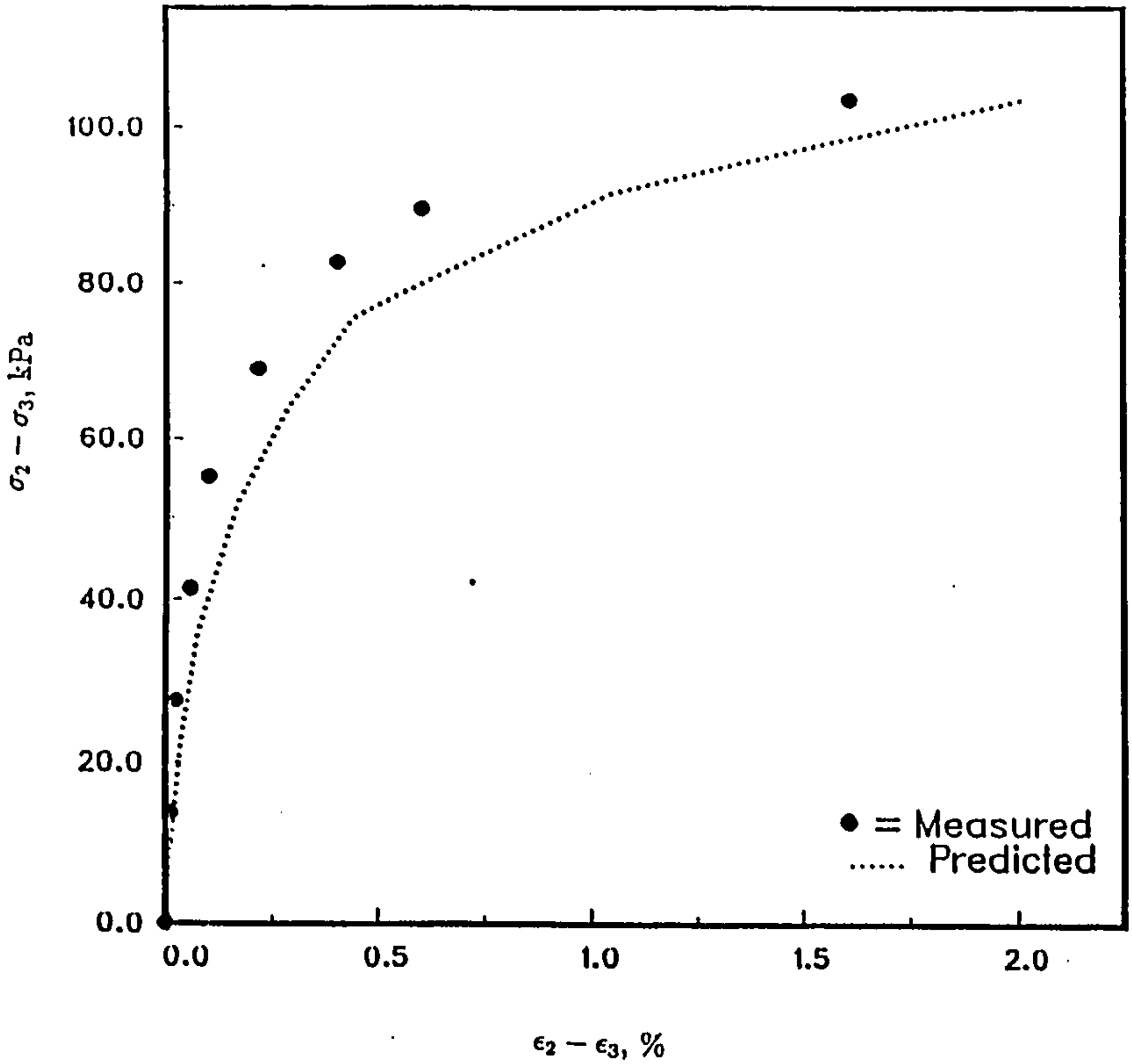

Figure D.29: Ottawa sand, SS test, constant mean pressure = $137.89kPa$. Comparison of predicted and measured shear stress strain curves. $\sigma_2 - \sigma_3$ versus $\epsilon_2 - \epsilon_3$

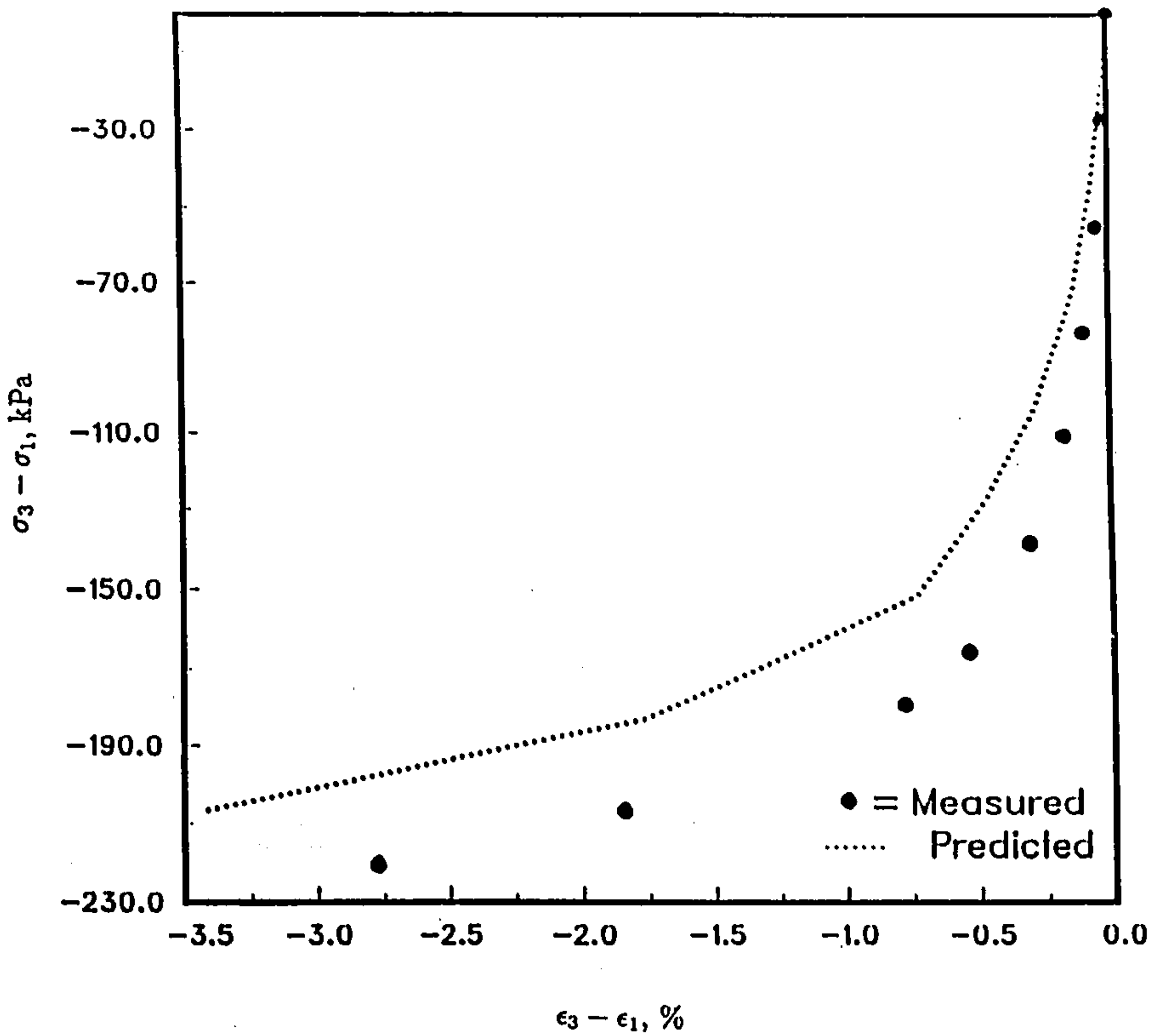

Figure D.30: Ottawa sand, SS test, constant mean pressure = $137.89kPa$. Comparison of predicted and measured shear stress strain curves. $\sigma_3 - \sigma_1$ versus $\epsilon_3 - \epsilon_1$

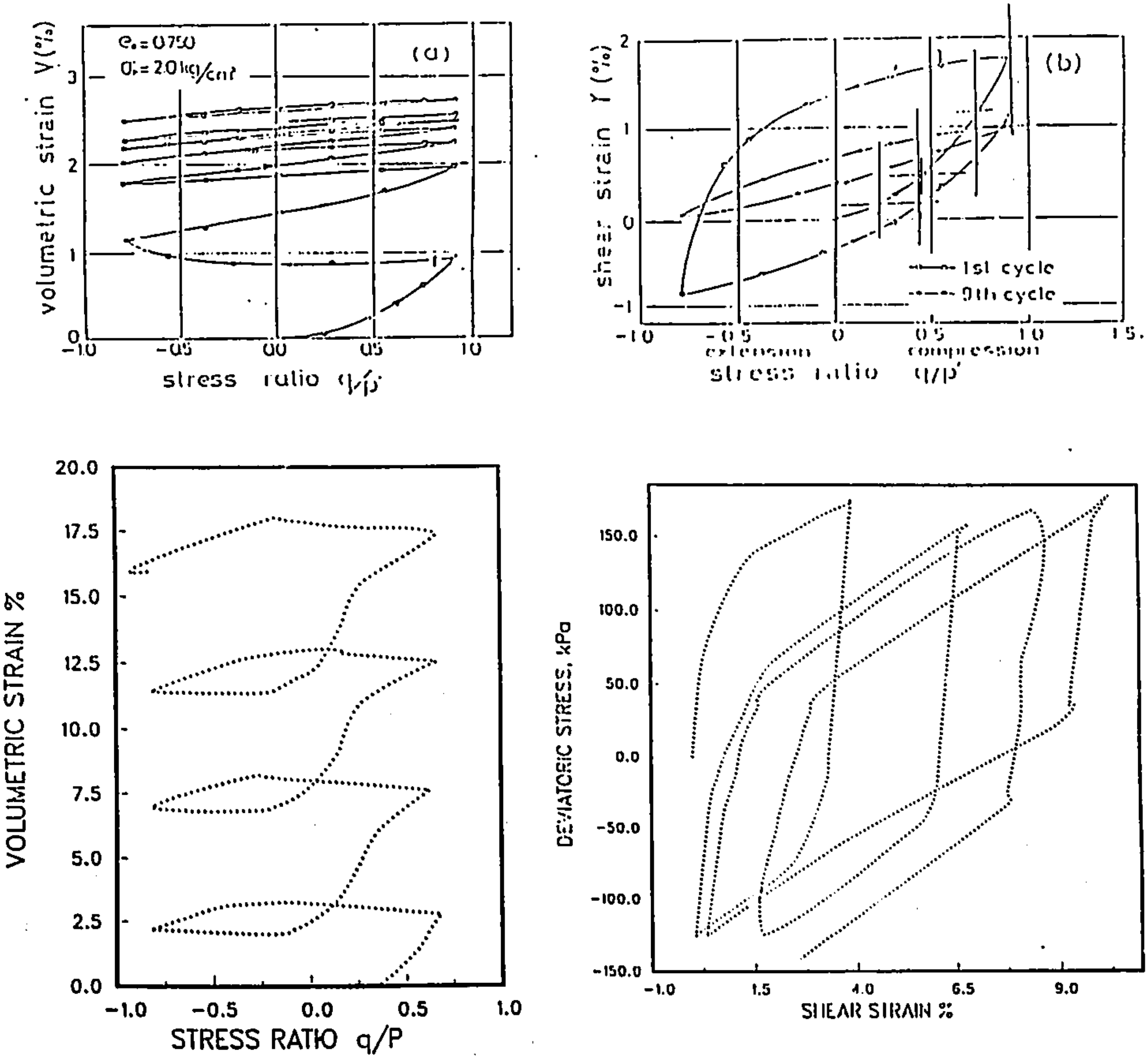

Figure D.31: Drained Cyclic test.
Comparison of predicted and measured shear stress strain curves, loose sample of Fuji river sand, $\sigma_3 = 196.14$ kPa.

Appendix E

AN EVALUATION OF THE ADDITIONAL CAPABILITIES OF THE MODEL

This Appendix presents the results of the theoretical investigation discussed in Chapter 9. The figures are presented in the following sequence:

1. Figures regarding the strain softening.
2. Figures regarding the shakedown phenomenon.
3. Figures regarding the small amplitude cyclic loading.
4. Figures regarding the large amplitude cyclic loading.
5. Figures regarding the variable amplitude cyclic loading.

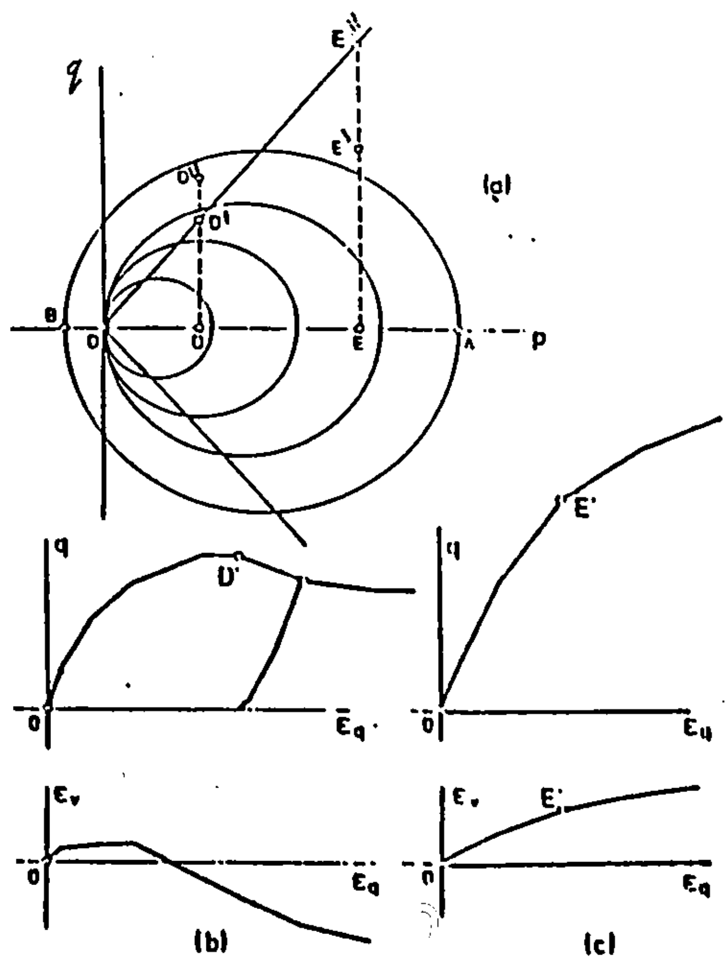

Figure E.1: Typical predicted softening and hardening of the stress strain curve.
a) Geometric representation of the stress space including the stress paths D-D', E-E'' and the critical state line O-E''.
b) Typical stress-strain curve regarding the stress path D-D'.
c) Typical stress-strain curve regarding the stress path E-E''.

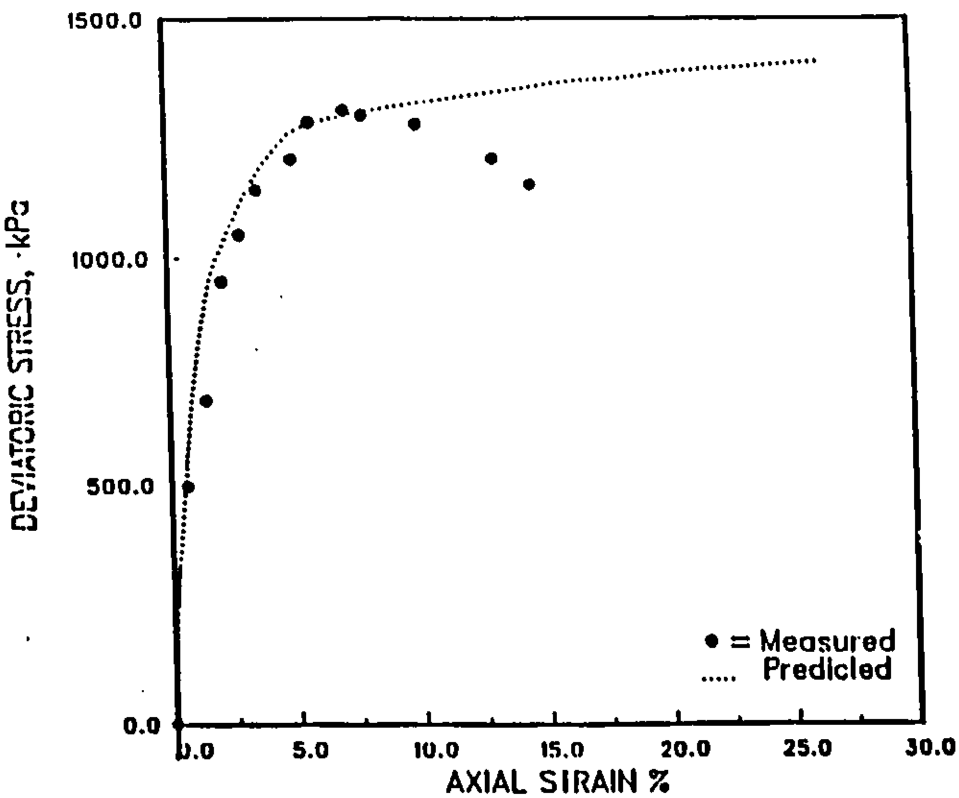

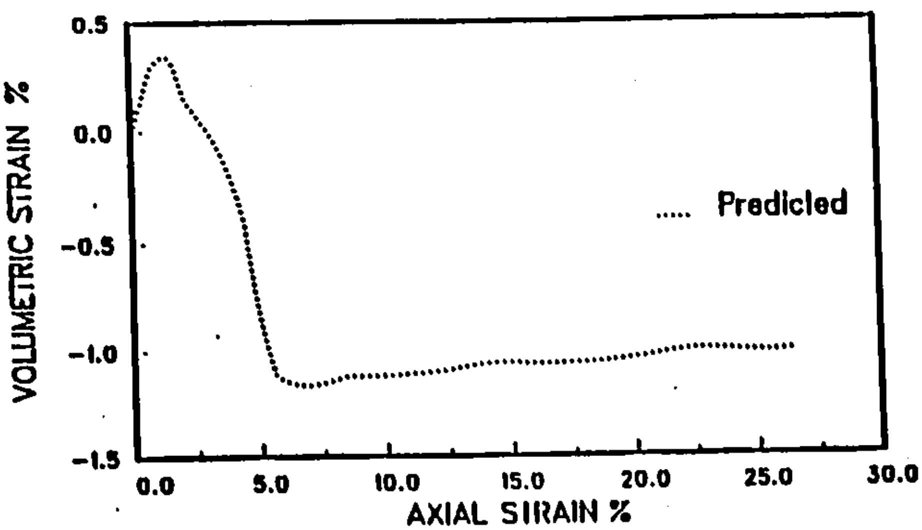

Figure E.2: Comparison of the predicted and measured stress-strain curve of drained CTC test, a dense soil sample of crushed quartz sand $\sigma_3 = 344.72kPa$.

a) Shear stress strain curves.

b) Volumetric strain versus axial strain curves.

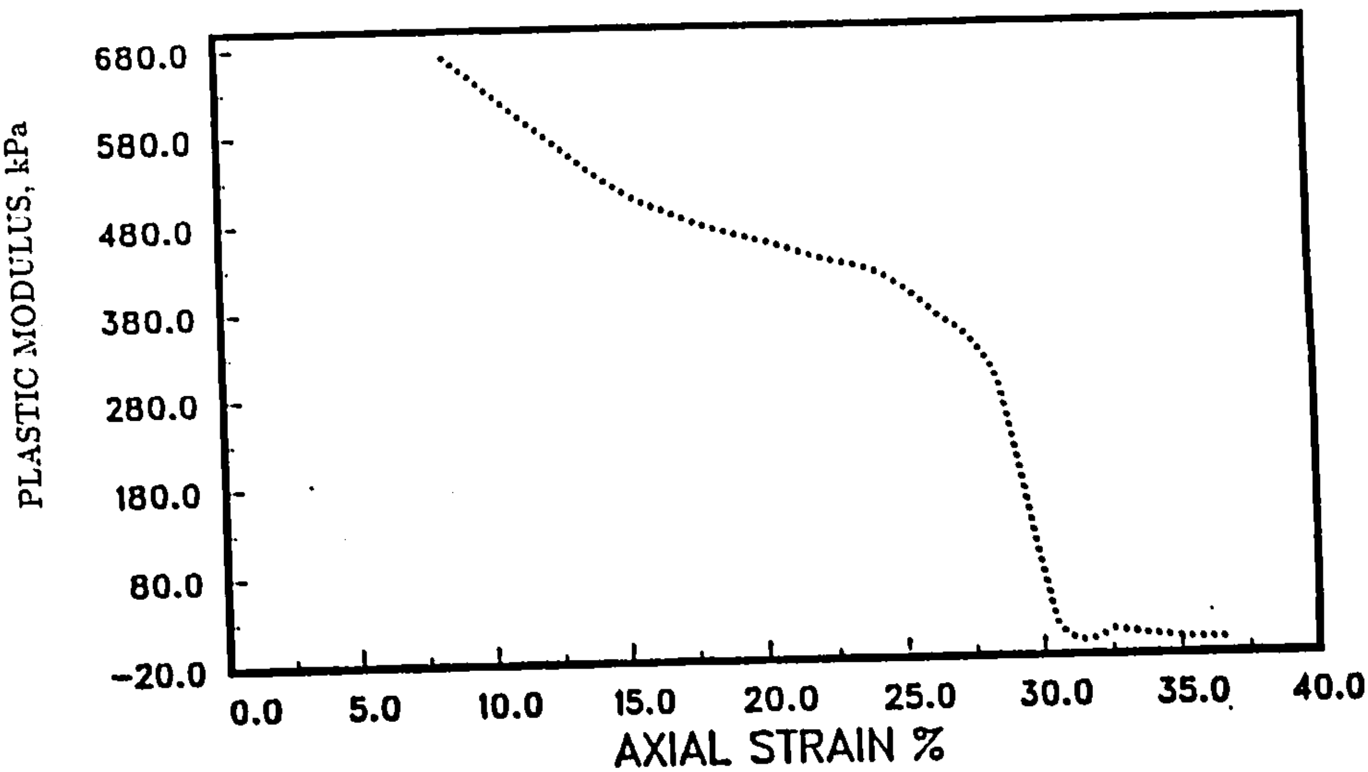

Figure E.3: Variation of the plastic modulus related to the outermost yield surface of the test shown in Fig E.2.
Plastic moduli versus axial strain plot.

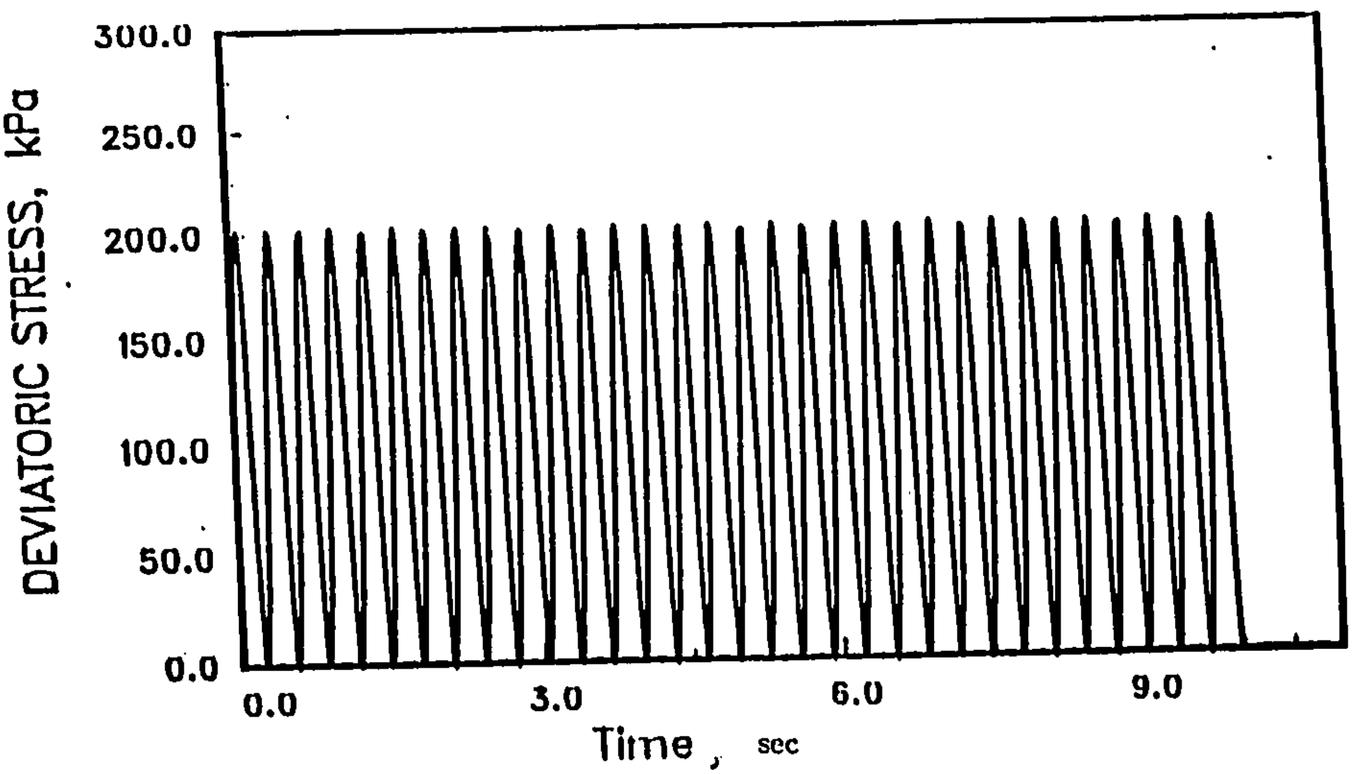

Figure E.4: Cyclic input data

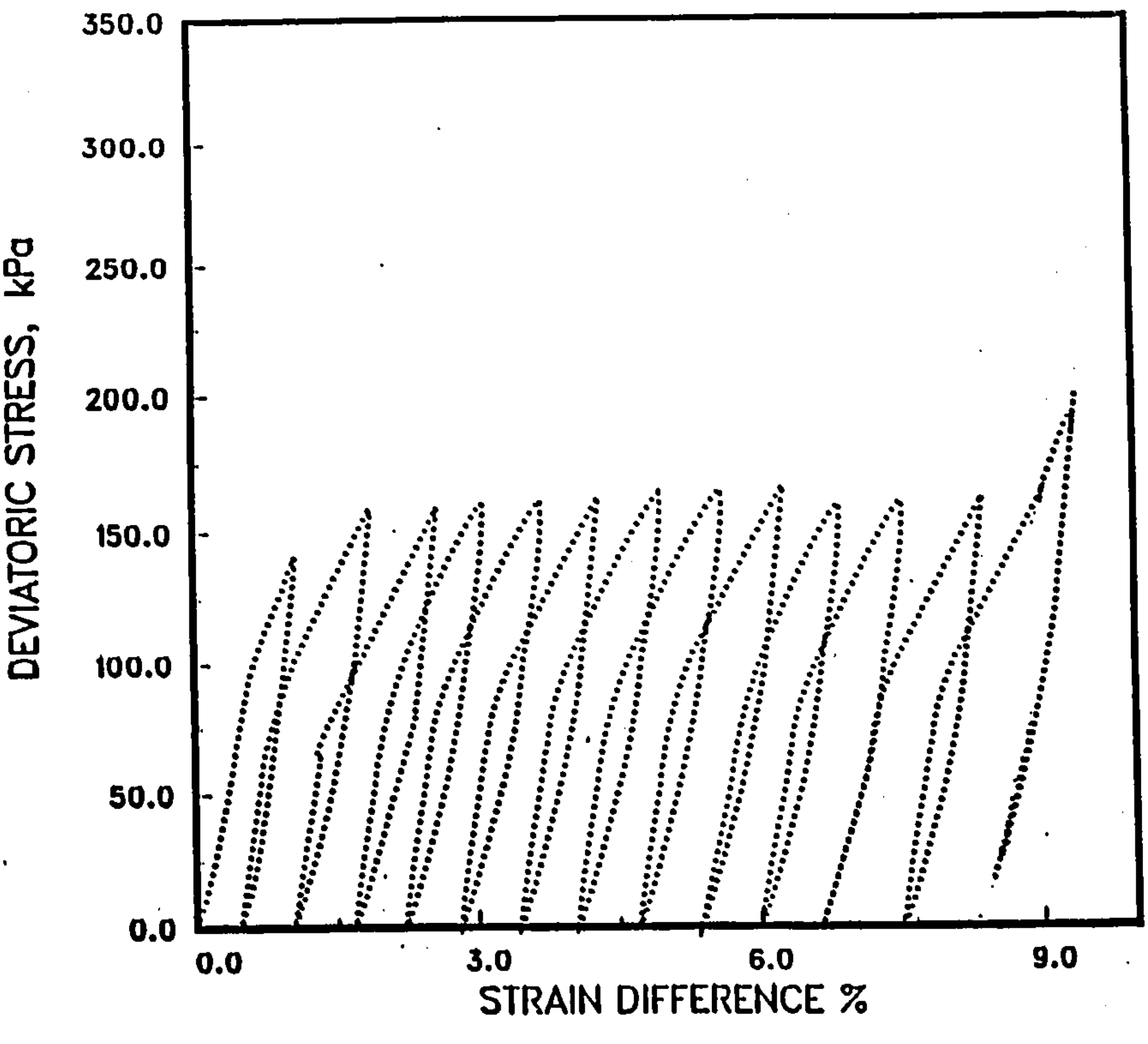

Figure E.5: Model simulation of the shear stress versus shear strain curve.

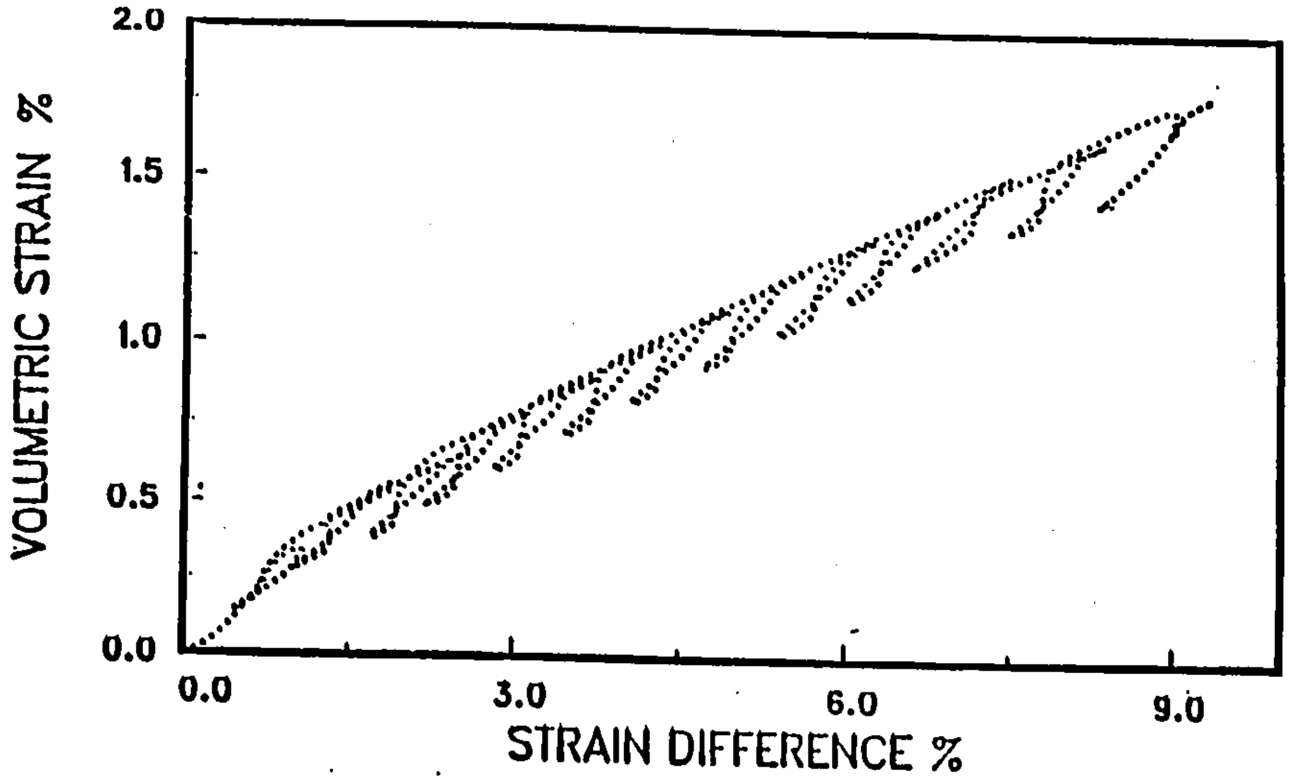

Figure E.6: Model simulation of the volumetric strain.

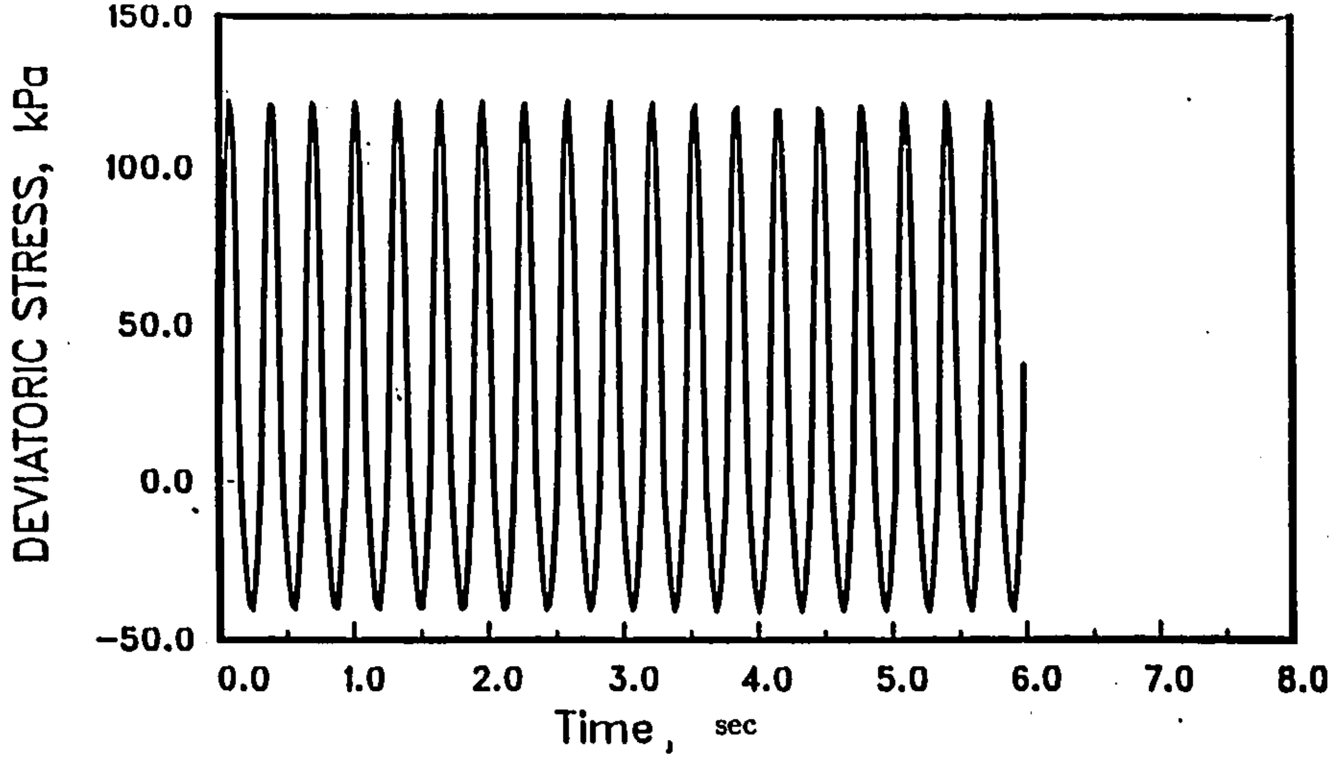

Figure E.7: Small amplitude cyclic loading input data

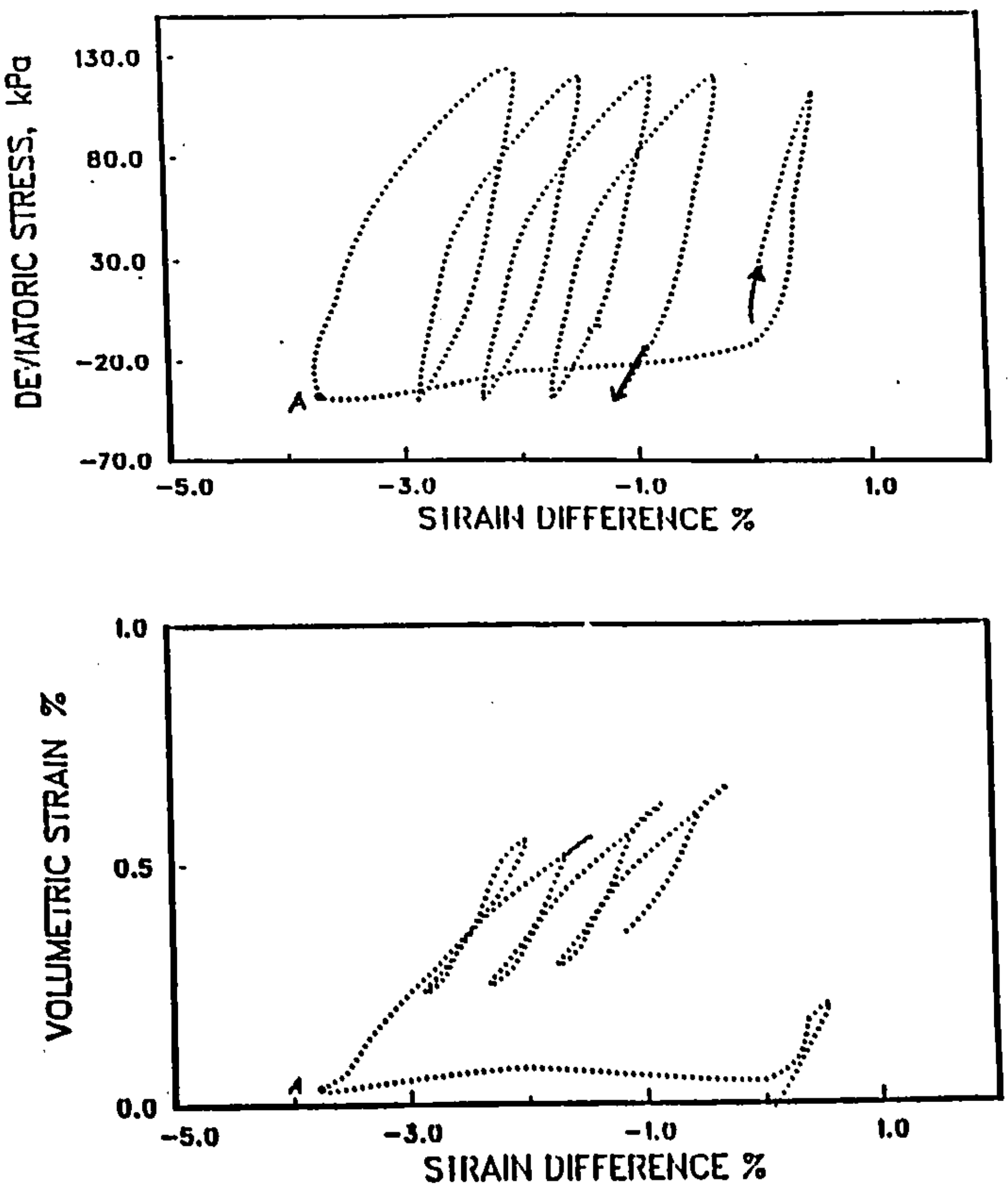

Figure E.8: Model simulation of the shear stress strain and the volumetric strain versus shear strain curves for small amplitude cyclic loading.

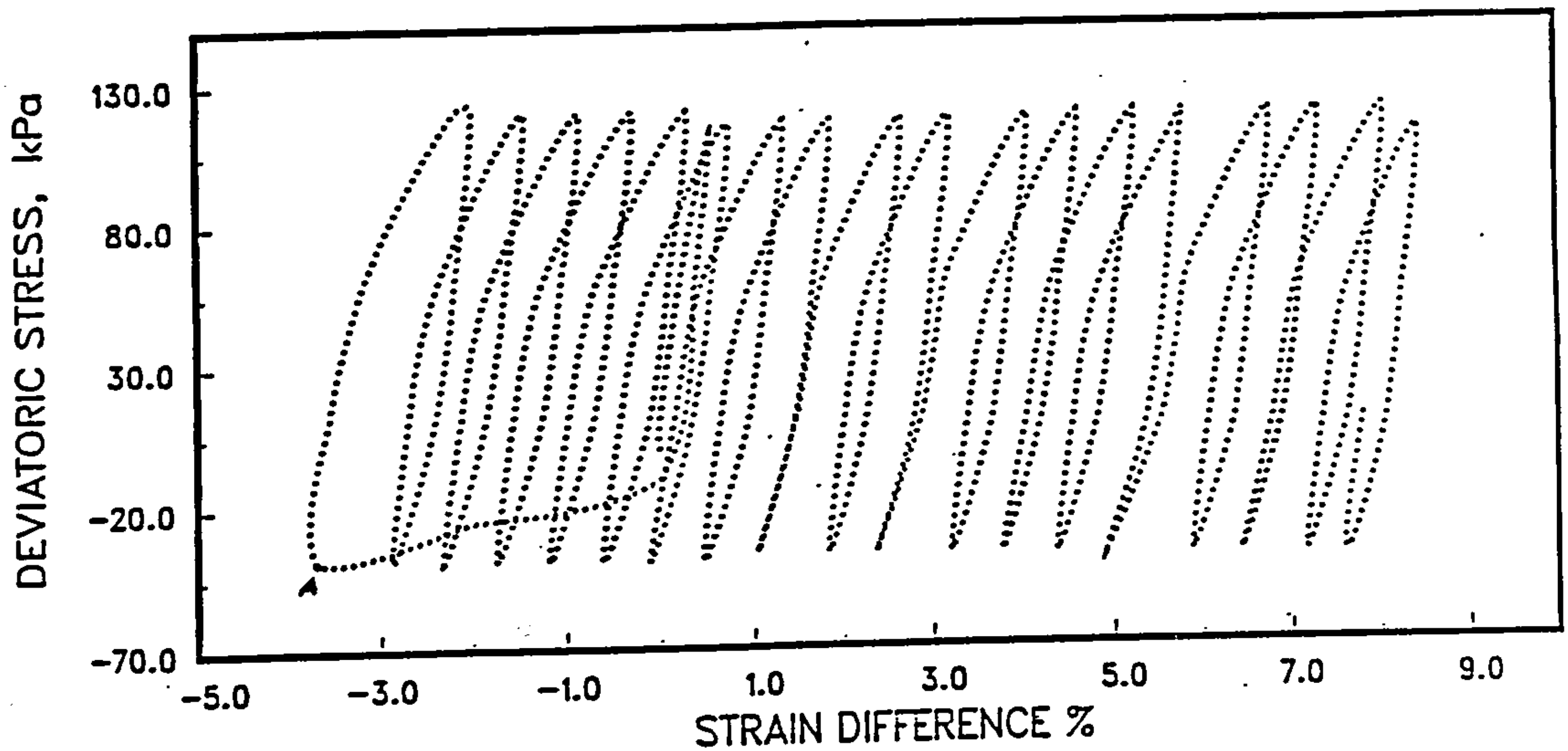

Figure E.9: Model simulation of the shear stress versus shear strain curve for small amplitude cyclic loading.

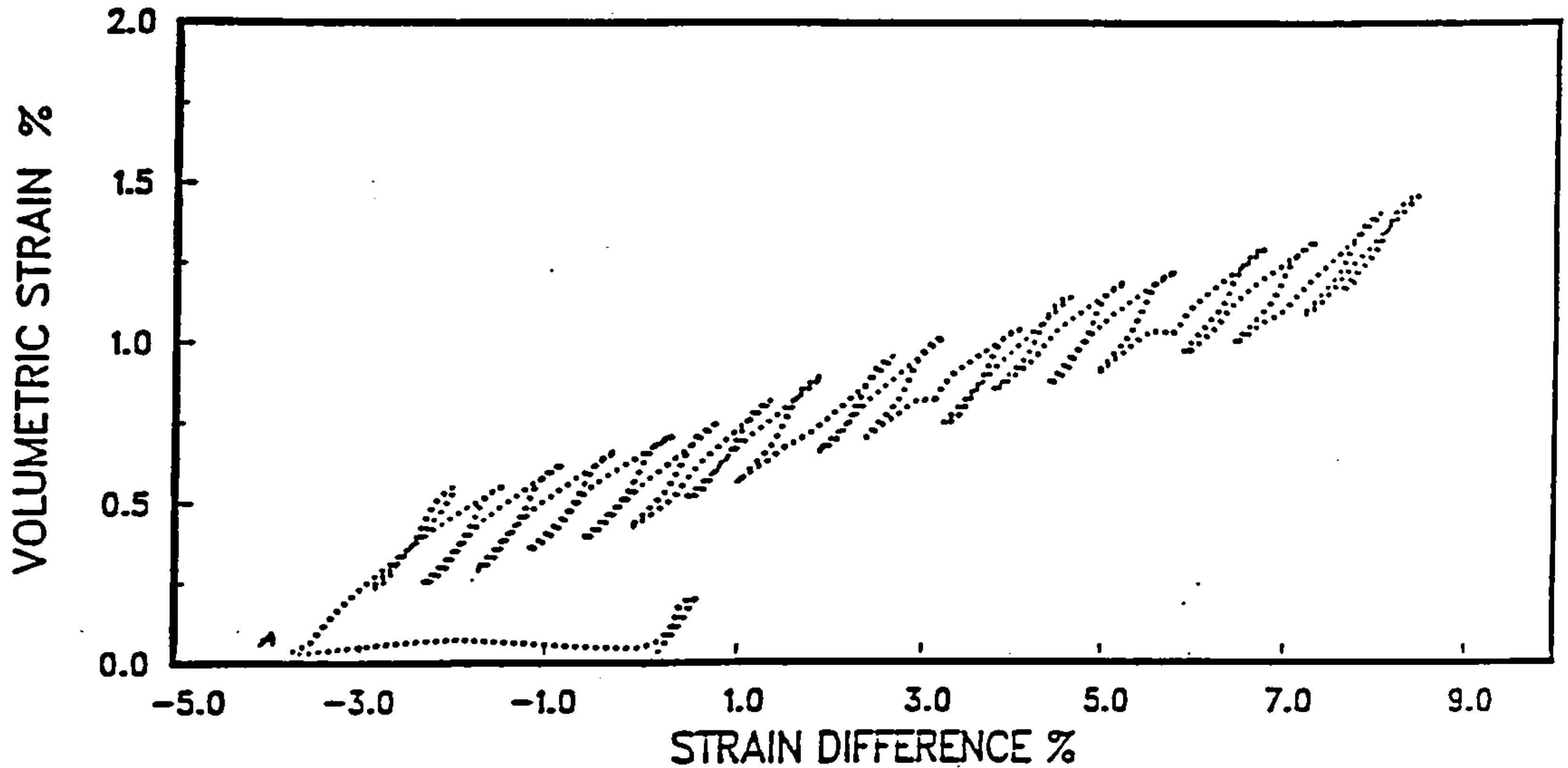

Figure E.10: Model simulation of the volumetric strain versus shear strain curve for small amplitude cyclic loading.

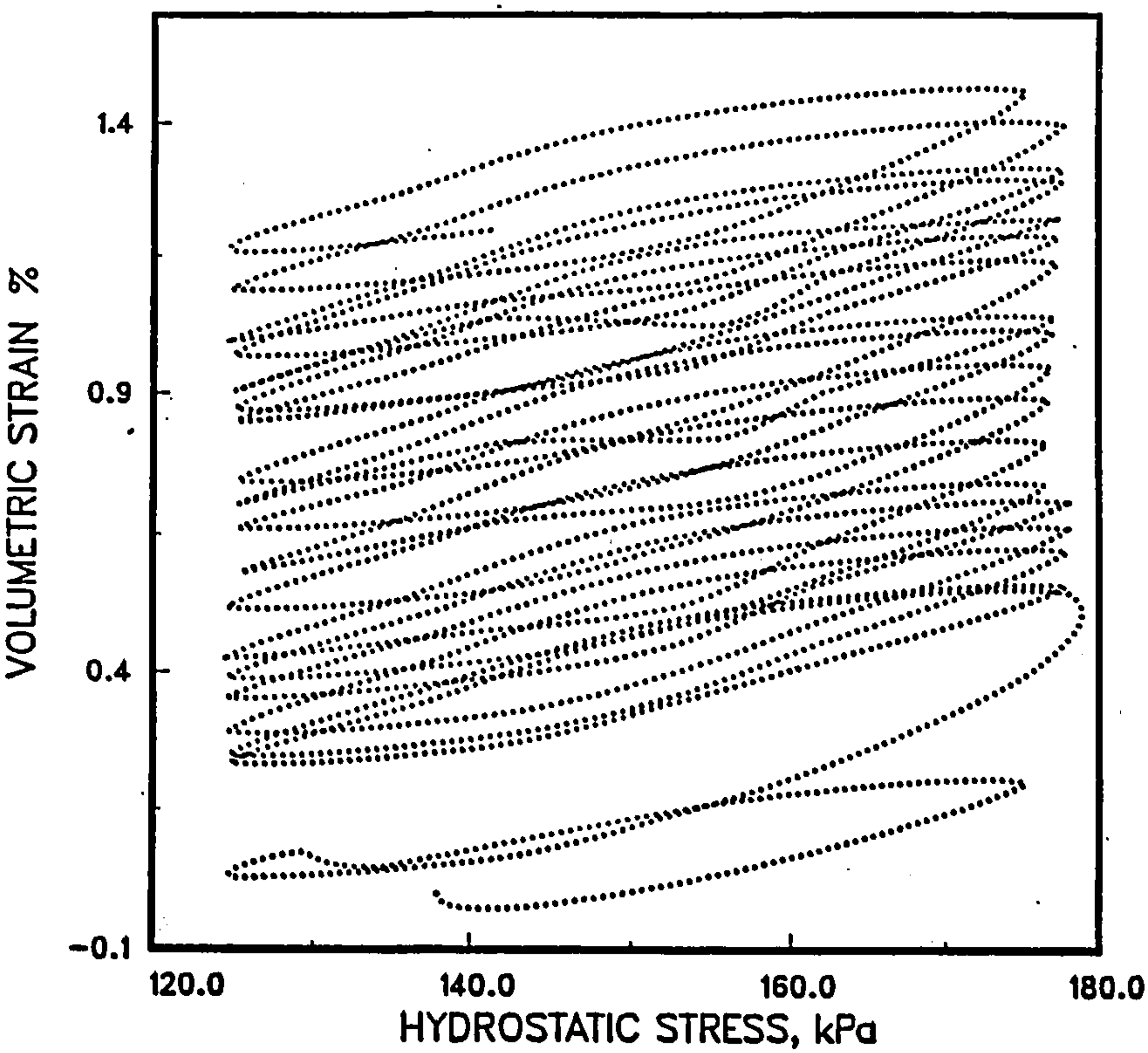

Figure E.11: Model simulation of the volumetric stress strain curve for small amplitude cyclic loading.

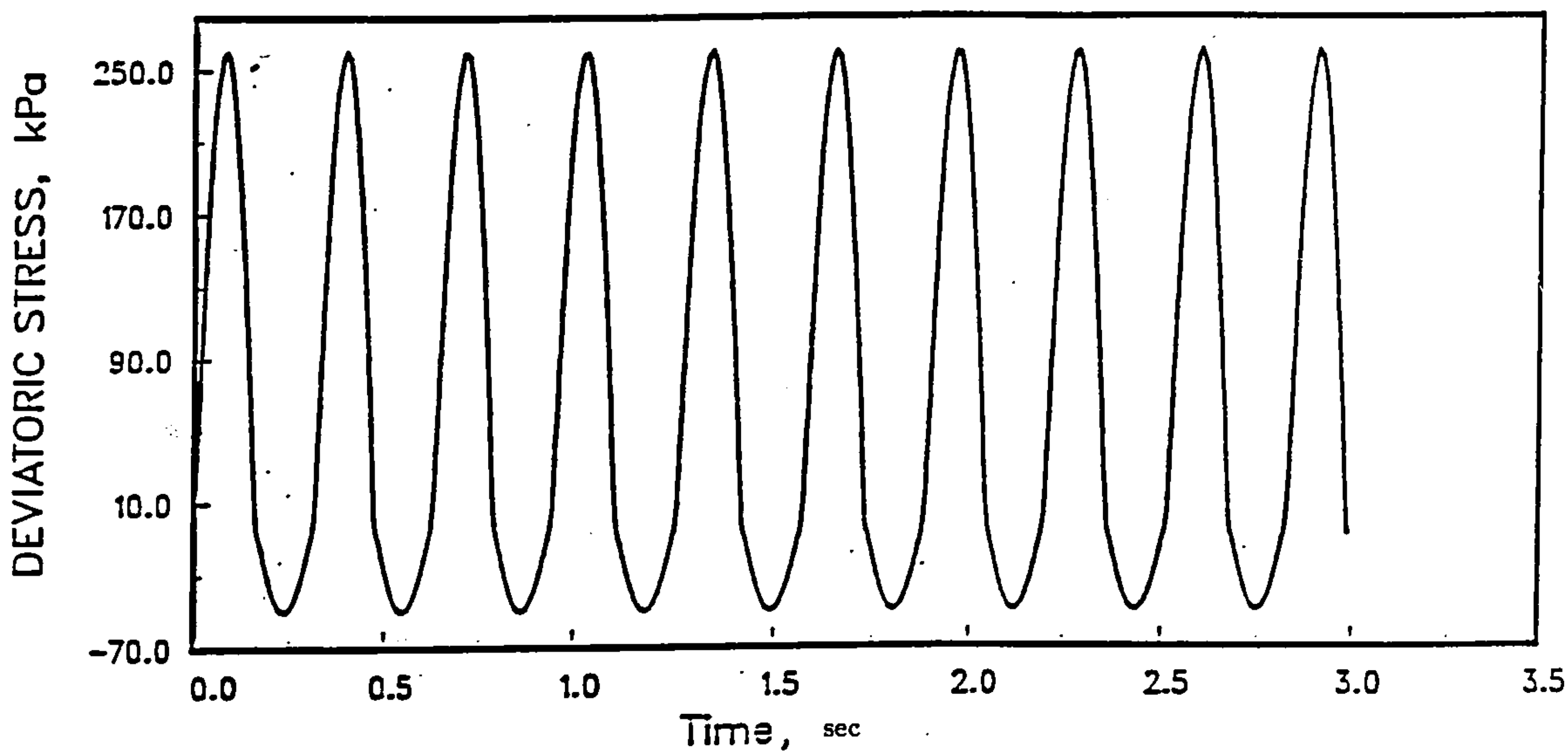

Figure E.12: Large amplitude cyclic loading input data

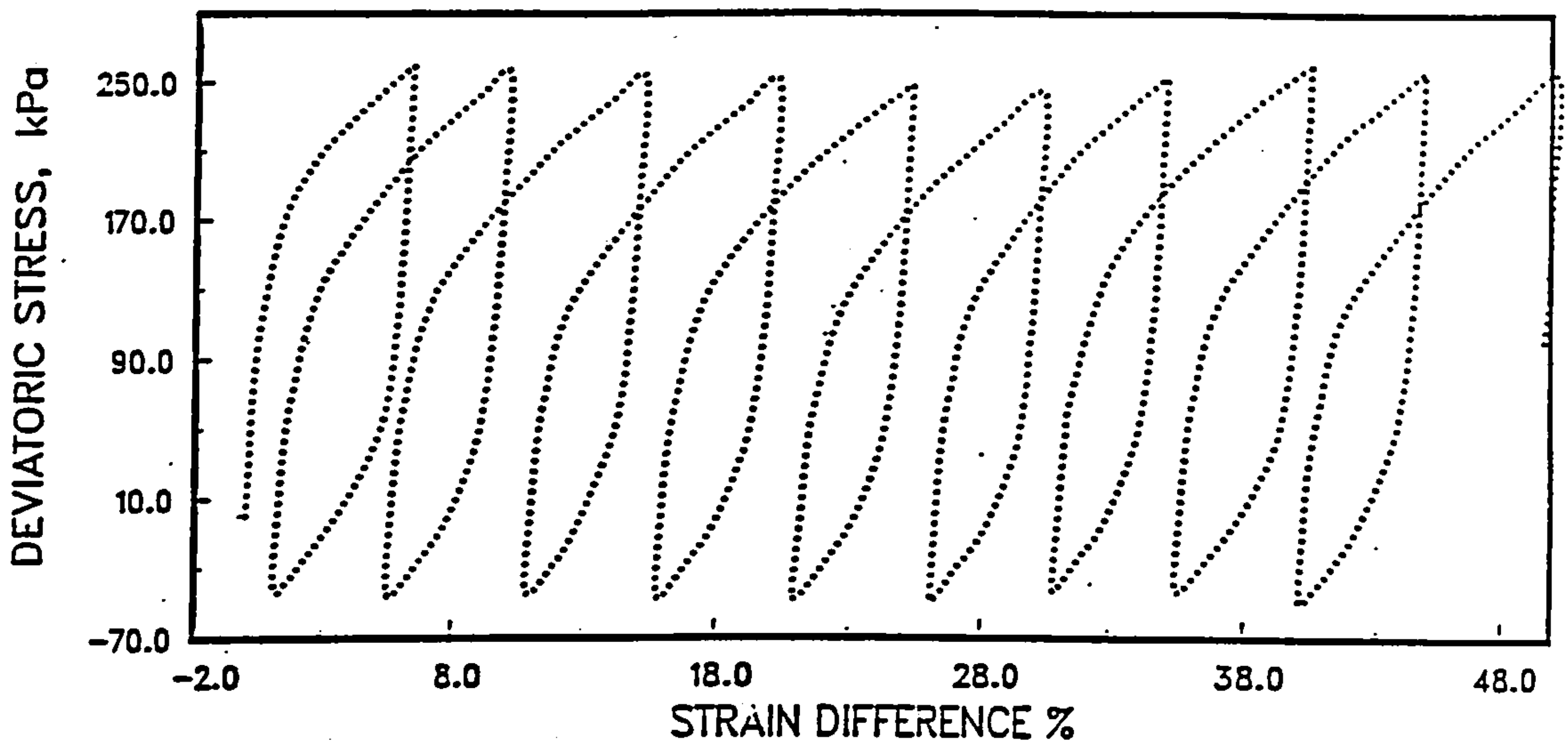

Figure E.13: Model simulation of the shear stress versus shear strain curve for large amplitude cyclic loading.

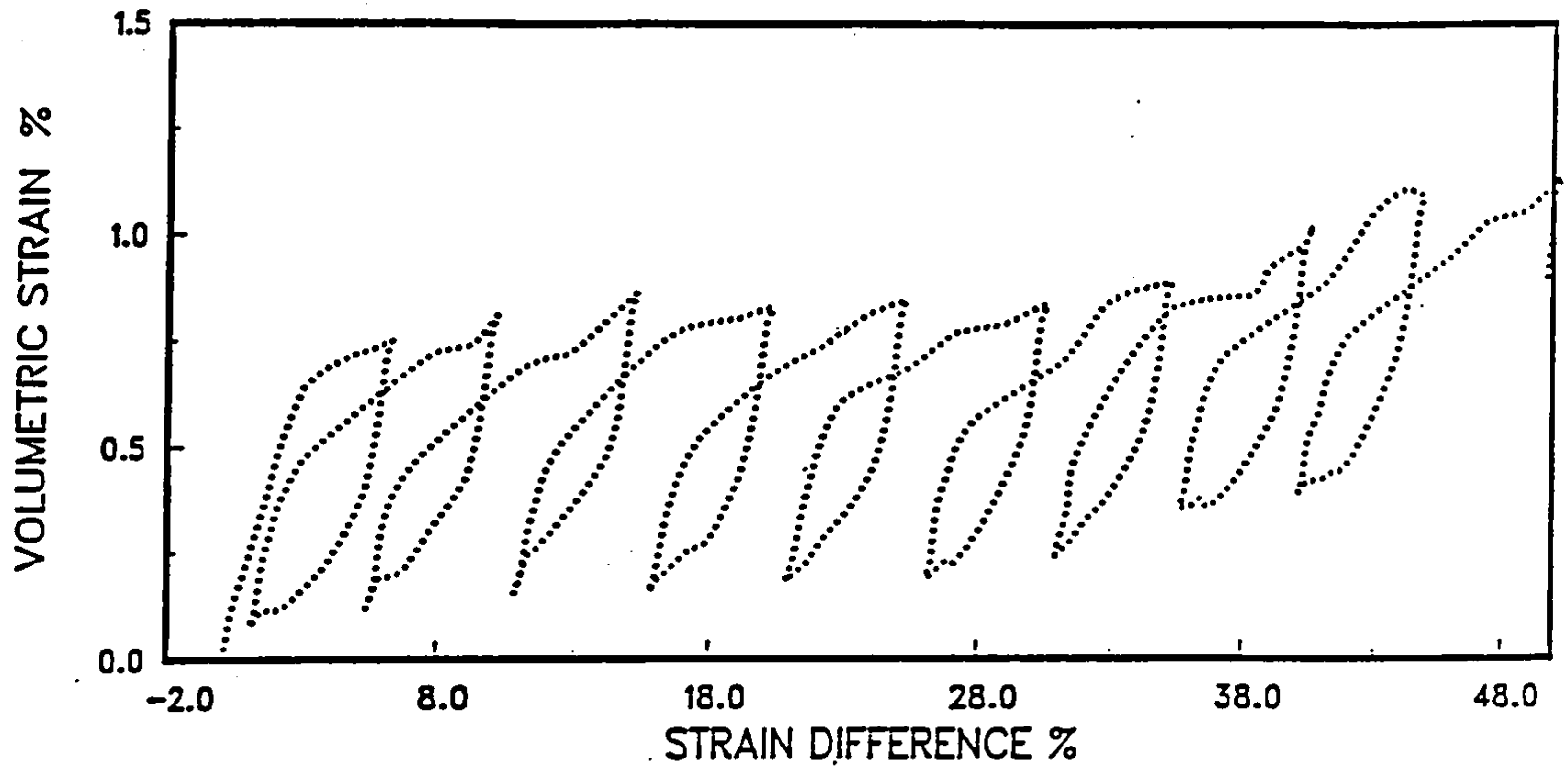

Figure E.14: Model simulation of the volumetric strain versus shear strain curve for large amplitude cyclic loading.

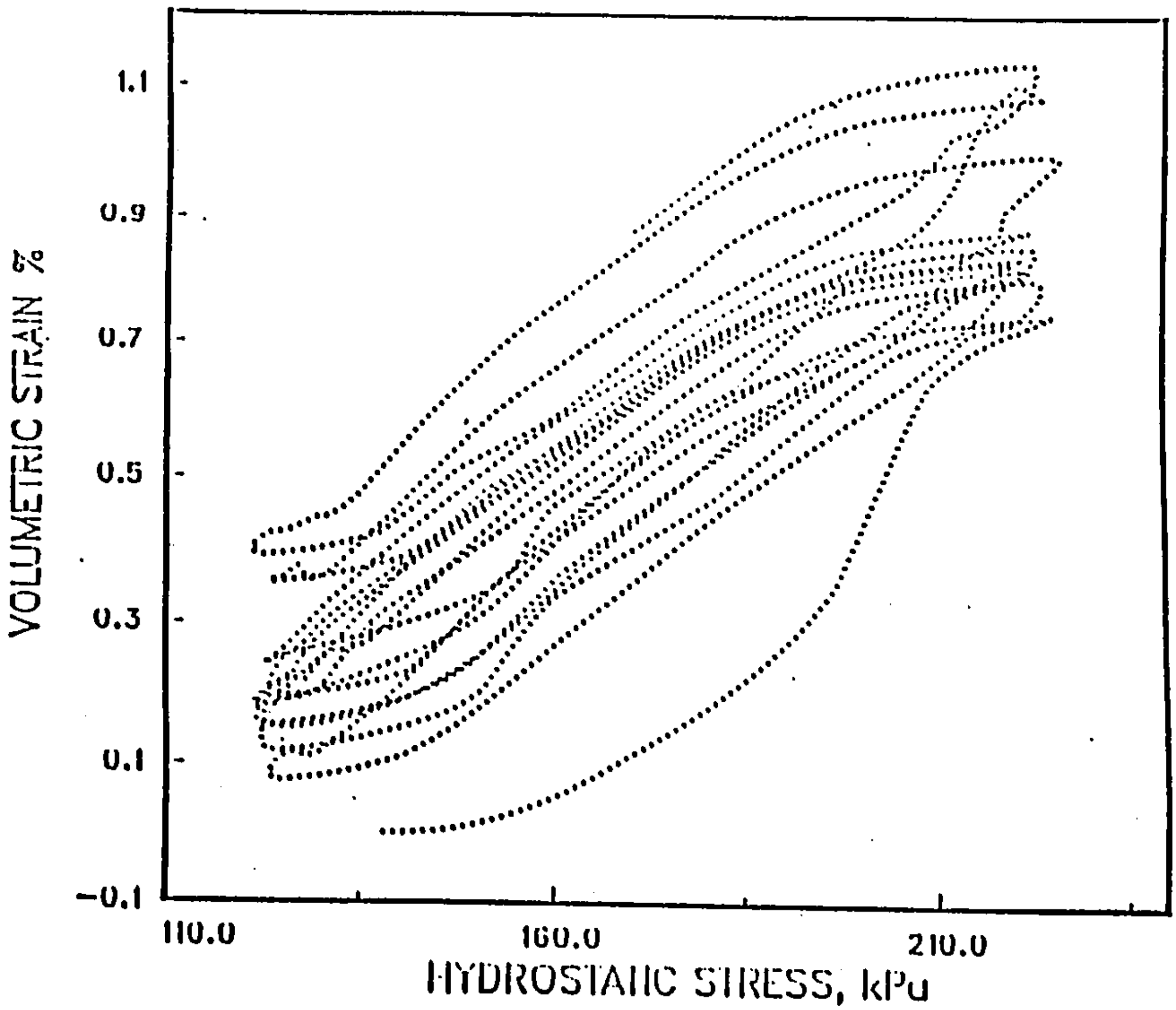

Figure E.15: Model simulation of the volumetric stress strain curve for large amplitude cyclic loading.

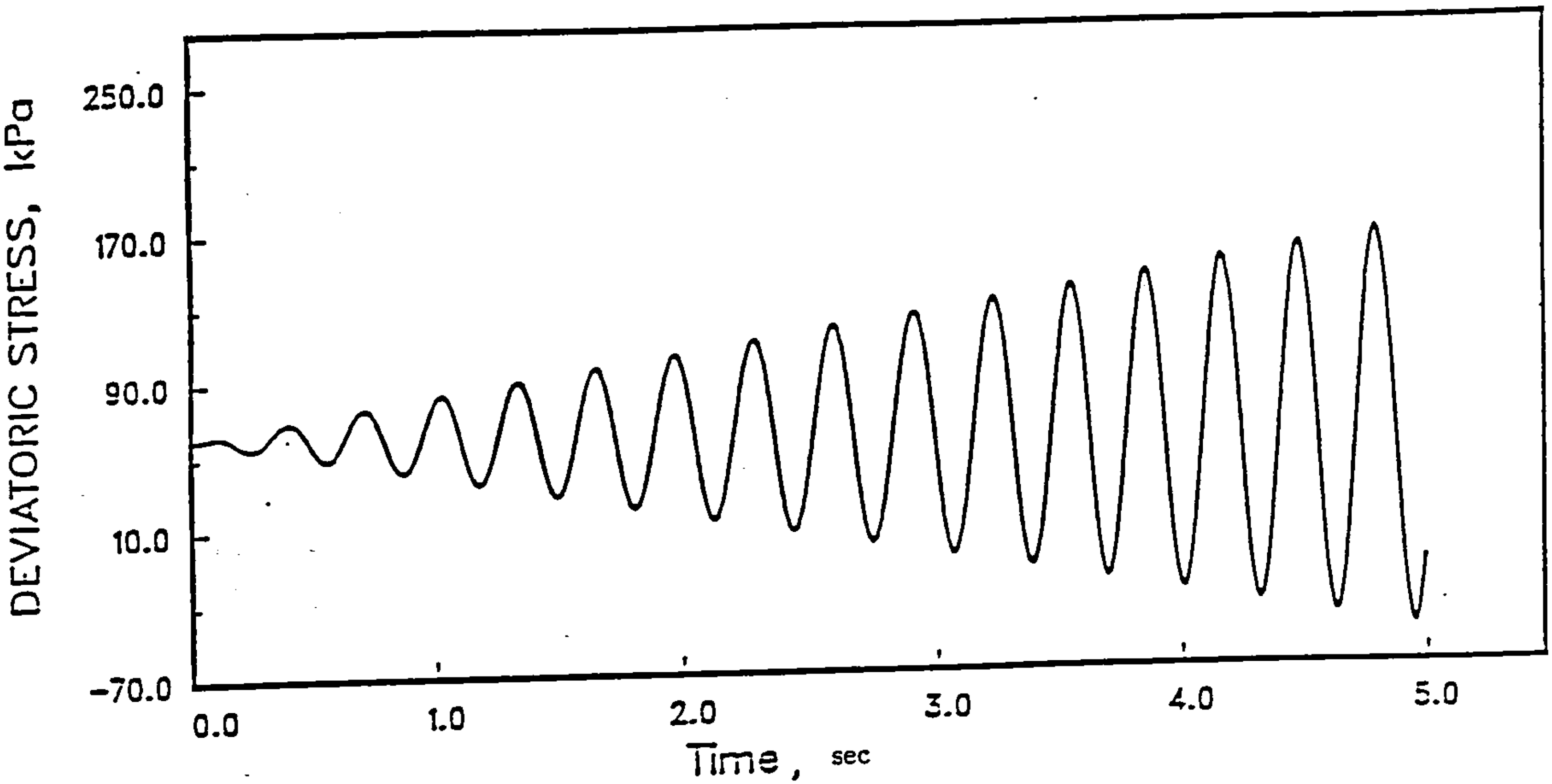

Figure E.16: Variable amplitude cyclic loading input data

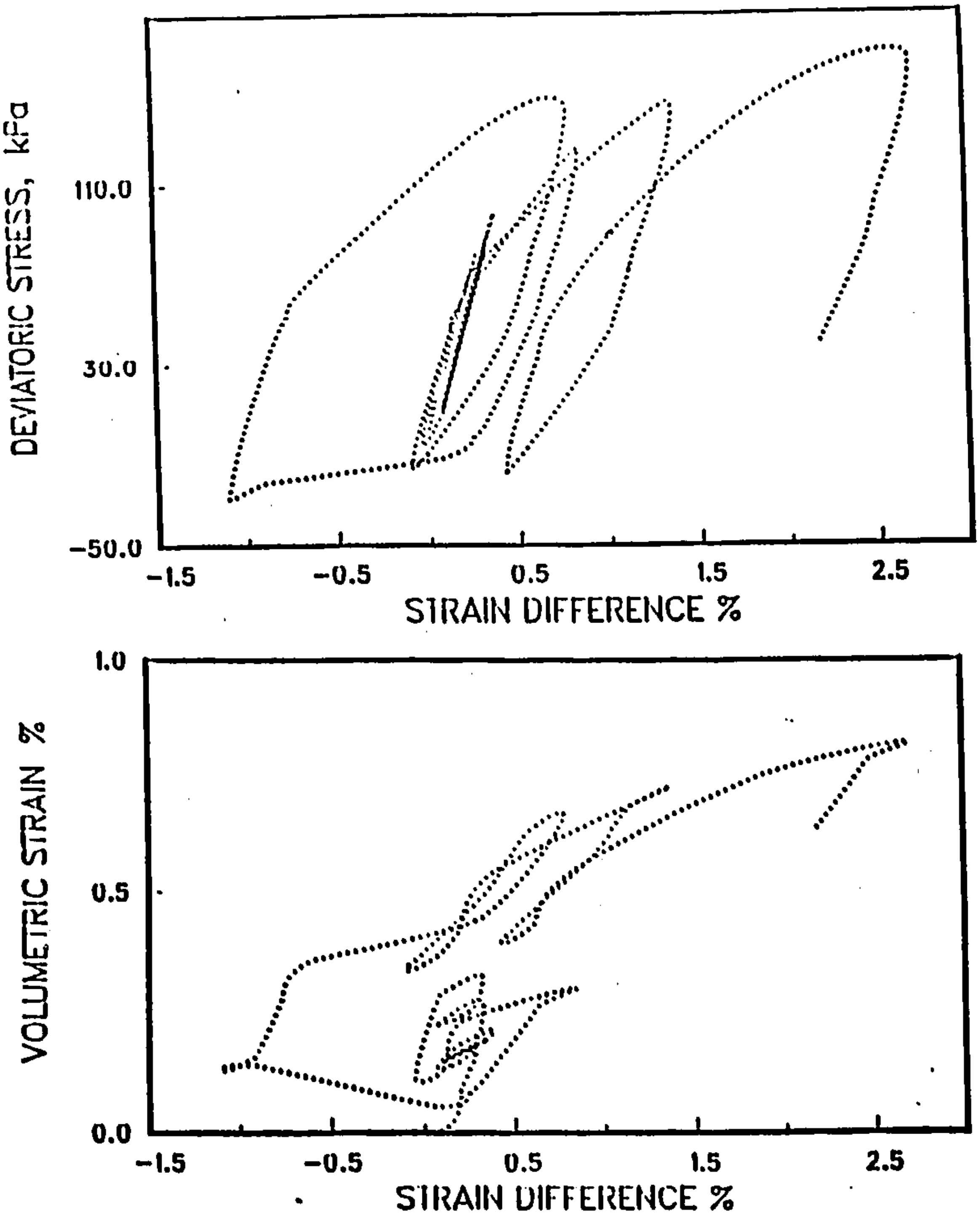

Figure E.17: Model simulation of the shear stress strain and volumetric strain versus shear strain curves for variable amplitude cyclic loading.

a) Shear stress versus shear strain curve.

b) Volumetric strain versus shear strain curve.

Appendix F

COMPUTER PROGRAM PREDICTIONS

F.1 Introduction

The computer program PREDICTIONS consists of a driver and a constitutive pressure sensitive subroutine, Derradji-Aouat and Evgin (1988a). This appendix contains guide to input data and examples of input data and output results.

F.1.1 Guide to Input Data

The input data to the computer program PREDICTIONS consists of control constants and numerical values of the parameters used in the constitutive equations of the model. It should be noted that the input data are free formatted and has to be read in the following sequence:

Card 1: TSO,DATYP,TTYP,CTS.
Card 2: NYS,P_0, W, G_0,B_0.
Card 3: (PP(I,J), I = 1,NYS), J = 1,6)
IF (DATYP = 1) GOTO 4.1
IF (TTYP = 1) GOTO 4.2

4.2 Card 4: STR3, NUC, QINC.

Card 5: (QUN(I), I=1,NUC)

GOTO 5

4.3 Card 4: PE, NUC, QINC, BB.

Card 5: (QUN(I), I=1,NUC)

GOTO 5

4.4 Card 4: AME,CQ_0,CQ,T,TIN

:

5. End

F.1.3 Example of the Input Data

In the following, the input data corresponding to the test shown in Fig 7.4 is presented as an example to illustrate the sequence of input presented in section F.1.2.

```
2     ,    2    ,   1
11    ,  137.89 ,  84.19  ,  14119.66 ,   55066.69  , 137.89
0.    ,  137.89 ,  0.     ,        0. ,          0. ,   0.00
20.96 ,  150.50 ,  27.35  ,  540000.  , -11000000.  ,   0.20
58.05 ,  121.18 ,  70.08  ,   99000.  ,    -84000.  ,  -4.67
65.78 ,  118.53 ,  79.59  ,   15000.  ,     -9200.  ,  -2.81
66.87 ,  111.09 ,  85.88  ,    6900.  ,     -2500.  ,  -1.70
60.83 ,   97.56 ,  87.62  ,    2500.  ,     -1200.  ,  -1.12
54.29 ,  102.23 ,  91.50  ,    1600.  ,      -540.  ,  -0.83
55.06 ,   99.32 ,  96.56  ,    1400.  ,      -500.  ,  -0.92
58.16 ,  100.27 , 104.74  ,    1200.  ,      -480.  ,  -0.95
56.82 ,   97.89 , 110.63  ,     620.  ,      -240.  ,  -0.93
49.38 ,   98.24 , 120.48  ,     230.  ,       -37.  ,  -0.87
137.89,2,10
  0.,400.
```

F.1.3 Example of the Output Results

The results corresponding to the test shown in Fig 7.4 are presented in the following pages. For a given arbitrary stress increment, the computer program provides the following results:

1. The converged stress increment.
2. Active yield surface.
3. The update geometric configuration of the yield surfaces.
4. The strains corresponding to the converged stress increment.

CONVERGED STRESS STATE

SIGMA 1-1	187.890
SIGMA 1-2	0.000
SIGMA 1-3	0.000
SIGMA 2-2	137.890
SIGMA 2-3	0.000
SIGMA 3-3	137.890

ACTIVE YIELD SURFACE 2

UPDATE GEOMETRIC CONFIGURATION

YS	ALPHA 1-1	ALPHA 2-2	ALPHA 3-3	BETA	SIZE
1	33.3335	-16.6665	-16.6665	154.5565	0.0137
2	14.3925	-7.1962	-7.1962	155.0145	28.1704
3	39.6620	-19.8310	-19.8310	124.1924	71.8221
4	44.9435	-22.4717	-22.4717	121.4766	81.5686
5	45.6882	-22.8441	-22.8441	113.8516	88.0149
6	41.5614	-20.7807	-20.7807	99.9853	89.7982
7	37.0931	-18.5465	-18.5465	104.7714	93.7746
8	37.6192	-18.8096	-18.8096	101.7890	98.9604
9	39.7372	-19.8686	-19.8686	102.7626	107.3438
10	38.8217	-19.4108	-19.4108	100.3235	113.3802
11	33.7384	-16.8692	-16.8692	100.6822	123.4751

CORRESPENDING PREDICTED STRAINS

EPSILON 1-1	0.125
EPSILON 1-2	0.000
EPSILON 1-3	0.000
EPSILON 2-2	-0.048
EPSILON 2-3	0.000
EPSILON 3-3	-0.048

CONVERGED STRESS STATE

SIGMA 1-1	227.275
SIGMA 1-2	0.000
SIGMA 1-3	0.000
SIGMA 2-2	137.890
SIGMA 2-3	0.000
SIGMA 3-3	137.890

ACTIVE YIELD SURFACE 3

UPDATE GEOMETRIC CONFIGURATION

YS	ALPHA 1-1	ALPHA 2-2	ALPHA 3-3	BETA	SIZE
1	59.0019	-29.5007	-29.5007	165.9539	3.8360
2	40.0610	-20.0304	-20.0304	156.4119	31.9927
3	42.4381	-21.2191	-21.2191	132.8852	76.8493
4	48.1030	-24.0515	-24.0515	130.0164	87.3028
5	48.9001	-24.4500	-24.4500	121.8554	94.2024
6	44.4832	-22.2416	-22.2416	107.0142	96.1110
7	39.7007	-19.8503	-19.8503	112.1368	100.3670
8	40.2638	-20.1319	-20.1319	108.9448	105.9173
9	42.5307	-21.2654	-21.2654	109.9869	114.8900
10	41.5508	-20.7754	-20.7754	107.3762	121.3508
11	36.1102	-18.0551	-18.0551	107.7601	132.1553

CORRESPENDING PREDICTED STRAINS

EPSILON 1-1	0.280
EPSILON 1-2	0.000
EPSILON 1-3	0.000
EPSILON 2-2	-0.085
EPSILON 2-3	0.000
EPSILON 3-3	-0.085

CONVERGED STRESS STATE

SIGMA 1-1	267.167
SIGMA 1-2	0.000
SIGMA 1-3	0.000
SIGMA 2-2	137.890
SIGMA 2-3	0.000
SIGMA 3-3	137.890

ACTIVE YIELD SURFACE 4

UPDATE GEOMETRIC CONFIGURATION

YS	ALPHA 1-1	ALPHA 2-2	ALPHA 3-3	BETA	SIZE
1	83.8575	-41.9285	-41.9285	176.8022	9.7711
2	64.9166	-32.4582	-32.4582	177.2602	37.9278
3	67.2937	-33.6468	-33.6468	143.7335	82.7843
4	52.4319	-26.2159	-26.2159	141.7169	95.1594
5	52.9790	-26.4895	-26.4895	132.0196	102.0600
6	48.1936	-24.0968	-24.0968	115.9405	104.1278
7	43.0122	-21.5061	-21.5061	121.4904	108.7388
8	43.6223	-21.8111	-21.8111	118.0321	114.7521
9	46.0783	-23.0391	-23.0391	119.1611	124.4733
10	45.0167	-22.5083	-22.5083	116.3327	131.4730
11	39.1222	-19.5611	-19.5611	116.7486	143.1787

CORRESPENDING PREDICTED STRAINS

EPSILON 1-1	0.599
EPSILON 1-2	0.000
EPSILON 1-3	0.000
EPSILON 2-2	-0.197
EPSILON 2-3	0.000
EPSILON 3-3	-0.197

CONVERGED STRESS STATE

SIGMA 1-1	306.227
SIGMA 1-2	0.000
SIGMA 1-3	0.000
SIGMA 2-2	137.890
SIGMA 2-3	0.000
SIGMA 3-3	137.890

ACTIVE YIELD SURFACE 5

UPDATE GEOMETRIC CONFIGURATION

YS	ALPHA 1-1	ALPHA 2-2	ALPHA 3-3	BETA	SIZE
1	103.9329	-51.9662	-51.9662	184.7879	23.7795
2	84.9920	-42.4958	-42.4958	185.2458	51.9362
3	87.3691	-43.6845	-43.6845	151.7191	96.7928
4	72.5073	-36.2536	-36.2536	149.7025	109.1678
5	60.9252	-30.4626	-30.4626	151.8210	117.3678
6	55.2221	-27.6110	-27.6110	132.8491	119.3137
7	49.2850	-24.6425	-24.6425	139.2083	124.5971
8	49.9841	-24.9921	-24.9921	135.2458	131.4874
9	52.7983	-26.3[illegible]1	-26.3991	136.5394	142.6263
10	51.5818	-25.7909	-25.7909	133.2985	150.6468
11	44.8277	-22.4138	-22.4138	133.7751	164.0597

CORRESPENDING PREDICTED STRAINS

EPSILON 1-1	1.074
EPSILON 1-2	0.000
EPSILON 1-3	0.000
EPSILON 2-2	-0.354
EPSILON 2-3	0.000
EPSILON 3-3	-0.354

CONVERGED STRESS STATE

SIGMA 1-1	374.489
SIGMA 1-2	0.000
SIGMA 1-3	0.000
SIGMA 2-2	137.890
SIGMA 2-3	0.000
SIGMA 3-3	137.890

ACTIVE YIELD SURFACE 6

UPDATE GEOMETRIC CONFIGURATION

YS	ALPHA 1-1	ALPHA 2-2	ALPHA 3-3	BETA	SIZE
1	129.6441	-64.8217	-64.8217	197.5185	60.4452
2	110.7032	-55.3514	-55.3514	197.9765	88.6019
3	113.0804	-56.5400	-56.5400	164.4498	133.4585
4	98.2186	-49.1092	-49.1092	162.4332	145.8335
5	86.6364	-43.3181	-43.3181	164.5517	154.0335
6	72.3397	-36.1698	-36.1698	174.0293	156.2981
7	64.0687	-32.0343	-32.0343	180.9656	161.9715
8	64.9774	-32.4887	-32.4887	175.8144	170.9287
9	68.6358	-34.3179	-34.3179	177.4960	185.4088
10	67.0544	-33.5272	-33.5272	173.2830	195.8351
11	58.2743	-29.1371	-29.1371	173.9026	213.2714

CORRESPENDING PREDICTED STRAINS

EPSILON 1-1	3.334
EPSILON 1-2	0.000
EPSILON 1-3	0.000
EPSILON 2-2	-1.328
EPSILON 2-3	0.000
EPSILON 3-3	-1.328

CONVERGED STRESS STATE

SIGMA 1-1	387.890
SIGMA 1-2	0.000
SIGMA 1-3	0.000
SIGMA 2-2	137.890
SIGMA 2-3	0.000
SIGMA 3-3	137.890

ACTIVE YIELD SURFACE 7

UPDATE GEOMETRIC CONFIGURATION

YS	ALPHA 1-1	ALPHA 2-2	ALPHA 3-3	BETA	SIZE
1	137.0941	-68.5631	-68.5631	201.4661	62.9335
2	118.1531	-59.0928	-59.0928	201.9241	91.0902
3	120.5303	-60.2814	-60.2814	168.3973	135.9468
4	105.6685	-52.8506	-52.8506	166.3807	148.3219
5	94.0863	-47.0595	-47.0595	168.4992	156.5218
6	79.7897	-39.9112	-39.9112	177.9768	158.7864
7	65.9905	-32.9952	-32.9952	186.3940	166.8302
8	66.3104	-33.1552	-33.1552	179.4211	174.4352
9	70.0438	-35.0219	-35.0219	181.1373	189.2123
10	68.4300	-34.2150	-34.2150	176.8378	199.8526
11	59.4698	-29.7349	-29.7349	177.4701	217.6465

CORRESPENDING PREDICTED STRAINS

EPSILON 1-1	3.939
EPSILON 1-2	0.000
EPSILON 1-3	0.000
EPSILON 2-2	-1.618
EPSILON 2-3	0.000
EPSILON 3-3	-1.618

CONVERGED STRESS STATE

SIGMA 1-1	395.383
SIGMA 1-2	0.000
SIGMA 1-3	0.000
SIGMA 2-2	137.890
SIGMA 2-3	0.000
SIGMA 3-3	137.890

ACTIVE YIELD SURFACE 8

UPDATE GEOMETRIC CONFIGURATION

YS	ALPHA 1-1	ALPHA 2-2	ALPHA 3-3	BETA	SIZE
1	140.4861	-70.2591	-70.2591	203.3324	65.6929
2	121.5452	-60.7888	-60.7888	203.7904	93.8496
3	123.9223	-61.9774	-61.9774	170.2636	138.7062
4	109.0605	-54.5466	-54.5466	168.2470	151.0813
5	97.4784	-48.7555	-48.7555	170.3655	159.2812
6	83.1817	-41.6072	-41.6072	179.8431	161.5458
7	69.3826	-34.6913	-34.6913	188.2603	169.5896
8	67.6364	-33.8182	-33.8182	183.0091	177.9235
9	71.3522	-35.6761	-35.6761	184.5208	192.7467
10	69.7082	-34.8541	-34.8541	180.1411	203.5857
11	60.5806	-30.2903	-30.2903	180.7852	221.7121

CORRESPENDING PREDICTED STRAINS

EPSILON 1-1	4.323
EPSILON 1-2	0.000
EPSILON 1-3	0.000
EPSILON 2-2	-1.799
EPSILON 2-3	0.000
EPSILON 3-3	-1.799

CONVERGED STRESS STATE

SIGMA 1-1	415.633
SIGMA 1-2	0.000
SIGMA 1-3	0.000
SIGMA 2-2	137.890
SIGMA 2-3	0.000
SIGMA 3-3	137.890

ACTIVE YIELD SURFACE 9

UPDATE GEOMETRIC CONFIGURATION

YS	ALPHA 1-1	ALPHA 2-2	ALPHA 3-3	BETA	SIZE
1	154.0874	-77.0597	-77.0597	210.1214	65.5209
2	135.1464	-67.5894	-67.5894	210.5793	93.6776
3	137.5236	-68.7780	-68.7780	177.0526	138.5341
4	122.6618	-61.3472	-61.3472	175.0360	150.9092
5	111.0796	-55.5561	-55.5561	177.1545	159.1091
6	96.7829	-48.4078	-48.4078	186.6321	161.3738
7	82.9838	-41.4918	-41.4918	195.0492	169.4175
8	81.2377	-40.6188	-40.6188	189.7980	177.7514
9	72.0656	-36.0327	-36.0327	186.3657	194.6739
10	70.2048	-35.1024	-35.1024	181.4244	205.0361
11	61.0122	-30.5061	-30.5061	182.0731	223.2915

CORRESPENDING PREDICTED STRAINS

EPSILON 1-1	5.500
EPSILON 1-2	0.000
EPSILON 1-3	0.000
EPSILON 2-2	-2.383
EPSILON 2-3	0.000
EPSILON 3-3	-2.383

CONVERGED STRESS STATE

SIGMA 1-1	434.343
SIGMA 1-2	0.000
SIGMA 1-3	0.000
SIGMA 2-2	137.890
SIGMA 2-3	0.000
SIGMA 3-3	137.890

ACTIVE YIELD SURFACE 10

UPDATE GEOMETRIC CONFIGURATION

YS	ALPHA 1-1	ALPHA 2-2	ALPHA 3-3	BETA	SIZE
1	163.4444	-81.7382	-81.7382	215.1620	70.8305
2	144.5034	-72.2679	-72.2679	215.6200	98.9872
3	146.8806	-73.4565	-73.4565	182.0933	143.8438
4	132.0188	-66.0257	-66.0257	180.0767	156.2189
5	120.4367	-60.2346	-60.2346	182.1952	164.4188
6	106.1400	-53.0863	-53.0863	191.6728	166.6834
7	92.3409	-46.1703	-46.1703	200.0899	174.7272
8	90.5947	-45.2973	-45.2973	194.8387	183.0611
9	81.4226	-40.7112	-40.7112	191.4064	199.9835
10	73.0128	-36.5063	-36.5063	188.6807	213.2367
11	63.0073	-31.5036	-31.5036	188.0269	230.5933

CORRESPENDING PREDICTED STRAINS

EPSILON 1-1	7.552
EPSILON 1-2	0.000
EPSILON 1-3	0.000
EPSILON 2-2	-3.390
EPSILON 2-3	0.000
EPSILON 3-3	-3.390

CONVERGED STRESS STATE

SIGMA 1-1	442.246
SIGMA 1-2	0.000
SIGMA 1-3	0.000
SIGMA 2-2	137.890
SIGMA 2-3	0.000
SIGMA 3-3	137.890

ACTIVE YIELD SURFACE 11

UPDATE GEOMETRIC CONFIGURATION

YS	ALPHA 1-1	ALPHA 2-2	ALPHA 3-3	BETA	SIZE
1	167.7158	-83.8739	-83.8739	217.4392	72.5137
2	148.7749	-74.4036	-74.4036	217.8972	100.6704
3	151.1520	-75.5923	-75.5923	184.3704	145.5270
4	136.2902	-68.1614	-68.1614	182.3538	157.9021
5	124.7081	-62.3703	-62.3703	184.4723	166.1020
6	110.4114	-55.2220	-55.2220	193.9499	168.3666
7	96.6123	-48.3061	-48.3061	202.3671	176.4104
8	94.8661	-47.4330	-47.4330	197.1159	184.7443
9	85.6941	-42.8470	-42.8470	193.6835	201.6667
10	77.2842	-38.6421	-38.6421	190.9578	214.9199
11	63.6373	-31.8186	-31.8186	189.9069	232.8988

CORRESPENDING PREDICTED STRAINS

EPSILON 1-1	9.614
EPSILON 1-2	0.000
EPSILON 1-3	0.000
EPSILON 2-2	-4.415
EPSILON 2-3	0.000
EPSILON 3-3	-4.415

Appendix G

COMPUTER PROGRAM SIMULATIONS

G.1 User's Guide for SIMULATIONS

The computer program SIMULATIONS consists of a driver and a subroutine for the pressure non-sensitive model, Derradji-Aouat and Evgin(1988b). This appendix contains guide to input data and examples of input data and output results.

The input data to the computer program SIMULATIONS is the same as the PREDICTIONS input data. Since the computer code SIMULATIONS was restricted to monotonic loading conditions, the value of CST does not exist.

G.1.1 Example of the Input Data

In the following, the input data correspending to the test shown in Fig 7.7 is presented as an example to illustrate the sequence of input data.

```
2    ,    2     ,   1     ,   1
10   ,  137.89  ,  00.00  ,  6090.79  ,    16242.09
0.   ,  137.89  ,  0.     ,       0.  ,          0.  ,    0.00
         26.06     148.13         49.27    0.26E+06     -.14E+07       -3.74
         55.80     131.02         93.75    0.80E+04     -.11E+05       -1.02
         53.18     124.67        117.36    0.88E+03     -.50E+04       -0.89
         58.53     119.50        137.68    0.48E+03     -.84E+03       -0.85
         66.65     118.94        167.86    0.51E+03     -.63E+03       -1.10
         72.85     121.41        189.66    0.56E+03     -.24E+03       -1.25
         83.33     131.59        214.46    0.55E+03     -.24E+03       -1.38
         91.08     133.40        230.77    0.28E+03     -.15E+03       -1.41
         94.64     135.28        244.72    0.25E+03     -.50E+02       -1.50
137.89,2,10
0.,900.
```

G.1.2 Example of the Output Results

The results corresponding to the test shown in Fig 7.7 are presented in the following pages. For a given arbitrary total stress increment, the computer program provides the following results:

1. The converged effective stress increment.
2. Active yield surface.
3. The strains and pore water pressure corresponding to the converged effective stress increment.

INITIAL MODEL PARAMETERS

GO = 6090.79 BO = 16242.09 lambda = 0.00000

	ALPHA	BETA	K	H	B	A
1	0.00	137.89	0.00	0.00E+00	0.00E+00	0.00
2	26.06	148.13	49.27	0.26E+06	-.14E+07	-3.74
3	55.80	131.02	93.75	0.80E+04	-.11E+05	-1.02
4	53.18	124.67	117.36	0.88E+03	-.50E+04	-0.89
5	58.53	119.50	137.68	0.48E+03	-.84E+03	-0.85
6	66.65	118.94	167.86	0.51E+03	-.63E+03	-1.10
7	72.85	121.41	189.66	0.56E+03	-.24E+03	-1.25
8	83.33	131.59	214.46	0.55E+03	-.24E+03	-1.38
9	91.08	133.40	230.77	0.28E+03	-.15E+03	-1.41
10	94.64	135.28	244.72	0.25E+03	-.50E+02	-1.60

PRESSURE NON SENSITIVE SIMULATION

ACTIVE YIELD SURFACE 2

CONVERGED EFFECTIVE STRESS STATE

SIGMA 1-1	212.302
SIGMA 1-2	0.000
SIGMA 1-3	0.000
SIGMA 2-2	137.890
SIGMA 2-3	0.000
SIGMA 3-3	137.890

CORRESPENDING PREDICTED STRAINS

EPSILON 1-1	0.406
EPSILON 1-2	0.000
EPSILON 1-3	0.000
EPSILON 2-2	-0.203
EPSILON 2-3	0.000
EPSILON 3-3	-0.203

GENERATED PORE WATER PRESSURE 10.102

ACTIVE YIELD SURFACE 3

CONVERGED EFFECTIVE STRESS STATE

SIGMA 1-1	274.656
SIGMA 1-2	0.000
SIGMA 1-3	0.000
SIGMA 2-2	137.890
SIGMA 2-3	0.000
SIGMA 3-3	137.890

CORRESPENDING PREDICTED STRAINS

EPSILON 1-1	1.102
EPSILON 1-2	0.000
EPSILON 1-3	0.000
EPSILON 2-2	-0.551
EPSILON 2-3	0.000
EPSILON 3-3	-0.551

GENERATED PORE WATER PRESSURE 30.180

ACTIVE YIELD SURFACE 4

CONVERGED EFFECTIVE STRESS STATE

SIGMA 1-1	295.091
SIGMA 1-2	0.000
SIGMA 1-3	0.000
SIGMA 2-2	137.890
SIGMA 2-3	0.000
SIGMA 3-3	137.890

CORRESPENDING PREDICTED STRAINS

EPSILON 1-1	2.184
EPSILON 1-2	0.000
EPSILON 1-3	0.000
EPSILON 2-2	-1.092
EPSILON 2-3	0.000
EPSILON 3-3	-1.092

GENERATED PORE WATER PRESSURE 40.003

ACTIVE YIELD SURFACE 5

CONVERGED EFFECTIVE STRESS STATE

SIGMA 1-1	319.907
SIGMA 1-2	0.000
SIGMA 1-3	0.000
SIGMA 2-2	137.890
SIGMA 2-3	0.000
SIGMA 3-3	137.890

CORRESPENDING PREDICTED STRAINS

EPSILON 1-1	4.755
EPSILON 1-2	0.000
EPSILON 1-3	0.000
EPSILON 2-2	-2.377
EPSILON 2-3	0.000
EPSILON 3-3	-2.377

GENERATED PORE WATER PRESSURE 50.362

ACTIVE YIELD SURFACE 6

CONVERGED EFFECTIVE STRESS STATE

SIGMA 1-1	346.784
SIGMA 1-2	0.000
SIGMA 1-3	0.000
SIGMA 2-2	137.890
SIGMA 2-3	0.000
SIGMA 3-3	137.890

CORRESPENDING PREDICTED STRAINS

EPSILON 1-1	8.699
EPSILON 1-2	0.000
EPSILON 1-3	0.000
EPSILON 2-2	-4.349
EPSILON 2-3	0.000
EPSILON 3-3	-4.349

GENERATED PORE WATER PRESSURE 46.566

ACTIVE YIELD SURFACE 7

CONVERGED EFFECTIVE STRESS STATE

SIGMA 1-1	365.371
SIGMA 1-2	0.000
SIGMA 1-3	0.000
SIGMA 2-2	137.890
SIGMA 2-3	0.000
SIGMA 3-3	137.890

CORRESPENDING PREDICTED STRAINS

EPSILON 1-1	11.402
EPSILON 1-2	0.000
EPSILON 1-3	0.000
EPSILON 2-2	-5.701
EPSILON 2-3	0.000
EPSILON 3-3	-5.701

GENERATED PORE WATER PRESSURE 40.538

ACTIVE YIELD SURFACE 8

CONVERGED EFFECTIVE STRESS STATE

SIGMA 1-1	389.980
SIGMA 1-2	0.000
SIGMA 1-3	0.000
SIGMA 2-2	137.890
SIGMA 2-3	0.000
SIGMA 3-3	137.890

CORRESPENDING PREDICTED STRAINS

EPSILON 1-1	15.262
EPSILON 1-2	0.000
EPSILON 1-3	0.000
EPSILON 2-2	-7.631
EPSILON 2-3	0.000
EPSILON 3-3	-7.631

GENERATED PORE WATER PRESSURE 27.946

ACTIVE YIELD SURFACE 9

CONVERGED EFFECTIVE STRESS STATE

SIGMA 1-1	408.380
SIGMA 1-2	0.000
SIGMA 1-3	0.000
SIGMA 2-2	137.890
SIGMA 2-3	0.000
SIGMA 3-3	137.890

CORRESPENDING PREDICTED STRAINS

EPSILON 1-1	19.136
EPSILON 1-2	0.000
EPSILON 1-3	0.000
EPSILON 2-2	-9.568
EPSILON 2-3	0.000
EPSILON 3-3	-9.568

GENERATED PORE WATER PRESSURE 26.232

ACTIVE YIELD SURFACE 10

CONVERGED EFFECTIVE STRESS STATE

SIGMA 1-1	418.137
SIGMA 1-2	0.000
SIGMA 1-3	0.000
SIGMA 2-2	137.890
SIGMA 2-3	0.000
SIGMA 3-3	137.890

CORRESPENDING PREDICTED STRAINS

EPSILON 1-1	22.347
EPSILON 1-2	0.000
EPSILON 1-3	0.000
EPSILON 2-2	-11.174
EPSILON 2-3	0.000
EPSILON 3-3	-11.174

GENERATED PORE WATER PRESSURE 20.840

UNIVERSITÉ D'OTTAWA
UNIVERSITY OF OTTAWA